Development of Plough-able RFID Sensor Network Systems for Precision Agriculture

A thesis submitted to the University of Manchester
for the degree of Doctor of Philosophy
in the Faculty of Engineering and Physical Sciences

2016

By
Chuan Wang
School of Electrical and Electronic Engineering

Contents

List of Tables

List of Figures

Abstract

There is a growing interest in employing sub-soil sensing systems to support precision agriculture. This thesis presents the design of an RFID sub-soil sensing system which is based on integrating passive RFID technology and sub-soil sensing technology. The proposed RFID sub-soil system comprises of an above-ground RFID reader and a number of RFID sub-soil sensor nodes. The key feature of the system is that the sensor nodes do not require an on-board battery, as they are capable of harvesting energy from the ElectroMagnetic (EM) field generated by the RFID reader. The sensor nodes then transmit sensor measurements to the reader wirelessly through soil. With the proposed RFID sub-soil system, the high path loss of the sub-soil wireless channel is a significant problem which leads to the challenge for the system to achieve an acceptable Quality of Service (QoS). In this project, the path loss in soil has been characterised through CST simulations. In the simulations, the effect of the soil on the sensor node antenna has also been investigated. This thesis also presents the design and implementation of a programmable RFID reader platform and an embedded RFID sensor node prototype. The RFID reader platform is implemented using a National Instruments (NI) PXI system, and it is configured and controlled by NI LabVIEW software. The sensor node prototype is capable of harvesting RF energy and transmitting sensor measurements from a temperature sensor through backscatter communication. A series of sub-soil experiments have been carried out to evaluate the performance of the RFID sensor node prototype using the PXI-based RFID reader platform. The experimental results are presented and analysed in this thesis. Additionally, this work has explored trade-offs in the system design, and these design trade-offs are summarised and described.

Declaration

No portion of the work referred to in this thesis has been submitted in support of an application for another degree or qualification of this or any other university or other institute of learning.

Copyright

Acknowledgements

I'm truly indebted and grateful to my supervisors, Mr. Peter R. Green and Prof. Danielle George for their guidance, advice and encouragement throughout this undertaking. I am immensely thankful to National Instruments (UK) and the School of Electrical and Electronic Engineering at the University for their financial support. I would also like to express my deep gratitude to Mr. Sacha Emery and Ms. Hannah Wade of National Instruments (UK) for their technical support, Mr. Hassan Khalili, Mr. David Cuadrado-Calle, Dr. William Mcgenn, Mr. Lee Evans, and Mr. Matthew Nancekievill for their kind help and friendship. Last but not least, I would like to thank my beloved parents and Xia, for their endless support, love and understanding.

Glossary

ADC	Analogue-to-Digital Converter
ASK	Amplitude Shift Keying
BER	Bit Error Rate
BLE	Backscatter Link Frequency
C1G2	Class 1 Generation 2
CW	Continuous Wave
CPU	Central Processing Unit
CPWG	CoPlanar WaveGuide
CRC	Cyclic-Redundancy Check
CST	Computer Simulation Technology
DAC	Digital-to-Analogue Converter
DDC	Digital Down-Converter
EC	Electrical Conductivity
EDLC	Electric Double-Layer Capacitor
EM	ElectroMagnetic
ERP	Effective Radiated Power
ESA	Electrical Sub-Assembly
ESR	Equivalent Series Resistance
FCC	Federal Communications Commission
FIFO	First In First Out
FM0	Bi-phase space coding format
FPGA	Field-Programmable Gate Array
FSPL	Free-Space Path Loss
GIS	Geographic Information System
GPR	Ground-Penetrating Radar
GPS	Global Positioning System

GUI	Graphic User Interface
I2C	Inter-Integrated Circuit
IC	Integrated Circuit
IDE	Integrated Development Environment
IF	Intermediate Frequency
IQ	In-phase and Quadrature-phase
ISM	Industrial, Scientific and Medical
kph	Kilometres Per Hour
LAN	Local-Area Network
NI	National Instruments
OFCOM	Office of Communications UK
OS	Operating System
P2P	Peer-to-Peer
PC	Personal Computer
PCB	Printed Circuit Board
PEC	Perfect Electric Conductor
PIE	Pulse Interval Encoding
PSK	Phase Shift Keying
PVC	PolyVinyl Chloride
QoS	Quality of Service
RF	Radio Frequency
RFID	Radio Frequency IDentification
RTC	Real-Time Clock
Rx	Receiver
PW	Pulse Width
SD	Secure Digital
SDR	Software-Defined Radio
SMA	SubMiniature version A
SMD	Surface Mounted Devices
SNR	Signal-to-Noise Ratio
SPI	Serial Peripheral Interface
SRR	Successful Reading Rate

Tx	Transmitter
UHF	Ultra High Frequency
VI	Virtual Instruments
VNA	Vector Network Analyser
VSA	Vector Signal Analyse
VSG	Vector Signal Generator
WSN	Wireless Sensor Network
XLP	eXtremely Low Power

Chapter 1

Introduction

More than 2.8 billion people around the World are affected by water scarcity. This problem is becoming increasingly serious owing to the need for the use of new agricultural lands, for example in the desert [9], to feed a growing World population. There is a growing interest in implementing electronic systems using emerging modern technologies for precision agriculture to tackle the challenge of world food and water shortages. Precision agriculture is commonly defined as a farming management concept, which merges modern technologies such as sensing technology and wireless communication technology with farming methods [10]. The aim of developing precision agriculture is to optimise the field-level management to improve farming efficiency and also enhance quality of the farm products [11].

1.1 Motivations

The research described in this thesis is primarily motivated by the significant benefits of tackling the challenge of world food and water shortage using sub-soil sensing systems for supporting precision agriculture. Sub-soil sensing systems enable farmers to monitor the sub-soil environmental parameters, such as soil temperature, moisture and nutrients which are essential for crop growth. Sensor measurements provided by these systems can be typically used to predict the actual amount of elements, such as nutrients, water, herbicides and pesticides, required by a field. Compared to traditional terrestrial sensing systems, sub-soil sensing systems enable more precise control in adjusting suitable underground

conditions for crop growth. For example, a sub-soil sensing system equipped with moisture sensors is able to measure the soil moisture content at the vicinity of the rhizosphere. This helps farmers to supply the amount of water actually needed by the crops and also to avoid over-watering.

The other motivation of this work is the potential benefits to farmers from a battery-free communication system being capable of wireless sub-soil sensing. The vast majority of sub-soil sensing systems [3, 12, 13, 14, 15, 16, 17, 18, 19, 20] do not meet requirements of modern farming practice. These systems have two common systems designs: 1) wired sensor nodes are used to avoid the problems of wireless communication through soil, and 2) the sensor nodes are equipped with an on-board battery to supply the sensor node. These two designs will give rise to problems in practice. The wired systems are slow to deploy and are at risk of being damaged by farm machinery. There are farm fields, such as vineyards, where the wired systems can be feasible. When using batteries to supply sub-soil sensor nodes, it is infeasible to retrieve the sensor nodes from below the ground regularly to charge or replace their batteries. In addition, there is a concern that most batteries contain chemical materials [21] which are environmentally unacceptable.

1.2 Aims and Objectives

This PhD project aims to design, implement and evaluate a Radio-Frequency IDentification (RFID) sub-soil sensing system for supporting precision agriculture. The proposed system integrates passive RFID technology and sub-soil sensing technology. Passive RFID is an evolving technology which was originally utilised for identification purposes [22]. With a passive RFID system, the RFID tags are not equipped with an on-board battery, and the tag antenna harvests energy from the EM field generated by the RFID reader. An on-tag microcontroller and RF circuit then transmit data back to the RFID reader. Passive RFID technology provides a potential solution for the implementation of a sensor node in environments where batteries are undesirable or prohibited.

The proposed RFID sub-soil system consists of an RFID reader (interrogator) and a number of RFID sensor nodes. The key feature of the proposed system

is that the sensor nodes do not contain an on-board battery and are capable of harvesting energy from the ElectroMagnetic (EM) field generated by the RFID reader. The sensor nodes transmit sensor measurements to the RFID reader wirelessly through the soil. Chapter 3 describes and analyses the operational requirements of the proposed RFID sub-soil system system. The high level design of the proposed system is presented in Chapter 4.

The primary emphasis of this research is on achieving effective RFID communication through soil. A complete RFID communication involves two links: the power link and the communication link. In the power link, a sub-soil sensor node harvests energy from the RF field generated by the RFID reader. The communication link refers to the transmission of sensor measurements from the sensor node to the RFID reader. The development of sensing technology has not been a focus in this research, but the energy budget of on-board sensors has been considered in the system design. The main objectives of this work can be divided into four categories as described below.

- **EM modelling and simulation** - The first objective was to develop an EM model of the RFID sub-soil system. The EM model can be used to investigate the effect of the soil on the performance of the sub-soil antenna and the path loss in soil.

- **Implementation of a programmable RFID reader platform** - The second objective was to implement a software-defined RFID reader platform, which can be configured to implement a custom communication protocol and to perform system performance evaluation.

- **Design and implementation of a passive RFID sensor node prototype** - The third objective was to design and prototype a passive RFID sensor node by integrating passive RFID technology, embedded system technology and commercial sensors. The sensor node prototype is expected to harvest energy from EM fields and transmitting sensor measurements wirelessly.

- **Evaluation of the RFID sensor node prototype through practical trials** - The fourth objective was to evaluate the performance of the RFID

sensor node prototype. The evaluation involves a series of practical experiments. In the experiments, the following parameters should be considered: the depth of the sensor node within the soil, the height of the reader antenna above the soil, the transmission power of the RFID reader, and the soil moisture content. Soil moisture contents stated in this work refer to a soil volumetric moisture level.

- **Exploration of design trade-offs of the system** - The final objective was to explore design trade-offs of the system by considering a range of parameters such as: the depth of the sensor node, the volume of the sensor node, the energy budget of the sensor node, the transmission power of the RFID reader and the height of the reader antenna.

1.3 Challenges

The challenge for the proposed RFID sub-soil system is to achieve effective wireless communication through soil, and the high path loss of the sub-soil wireless channel is a significant problem. The frequency band of 860 MHz to 960 MHz [6] is a popular range in which most of commercial RFID systems operate. At 900 MHz, the path loss in soil can easily be 40 dB/m greater than in air due to RF absorption by soil constituents [7].

Without an on-board battery, the RFID sub-soil sensor node must harvest energy from the EM field generated by the RFID reader which is positioned above the ground surface. The harvested energy will be typically stored using an energy storage component and then converted to system voltages using a DC/DC converter. Therefore, there will be a charging time for the sensor node to harvest sufficient energy in order to meet the energy budget of the sensor node. The high path loss limits the energy that can be harvested by the sensor node, and so can lead to a long charging time. As will be presented in Chapter 4, the RFID reader can be mounted on a moving tractor to interrogate the sub-soil sensor nodes within a farm field. A long charging time of the sensor node requires the tractor to move at an unacceptably slow speed. Thus, the energy harvesting efficiency of the sensor node and the transmission power of the RFID reader need to be maximised.

In the communication link, the RFID sensor node transmits sensor measurements back to the RFID reader using backscatter modulation. The high path loss in the soil can result in a heavily attenuated signal arriving back at the RFID reader. This would have a direct impact on the Bit Error Rate (BER) performance of the communication link. Thus, there is a need to maximise the power of the backscattered signal arriving at the RFID reader. Potential methods include: increasing the transmission power of the RFID reader, decreasing the depth of the sensor node, and lowering the height of the reader antenna.

In practice, a physically small sensor node is desirable, which makes the node easy to deploy. The node antenna is the size-limiting factor. A larger antenna is typically more efficient at harvesting RF power. However, a larger antenna can lead to a larger sensor node enclosure which affects the system deployment efficiency. Operating at higher frequency will reduce the size of antenna, but the path loss in soil increases with increasing frequency. Hence, there is a need to explore the trade-off between the antenna size and the overall system performance.

With the proposed RFID sub-soil system, the sensor node antenna is positioned in close proximity to the soil which behaves as a lossy medium to EM waves. The soil can affect the antenna radiation pattern, efficiency and resonant frequency [23, 24, 25]. This has the potential to degrade the performance of the proposed RFID sub-soil system. Hence, the influence of the soil on the node antenna must be minimised.

1.4 Structure of Thesis

This thesis consists of 12 chapters, and the descriptions of these chapters are summarised below.

- **Chapter 1 - Introduction**: describes the motivations, aim, objectives and challenges of this project.
- **Chapter 2 - Literature Review**: reviews the development of precision agriculture, the implementations of Wireless Sensor Networks (WSNs) in

agricultural applications, passive RFID technology and the characterisation of wireless underground channels.

- **Chapter 3 - System Requirements Analysis**: captures and analyses the design requirements of the proposed RFID sub-soil system.
- **Chapter 4 - High Level Design**: illustrates the high level design of the proposed RFID sub-soil system.
- **Chapter 5 - CST Electromagnetic Modelling**: presents the design of CST EM models for simulating the proposed RFID sub-soil system.
- **Chapter 6 - CST Simulations and Results**: describes CST simulations for investigating the impact of the soil on a sub-soil antenna and characterising the path loss in soil, and presents the simulation results.
- **Chapter 7 - PXI-based RFID Reader Platform**: shows the design and implementation of an RFID reader platform using a National Instruments (NI) PXI system.
- **Chapter 8 - RFID Sensor Node Prototype**: details the design, implementation and evaluation of a passive RFID sensor node prototype which is capable of harvesting energy from EM fields and transmitting measurements from a temperature sensor through backscatter modulation.
- **Chapter 9 - Sub-soil Experiments**: describes the methods and arrangement of a series of sub-soil experiments for evaluating the performance of the RFID sensor node prototype as well as characterising the path loss in the soil.
- **Chapter 10 - Experimental Results and Analysis**: presents and analyses the experimental results of the sensor node performance evaluation and the path loss characterisation.
- **Chapter 11 - System Design Considerations**: considers the future system design and provides design trade-off analyses.
- **Chapter 12 - Conclusions and Future Work**: summaries the achievements over the period of this project and describes the work which needs to be undertaken in the future.

Chapter 2

Literature Review

2.1 Introduction

This chapter primarily reviews the existing research on developing precision agriculture and Wireless Sensor Networks technology for sub-soil sensing. Section 2.2 describes the development of technologies in precision agriculture. In Section 2.3 recent implementations of Wireless Sensor Networks (WSNs) systems for underground sensing are reviewed. Section 2.4 introduces passive RFID technology in terms of near-field RFID systems and far-field RFID systems. Finally, the research on sub-soil wireless channel is presented in Section 2.5.

2.2 Development of Precision Agriculture

2.2.1 Technologies in precision agriculture

The development of precision agriculture was started in the late 20th century when Johnson et al. [26] put forward the idea of implementing technologies including automation, sensing and location systems in agriculture. The basis of precision agriculture is summarised as - "the spatial and temporal variability in soil and crop factors within a field [27]". Since this variability is significantly affected by soil conditions, such as soil moisture and soil temperature, there is an increasing requirement in precision agriculture for collecting accurate information about the variability of selected soil parameters within a field. Soil samples were taken manually from regions of fields to a laboratory for analysing soil nutrients

in the first application of precision agriculture developed by Soil Teq in USA [28], and this method is called *soil sampling*. Based on the analysed results, farmers are able to map nutritional needs within a field. Fertilising efficiency can then be significantly improved by meeting actual needs of crops and avoiding over-fertilising. *Soil sampling* is still being used in precision agriculture [29], but it is not an efficient method due to the manual nature of the sampling task.

Global Positioning Systems (GPSs), Geographic Information Systems (GISs) and Remote Sensing systems can also provide technologies which maximise benefits to farmers from precision agriculture. A GPS is able to provide accurate location information which helps farmers map the measured data in a field and analyse the in-field variability. A GIS enables farmers to visualise agricultural environments by collecting, computing and analysing background information such as ecological conditions, actual physiognomy, and crops conditions [30]. There is an increasing interest in developing Remote Sensing systems for large-scale crop inventory and yield predictions [31],[32] [33] and [34]. Most of the Remote Sensing systems typically integrate GPS technology, GIS technology and satellite imagery or camera imagery. But using those systems is always expensive and most of farmers cannot afford it. In addition, farmers will need training to extract useful information from these systems [31].

There are researchers who are seeking to develop sensors technology for achieving efficient sub-soil sensing. Those sensors generally convert physical quantities into signals which can be measured by an observer or an instrument. Adamchuk et al. [11] reviewed the recent reported concepts for the on-the-go measurements of soil mechanical, physical and chemical characteristics, and summarised five sensors types:

- electrical and electromagnetic;
- optical and radiometric sensors;
- mechanical sensors;
- acoustic sensors;
- pneumatic sensors.

With the exception of electrical and electromagnetic, most of sensors technologies are still under development. For example, Electrical Conductivity (EC) sensors have been already deployed in several commercial implementations for precision agriculture [35, 36]. These sensors are designed to measure the soil EC map which correlates with soil properties including soil texture, soil moisture, organic matter level and salinity [37]. Two commercial EC sensing systems, Veris 3100 [38] and EM38 [39] designed for agricultural applications were described and compared by Sudduth et al.[40]. The Veris 3100 system is equipped with six coulters which are rolled through the field for measuring the Electrical Conductivity (EC) of the soil [38]. The EM38 system measures the soil EC map using the non-contact electromagnetic induction sensors which can be moved over a field with farm machinery [39].

These EC sensing systems provide an automated method of sampling soil properties with farm machinery which is more efficient than manual *soil sampling*. But the EC sensing systems still cannot significantly improve farming efficiency as the information provided by the system cannot be directly used in farming activities. For example, when using an EC sensing system for irrigation, the farmers will need to firstly analyse and calibrate the collected soil EC data, and then implement irrigation through controlling the volume of water outputs based on the analysed result. However, the change of soil environments is dynamic, and the analysed data cannot reflect the actual soil moisture levels in real time. In addition, factors such as farm machinery speed, soil temperature and moisture can have significant effects on EC measurements in soil [40], which will lead to an inaccurate analysis.

2.2.2 Wired and fixed sensor networks systems

Rather than the EC sensing system, an increasing number of farmers are considering commercial sensors which are capable of directly providing measurements of environmental parameters. For example, the SM 150 moisture sensor [41] provides the measurement of soil moisture level by generating a stable analogue output which is a function of the soil moisture level. When burying the SM 150 moisture sensor within soil, the farmers can simply obtain the soil moisture

measurements within seconds by electrically powering the sensor and then measuring the voltage output from the sensor. The energy budget of the sensor is approximately 90 mW with a warm-up time of 0.5 s - 1.0 s, and the sensor can be powered using batteries. In addition to soil moisture, there are commercial sensors which can be used in agriculture for measuring environmental parameters such as temperature, pH value, pressure and oxygen which farmers are interested in. Table 2.1 presents the examples of the sensors.

Table 2.1: Attributes of commercial sensors.

Sensors	Power budget (mW)	Maximum dimension (cm)
SM 150 soil moisture [41]	90	5.1
LMP91200-based pH [42]	0.195 (pH mode)	0.66
ICT02 soil oxygen [43]	240	6.5
Honeywell pressure [44]	10	1.6
TMP 37 temperature [45]	0.165	0.5

The LMP91200-based pH sensor or the SM 150 soil moisture sensor requires two electrodes to have a physical contact with soil for sensing soil pH values or soil moisture levels. The use of the electrodes increases the size of the sensors. For example the SM 150 typically uses the 9.1 cm long electrodes, which increases the overall sensor size to 14 cm [41]. The ICT02 soil oxygen sensor does not need to use electrodes for sensing soil oxygen content, but it is required to be totally buried within soil [43]. Regarding the TMP37 temperature sensor [45] and the Honeywell pressure sensor [44], they have to be enclosed by water-proof materials when using them for measuring temperature and pressure in sub-soil environments. Some of the sensors will operate with response time or warm-up time which can lead to the high energy budget. The SM 150 soil moisture sensor requires a warm-up time of 0.5 s - 1.0 s [41], the ICT02 soil oxygen sensor can spend approximately 1 s [43] on logging sensor measurements, and the Honeywell pressure sensor has a response time of 5 ms [44].

Current sensing technologies potentially provide a method of sensing farming environments which is based on in-situ sensing using commercial sensors. Farmers

can physically walk over a field to repeat the process of manually burying commercial sensors and then logging sensor measurements from the sensors. But this method has a low efficiency in achieving sub-soil sensing especially in large-scale farms. Alternatively, a sensor network can be designed based on burying sensors at various locations in soil and wiring the sensors to data-loggers on the surface (as shown in Figure 2.1). The data-logger will store readings from the sensors and then transmit the sensory data to a hub through cables. Farmers always use fixed frames for planting grapes. A vineyard is a potential field for implementing a wired sensor network system, where the sensors and the data-loggers have a fixed deployment. However, for those farm fields which involve periodical farming activities such as ploughing, seeding or crop harvesting with farm machinery, it is hard to see any possibility of using the fixed and wired sensor network system in the farm fields. In addition, the wired system has the risk of mechanical damage from farm machinery and the risk of theft.

Figure 2.1: A CR5000 data-logger from Campbell Scientific is capable of monitoring up to 40 sensors and communicating with a PC via direct connection [3] .

In order to find a more efficient solution to the implementation of sub-soil

sensing systems for supporting precision agriculture, there is an increasing focus on integrating sensing technology and wireless communication technology.

2.3 Wireless Sensor Networks Systems

2.3.1 About wireless sensor networks

The development of sensing technology, wireless communication technology and computation technology in recent years has lead to increasing research in developing wireless data-collection devices for supporting precision agriculture, and Wireless Sensor Networks (WSNs) system is one example [46]. A WSN system shown in Figure 2.2 comprises of a number of sensor nodes which are capable of measuring physical and/or environmental conditions (e.g. temperature, pressure, humidity or vibration) at different locations, and a data-logger which interrogates the sensor nodes. The sensor measurements are transmitted from the sensor nodes by an on-board communication unit to the data-logger through wireless links [47].

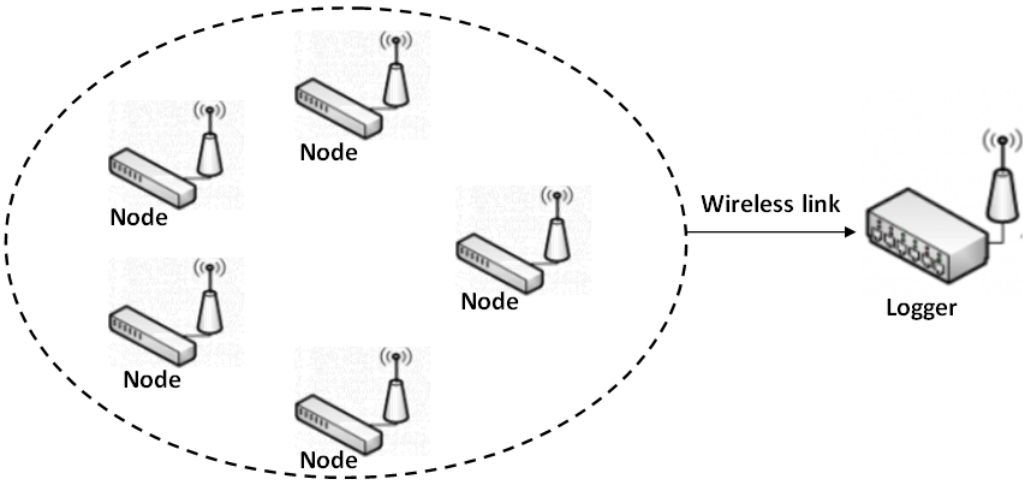

Figure 2.2: WSNs system diagram [4].

Johnson et al. [48] reviewed and compared six of the currently available WSN node (mote) platforms: TelosB/Tmote Sky [49], Mica2/MicaZ [50], SHIMMER [51], IRIS [52], Sun SPOT [53] and EZ430-RF2500 [54]. Those node platforms are compatible with the majority of commercial sensors, and they primarily include a microcontroller for data-logging sensor information and a radio integrated circuit for transmitting the logged sensory data. Table 2.2 presents the summarised

attributes of the node platforms in physical size, communication protocol, and current consumption of the on-board radio integrated circuit.

Table 2.2: Attributes of the commercial node platforms.

Node Platform	Physical Size (cm)	Communication Protocol	Current Consumption (mA)
TelosB/Tmote Sky	3.2 x 6.55 x 0.66	Zigbee	17.4
Mica2/MicaZ	3.175 x 5.72 x 0.635	ISM	10.4
SHIMMER	2.03 x 4.45 x 1.2	Zigbee/Bluetooth	17.4
IRIS	3.175 x 5.72 x 0.64	Zigbee	16.5
Sun SPOT	6.35 x 3.81 x 2.54	Zigbee	17.4
EZ430-RF2500	2.95 x 8.06 x 1.09	Zigbee	21.2

The current consumption in Table 2.2 refers to the typical current consumption of the on-board radio integrated circuit when transmitting data. TelosB/Tmote Sky, IRIS, Sun SPOT and EZ430-RF2500 motes primarily employ the radio integrated circuits which are based on Zigbee technology [55]. In addition to the Zigbee radio, SHIMMER mote contains a second Bluetooth [56] radio. Mica2/MicaZ mote can operate in the Industrial, Scientific and Medical (ISM) frequency range from 300 MHz to 1000 MHz, and its power consumption in Table 2.2 is measured at 433 MHz. All node platforms are powered using on-board batteries.

WSNs technology can be an integral part of other system. Akyildiz et.al [57] reviewed the applications of WSNs systems which primarily include:

- military applications;
- environmental applications;
- health applications;
- home applications.

WSNs systems have also been considered as useful tools which can help develop precision agriculture due to their potential benefits to environmental sensing in farm fields. With a WSN system, farmers can achieve efficient environmental monitoring based on wirelessly logging sensor measurements from the sensor nodes.

2.3.2 Wireless sensor network systems in precision agriculture

The implementations of WSNs in precision agriculture were reviewed by Ruiz-Garcia et al. [12], and most of them were designed for farm environmental monitoring. Greenhouses have strict requirements on environmental conditions including temperature, humidity and soil properties. Yoo et al. [13] placed a range of Agriculture sensor nodes (A-nodes) for monitoring the greenhouses in Dongbu Handong Seed Research Centre. The A-node integrates various sensors including ambient light sensor, temperature sensor and humidity sensor with a ZigBee compatible transceiver which is able to transmit the sensor measurements to a sink node wirelessly through air. The sensor measurements that are collected by the sink nodes can be used to control the climate in the greenhouses within an acceptable range.

Efficient water management is a major concern in precision agriculture, particularly when problems of drought have been increasing in seriousness. Kim et al. [14] developed and tested an in-field distributed WSN system for remote sensing and site specific irrigation. The system provides sensory data including soil temperature, moisture, humidity, and solar radiation level. All sensor measurements are transmitted from the sensor node to a control station using a low-cost Bluetooth wireless radio unit above ground. The received sensory data is then used to control the volume of water output using an irrigation controller. The daily energy consumption of the sensor node is estimated as 23.8 Wh, which is based on a data logger that is running at a scanning interval of 10 s and the Bluetooth radio transmission at a downloading interval of 15 min.

Garcia-Sanchez presented an integrated WSNs system for small-size and scattered crops monitoring, video-surveillance and process of cultivations control [15]. The system communicates wirelessly using IEEE 802.15.4 technology [55] and provides sensor measurements from a soil moisture sensor. The monitoring node has a peak current consumption of 110 mA with a required power-on time of 2 s. WSN systems have also been implemented in other farming applications, for instance precision viticulture [16] and pest control [17]. In summary, there is a common design element to these systems in achieving sub-soil sensing, which is based on using wired sensors in order to avoid communication links through soil.

2.3.3 Underground sensing systems

In addition to agricultural applications, WSNs can significantly facilitate the communication in underground tunnels, such as caverns, road/subway tunnels and underground mines. Underground mining is a hazardous industrial activity, and the major factors leading to the risk of fatality in an underground mine primarily include [58]:

- underground explosions and fires;
- geotechnical hazards;
- underground transport.

Reliable and efficient communication networks are needed to improve the safety and productivity in underground mines by providing a communication link between the underground mine and locations above the ground [18]. Since the traditional wired communication system is typically high-cost and hard to deploy, there is increasing research in implementing WSNs systems in underground mines or road/subway tunnels to achieve underground communication and monitoring [59], [60], [61], [62], [63], [64]. It has been found that radio waves propagation in underground mines or road tunnels can be affected by the bounding of the passageway or the tunnel walls [59], [60]. The primary focus of most research is either on analysing models for the wireless channel or on investigating EM wave propagation behaviour in underground mines and underground tunnels [61], [62], [63], [64]. For example, Sun and Akyildiz [61] analysed the typical structures of current underground mine and road tunnels and theoretically investigated the

wireless tunnel channel and the underground mine channel. Practical experiments have been carried out in an underground gallery at a 70 m depth by Boutin et al. [64] to investigate wireless propagation behaviours in the mine channel at the frequency of 2.4 GHz and 5.8 GHz. Although the mine is underground, the wireless communication of the system is through the air in the passageways of the mine.

WSNs technology has also been used to implement the sub-soil sensing systems for predicting landslides [20] and detecting volcano activities [19]. The system for predicting landslides used Mica2 [50] nodes which were interfaced with stain gauges. Although the sensors were buried at depths ranging from 25 cm to 30 cm, the communication link of the system was through air. The communication devices of the sensor nodes for detecting volcano activities were buried in soil, but the antennas of the sensor nodes were located above ground and so the communication was still through air. There is no need to further review more implementations of WSN systems for sub-soil sensing as the majority of them do not have the same challenge as this project, which was described in Chapter 1.

2.3.4 Wireless underground sensor networks

The concept of Wireless Underground Sensors Networks (WUSNs) was introduced by Akyuldiz and Stuntebeck [65] to address the shortcomings of current sub-soil sensing systems. The proposed WUSNs system comprises of a number of sub-soil sensor nodes and an above-soil data-logger. The wireless communications between the sensor nodes and the logger are through soil. They also described four considerations for the design of WUSNs systems: 1) power conservation, 2) topology design, 3) antenna design and 4) environmental extremes. All these considerations come from the unique nature of underground environments.

Sun and Akyildiz [66] planned to implement underground wireless communications through magnetic induction, instead of ElectroMagnetic (EM) waves as they thought the magnetic induction communication system could achieve a better performance in soil. They proposed a waveguide technique in order to maximise the sensing depth. With the waveguide technique, a number of coils

are deployed in soil as relays between the sub-soil sensor nodes and the data-logger above the ground. The simulated results showed the magnetic induction waveguide technique could greatly improve the system performance in soil. However, the relay coils can be the obstacle of deploying the system in practice and so affect the system deployment efficiency. In addition, the relay coils have to be deployed vertically above the sensor nodes, which increases the difficulty in deploying the system. Moreover, this is still a concept and there is little evidence of practical implementations.

Silva [67] and Xu et al. [68] have designed and implemented the sensor nodes which can be buried in soil for achieving wireless sub-soil sensing. These sensor nodes were used to investigate wireless communication in soil through practical experiments. In their research, the sensor nodes were buried with on-board batteries for powering the sensor nodes. This design can bring problems in practice. The use of a battery in a sub-soil sensor node limits the operating lifetime of the sensor node. There is a potential need to retrieve the node from below soil for charging or replacing the battery. In addition, batteries are environmentally unacceptable as they typically contain heavy metal elements such as zinc (Zn), nickel (Ni), copper (Cu) and lead (Pb) [21] which could potentially leak and result in contaminations in soil. This will be further discussed in Chapter 3.

2.4 RFID Technology

Radio Frequency IDentification (RFID) is a wireless communication technology primarily used to identify specific objects [22]. RFID technology has been rapidly developed and widely applied to various fields, ranging from retail industry and public transport to sport events and medical applications [69]. RFID systems are generally divided into two types according to the type of RFID tag: active RFID systems and passive RFID systems [70]. Active RFID systems refer to those systems employing active RFID tags which require on-board power supplies (batteries) [71]. Passive RFID tags are able to harvest energy from the RF field generated by the RFID reader, and so do not need any power supply [72]. Passive RFID technology potentially provides a solution to the implementation of a wireless sub-soil sensing system which employs battery-free sensor nodes.

Figure 2.3 presents the diagram of a passive RFID system which consists of an RFID reader and an RFID tag, where the RFID reader transmits RF signals to power and interrogate the RFID tag. The block diagram of passive RFID tags is shown in Figure 2.4. The tag harvests energy from the RF field generated by the RFID reader through a tag antenna and an RF rectifier. The tag then modulates and transmits the data which is pre-stored in an on-board memory using a controller and a modulator. The operating principles of the modulator will be described in Section 2.4.1 and Section 2.4.2.

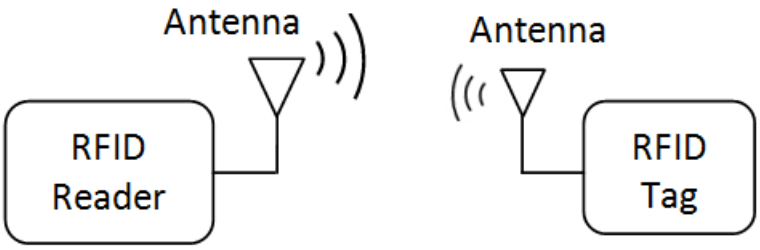

Figure 2.3: Diagram of a basic RFID system

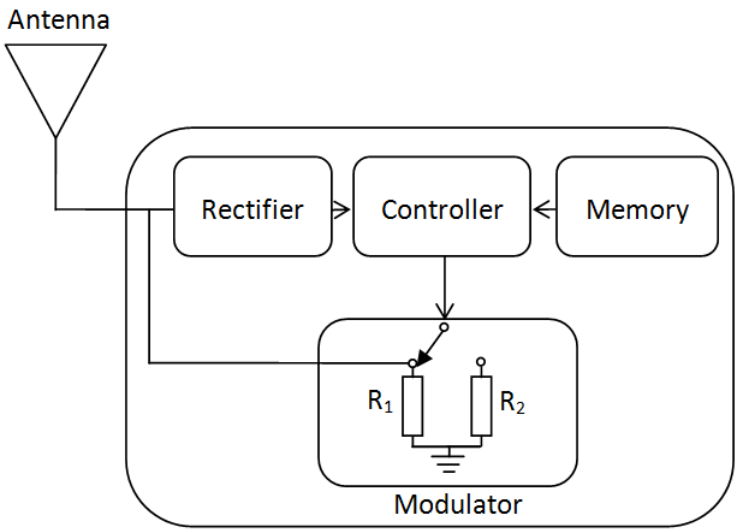

Figure 2.4: Passive RFID tag diagram

For commercial passive RFID systems, RF energy harvesting is based on near-field coupling or far-field coupling [72]. As shown in Figure 2.5, the near-field and the far-field of a source antenna are two regions of radiation around the antenna.

The near-field is the zone from the source antenna to the boundary where the electromagnetic waves have formed and have been propagated into free-space [73]. The near-field is further divided into the reactive near-field and radiating near-field. In the reactive near-field the reactive power density dominates, and the relationship between the electric field and magnetic field components is unpredictable [74]. Power starts to radiate in the radiating near-field and the radiating power density is greater than the reactive power density [74]. The far-field is the region which is dominated by radiated fields, where the electric field and magnetic field components are perpendicular to each other [73],[75]. The most commonly used criterion for minimum distance of far-field regions is determined by [74]

$$r \geqslant 2D^2/\lambda \tag{2.1}$$

where r (m) is a distance from the antenna, D (m) is the largest dimension of the antenna and λ (m) is the wavelength of the propagated signal. This equation is typically used to approximate the far-field region of the antenna with an overall length (the maximum dimension) greater than a wavelength [74].

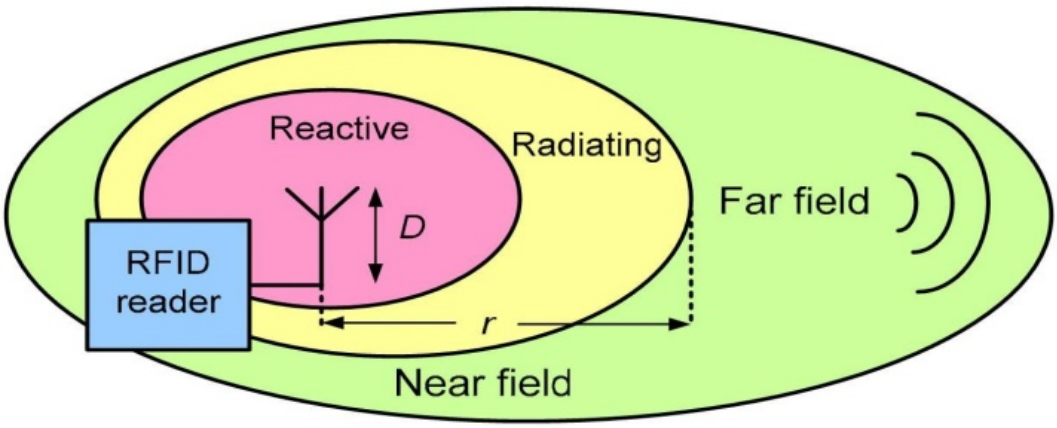

Figure 2.5: Antenna near-field and far-field regions [5]

2.4.1 Near-field RFID

A near-field RFID system typically implements inductive coupling (magnetic coupling) to transfer energy from the RFID reader to the RFID tag by using coil antennas, and there are strong inductive effects from the currents in the antenna [22]. The energy coupled from the magnetic field by the tag antenna is rectified

and converted to a DC voltage which supplies the tag circuit. The tag modulates the data pre-stored in the on-board memory through varying its load resistance (as shown in Figure 2.4) in order to generate a current variation in the tag coil antenna. Therefore there will be a current variation induced in the reader soil antenna due to the mutual inductance between the reader antenna and the tag antenna. This process of communication is called load modulation [22].

The majority of the current near-field RFID commercial systems operate at frequencies ranging from 30 kHz to 30 MHz. They have a wide range of applications including access security, transportation and contactless payment systems [69]. One of the key advantages of the near-field systems is that the system performance will not be significantly affected by lossy materials between the RFID reader and the tag, such as soil [66] and water [5]. Near-field RFID technology has been used to implement a remotely powered and implantable biosensing system which facilitates treatments for diseases and conditions [76]. The system employs swallow-able sensor nodes which harvest energy and transmit sensory data through inductive coupling with a data-logger outside the body. However, inductive coupling only works at short distances from the RFID reader antenna, as the magnetic field strength in near-field decays inversely with the cube of the distance from the antenna ($\frac{1}{r^3}$). A typical operating range of the near-field system is less then 20 cm [77, 78]. The operating range of a near-field system can be improved by increasing the diameter of the tag coil antenna or increasing the number of turns of the tag coil antenna [79], but this will lead to a large tag size. For example, power was successfully delivered wirelessly to a 60 W bulb from a distance of 2 m through inductive coupling, but the coil antennas had a size with the diameter of approximately 1 m [80]. Neither a short operating range nor a large tag size is desirable for designing a sub-soil sensing system based on RFID technology.

2.4.2 Far-field RFID

In the region of far-field, EM waves are formed and the electric field and magnetic field components are perpendicular to each other. With a far-field RFID system, the RFID tag harvests energy from the EM wave through radiative coupling. The harvested power is also rectified and converted to a DC voltage for supplying the

tag circuit. Regarding the communication link, the RFID tag transmits data back to the RFID reader through backscatter modulation [22]. Backscattering is the reflection of waves back to the direction of the source. When the electromagnetic wave emitted by the RFID reader antenna arrives at the RFID tag antenna, a fraction of the wave is reflected back to the RFID reader, therefore the RFID tag modulates data by varying the amplitude of the reflected power. A far-field RFID tag also achieves backscatter modulation by switching its load between two impedance states, and the design of backscatter modulator is typically based on using a transistor as shown in Figure 2.6. Switching on and off the transistor affects the antenna-load reflection coefficient which determines the amount of the wave reflected from the tag antenna [22].

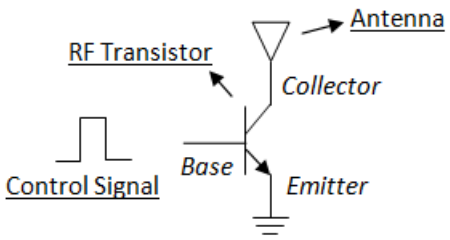

Figure 2.6: Design of a backscatter modulator based on RF transistor.

The Ultra High Frequency (UHF) band between 300 MHz to 3 GHz is a popular range in which most of far-field RFID industrial protocols operate. For example the RFID systems based on the ISO18000-6C protocol [6] operate at frequencies from 860 MHz to 960 MHz. Based on the Friis equation [81], the power of the EM wave propagating in free space attenuates inversely as the square of the distance. Far-field passive RFID tags may reach an operating range of approximately 29 m at 916 MHz based on U.S. regulations [1], which is much longer than near-field systems' typical operating range (less than 20 cm [77, 78]). Most of the commercial UHF passive RFID systems use compact printed paper tags that can be conveniently attached to objects [82]. However, far-field RFID system performance can be potentially affected by lossy materials between the RFID tags and the RFID reader. The lossy materials will absorb energy from the RF signals generated by the RFID reader, and so lead to a high path loss between the reader and the tags. When applying far-field RFID technology in implementing sub-soil sensing systems, it is essential to characterise the sub-soil wireless channel as will be reviewed in Section 2.5.

Comparing the far-field RFID to the communication systems presented in Table 2.2 and in Section 2.3 , the far-field passive RFID communication system is advantageous in the following aspects:

- Size - passive RFID systems use compact paper tags with a printed antenna, and the tag chip (without the antenna) can have a dimension of 1.6 mm × 1.6 mm × 0.5 mm [82],[83].
- Power consumption - the typical power consumption of the passive tags is less than 1 mW [83].
- Power requirement - the passive RFID tags do not need on-board batteries and are capable of harvesting energy from EM waves.

It will be hard to integrate a commercial tag and commercial sensors for prototyping an RFID-based sensor node as the circuit of commercial RFID passive tags are typically integrated into an Integrated-Circuit (IC) and the tags strictly operate based on industrial protocols. Chapter 8 will present the design and implementation of a sensor node prototype based on far-field RFID technology.

2.4.3 Ultra High Frequency RFID protocols

Given the advantages of the operating range and the tag size, UHF passive RFID systems are being widely applied in supply chain applications. Glidden et al. [84] compared the first-generation protocol standards for UHF RFID systems including Auto-ID Class 0, Auto-ID Class 1, ISO 18000-6A, ISO 18000-6B. In 2004, the second generation UHF RFID standard ISO 18000-6C, or EPC Class 1 Generation 2 (C1G2) [6] was published by EPCglobal, and it has been widely selected by most commercial RFID systems. The detailed specifications of this protocol can be found in Appendix A.

2.4.3.1 The physical layer

A summary of the physical layer specified in the EPC C1G2 RFID protocol is presented in Table 2.3. Based on the EPC C1G2 protocol, the RFID system

Table 2.3: Summary of the physical layer of the EPC C1G2 RFID protocol.

Forward link		Backward link	
Modulation	Encoding	Modulation	Encoding
ASK	PIE	ASK/PSK	FM0

implements Amplitude Shift Keying (ASK) modulation scheme in both the forward link (from reader to tag) and the backward link (from tag to reader) of the communication by varying the amplitude (power) of the reflected wave. When the RFID tag switches its load between two impedances, it does not only vary the amplitude but also alters the phase of the reflected wave. Thus, data can be also modulated through Phase Shift Keying (PSK) modulation scheme in the backward link. Detailed information on digital modulation scheme can be found in [85]. The RFID reader implements Pulse Interval Encoding (PIE) format [6] to encode RFID commands. The primary advantage of PIE encoding in passive RFID technology over other encoding schemes is that it maximises the RF energy transferred from the RFID reader to the RFID tag. In the backward link of the communication the tag implements Bi-phase space (FM0) coding format [6] to encode data.

2.4.3.2 Tag-identification layer

With an RFID system based on EPC C1G2 protocol, the RFID reader manages the communications with the RFID tags using three basic operations [6]:

- *Select*: this operation is to select an RFID tag population for inventory and access, and it can be neglected for managing a single tag.
- *Inventory*: the operation of inventory comprises multiple commands for identifying the RFID tags, and detects a single tag reply.
- *Access*: this operation allows for getting access to the memory of an RFID tag, such as reading from or writing to the tag.

The whole process of identifying and accessing a single RFID tag by the RFID reader can be seen as a series of RFID reader commands and the tag responses,

and the process can be primarily divided into two rounds: the *Inventory* round and the *Access* round. Figure 2.7 shows the complete communications for reading the tag ID and writing data to the tag. In the *Inventory* round, the RFID reader transmits the RFID commands to identify the tag and also initialises the tag. Once the tag has been identified and initialised, the RFID commands in the *Access* round can be used to access the tag's on-board memory (as shown in Figure 2.4), such as reading data from the memory or writing data to the memory.

The RFID reader starts an *Inventory* round by transmitting a *Query* command to interrogate tags. Once a tag has received a valid *Query* command, it transmits a random 16-bit number tag response *RN16* to the reader. Then the reader issues an *ACK* command to echo the received tag response *RN16*. The tag will reply to a valid *ACK* command with a response including a specific length of the pre-stored data in the tag's memory, and this response is named as *PC+EPC+CRC16* in the protocol. Issuing the *PC+EPC+CRC16* tag response means that the tag is ready for accessing its memory, and the RFID reader can transmit the commands in the *Access* round to either read data from or write data to the tag's memory.

Regarding reading data from the tag's memory, the RFID reader should transmit a *ReqRN* command which echoes the prior *RN16* as the start of an *Access* round. Once a 16-bit number, termed as a *handle* has been replied to by the tag as the response to the *ReqRN* command, the reader then issues a *Read* command to specify the address of the tag's memory as well as the number of data bits to read. Finally, the RFID tag transmits the demanded data to the reader. Writing data to the tag's memory requires the RFID reader to issue an extra *ReqRN* command to echo the *handle* response. Once a new random 16-bits number response, termed as *New RN16* is given following the second *ReqRN* command, the RFID reader transmits a *Write* command which specifies the address of the tag's memory and the data to write. The tag then will issue a final tag response, termed as *Feedback* to indicate that whether the data has been successfully written or not.

When implementing an RFID-based communication system, there is a need to investigate the effect on the system performance from the physical layer and the frequency. However, commercial RFID readers provide limited abilities either

Figure 2.7: Communications for reading and writing RFID tag [6]

to modify the physical layer or to analyse the system performance in a wide frequency range. Chapter 7 will describe the implementation of a Software-Defined Radio (SDR) RFID reader platform.

2.5 Sub-soil Wireless Channel

As reviewed in Section 2.3, the wireless communication of the majority of the sub-soil sensing systems is through air, but the challenge of this work is to achieve wireless communication through soil. This section reviews the research on sub-soil wireless channels.

2.5.1 Dielectric properties of soil

The characteristics of sub-soil wireless channels were previously investigated for landmine detection using Ground-Penetrating Radar (GPR) [86], [87]. A GPR system transmits RF signals into the ground and detects a landmine by receiving the reflected signal [88]. It is found that the dielectric behaviour of the soil is heavily affected by the water content and the texture [86], and the RF signals propagating in soil can suffer energy loss (dielectric loss) due to RF absorption by the soil.

Soil can be represented as a mixture of soil particles, air voids, and liquid water which is a lossy dielectric medium to RF signals. Regarding the propagation of plane waves in a lossy medium, the relative dielectric constant of the medium ϵ is a complex value and can be expressed as:

$$\epsilon = \epsilon' - j\epsilon'', \tag{2.2}$$

where the real part of the constant ϵ' affects the propagation speed and the imaginary part ϵ'' gives rise to the dielectric loss - the energy loss due to RF absorption. The energy loss in a lossy medium is also often specified by another quantity loss tangent, $tan(\delta)$:

$$tan(\delta) = \frac{\epsilon''}{\epsilon'}. \tag{2.3}$$

A small value of the loss tangent $tan(\delta)$ decreases the dielectric loss. If the loss tangent is zero, there is no dielectric loss and the medium performs as an ideal conductor.

Research on the microwave dielectric behaviour of wet soil was carried out to evaluate the dielectric constants of the five soils through experimental measurements over 1.4 to 18 GHz frequency range [89]. Those five soils contain various textural compositions in terms of sand, silt, and clay percentages, and those compositions are defined in [90]. The measurement results indicated that the dielectric constant of the soil is primarily affected by the soil's volumetric moisture content, the soil's textural compositions, and the frequency. For all five soils, it was observed that both ϵ' and ϵ'' increase with increasing soil volumetric moisture, and ϵ' decreases and ϵ'' increases with increasing frequency. For a given soil volumetric moisture, ϵ' was proportional to sand content and inversely proportional to clay content, and ϵ'' was primarily affected by clay content below 5 GHz and by sand content above 5 GHz. Based on experimental data, two dielectric models describing the dielectric behaviour of wet soil, the semiempirical mixing model and the theoretical four-component dielectric mixing model were developed and presented in [91]. The semiempirical dielectric model offers the ability to predict the complex relative dielectric constant of a soil from the soil physical parameters such as the soil textural composition and the soil volumetric moisture level.

The relative dielectric constants of four soil mixtures over the 0.3 - 1.3 GHz frequency range were measured by Peplinski et al. [2]. The measured results were then compared to the calculated results according to the semiempirical mixing model in [91], and a semiemprircal mixing model over the 0.3 - 1.3 GHz frequency range was obtained. The semiemprircal mixing model over the 0.3 - 1.3 GHz will be applied to design an EM model for the RFID sub-soil system as shown in Chapter 5, which is expressed as [2]:

$$\epsilon' = 1.15[1 + \frac{\rho_b}{\rho_s}(\epsilon_s^{\alpha}) + m_v^{\beta'}\epsilon_{f\omega}^{'\alpha} - m_v]^{1/\alpha} - 0.68, \tag{2.4}$$

$$\epsilon'' = [m_v^{\beta''}\epsilon_{f\omega}^{''\alpha}]^{1/\alpha}, \tag{2.5}$$

where

m_v is volumetric moisture content of the soil,

ρ_b is the bulk density in grams per cubic centimetres (gcm_{-3}),

ρ_s is the specific density of the solid soil particles equal,

ϵ_s is determined by an empirical fitting of experimental data,

$\epsilon_{f\omega}^{'}$ is the real part of the relative dielectric constant of free water,

$\epsilon_{f\omega}^{''}$ is the imaginary part of the relative dielectric constant of free water,

α is an empirically determined constant,

$\beta^{'}$ and $\beta^{''}$ are empirically determined soil-type dependent constants given by [91]:

$$\beta^{'} = 1.2748 - 0.519S - 0.152C \tag{2.6}$$

and

$$\beta^{''} = 1.33797 - 0.603S - 0.166C \tag{2.7}$$

where S and C represent the mass fractions of sand and clay. The complex dielectric constants of free water $\epsilon_{f\omega}^{'}$ and $\epsilon_{f\omega}^{''}$ are calculated as [91]:

$$\epsilon_{f\omega}^{'} = \epsilon_{\omega\infty} + \frac{\epsilon_{wo} - \epsilon_{w\infty}}{1 + (2\pi f\tau_w)^2} \tag{2.8}$$

and

$$\epsilon_{f\omega}^{''} = \frac{2\pi f\tau_w(\epsilon_{wo} - \epsilon_{w\infty})}{1 + (2\pi f\tau_w)^2} + \frac{\sigma_{m_v}}{2\pi\epsilon_o f} \tag{2.9}$$

where

f is the frequency in hertz (Hz),
$\epsilon_{w\infty}$ is the high-frequency limit of ϵ_w,
ϵ_{w0} is the static dielectric constant of water,
τ_w is the relaxation time of water,
σ_{m_v} is the effective conductivity of water in Sm^{-1},
ϵ_o is the permittivity of free space equal. The detailed information about the parameters in the two expressions are described in [92] and [93].

2.5.2 Path loss in soil

For a system which achieves the wireless communication through soil, the performance of the communication link will be affected by the soil. Akyildiz [65] analysed the properties of the underground wireless channel and identified five main factors which could impact EM wave propagation in soil:

- Extreme path loss - power loss due to RF absorption by soil material.
- Reflection/refraction - power reflection when EM wave reaches the ground-air surface.
- Multi-path fading - objects, such as plant root and rock in soil scatter RF signals and produce fading.
- Reduced propagation velocity - EM wave propagation speed is slower in soil than in air because of high dielectric constant of soil.
- Noise - sources of underground noise, such as power lines, lighting and farming machinery.

Extreme path loss is the primary problem which hampers effective wireless communication in soil. Li et al. [7] characterised the sub-soil wireless channel by deriving the path loss of the sub-soil channel. In their work, a mathematical expression was developed to estimate the path loss in soil L_p, which includes three components:

$$L_p(dB) = L_{m1}(dB) + L_\alpha(dB) + L_o \tag{2.10}$$

where L_{m1} is the power loss due to the change of the wavelength when RF signals propagate into soil from air, L_α is the dielectric loss due to RF absorptions, and L_o is the Free-Space Path Loss (FSPL). The component L_α is determined by the soil's complex dielectric constant which is calculated based on the model presented in [91]. The calculation of the FSPL is based on Friis [81] equation:

$$FSPL(dB) = 10log_{10}((\frac{4\pi}{c}df)^2), \tag{2.11}$$

where f (Hz) is the centre frequency, d (m) is the distance between transmitter and receiver and c (m/s) is the speed of light. The FSPL is caused by the loss in the RF signal strength while the signal is radiating to various directions from the source. For a given propagation distance, higher frequency leads to higher FSPL. The path loss in the soil was evaluated with MATLAB [94] simulations over the 300 - 900 MHz frequency range. Figure 2.8 presents part of the results which show that the path loss in the soil can easily be 60 dB/m greater than in air at 300 MHz, and the attenuation significantly increases with increasing soil volumetric water content and frequency. It was also observed from the results that the path loss is also affected by the soil type, where the calculated path loss in the soil increases with increasing percentage of clay and sand particles in the soil.

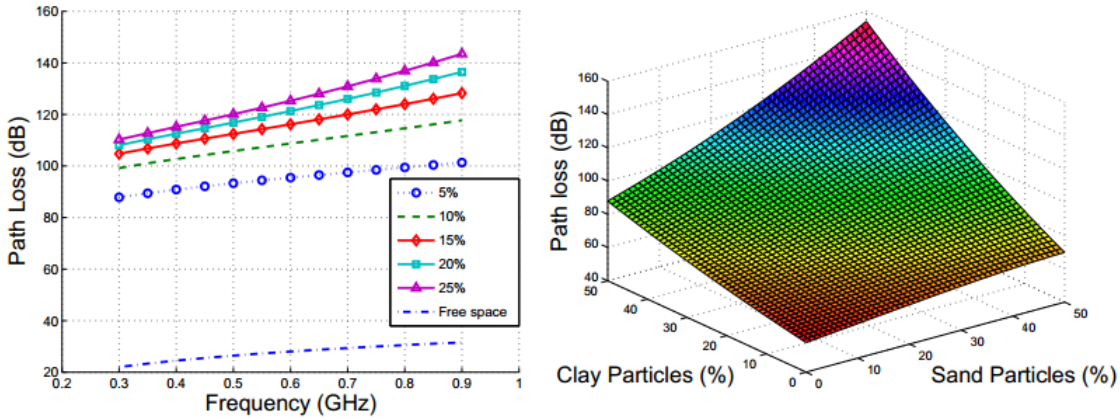

Figure 2.8: Simulation results of the path loss in soil [7].

Instead of measuring the path loss in soil through simulations, Yu [95] attempted to evaluate the path loss in the soil through experiments by deploying sensor nodes within a soil whose composition was 15 % clay, 35 % silt, and 50 % sand particles. In the experiments, the path loss in the soil was measured at soil moisture contents from 0 % - 25 % at three frequencies: 433 MHz, 868 MHz and 915 MHz. The experimental results also indicated that the path loss in the soil increased with increasing frequency and soil moisture, and the path loss in the dry soil can be 100 dB/m at 915 MHz. They also observed that the path loss could decrease with increasing depth of the sensor nodes, and that there was no obvious change in the measured path loss when the depth increased from 1 m to 2 m. However, the work provided limited information detailing the experimental method and arrangements, and it did not describe the effect of the path loss on the system performance.

When achieving wireless communication through soil, the high path loss can lead to a heavily attenuated signal arriving at the receiver antenna. The attenuated signal will degrade the Signal-to-Noise Ratio (SNR), and therefore affects the Bit Error Rate (BER) performance. Although an amplifier can be used to amplify the received signal by the antenna, it will also amplify background noise around the receiver. In this work, the path loss in soil is further investigated through CST simulations as will be presented in Chapter 6 and also through a range of practical experiments as will be discussed in Chapter 9.

2.6 Conclusion

This chapter has reviewed the research in terms of the development of precision agriculture, the implementations of WSN systems for underground sensing, RFID technology and the characterisation of sub-soil wireless channels.

Modern technologies have been used to support precision agriculture, which include GPS, GIS, remote sensing systems, EC sensing systems and a variety of commercial sensors. Also, there is increasing research into reliable and efficient underground sensing systems by integrating wireless communication technology and commercial sensors. WSNs technology has been implemented in agriculture,

underground mines/tunnels and other sub-soil environmental monitoring fields. All of these systems avoid sub-soil wireless channel and transmit data wirelessly through the air. WUSN systems have been designed to achieve sub-soil sensing with the communication link in soil. However, they employ sub-soil sensor nodes with on-board batteries which have environmental concerns.

With a passive RFID system, the RFID tag is capable of harvesting energy from the RF field generated by the RFID reader and transmitting data back to the reader wirelessly. Passive RFID technology provides a potential solution to the implementation of sub-soil sensing systems based on using battery-free sensor nodes within the soil. Compared to other communication protocols, far-field passive RFID systems, especially those operate at the UHF band have the following advantages :

- small physical size;
- low power consumption for transmission;
- no requirement of using on-board battery.

The primary problem of achieving wireless communication through soil is the high path loss. Based on the research characterising sub-soil wireless channels, the path loss is primarily due to RF absorption by soil materials, especially soil moisture content. In addition to soil moisture content, the path loss in soil is affected by the frequency and the soil type. It is necessary to further investigate the path loss in soil and the effect of the soil on the system performance through practical experiments.

Chapter 3

System Requirements Analysis

3.1 Introduction

This chapter lists seven design requirements for the proposed sub-soil sensing system. Details of the design requirements are described in Section 3.2 and the analysis of the requirements is presented in Section 3.3.

3.2 System Requirements Descriptions

A sub-soil sensing system will typically comprise a number of sub-soil sensor nodes which are capable of measuring the sub-soil environmental parameters, such as soil temperature and soil moisture. There are seven design requirements for the proposed sub-soil system as summarised below:

1. Nodes are totally buried within soil at depths range up to 0.5 m.
2. Nodes do not contain on-board batteries.
3. Nodes are readily deployable with farm machinery.
4. The system is compatible with modern farming practice.
5. The system is able to achieve a successful reading rate higher than 80 %.
6. The system provides multiple sensor measurements based on state-of-the-art sensing technology.
7. The system has an operating lifetime of more than 2 years.

3.2.1 Nodes are totally buried within soil at depths range up to 0.5 m

The proposed sub-soil system employs sensor nodes which are totally buried within soil and are not wired to any other devices. The sensor nodes are capable of measuring environmental parameters, for example soil moisture at the vicinity of the rhizosphere. Compared to sensor measurements that are taken at the soil surface, the sensor measurements that are provided by the system will be able to reflect the actual needs of the crops. The depth of the sub-soil sensor nodes will range up to 0.5 m, and this value is based on the effective rooting depths of typical crops, such as potato, wheat and field corn [96, 97]. The proposed system will also include an interrogator above the ground, which is used to interrogate the sub-soil sensor nodes and to log sensor measurements from the sensor nodes. There will be no wiring between the sensor nodes and the interrogator and the sensor nodes will wirelessly transmit sensor measurements to the interrogator using on-board communication devices. The interrogator will include an antenna for communicating with the sensor nodes and an in-built memory module for logging the received sensor measurements.

3.2.2 Nodes do not contain on-board batteries

As reviewed in Section 2.3, most commercial Wireless Sensor Network (WSN) systems employ sensor nodes which are equipped with on-board batteries. However, those batteries can contain heavy metals, such as zinc (Zn), nickel (Ni), copper (Cu) and lead (Pb) [21]. When burying a sensor node into soil with an on-board battery, the soil can be potentially contaminated by heavy metals from the battery. The contamination can decrease soil fertility and therefore affect crop growth. More seriously, crops grown on the contaminated soil will finally transfer the heavy metal contamination to human bodies, which could result in sicknesses and health problems. Thus, the use of battery-free sensor nodes in soil is environmentally friendly and also avoids a potential threat to human health. Since energy will be required to supply the on-board devices of the sensor nodes, such as the communication device and the sensors, the sub-soil sensor nodes will harvest energy from the ambient environments using energy harvesting devices.

3.2.3 Nodes are readily deployable with farm machinery

The proposed sub-soil sensing system comprises a number of sub-soil sensor nodes. These sensor nodes can be deployed into soil manually by hand, but this method is inefficient, especially when there is a need to deploy hundreds of sensor nodes in a large field. The sub-soil sensor nodes will be plough-able, and so they can be readily deployed into soil, like when seeds planting with farm machinery. It is desirable to design the sub-soil sensor nodes with spherical shape. A spherical node is always smooth to deploy with mechanical tools and the node can automatically roll into soil. The sensor nodes are typically not larger than a tennis ball. Otherwise, the size of sensor nodes may not be able to fit into the width of furrows that are ploughed by farm machinery, or the achievable depth of the sensor nodes could be limited.

3.2.4 The system is compatible with modern farming practice

As described in the system requirement in Section 3.2.1, the proposed system includes an interrogator at above-ground for interrogating the sub-soil sensor nodes and logging sensor measurements. Within a farm, it is not desirable to locate the interrogator at the soil surface as there is the potential risk of mechanical damage from farm machinery or the risk of theft. Some farmers may prefer to interrogate sub-soil sensor nodes by manually moving the interrogator. However, hand reading is always inefficient and it is hard to see this possibility in large modern farms. The proposed system is compatible with modern farming practice, and it achieves a high efficiency in interrogating the sub-soil sensor nodes by installing the interrogator on a piece of farm machinery. When the farm machinery drives over a field, the on-vehicle interrogator automatically interrogates the sub-soil sensor nodes and receives the signals from them. The interrogator then demodulates the received signals and recovers the sensor measurements from the demodulated signals. The whole process of the sub-soil sensing does not affect normal farming activities by the farm machinery, such as fertilising, irrigating and sowing. The height of the interrogator (including its antenna) should be at least 0.5 m above soil surface as farming arrangements on ground may damage the interrogator.

3.2.5 The system is able to achieve a successful reading rate higher than 80%

A major concern with sub-soil sensing system is the system communication performance which can be assessed by the Successful Reading Rate (SRR). The SRR of a sub-soil system is typically termed as the number of the successfully interrogated sensor nodes over the total number of the sensor nodes. For example: when a farm machinery runs over a field where there are 100 sub-soil sensor nodes, the SRR is 50 % if the on-vehicle interrogator receives valid readings from 50 sensor nodes. The proposed sub-soil sensing system is required to achieve a SRR higher than 80%. Otherwise, farmers can loose confidence in the capability of the system as the logged sensor measurements by the system may not be able to completely reflect sub-soil environments. The required performance has to be achieved at normal farm machinery speeds and in extreme weathers, for example when it is raining or the ground surface is frozen or is covered by snow. Both the interrogator and the sub-soil sensor nodes hardware have to be water-proof. There is a possibility to improve the SRR by moving the interrogator over the field multiple times and repeating the interrogation of the sub-soil sensor nodes.

3.2.6 The system provides multiple sensor measurements based on state-of-the-art sensing technologies

Regarding the proposed sub-soil sensing system, each sensor node consists of multiple on-board sensors. These sensors are capable of measuring sub-soil environmental parameters which are essential for crop growth and crop quality. The potential parameters include: soil moisture, temperature, pH value and oxygen, and Chapter 2 has presented the commercial sensors for measuring these parameters. Based on state-of-the-art sensing technologies, some types of sensors need to contact the soil. For example, a soil moisture sensor typically measures the soil moisture using two mental electrodes which needs to have a physical contact with soil. The sensor node enclosure has to be compatible with those types of sensors, and has to be water-proof, especially at potential intersections of the sensor node enclosure and the sensor hardware. It is desirable to employ passive sensors or low-powered sensors in a sensor node as the sensor node does not include on-board battery and the harvested energy from the ambient environments

can be limited.

3.2.7 The system has an operating lifetime of longer than 2 years

Once a sub-soil sensing system has been deployed, it is always undesirable to replace it, especially its sub-soil sensor nodes. The replacement of the sub-soil sensor nodes in a field will typically involve retrieving them from below the soil and then deploying new sensor nodes. This process results in an increase in farming cost, and will cause problems when a replacement is needed during a crop growth period. However, it is impossible to design a sub-soil system which can operate with an infinite lifetime. With a sensor node, its operating lifetime can be potentially affected by the lifetime of on-board electronic components, the ageing of the sensor node enclosure material or the degradation of the on-board sensor performance. The requirement for the length of the system operating lifetime is at least 2 years. As for most of crops, such as vegetables, rice and wheat, the length of their growing periods ranges from 1 month to 6 months [98, 99]. Therefore, the system with a minimum lifetime of 2 years can be used for at least 4 growing periods of most crops. Within the operating lifetime, the sensor nodes are left in the soil without any maintenance and the system performance must not degrade with increasing of the system operating time.

3.3 System Requirements Analysis

3.3.1 Nodes are totally buried within soil at depths range up to 0.5 m

The environment in soil is very different from that in air, and a sub-soil sensor node can be at risk from the soil. For example, a sub-soil sensor node will be physically damaged if it cannot withstand the high pressure from the soil above it. In addition, soil materials such as water content and living beings in the soil such as insects can also threaten the sensor node circuit. Therefore the proposed sub-soil sensor node enclosure must be able to protect the sensor node circuit from potential threats in the soil. Although the design of sub-soil sensor node

enclosure is not an emphasis in this thesis, the following factors are listed, which will be necessary to be considered:

- the physical strength of the material for making the sensor node enclosure;
- the levels of pressure to the sensor node enclosure at the depths from 0 m to 0.5 m.
- the sealing of the sensor node enclosure;
- the ability of the sensor node enclosure against corrosion or oxidation by the soil ingredients.

As described in Section 3.2.1, the sub-soil sensor nodes include an on-board wireless communication device to transmit sensor measurements to the interrogator at above-ground. However, the wireless communication through soil can be challenging due to the dielectric properties of the soil. As reviewed in Section 2.5, the dielectric properties of soil behave differently from those of air [89], and there is a high Radio Frequency (RF) path loss in the sub-soil wireless channel due to RF absorptions by the soil materials [7]. With increasing depth of a sensor node, the path loss between the sensor node and the interrogator will typically increase [7] and so can affect the system communication performance as will be analysed in Section 3.3.5. Therefore it is necessary to explore the following questions in this research:

- Will the on-board communication devices, especially their antennas be affected by the soil?
- What is the difference between the path loss in soil and in air?
- What is the level of the path loss per metre in soil? and how does it depend on the soil?

3.3.2 Nodes do not contain on-board batteries

There are three potential sources where the sub-soil sensor nodes can harvest energy: solar energy, thermal energy and RF energy. A solar energy harvesting system typically uses a solar panel to harvest energy. However, the use of a solar

panel leads to wirings between the above-ground solar panel and the sub-soil sensor nodes, which are not desirable. Energy can also be harvested by the sub-soil sensor nodes from thermal differences in the soil, however this source is limited in the amount of energy that can be supplied to the sensor nodes. With an on-board RF energy harvesting module in a sub-soil sensor node, there is no need to wire the sub-soil sensor node to any devices. Energy can be harvested by the sensor node from RF fields, and an RF field can be generated by an RF signal generator at the above-ground. In practice, the RF signal generator can be integrated with the interrogator. When the interrogator travels with a farm machinery over a field, it firstly powers a sensor node and then receives sensor measurements that are transmitted. Therefore RF energy seems to be an appropriate choice.

A problem of using RF energy harvesting is that the high path loss in the soil will limit the energy that can be harvested by the sensor node. So the harvested energy by the sensor node may not be sufficient to supply the on-board sensors and the communication device. Increasing transmission power at the interrogator helps improve the energy harvested by the sensor node. But care needs to be taken as a high RF power will not be allowed if it exceeds the levels that are specified in regulations, for example the UK Office of Communications (OFCOM) requirements. With this problem, the explorations of the following questions are required in this research:

- What will the maximum and the minimum energy budget of the sensor nodes be?
- What is the maximum RF power that is allowed to be transmitted by the interrogator? Is this maximum power different in various countries?
- Are there any other methods that are capable of improving the amount of energy harvested by the sensor nodes?

3.3.3 Nodes are readily deployable with farm machinery

The proposed sub-soil sensor node will use an antenna to harvest energy from the RF field that is generated by the above-ground interrogator. The antenna is a size-limiting factor in the sensor node design. It is desirable to have a small

antenna size which leads to a small node size. But a large antenna is typically more efficient in harvesting RF energy, which helps improve the amount of energy harvested by the sensor node. Operating at high frequency reduces the size of the antenna, but the path loss in soil increases with increasing frequency. With this conflict, the system design will need to investigate:

- the appropriate frequency for the proposed system;
- the differences of the path loss in soil at various frequencies.

When there is a need to use large sensor nodes, it will be necessary to consider a ploughing tool design for deploying large sensor nodes. For example, a driller may be required in the ploughing tool, which is able to drill large holes in the soil surface.

Regarding the deployment of the sphere shape sensor nodes with farm machinery, it is hard to control the orientation of the nodes within soil as they will roll into the soil from the farm machinery. Thus, directional antennas such as the patch antenna are not appropriate in the sensor node design. Therefore, it is also important to consider the design of an antenna for the sub-soil sensor node, and following factors will need to be considered:

- type;
- gain;
- radiation pattern;
- size.

This thesis will not discuss the sensor node antenna design, but will analyse the system performance based on using a dipole antenna[100].

3.3.4 The system is compatible with modern farming practice

When the interrogator of the proposed system moves with a farm machinery, the speed of the farm machinery is one of primary factors which affects the system performance in harvesting energy. Farming tractors typically run at the speeds

ranging from 5.5 to 7.5 Kilometres Per Hour (kph) [101]. With the speeds in that range, the on-vehicle interrogator can easily travel more than 1.5 metres per second. So the time when the sensor nodes can harvest energy from the RF field that is generated by the interrogator, termed as the *powering time* becomes limited. The *powering time* can be maximised by slowing down the speed of the farm machinery, but farming efficiency will be affected at slow speeds. In addition, the farm machinery can consist of other on-board electronic systems, for example cellular communication device, so the system communication performance can be affected by the noise that is generated by those systems. Based on the system analysis, in this thesis system design is necessary to explore:

- the potential trade-off between the farming efficiency (the farm machinery speed) and the *powering time*;
- the level of background RF noise around farm machinery;
- the methods of maximising the *powering time*.

3.3.5 The system is able to achieve a successful reading rate higher than 80%

If the interrogator fails to get readings from a sensor node, there are two potential causes of the failure: 1) the harvested energy by the sensor node fails to meet the energy budget; and 2) the interrogator fails to detect the transmitted signal from the sensor node. The path loss between the interrogator and the sensor node is the primary concern for the both causes. Figure 3.1 presents a diagram showing the gains and losses of signal power with a communication system, where P_t is the signal output power of the transmitter, P_r is the signal power received by the receiver antenna, G_t and G_r are the gains of the transmitter antenna and the receiver antenna, and the path loss between the antennas includes all power losses during energy transfer between the antennas. In the forward link, the interrogator transmits RF signals to power the sub-soil sensor node and the path loss limits the energy that can be harvested by the sensor node. In the backward link, the sensor node transmits sensor measurements to the interrogator. The path loss leads to an attenuation in the signal (from the sensor node) arriving at the interrogator antenna, and degrades the Signal-to-Noise Ratio (SNR) performance

at the interrogator receiver. The degradation of the SNR performance can make the interrogator fail to detect the signals transmitted from the sensor node. Under extreme weathers, such as cold weather, snowy weather and rainy weather, the path loss between the interrogator and the sensor node will increase due to RF absorption by the water content in the ice, the snow and the soil. Therefore it will be necessary to explore:

- improving the energy harvested by the sensor node;
- enhancing the SNR performance at the interrogator receiver;
- the effect of the path loss in soil at various soil moisture contents.

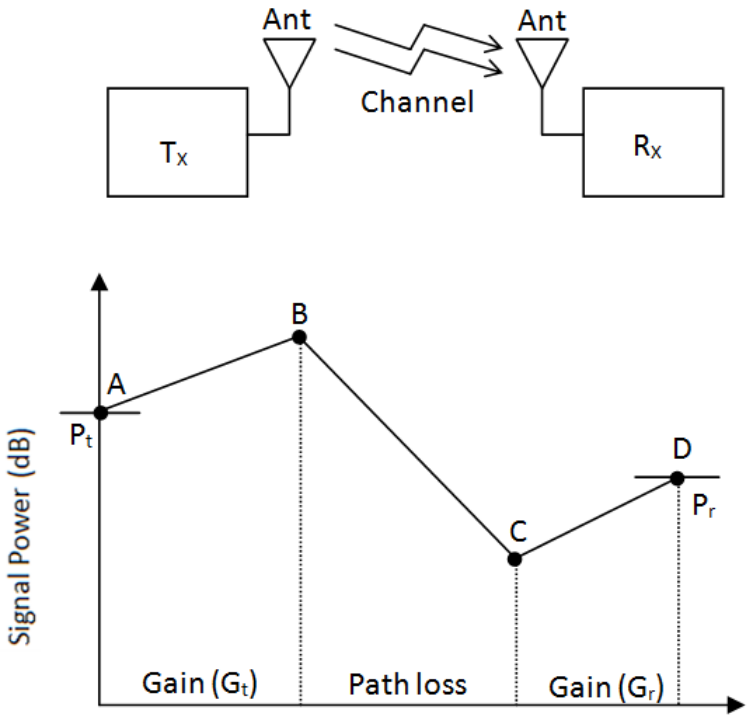

Figure 3.1: Diagram showing the gains and losses of signal power in a communication system.

As analysed in Sections 3.3.1 to 3.3.4, the factors that can limit the harvested energy by the sensor nodes also include depths of the sensor node, sizes of the sensor node (sensor node antenna), and speeds of the farm machinery. There will be potential needs to make:

- the trade-off between the system communication performance and the depth of the sensor nodes;

- the trade-off between the system communication performance and the size of the sensor nodes;
- the trade-off between the system communication performance and the farm machinery speed.

3.3.6 The system provides multiple sensor measurements based on state-of-the-art sensing technologies

The development of sensing technology is not a focus in this thesis, but energy budgets of the on-board sensors will be considered. The proposed sub-soil system employs battery-free sensor nodes which harvest energy from RF fields. Total energy budget of the on-board sensors is an crucial parameter in the system design. High energy budget requires longer *powering time*, which can lead to unacceptably slow speeds of the farm machinery. Therefore, it is always desirable to use low-powered sensors. For example, the Analog Devices TMP 37 temperature sensor [45] only consumes 50 μA at 3.3 V. There are no reported soil measuring sensors at this level of power consumption. For example, the SM150 moisture sensor [41] is widely used in various applications, which operates with a power consumption of 18 mA at 5 V and also needs a warming-up time of 1 second. The energy budget of the SM 150 moisture sensor is approximately 500 times higher that of the TMP 37 temperature sensor. When using the sensors with high energy budgets, there will be a potential need to either increase the transmit power or to maximise the time when the sensor nodes can harvest energy. The following trade-offs may be required when designing the system:

- the trade-off between the total energy budget of the on-board sensor node and the system's communication system;
- the trade-off between the total energy budget of the on-board sensor node and the farming efficiency (the farm machinery speed);
- the trade-off between the total energy budget of the on-board sensor node and the depth of the sensor node;
- the trade-off between the total energy budget of the on-board sensor node and the size of the sensor node.

3.3.7 The system has an operating lifetime longer than 2 years

The lifetime of a sensor node will primarily depend on four parts of the sensor node which are the sensors, the wireless communication device, the RF energy harvesting module and the sensor node enclosure. Most of the commercial wireless communication devices and RF energy harvesting modules can easily achieve lifetimes longer than 2 years. A well sealed sensor node enclosure that is made of strong material should be also able to protect the sensor node circuit for two years. Regarding the sensors, the focus is not only on their lifetimes but also on their performance, such as sensitivity and accuracy. Most commercial sensors have the operating times more than 2 years, but their performance may not be guaranteed for that length of time. The degradation of the sensors performance can result in inaccurate sensor measurements, which is not acceptable for the farmers. Therefore, it will be necessary to further explore the performance of the on-board sensors as time increases.

There will be a problem when replacing the sub-soil sensor nodes - where are the sub-soil sensors? Since some of the sensor nodes may fail working beyond the operating lifetime, it will be difficult to interrogate and locate them. So it is necessary to explore the integration of a GPS with the interrogator. When the interrogator travels over a field with farm machinery, the location information of the sensor nodes will be recorded whenever the interrogator has received the readings. This will help locate the sensor nodes in the future when there is a need to replace them.

3.4 Summary

In this chapter, the system design requirements have been described and analysed. The proposed sub-soil sensing system will consist of an above-ground interrogator and a number of sub-soil and battery-free sensor nodes. The sensor nodes are plough-able and can be deployed like planting seeds with farm machinery. Once

the proposed system has been deployed, it is expected to have an operating lifetime longer than 2 years without replacing the sub-soil sensor nodes. The sub-soil sensor nodes are capable of harvesting energy from the RF field that is generated by the interrogator and transmitting multiple sensor measurements to the interrogator wirelessly through soil. In practice, the interrogator is installed on farm machinery. When the on-vehicle interrogator travels over a field, it transmits RF signals to power the sub-soil sensor nodes and then receives sensor measurements from the sensor nodes. The system should be able to achieve a communication performance where the successful reading rate is higher than 80%. Based on the system requirements analysis, a series of research questions or tasks about the system design have been raised and listed, these need to be considered and explored during the course of this research.

Chapter 4

High Level Design

4.1 Introduction

This chapter describes the high level design of the proposed RFID sub-soil system. In Section 4.2, the system overview and design are presented. The details of the RFID reader design and the RFID sensor node design are described in Section 4.3 and Section 4.4.

4.2 System Overview and Design

Figure 4.1 shows the concept diagram of the proposed sub-soil system which comprises a number of sub-soil RFID sensor nodes in a field and an above-ground RFID reader. The RFID sensor nodes will be totally buried in soil and each sensor node is not wired to any other devices. The depth of the sensor nodes within the soil ranges up to 0.5 m, and the specific value will depend on the effective rooting depths of typical crops, such as potato, wheat and field corn [96]. The RFID reader is mounted on a tractor which is common farm machinery for most farming activities, such as ploughing, fertilising and irrigating. The system integrates passive far-field RFID technology, sensing technology and embedded system technology, and each sensor node typically includes an RFID circuit and sensors. The RFID circuit primarily consists of an antenna, a microcontroller and RF components, which is capable of harvesting energy from electromagnetic fields and transmitting sensor measurements from the on-board sensors to the RFID reader wirelessly through backscatter communication.

In practice, when the tractor that holds the RFID reader drives over a field, the sensor nodes will harvest energy from the electromagnetic field generated by the RFID reader, and the harvested energy will be typically stored using an energy storage component, for example ordinary capacitor or super-capacitor. For each sensor node, there will be a *powering time* when the generated electromagnetic fields cover the sensor node antenna and the sensor node is able to harvest energy. Once the sensor node has harvested sufficient energy to supply the on-board power-required components including the active on-board sensors, microcontroller and RF components, it transmits sensory data to the RFID reader wirelessly. The energy budget of a sensor node in this thesis refers to the total required energy for supplying the components that require power.

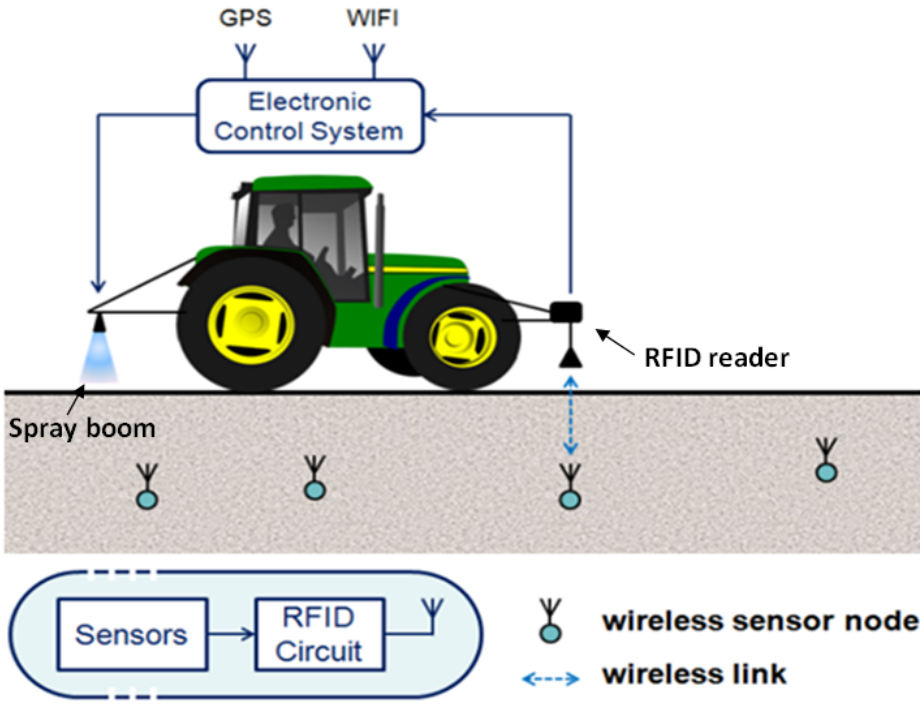

Figure 4.1: Concept diagram of the proposed RFID sub-soil system for agriculture

The RFID reader can be interfaced to other farming systems, for instance, as shown in Figure 4.1 the sensor measurements can be used to control an on-board spray boom for selective application of fertiliser. The sensor measurements can also be shared to remote stations for monitoring via Wireless Local-Area Network (LAN), or cellular mobile systems. An on-board GPS will typically provide

sensory data with location information, which allows mapping of the sensor measurements in a field. The proposed RFID sub-soil sensing system can also be a part of a remote sensing system which helps farmers efficiently monitor farm fields and improve the efficiency in farming activities.

4.3 RFID Reader Design

Figure 4.2 presents the diagram of an RFID reader system which fundamentally comprises a receiver and a transmitter. Similar to most commercial RFID system designs, the transmitter generates Continuous Wave (CW) signals to power the RFID sensor nodes and the receiver amplifiers and demodulates the backscattered signal from the RFID sensor nodes. However, commercial RFID readers are based on the industrial protocols, and they cannot be used to explore the modification to the physical layer nor the system performance in a wide frequency range. Chapter 7 presents the implementation of a software-controlled RFID reader platform using a NI PXI system. An Radio Frequency (RF) circulator [102] is typically used to isolate the transmitting signals and the receiving signals. Since the RFID reader only transmits and receives signals to and from underground sensor nodes, a directional antenna, such as patch antennas [74] is an ideal choice for the reader antenna design. A directional antenna can be used to maximise the radiated RF power in the direction of the sub-soil sensor nodes. The demodulated sensor measurements are typically communicated to an embedded computing system or a portable Personal Computer (PC) using an industry standard serial or network interface. The power for the RFID reader system will be supplied by an on-vehicle battery.

Due to the high path loss in soil [7], the sub-soil sensor node may not be able to harvest sufficient energy within the *powering time*. Slowing down the tractor speed helps maximise the *powering time* and improves the harvested energy by the sensor nodes. However, slow speeds affect farming efficiency, which may not be acceptable to farmers. Regarding this problem, there is a possibility of using two RFID readers. Two RFID readers would be mounted in the front and rear of the tractor separately. The front mounted system, as shown in Figure 4.3a, provides the electromagnetic fields from which the sub-soil node harvests its energy, and

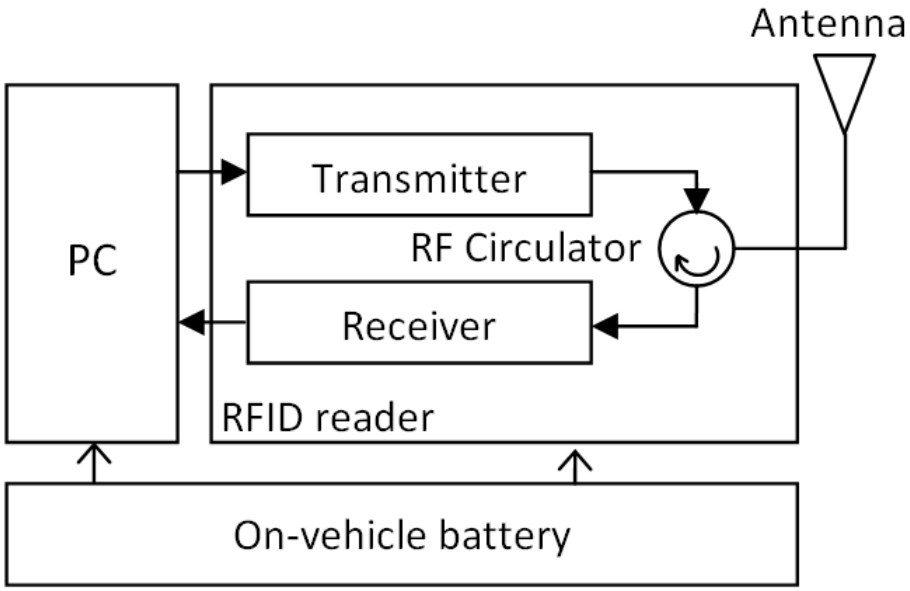

Figure 4.2: Diagram of the RFID reader system.

the rear one, as show in Figure 4.3b, is primarily used for communicating with the sub-soil sensor nodes, although it can also take over the role of providing power to the sensor node. This approach efficiently maximises the *powering time* without affecting the tractor speed.

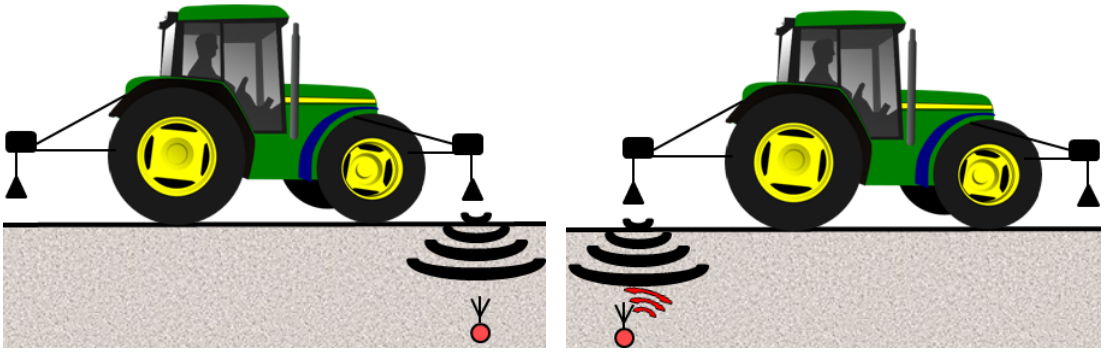

(a) The front reader powers the sensor node (b) The rear reader continues to provide power and communicates with the sensor node

Figure 4.3: System diagram of two-reader design

4.4 RFID Sensor Node Design

It is hard to design the RFID sensor nodes directly using commercial RFID tags as they provide limited ability to integrate with commercial sensors nor to analyse

their performance in RF energy harvesting. Prototyping a passive RFID sensor node is described in Chapter 8. Figure 4.4 presents the block diagram of the passive RFID sensor node prototype design, where the antenna and rectifier circuit harvest energy from the electromagnetic field generated by the RFID reader. An energy storage component accumulates the harvested energy and the stored energy will be only discharged when the voltage of the energy storage component increases to a specific level. At this level of voltage, the stored energy is sufficient to meet the energy budget of the sensor node. A power management circuit then provides the required system voltages using a DC/DC converter. A microcontroller interfaces with the sensors and provides data-logging and data-encoding functions. The encoded sensor measurements are finally backscatter modulated and transmitted by the antenna. Since soil temperature and soil moisture are two key parameters that most of WSN systems [12] will provide, the energy budget of the sensor node should be able to power at least a temperature sensor and a soil moisture sensor.

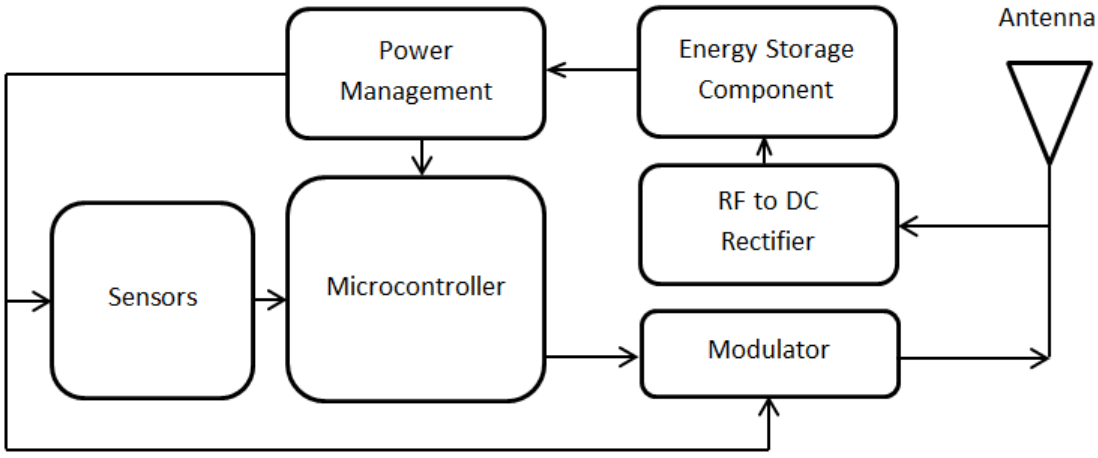

Figure 4.4: Block diagram of sensor node design

The whole sensor node circuit is contained inside an enclosure. The use of the enclosure is primarily motivated to protect the sensor node from the sub-soil environment. In soil, there are potential threats to a sensor node circuit, such as water, roots and insects. A sealed and water-proof sensor node enclosure will efficiently isolate the node circuit from the soil environment. The sensor node enclosure has to be compatible with most of the commercial sensors as reviewed

in Chapter 2. A temperature sensor or a pressure sensor will be completely enclosed within the enclosure. Regarding a soil moisture sensor or a soil pH sensor, the electronic circuit of the sensor has to be enclosed within the enclosure and the metal electrodes of the sensor need to have a physical contact with the soil surrounding the enclosure. Thus, there will be water-proof connectors on the enclosure surface, and these connectors wire the electrodes and the electronic circuit of the sensors. In addition, the material for fabricating the enclosure has to be strong enough to withstand the pressure from the soil, and it also has to be lossless to RF signals so that it will not affect the system communication performance.

4.5 Summary

The proposed RFID system comprises an above-ground RFID reader and a range of sub-soil RFID sensor nodes, which integrates passive RFID technology and sensing technology. The system overview in practice has been presented, where the RFID reader travels with a tractor to interrogate the sub-soil sensor nodes. The sub-soil sensor node will not contain an on-board battery. It is capable of harvesting energy from the EM field generated by the RFID reader and transmitting sensory data wirelessly to the reader through backscatter modulation. Both the designs of the RFID reader and the RFID sensor node have been illustrated with the system block digram presented.

Chapter 5

System Electromagnetic Modelling

5.1 Introduction

As described in Section 1.3, the sub-soil wireless channel brings the challenge of achieving RFID communication through soil: the path loss in the soil limits the energy that can be harvested by an RFID sub-soil sensor node, and also affects the system performance in the communication link. It is important to investigate the potential impact of the soil on a sub-soil communication system. The primary objectives of the investigation are to characterise:

1. the path loss in soil,
2. the effect of the soil on the performance of a sub-soil sensor node antenna,
3. the effect of a sensor node enclosure and the associated air gap on the performance of the sub-soil sensor node antenna.

There are two potential methods to carry out the investigation: by practical measurements or by simulations. The method of practical measurements is typically based on fabricating system prototypes and setting up arrangements for practical experiments. This method can lead to an unpredictably long research time as the experiments will involve physical configurations of the factors including soil moisture, frequency, the depth of the sensor node, and the size of the sensor node enclosure. In addition, the experiments will potentially have the problem of measuring the performance of a buried antenna. It is not always easy

to transfer a massive amount of soil into a laboratory for implementing a soil environment nor to measure the antenna's radiation efficiency or radiation pattern. In contrast, the method of simulations provides the flexibility and convenience in defining the physical structure of a sub-soil communication system as well as dielectric properties of a soil environment. It will be efficient to characterise either the path loss in soil or the performance of a buried antenna in simulations where the soil moisture, the frequency, the depth of the sensor node, and the size of the sensor node enclosure can be readily configured. In this work, the method of simulations is used to provide a basic understanding of the path loss in soil and the effects of the soil and the sensor node enclosure on the performance of a buried antenna. The simulation results will then help narrow down the focus of the practical experiments as will be presented in Chapter 9.

As reviewed in Chapter 2, simulation works have been designed to characterise underground channels. However, most of those works have the primary emphasis on investigating behaviours of EM waves propagating in the soil and analysing the path loss of an underground channel. They do not consider the effect of the soil on a buried antenna. This chapter describes a method of modelling the RFID sub-soil system using Computer Simulation Technology (CST) STUDIO SUITE time-domain solver [103]. System models were constructed to characterise the path loss in soil in the frequency band from 600 MHz to 1200 MHz, the effect of the soil on a buried antenna, and the effect of an air gap around the buried antenna, which will be discussed in Chapter 6. CST STUDIO SUITE is an EM 3D simulation software package which has been widely used to provide characterisations for 3D EM designs. CST EM models are designed within a visual environment by creating multiple objects and defining the dielectric properties and the dimensions of the objects. It provides a flexible and intuitive method to customise and characterise EM designs. In this chapter, the design of a CST EM model for the RFID sub-soil system is presented along with the methods of characterising the performance of a half-wavelength dipole antenna and the path loss between two antennas.

5.2 Electromagnetic Model Design

5.2.1 RFID system model structure

The CST EM model in this work is designed based on the features of the proposed RFID sub-soil system, which consists of an aboveground RFID reader and a sub-soil sensor node. Figure 5.1a presents the screenshot of the CST EM model and the schematic diagram of the model is shown in Figure 5.1b. The CST files containing the model design can be found in Appendix B. The RFID system is modelled using two antennas: a reader antenna and a node antenna. Typical antenna types used in commercial communication systems include the dipole antenna, the patch antenna, the coil antenna and the monopole antenna. As described in Chapter 3, it will be desirable to design a sensor node with an omnidirectional antenna as the sub-soil sensor node can be deployed into soil with a random orientation. The CST EM model adopts the half-wavelength dipole antenna for modelling both the reader antenna and the sensor node antenna. The primary reason for using the half-wavelength dipole antenna is that the antenna has been theoretically analysed and it is usually used as a reference antenna to characterise antenna gain with a unit of dBd [74]. In practice, the half-wavelength antenna has wide acceptance since the radiation resistance of a half-wavelength dipole antenna is very near the characteristic impedance (75 Ω) of some transmission cables [74]. Another reason for using the half-wavelength dipole antenna in the model is due to its simple structure which makes it easy to construct in CST models. An antenna with a simple structure always provides benefits in simulation efficiency as a complex antenna structure will typically lead to long simulation times. The dipole antenna in the CST model, as shown in Figure 5.2 is created by two straight wires oriented end to end on the same axis. A discrete port with 1 Watt excitation is applied to the antenna. In theory, the whole length of the dipole antenna has to be a half-wavelength long for resonance [74]. The length of each of the two wire elements is defined as l in the CST model, which can be used for varying the resonant frequency of the antenna.

The reader antenna is placed above the top surface of a soil tank which is designed in the shape of a cube with side length s. The height of the reader antenna refers to the distance between the antenna and the top surface of the soil. Based on the minimum distance of far-field regions as shown in Equation 2.1,

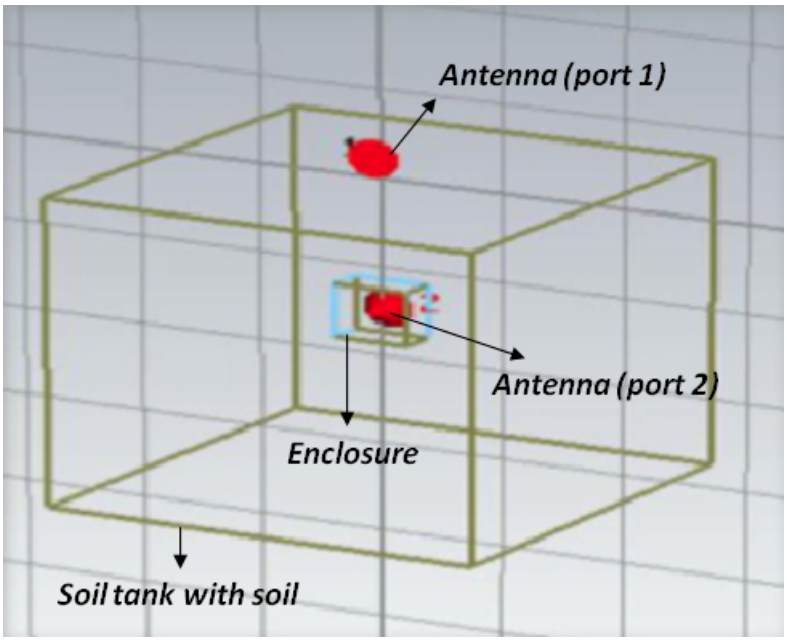

(a) Screenshot of CST EM model

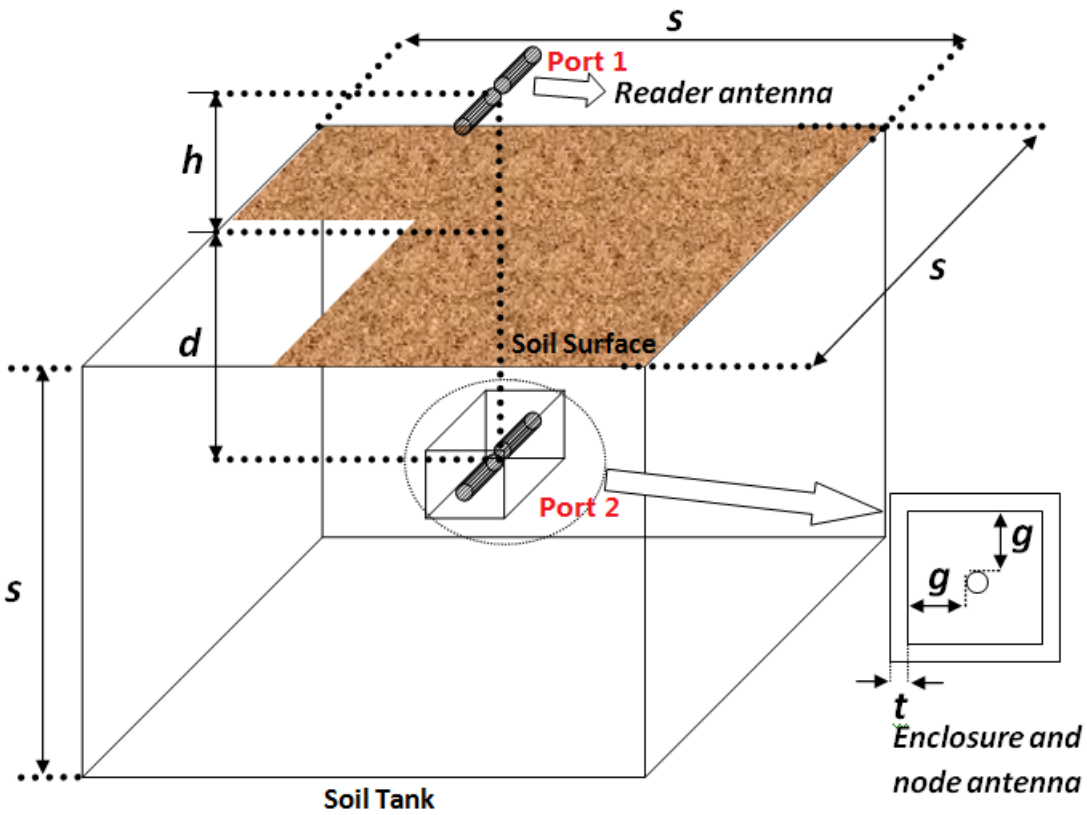

(b) Schematic diagram of CST EM model

Figure 5.1: CST EM model design of the RFID sub-soil system for the simulations.

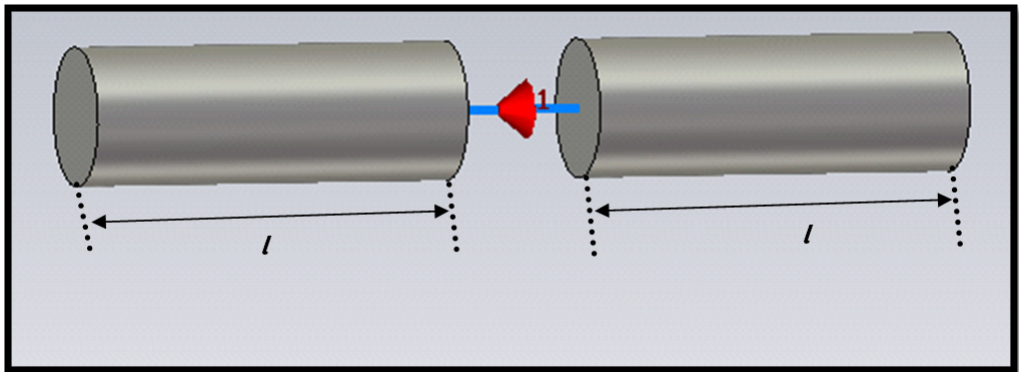

Figure 5.2: Screenshot of the dipole antenna model in CST.

the reader antenna should be at least a half-wavelength of the signal above the soil surface in order to ensure that the soil tank is in the far-field region. The frequency band in this work is from 600 MHz to 1200 MHz, which is the band that most passive far-field RFID systems operate in, therefore the value of the height of the reader antenna is set to 0.5 m. It is not sensible to bury the node antenna directly into the soil tank as the high relative permittivity of the soil has a significant impact on the characteristics of the antenna, such as the bandwidth, input impedance, resonant frequency and efficiency [104, 23, 25]. This effect has been investigated through simulations, and the simulations results will be shown in Section 6.3. In the model design, the node antenna is placed within an enclosure, which is then buried within the soil tank. The enclosure provides an air gap around the antenna. As shown in Figure 5.1a, the antenna is located at the centre of the enclosure. The size of the enclosure is determined by the air gap between the node antenna to each inner surface of the enclosure g, and the parameter t defines the thickness of the enclosure's walls. The air gap will potentially help the antenna performance in the soil and the effect of the gap g on the node antenna performance will be investigated in Chapter 6. The depth of the node enclosure, d refers to the vertical distance between the soil surface to the node antenna. So the overall distance between the reader antenna and the node antenna is $h+d$, and the thickness of soil layer above the node enclosure is $d-(g+t)$. All parameters for defining the model's physical size are listed in Table 5.1.

Table 5.1: List of parameters in the EM model design.

Symbols	Descriptions
h	height of reader antenna above soil surface
d	depth of node antenna in soil tank
s	side length of soil tank
g	gap between enclosure surface and node antenna
t	thickness of enclosure's walls
l	half length of dipole antenna

5.2.2 RFID system model material and soil environment

The dielectric properties of the EM model are required to be defined, and the objects of the EM model include the antennas, the enclosure, the air gaps (outside the soil tank and inside the enclosure) and the soil. The CST package provides a material library where the properties of typical materials for EM model designs are given. The brief descriptions of the selected materials for the four objects are shown in Table 5.2, where ϵ_r is the relative dielectric constant and $tan(\delta)$ is the loss tangent of the materials. The antennas of the EM model use the Perfect Electric Conductor (PEC) which has zero electrical resistance, although PEC does not exist in nature. A PolyVinyl Chloride(PVC) material is selected for the enclosure design. PVC materials are widely used in underground sewage pipes due to their low cost, chemical resistance and ease of joining [105]. The selected PVC material is lossless to RF signals and has a relative dielectric constant ϵ_r of 3.5. The air gaps in the model have typical free-space dielectric properties with the relative dielectric constant ϵ_r of 1 and loss tangent $tan(\delta)$ of 0. The soil material modelling is the most complex work, as the microwave properties of soil are affected by a range of parameters such as frequency, soil texture and soil moisture. The CST material library only provides dry and wet sandy soils, and the microwave properties of the soils are characterised at a single frequency of 10 GHz. It is impossible to use the information provided by the CST material library to simulate dielectric properties of a soil in a wide range of frequencies

and at various moisture content levels. Thus, the soil material modelling in this work is achieved by manually defining the soil dielectric properties based on the semiempirical dielectric model of soil's microwave behaviour [2] as presented in Equations (2.4) and (2.5).

Table 5.2: List of materials used in the EM model.

Material	Description
PEC	zero electrical resistance
PVC	$\epsilon_r = 3.5$ and $tan(\delta) = 0$
air	$\epsilon_r = 1$ and $tan(\delta) = 0$

As discussed in Chapter 3, the semiempirical dielectric model expresses the complex permittivity ($\epsilon^{'}$ and $\epsilon^{''}$) of soils as a function of water content, frequency and soil texture. Thus, given a specific soil type its complex permittivity at various moisture levels and frequencies can be calculated. The CST package allows the creation of a new material by manually specifying its microwave properties: the real part of the relative permittivity $\epsilon^{'}$ and loss tangent $tan(\delta)$. The loss tangent is the ratio of the imaginary part of the complex permittivity to the real part of the complex permittivity. Thus, the method of modelling the soil material can be summarised in two steps: 1) calculate the complex permittivity and loss tangent of the soil material by considering the soil type, the soil moisture and the frequency, and 2) define the microwave properties of the soil in CST by applying the calculated results. For the simulations, the soil material was modelled based on the properties of a sandy soil, which is one of the common soils in agriculture. The properties of the sandy soil are provided in [89], whose sand percentage is 50 %, clay percentage is 15 %, the bulk density is 1.5 g/cm^3, and the solid soil particle density is 2.66 grams/cm^3. Figure 5.3 shows the calculated complex permittivity of the sandy soil at 900 MHz. Both the real and the imaginary parts of the permittivity rise with increasing soil moisture, which means that the moisture content will significantly affect the dielectric properties of the soil.

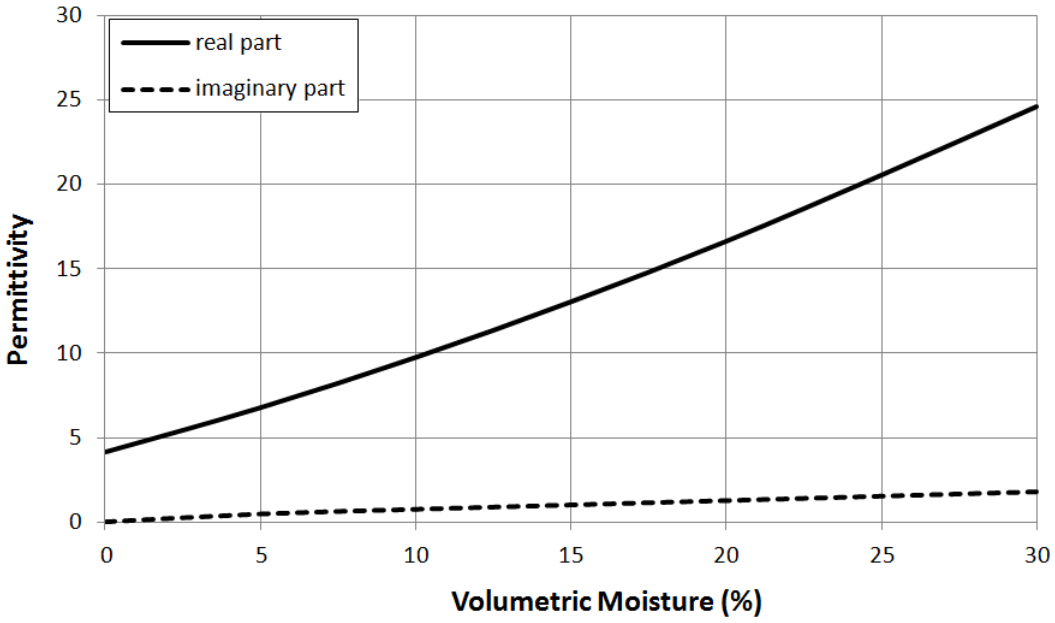

Figure 5.3: Calculated permittivity of the sandy soil at 900 MHz.

5.3 Simulation Method

In this section, the methods of characterising the performance of a buried antenna and the path loss between two antennas through the CST simulations are described. The antenna performance includes return loss, radiation efficiency and radiation pattern. All simulation examples given in this section are based on using the two half-wavelength dipole antennas in air without the soil tank and the sensor node enclosure.

Return loss performance of an antenna is typically characterised from the S (Scattering)-parameter, S_{11}. S-parameters refer to the scattering matrix which is a mathematical construct that has been widely used to quantify how electromagnetic signals propagate through a multi-port network [106]. Figure 5.4 presents the simplified block diagram of a two-port network, and its S-parameter matrix can be expressed as:

$$\begin{bmatrix} b_1 \\ b_2 \end{bmatrix} = \begin{bmatrix} S_{11} & S_{12} \\ S_{21} & S_{22} \end{bmatrix} \begin{bmatrix} a_1 \\ a_2 \end{bmatrix}, \tag{5.1}$$

where a_1 and a_2 can represent the signal power inputs to port 1 and port 2, b_1 and

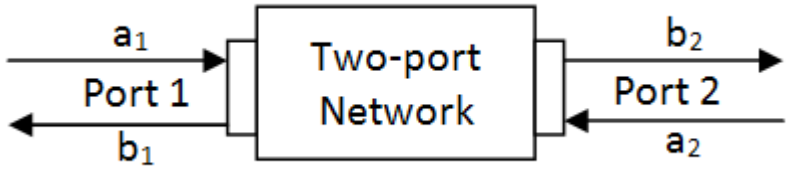

Figure 5.4: Block diagram of the simplified two-port network.

b_2 can represent the signal powers exiting from port 1 and port 2, and S_{11}, S_{12}, S_{21} and S_{22} are S-parameters. Two equations can be obtained from the matrix:

$$b_1 = S_{11}a_1 + S_{12}a_2 \tag{5.2}$$

$$b_2 = S_{21}a_1 + S_{22}a_2. \tag{5.3}$$

As presented in Equation 5.3, the signal power that exits port 2 consists of two element: $S_{21}a_1$ and $S_{22}a_2$. When $a_2 = 0$, $S_{21} = \frac{b_2}{a_1}$, which indicates the power loss or gain during the signal propagation through the network from port 1 to port 2. When $a_1 = 0$, $S_{22} = \frac{b_2}{a_2}$, which is the reflection coefficient at port 2. With the same principle, S_{12} expresses the power loss or gain from port 2 to port 1, and S_{11} expresses the return loss at port 1.

5.3.1 Antenna performance characterisation

5.3.1.1 Return loss and resonant frequency

The return loss of an antenna is also known as the reflection coefficient, which measures the ratio of the power applied to the antenna and the power reflected from the antenna to the source. The reflection loss is typically caused by the impedance mismatch between the antenna impedance and the input impedance of the feed cable at the resonant frequency. A high return loss in a transmitting antenna limits the power radiated out from the antenna. More seriously, it also leads to high reflected power, which can potentially damage components at the power source. The return loss is typically expressed in decibels (dB), for example, the return loss of commercial antennas is typically less than -10 dB over operating frequency bands, which means more than 90 % of the applied power can be

radiated out from the antenna.

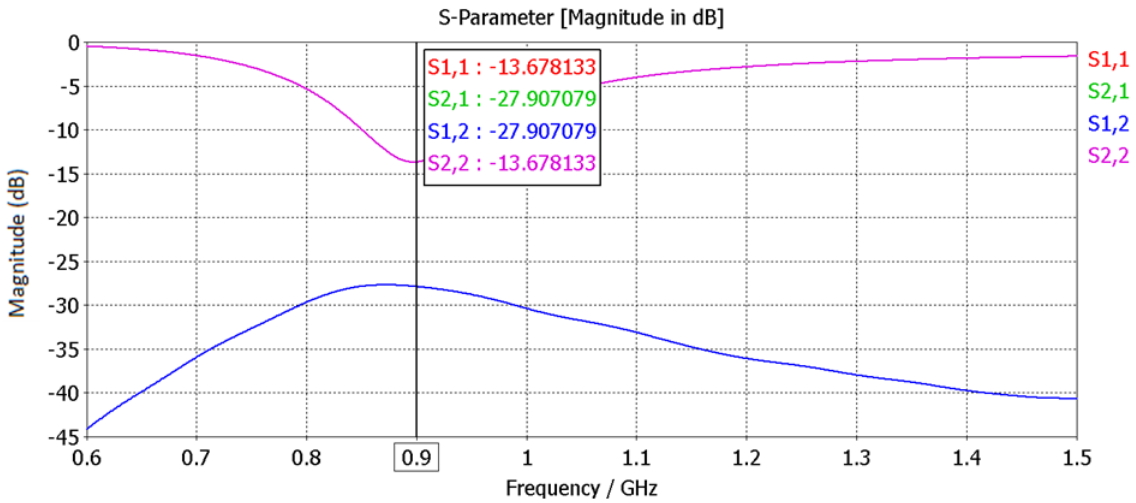

Figure 5.5: Simulated S-parameters for two dipole antennas (900 MHz) in air.

The S-parameter, S_{xx} in CST simulations characterises the return loss of an antenna, where x is the port number on the antenna. Figure 5.5 presents a screenshot of the CST simulation result showing the simulated S-parameters for the two identical dipole antennas (as shown in Figure 5.2) in free-space. The physical half length, l of the antennas is 72 mm and the antennas are separated by 1 m. As shown from the plots of the S_{11} and S_{22} in Figure 5.5, the antennas both achieve a lowest return loss value at 900 MHz (0.9 GHz), as this frequency is the resonant frequency of the antenna. The simulated parameters of S_{21} and S_{12} in Figure 5.5 show that the path loss between the antennas is -27.9 dB at 900 MHz, and characterising path loss will be described in Section 5.3.2. The resonant frequency of a dipole antenna will shift when varying the length of the antenna. Figure 5.6 shows the plot of the antenna model length versus the resonant frequency, which is obtained through the CST simulations. It is observed in Figure 5.6 that the resonant frequency of a half-wavelength dipole antenna increases with decreasing length of the antenna, and the overall length of the antenna is not exactly equal to a half-wavelength in the simulations. For example, the antenna achieves resonance at 900 MHz when its half length l increases to 72 mm which is shorter than the quarter-wavelength at 900 MHz, approximately 83 mm. Actually the half-wavelength at a specific frequency is only used to estimate the physical length of a have-wavelength dipole antenna, and the actual length of the dipole antenna

for resonance is affected by the feeding gap between the antenna wires and the radius of the wires [107]. Details of constructing the dipole antenna will not be further discussed in this thesis.

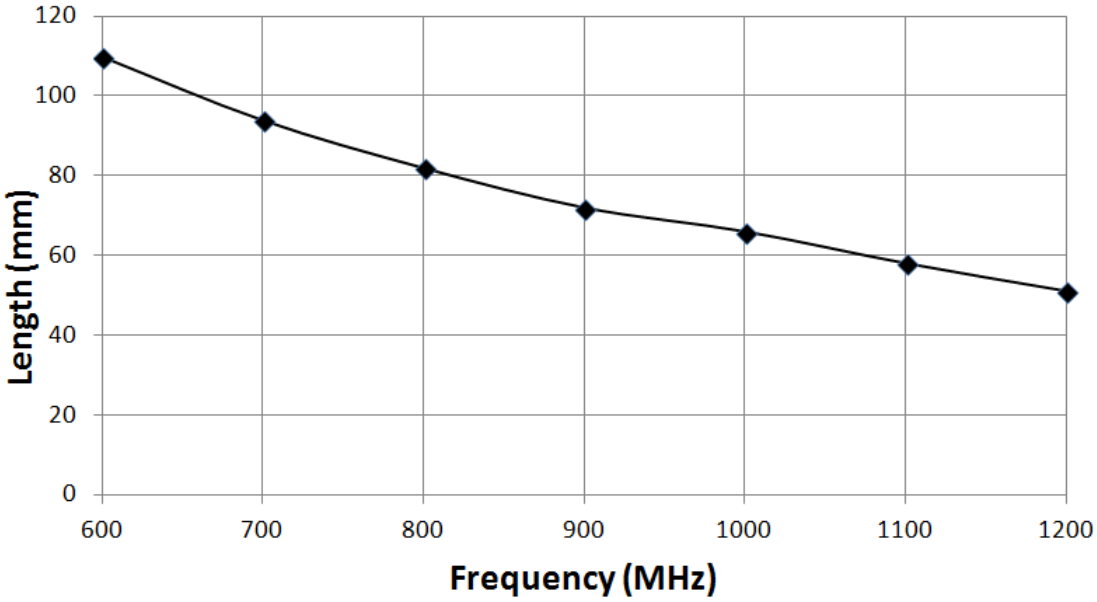

Figure 5.6: Dipole antenna half length, l versus resonant frequency.

5.3.1.2 Radiation efficiency and pattern

Assuming the impedance of the antenna is well matched to the characteristic impedance of the feed cable connecting to a radio system, the radiation efficiency is a measure of the ratio of the actual power radiated by the antenna to the power supplied to the antenna. The radiation efficiency of an antenna is affected by the conduction loss and the dielectric loss of the antenna [74]. The conduction loss is a result of the finite conductivity of the antenna, and the dielectric loss is due to RF absorption by the dielectric materials within or near the antenna. Since the antennas of the EM model use the PEC material, the conduction loss can be ignored in CST simulations.

An antenna radiation pattern is a graphic representation of the radiation properties of the antenna, and it is typically used to present the three-dimension spatial distribution of radiated energy as a function of space coordinates [74]. Antennas typically radiate energy with three pattern types: isotropic, directional

and omnidirectional patterns [74]. An isotropic pattern has equal radiation in all directions, but this pattern does not physically exist. A directional antenna radiates EM waves more effectively in some directions, and one example of directional antennas is the horn antenna [74]. An omnidirectional pattern is a special type of a directional pattern, but it has an essentially nondirectional pattern in a given plane [74]. The half-wavelength dipole antenna is an example of an omnidirectional antenna [74].

Figure 5.7 presents the screenshot of the CST simulation result showing the performance of the dipole antenna model whose resonant frequency is 900 MHz in free-space. The simulated performance includes radiation pattern, radiation efficiency, total efficiency and gain. The total efficiency η_{total} of an antenna takes into account the reflection loss and the radiation efficiency [74]:

$$\eta_{total} = \eta_{rad}(1 - \eta_{ref}) \tag{5.4}$$

where η_{ref} is the antenna reflection coefficient (return loss) and η_{rad} is the antenna radiation efficiency. The gain of an antenna measures the ratio of the radiated power from the antenna in a specific direction to the input power applied to the antenna [74]. Typically, an antenna gain is expressed in the unit of dBi which is based on using a lossless isotropic source as the reference antenna [74]. As shown in the simulation result in Figure 5.7, the dipole antenna model has an omnidirectional radiation pattern and it has a nondirectional pattern in the x-y plane. The antenna achieves a radiation efficiency of 0 dB (100 %), and this is because the antenna is created using an ideal PEC material and the antenna radiates energy into free-space. The total efficiency is -0.22 dB (95 %) and the power loss is because of the return loss. The simulated maximum gain of the antenna is 2.17 dBi, and this value is comparable to the theoretical gain of a half-wavelength dipole, which is 2.15 dBi [74].

5.3.2 Path loss characterisation

The path loss between two antennas typically refers to the overall power loss that occurs during the transfer of energy between the antennas. With the proposed RFID sub-soil system, the path loss between the reader antenna and the node

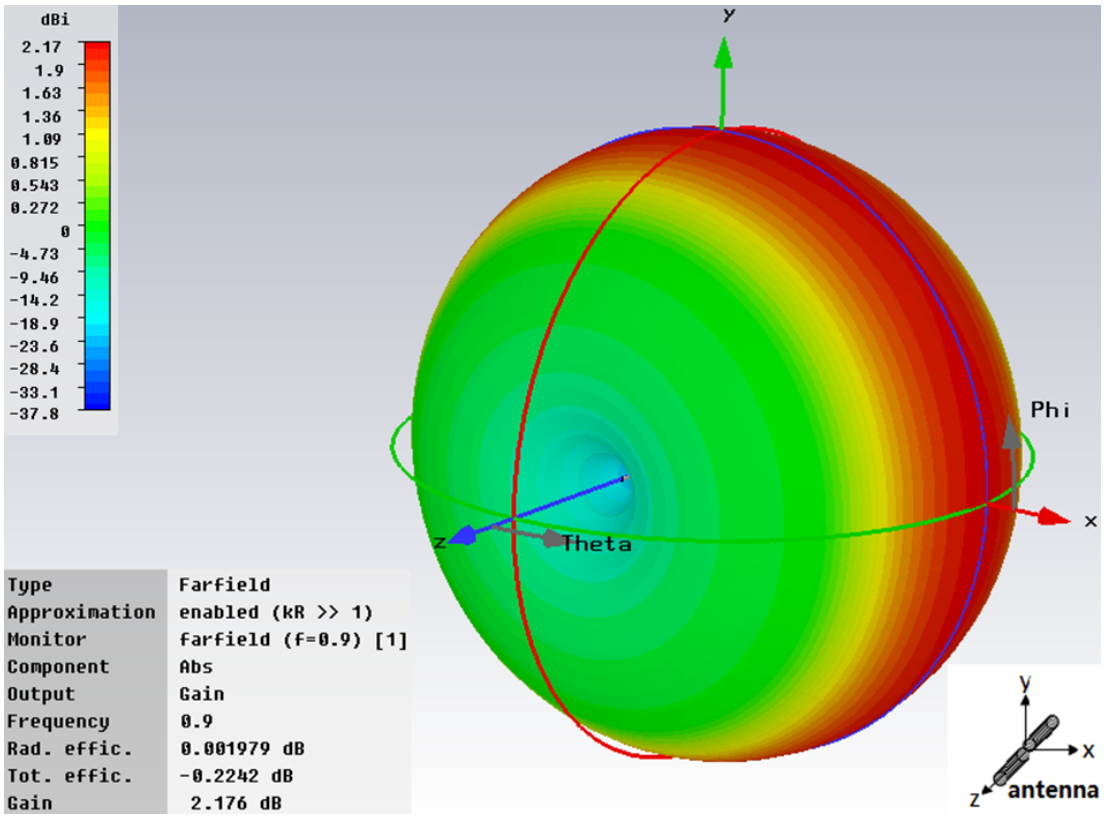

Figure 5.7: Simulated dipole antenna 3D pattern with antenna performance at 900 MHz.

antenna is primarily due to the RF energy absorption in the soil. Free-Space Path Loss (FSPL) will also contribute to the path loss, which can be expressed as shown in Equation 2.11. The EM model of the RFID sub-soil system can be seen as a two-port network where the reader antenna is port 1 and the node antenna is port 2, S_{21} measures the ratio of the received power by the node antenna to the supplied power input to the reader antenna. If S_{21} is equal to 0 dB, then the node antenna receives all the power transmitted by the reader antenna. A negative value of S_{21} (dB) indicates that there are power losses between two antennas. Based on Friis transmission equation [81], the path loss between two antennas in free-space can be expressed as:

$$S_{21}(dB) = P_r(dB) - P_t(dB) = G_t(dB) + G_r(dB) + FSPL(dB), \tag{5.5}$$

where G_t and G_r are the gains of the transmitter antenna and the receiver antenna, P_t is the power input at the transmitter antenna and P_r is the power received by the receiver antenna. Similar to S_{11}, the plot of S_{21} versus frequency is provided in the simulation result, as shown in Figure 5.5. Based on the Friis equation, simulations have been designed to characterise the FSPL at 900 MHz using two dipole antenna models (the port 1 and the port 2 of the simulation). In the simulations, the distance between the antennas was varied in the range of 0.2 m to 1.4 m, and the corresponding S_{21} was characterised. Figure 5.8 presents the simulated result, where the simulated FSPL is comparable to the calculated result based on Equation 5.8. It is observed in Figure 5.8 that the simulated plot and the calculated plot have a good agreement.

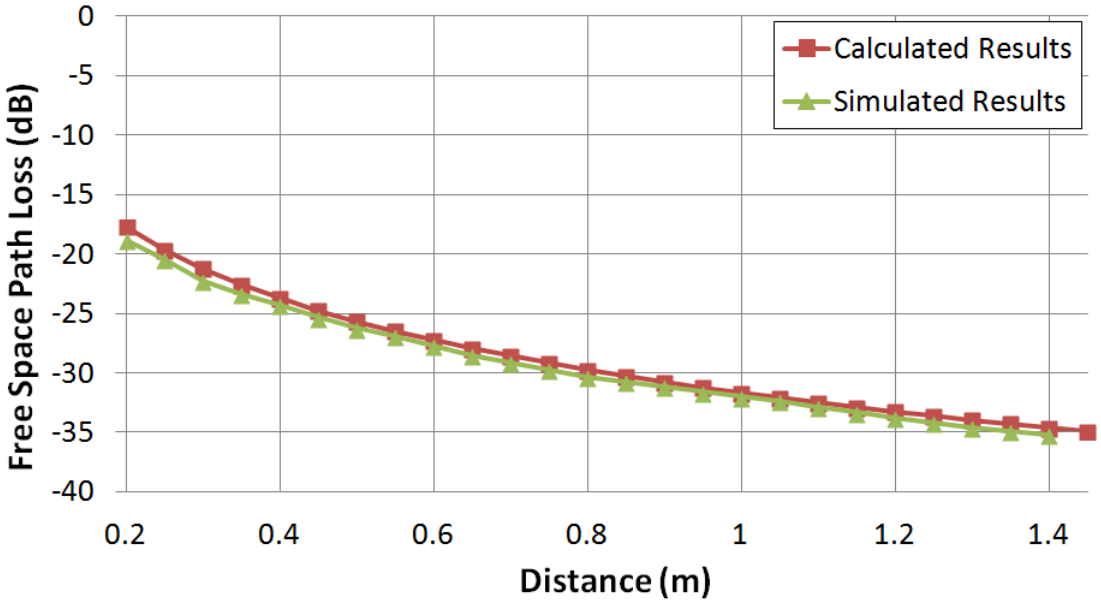

Figure 5.8: Simulated and calculated Free Space Path Loss at 900 MHz.

5.4 Summary

This chapter presents a method of modelling an RFID sub-soil system using the CST software package. The design of the CST electromagnetic model has been described, which includes two half-wavelength dipole antennas, a sensor node enclosure, and a soil tank. Except for the soil, the objects in the model use the materials that are provided by the CST material library. The soil is modelled

by deriving its complex permittivity according to parameters such as the soil texture, the soil moisture, and the frequency. The simulation methods of characterising the antenna performance and the path loss have been described. An example EM model containing two half-wavelength dipole antennas in free-space has been used in the simulations to illustrate how to characterise the antenna performance of return loss, radiation efficiency and radiation pattern, as well as how to characterise the FSPL between the two antennas.

Chapter 6

Electromagnetic Simulations and Results

6.1 Introduction

To a certain extent, soil especially wet soil behaves as a lossy medium as reviewed in Chapter 2, which will affect the performance of a buried antenna. For example, the high dielectric constant of the soil surrounding an antenna can alter the resonant frequency of the antenna. In addition, soil will absorb the energy of EM waves and will cause dielectric power loss in the sub-soil wireless channel. With an RFID sub-soil system, the soil around the sub-soil sensor nodes is one of the primary concerns which will affect the system performance. CST simulations have been undertaken based on using the EM model presented in Figure 5.1, which have explored the impact of sandy soil on the performance of a half-wavelength antenna. The simulations have also considered investigations which are not sensible to carry out by practical measurements, such as the effect of a sensor node enclosure and its size, and the impact of the soil tank size. In addition, the path loss between the above-ground reader antenna and the sub-soil node antenna has been investigated in the simulations. Parameters including frequency, the depth of the sensor node and soil moisture content are considered.

This chapter describes the CST simulations and presents the simulation results. In the simulations, the depth of the sensor node ranges from 0.1 m to 1 m, which covers the depth range proposed in the system design in Chapter 4 (0.2 m to 0.5 m). The frequency band that is considered in the simulations is from 600 MHz

to 1200 MHz. Choosing this frequency band is motivated by designing an RFID sub-soil system at UHF frequencies which can provide an acceptable compromise between antenna size and path loss in soil. The moisture content of the sandy soil in the simulations for measuring the path loss ranges from 5% (dry) to 25 % (wet). A moisture content higher than 25% is limited by the memory size of the PC on which the simulations run, and the limitations are discussed in Section 6.2.

6.2 Soil Tank Size

Based on the EM model presented in Figure 5.1, the required memory for running a simulation is primarily influenced by two factors: soil tank size and soil moisture content. A larger soil tank or a higher soil moisture level will demand a larger memory size and leads to a longer simulation time. In other words, the memory size of the PC will limit the size of the soil tank or the soil moisture content in the simulations. When the required memory size exceeds the PC's memory size which is 48 GigaBytes (GB), the simulation will abort with an error. For example, the simulation failed running when the size of the soil tank increased to 7000 mm $\times$ 7000 mm $\times$ 7000 mm with 10% moisture sandy soil. Although the problem can be solved by decreasing the the soil moisture content to 5%, this will limit the investigation on the effect of soil moisture content on the path loss in soil. With this limitation, it is not feasible to model the actual size of a soil environment in the simulations. The primary concern of decreasing the soil tank size is that the model does not match reality and so cannot provide a certain fidelity of result. This section describes CST simulations which have been undertaken to investigate the impact of the soil tank size. These simulation results help choose the soil tank size for the simulations in Section 6.3 - 6.5 and the size of a soil planter for the practical experiments as will be described in Chapter 9.

Figure 6.1 presents the diagram of the EM model for investigating the impact of the soil tank size, where the depth of the sensor node d and the side length of the soil tank s were varied in the simulations. The depth of the sub-soil antenna d was firstly set to 500 mm and then set to 1000 mm. The side length of the soil tank s gradually increased from 600 mm to 2500 mm when the depth d was 500 mm,

and from 1100 mm to 2500 mm when the depth d was 1000 mm. The half length l of the antennas was adjusted to 72 mm for achieving a resonant frequency of 900 MHz in air. Regarding other parameters, the height of reader antenna h was 500 mm, the air gap width (sensor node enclosure size) g was 20 mm and the thickness of the sensor node enclosure was 5 mm. As described in Chapter 5, the soil tank will be positioned within the far-field region of the reader antenna, in the frequency band from 600 MHz to 1200 MHz this requires the height of reader antenna to be 500 mm. The setting of the air gap is motivated by reducing the impact of the soil on the sensor node antenna. The value of the thickness is set to the thickness of the PVC material that will be used to fabricate a sensor node enclosure prototype for the practical experiments, as will be described in Chapter 9.

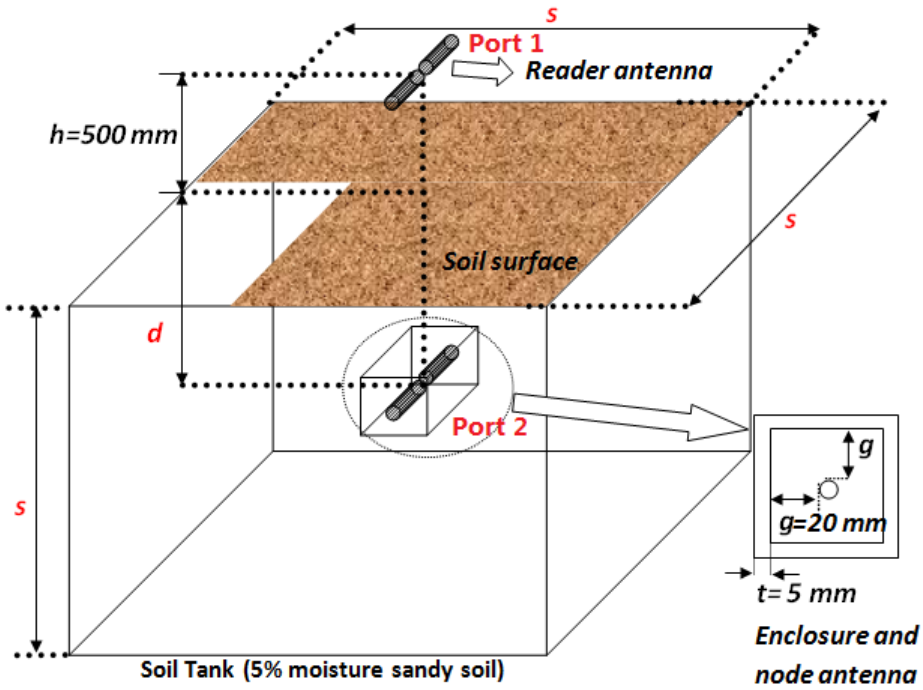

Figure 6.1: Diagram of EM model for investigating the impact of soil tank size

Figure 6.2 shows the simulated path gain, S_{21} at 900 MHz in dry sandy soil (5% soil moisture content) versus the soil tank size. It is shown in Figure 6.2 that the simulated path gain oscillates with increasing size of the soil tank and then becomes a constant (less than $\pm$ 1 dB error) when the side length of the soil tank is longer than 1500 mm at the depth of 500 mm, and 2000 mm at the depth of 1000 mm. This observation indicates that the simulation result can

have an error higher than ± 1 dB when using a soil tank with the size smaller than 2000 mm × 2000 mm × 2000 mm at the depth range up to 1000 mm and approximately 1500 mm × 1500 mm × 1500 mm at the depth range up 500 mm.

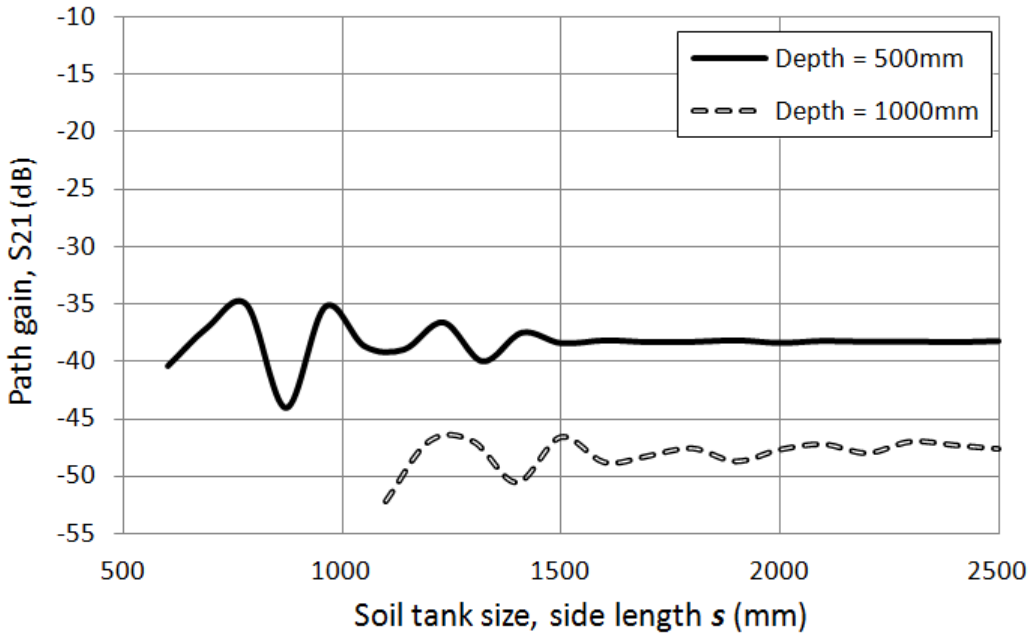

Figure 6.2: Simulated path gain S_{21} (at 900 MHz in dry sandy soil) versus the soil tank size (side length s) at the depths of 500 mm and 1000 mm.

When using a small soil tank size for a simulation, the primary concern is the potential power leakages along the side wall of the soil tank. The power leakage is not desirable in the simulation as it will affect the degree to which the EM model matches reality. Simulations then have been undertaken to investigate the power leakage by using an EM model whose diagram is shown in Figure 6.3. Comparing the EM model as shown in Figure 6.1, the EM model for investigating the power leakage includes four RF absorbers around the surface of the soil tank. The absorber dielectric properties were set to: $\epsilon' = 10$ and $tan(\delta) = 0.99$. With the loss tangent $tan(\delta)$ of 0.99, the surface absorber behaves as a nearly perfect absorbing material and is able to absorb the potential power leakages. In the simulations, the absorber has a fixed size, of which the width was 500 mm and the thickness was 200 mm.

Figure 6.4 shows the plots of the simulated path gain, S_{21} versus the side

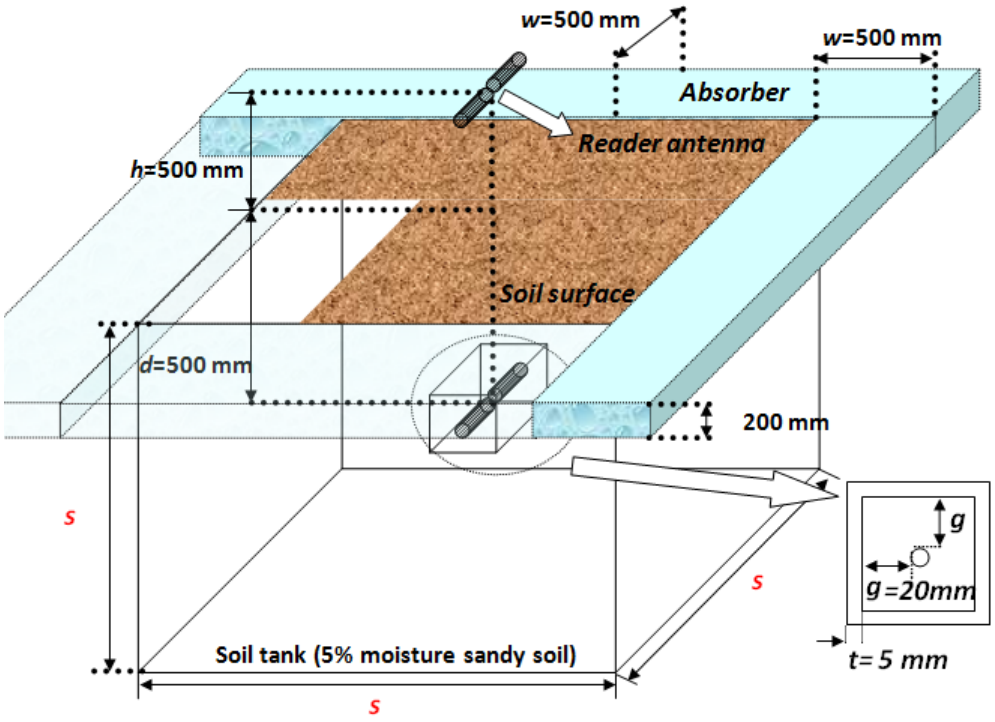

Figure 6.3: Diagram of EM model with RF absorbers at the top of soil tank.

length s of the soil tank with and without the surface absorbers. Both plots presented in Figure 6.4 show that the simulated path gain oscillates with increasing size of the soil tank s from 600 mm to 1500 mm and that the simulated path gain tends to be a constant, approximately -38 dB when the soil tank size s is longer than 1500 mm. When using the surface absorbers around the soil tank, there is an observation that the magnitude of the oscillation becomes lower, which indicates the potential existence of power leakage when using a small size soil tank. The reason for the oscillation could be due to the soil affecting the performance of the sensor node antenna and the level of the effect varies when changing the size of the soil tank. The effect of the soil tank on the simulation result will not be further analysed through simulations, but it has been considered when undertaking other simulations.

In order to improve the degree to which the model matches reality, the simulations as shown in Section 6.3 to Section 6.5 use the soil tank size of 2000 mm $\times$ 2000 mm $\times$ 2000 mm. As shown in Figure 6.2, the simulation result tends to be a constant with an error less than $\pm$ 1 dB when the side length of the soil tank s increases longer than 2000 mm. With this size of the soil tank, the maximum

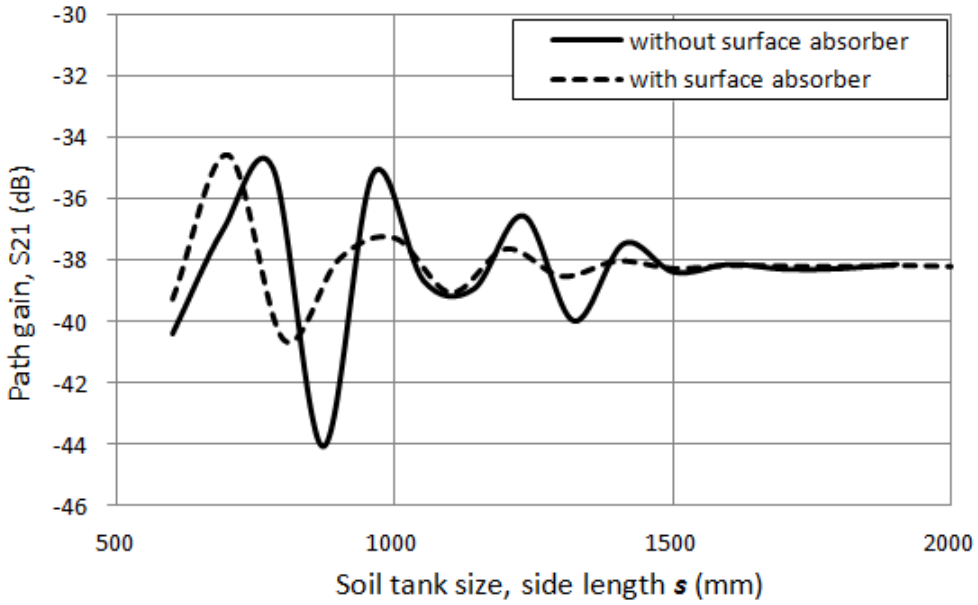

Figure 6.4: Plots of the simulated path gain (at 900 MHz and the depth d of 500 mm in dry sandy soil) versus the soil tank size (side length s) with and without surface absorbers.

achievable soil moisture is 25 % in the simulations, and this level represents a relatively high moisture level in farm fields at depths from 200 mm to 700 mm [108]. A soil tank with the volume of 2000 mm × 2000 mm × 2000 mm is easily created in CST simulations, but it is challenging to implement in practice. The soil volume of 2000 mm × 2000 mm × 2000 mm refers to at least 9 tons of soil, and it is not sensible to transfer such a mass of soil into a laboratory for practical experiments. As indicated from the simulation results in Figure 6.2 and Figure 6.4, there are two potential factors which affect the required soil tank volume at which the simulation result has an error less than ± 1 dB. One of the factors is the depth of the sensor node. As shown in Figure 6.2, the required soil tank size that leads to a simulation error less than ± 1 dB is decreased from 2000 mm × 2000 mm × 2000 mm to 1500 mm × 1500 mm × 1500 mm with decreasing depth from 1000 mm to 500 mm. The second factor is the RF absorbers around the soil tank surface. The plots in Figure 6.4 show that the use of the RF absorbers drops the required soil tank size, at the depth of 500 mm, to 1000 mm × 1000 mm × 1000 mm. These two factors have been considered when choosing the size of a soil planter for the practical experiments as will be described in Chapter 9.

6.3 Sub-soil Antenna Performance

As described in Section 5.3.1, the dipole antenna achieves a total efficiency of over 94.3% at 900 MHz in air. Since soil has different dielectric properties compared to air, it is interesting to know how this 900 MHz dipole antenna will behave in soil in terms of return loss, radiation efficiency as well as radiation pattern. As analysed in Chapter 5, it is not sensible to investigate the performance of a buried antenna by practical measurements due to the difficulty of configuring the experimental arrangement. Therefore CST simulations have been undertaken to characterise the performance of a half-wavelength dipole antenna which is directly buried in dry sandy soil. The simulations were based on the EM model as shown in Figure 5.1, but there was a modification to the model: the sensor node antenna was directly buried within the soil tank without the sensor node enclosure, and the updated diagram of the model is shown in Figure 6.5.

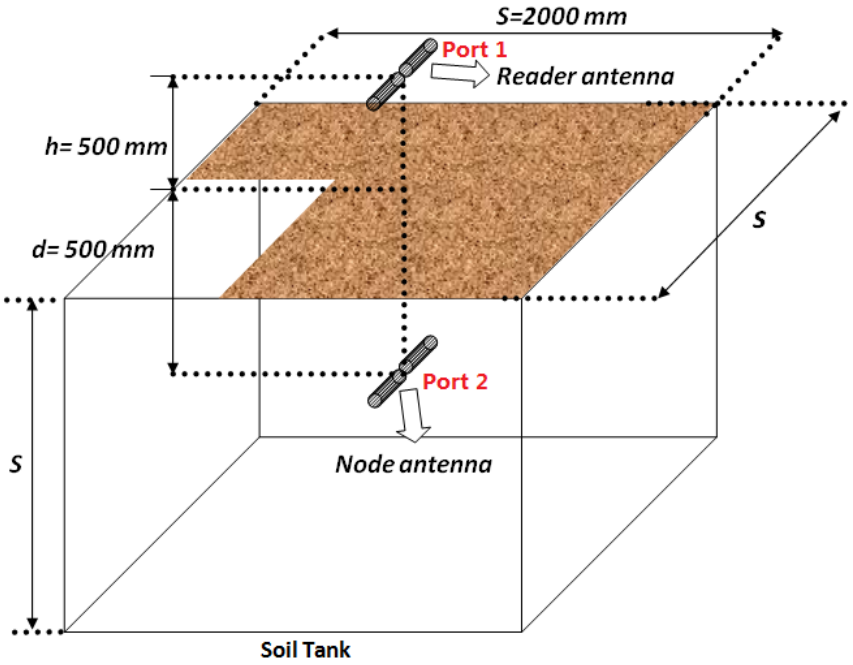

Figure 6.5: Diagram of the EM model for characterising the performance of a buried antenna without sensor node enclosure.

The model shown in Figure 6.5 allows for the characterisation of the complete

impact on the antenna performance only from the soil. As shown in Figure 6.5, the sensor node antenna was buried 500 mm below the soil tank top surface, where the most of crops' roots would be located [97]. The side length s of the soil tank was 2000 mm. The reason for choosing this size has been discussed in Section 6.2. The half length of the dipole antennas, l, was set to 72 mm, leading to a resonant frequency of 900 MHz in air. The soil material used in the simulation was the sandy soil with 5% moisture content. The soil dielectric properties are $\epsilon' = 6.78$ and $\epsilon'' = 0.48$, which are calculated based on the semiempirical model as expressed in Equations 2.4 - 2.9 [2]. The reader antenna was not considered in the simulations although it existed in the EM model.

Figure 6.6 presents the simulation results where the simulated S_{22} measurement in the soil is compared to the simulation result in air. It is obvious that the resonant frequency of the antenna is affected by the soil, and the antenna achieves the resonant frequency at 1150 MHz in the soil. At 900 MHz, the simulated return loss of the buried antenna is only -5 dB, which means that over 31.6% of the supplied power is reflected back to the source. The simulated antenna radiation performance in the soil is shown in Figure 6.7. The radiation efficiency of the antenna at 900 MHz drops to -14.77 dB (3.33%) in the soil compared to the value of -0.01 dB (99.74%) in air. The sharp decrease in the radiated power is primarily due to the RF absorption by the soil around the antenna. The 5% moisture sandy soil behaves as a lossy medium, and so the soil around the antenna causes a high dielectric power loss. The radiation pattern shown in Figure 6.7 shows a more directional pattern for the antenna in soil as opposed to in air.

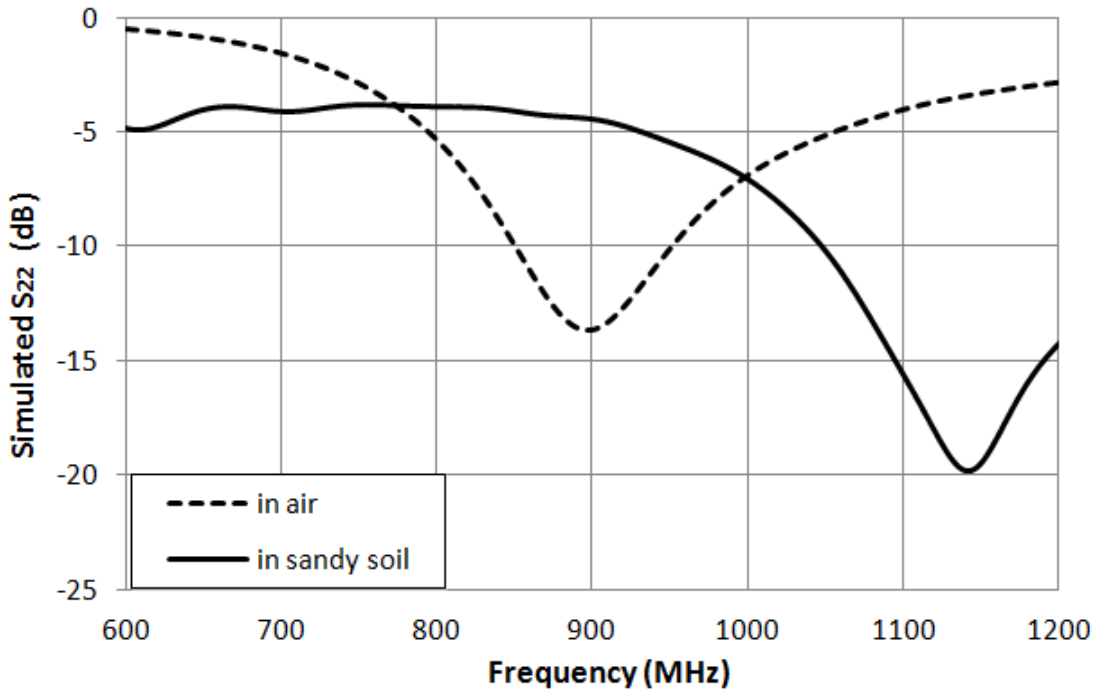

Figure 6.6: Comparison of the simulated S_{22} (return loss) of the antenna in air and in the sandy soil.

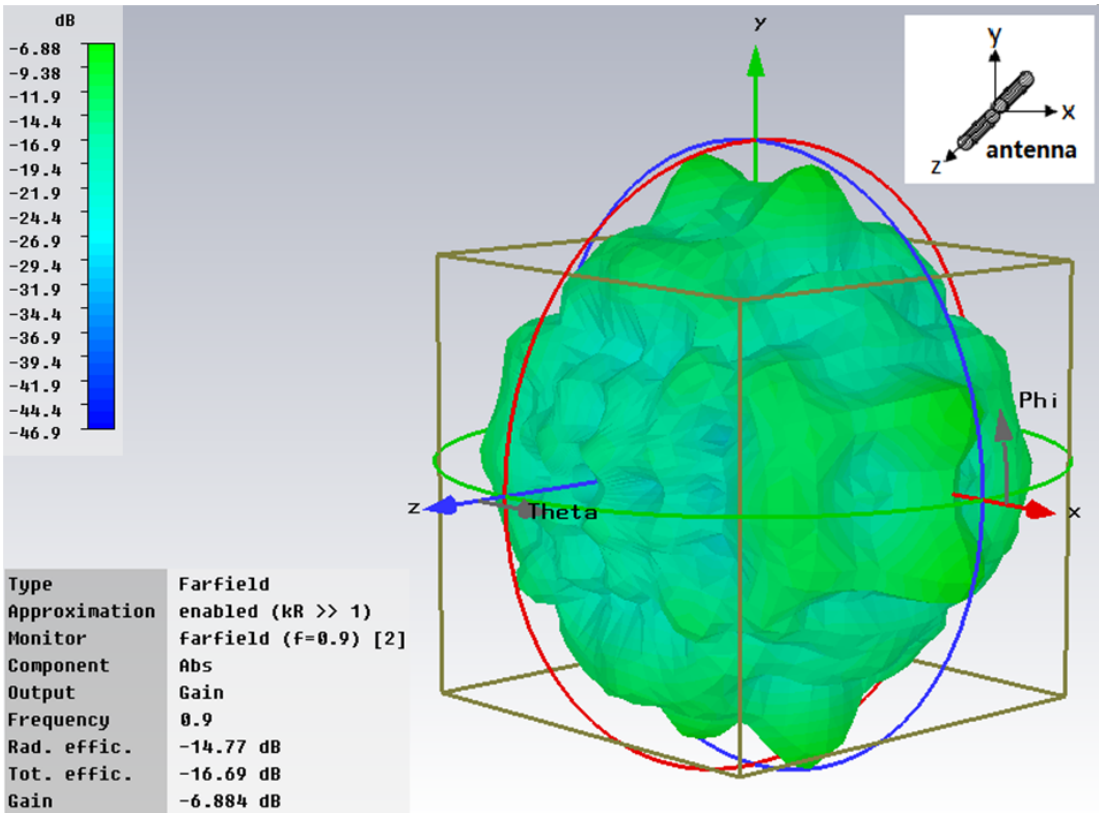

Figure 6.7: Simulated radiation pattern of the antenna at 900 MHz in the sandy soil.

6.4 Sensor Node Enclosure

An enclosure has been proposed in the system design to contain the sensor node circuit and the sensor node antenna. The original motivation of using the enclosure is to provide the sensor node circuit with protection from the sub-soil environment since the nature of underground environment is complex, where there are potential threats to the sensor node circuit such as water, roots and insects. The effort to improve the performance of a buried antenna also motivates the use of a sensor node enclosure, as it will provide an air gap around the antenna. The air gap is expected to minimise the impact of the soil on the antenna performance. In this research, it is necessary to investigate the effect of a sensor node enclosure on the antenna performance by considering the enclosure size, the enclosure material and the position of the sensor node antenna. The investigation was carried out by undertaking CST simulations, both the simulations and the simulation results are presented and discussed in this section.

Figure 6.8 shows the EM model for the simulations, where the sensor node antenna is enclosed at the centre of the sensor node enclosure. The thickness of the enclosure walls, t, was set to 5 mm. Choosing this value is for matching the thickness of the PVC material that was used to fabricate a sensor node enclosure prototype as will be described in Chapter 9. Other settings, such as the side length of the soil tank s, the depth of the sensor node antenna d, the height of the reader antenna h and the soil dielectric properties of the model remain the same as in the simulations described in Section 6.3. In the simulations, the gap, g between the antenna and inner surface of the enclosure was firstly set to 10 mm, a value that was originally motivated by the benefit of having a small enclosure size when deploying the system. The gap was then gradually increased to 20 mm with a step of 2 mm. The simulations only characterised the performance of the sensor node antenna and did not consider the reader antenna. The half length of the sensor node antenna was set to 72 mm for achieving a resonant frequency of 900 MHz in air.

Figure 6.9 compares the simulated return loss of the sensor node antenna at the enclosure sizes, g of 10 mm, 15 mm and 20 mm. As shown from the plots in Figure 6.9, the antenna's resonant frequency is approximately 650 MHz when using a small sensor node enclosure (g = 10 mm), which is decreased by

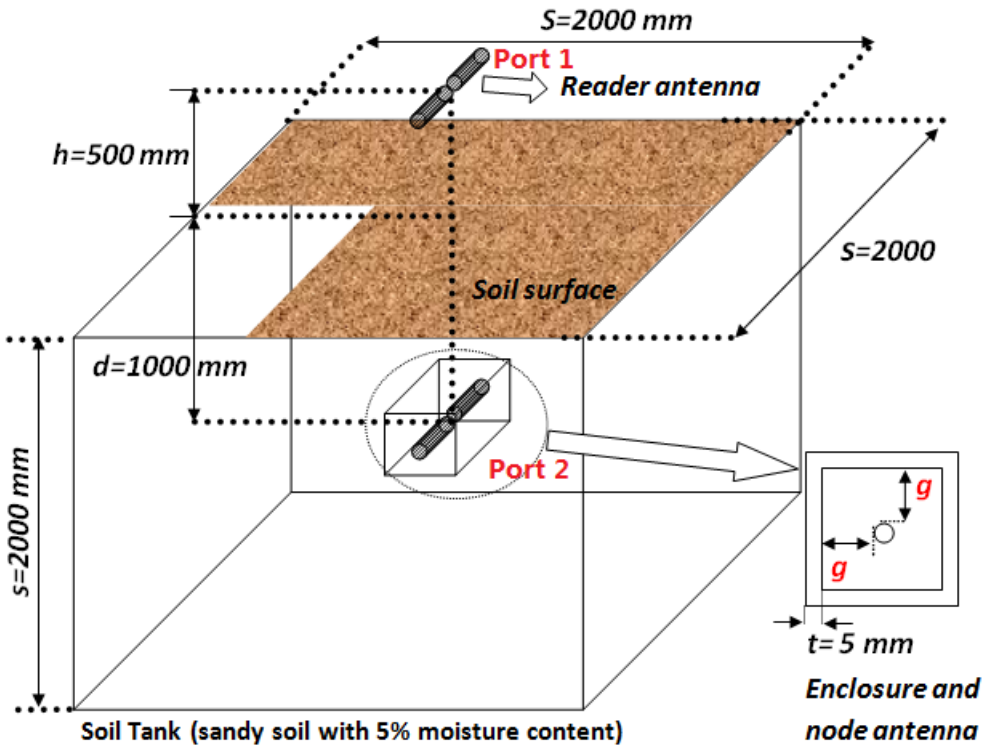

Figure 6.8: Digram of the EM model for investigating the effect of the sensor node enclosure.

250 MHz from the resonant frequency in air. With increasing of the enclosure size, g to 15 mm, the characterised resonant frequency increases to approximately 850 MHz, and the antenna achieves the resonant frequency of 900 MHz when the enclosure size, g increases to 20 mm. Figure 6.10 shows the simulated return loss at 900 MHz versus the enclosure size g, where it is found that increasing enclosure size (air gap) improves the antenna's return loss performance, and the simulated S_{22} at 900 MHz drops less than -10 dB when enclosure size, g increases above 15 mm.

The effect of the sensor node enclosure on the antenna's radiation performance is shown in Figure 6.11, which plots the simulated antenna efficiencies versus the enclosure size g. It is observed that large enclosure size helps to improve the total efficiency, but the radiation efficiency has little change with increasing of the enclosure size. When the gap g increases to 20 mm, the difference between the total efficiency and the radiation efficiency becomes small, approximately 0.2 %. This result indicates that the increase in the total efficiency is primarily due to the

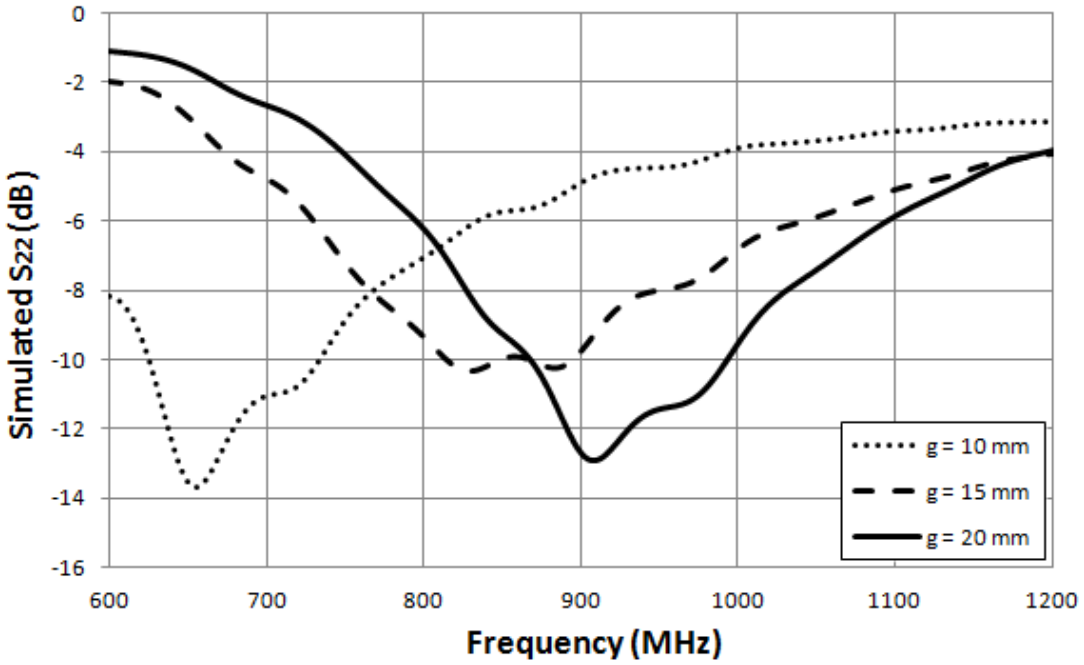

Figure 6.9: Comparison of the simulated S_{22} (return loss) of the sub-soil antenna at three sizes of the sensor node enclosure g.

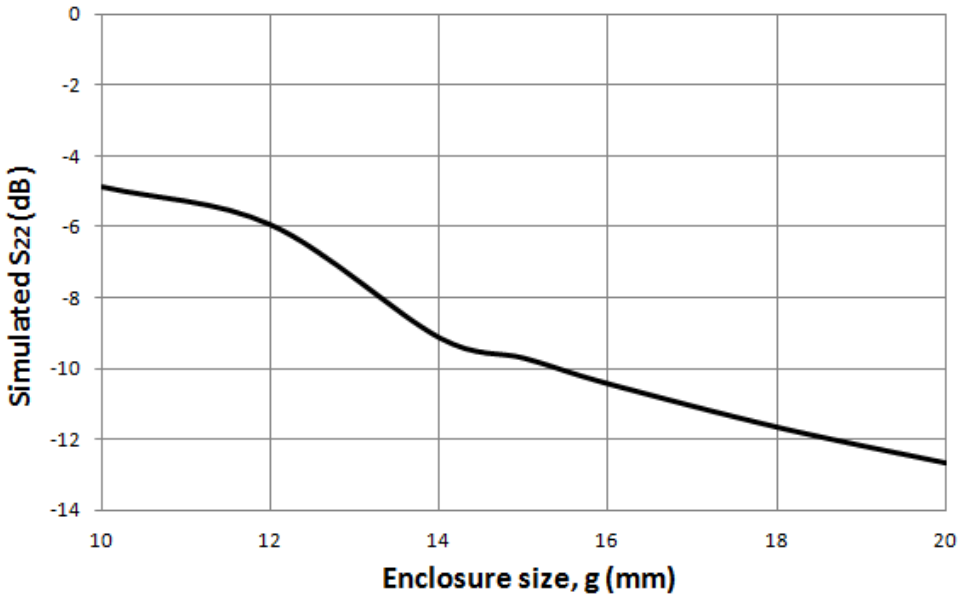

Figure 6.10: Simulated return loss versus the gap between the antenna and the inner wall of the sensor node enclosure (enclosure size) g at 900 MHz

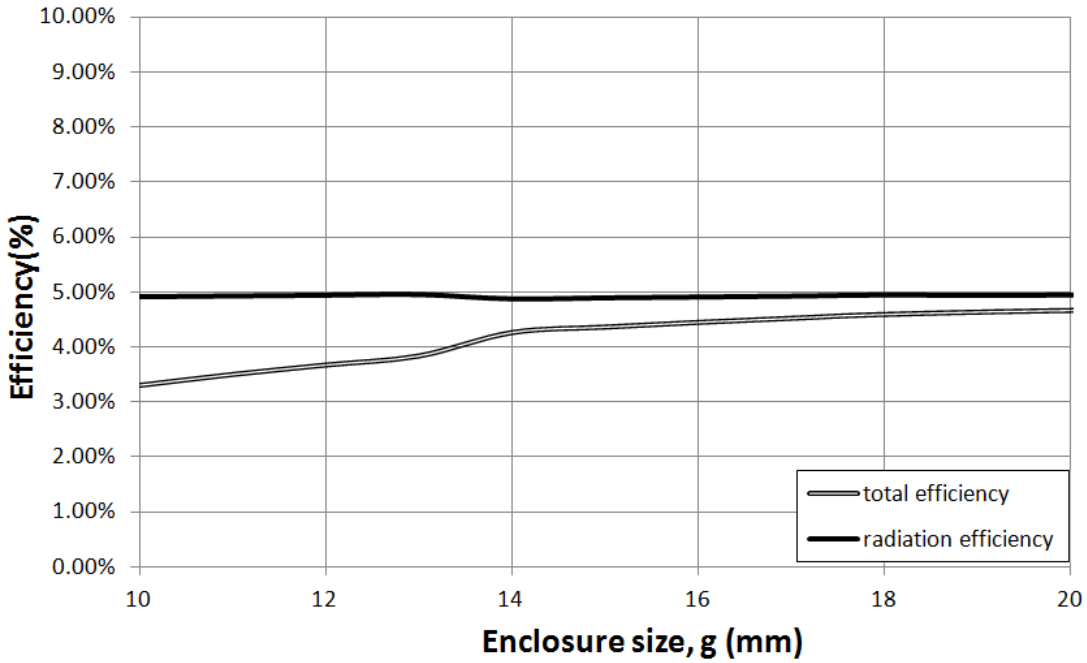

Figure 6.11: Simulated antenna efficiencies versus the enclosure size at 900 MHz

improvement in the antenna's return loss performance. The simulated radiation efficiency does not improve with increasing sensor node size as the dielectric power loss due to RF absorption by the soil around the antenna is the primary factor leading to the low radiation efficiency. In Section 6.5, the overall path loss between the reader antenna and the sensor node antenna will be investigated through simulations. Figure 6.12 presents the simulated 3D radiation pattern (gain) of the antenna with the sensor node enclosure whose size is g= 20 mm. When using the enclosure, the simulated radiation pattern of the antenna has little change comparing the pattern (as shown in Figure 6.7) characterised in the simulation where the antenna is directly buried without the enclosure.

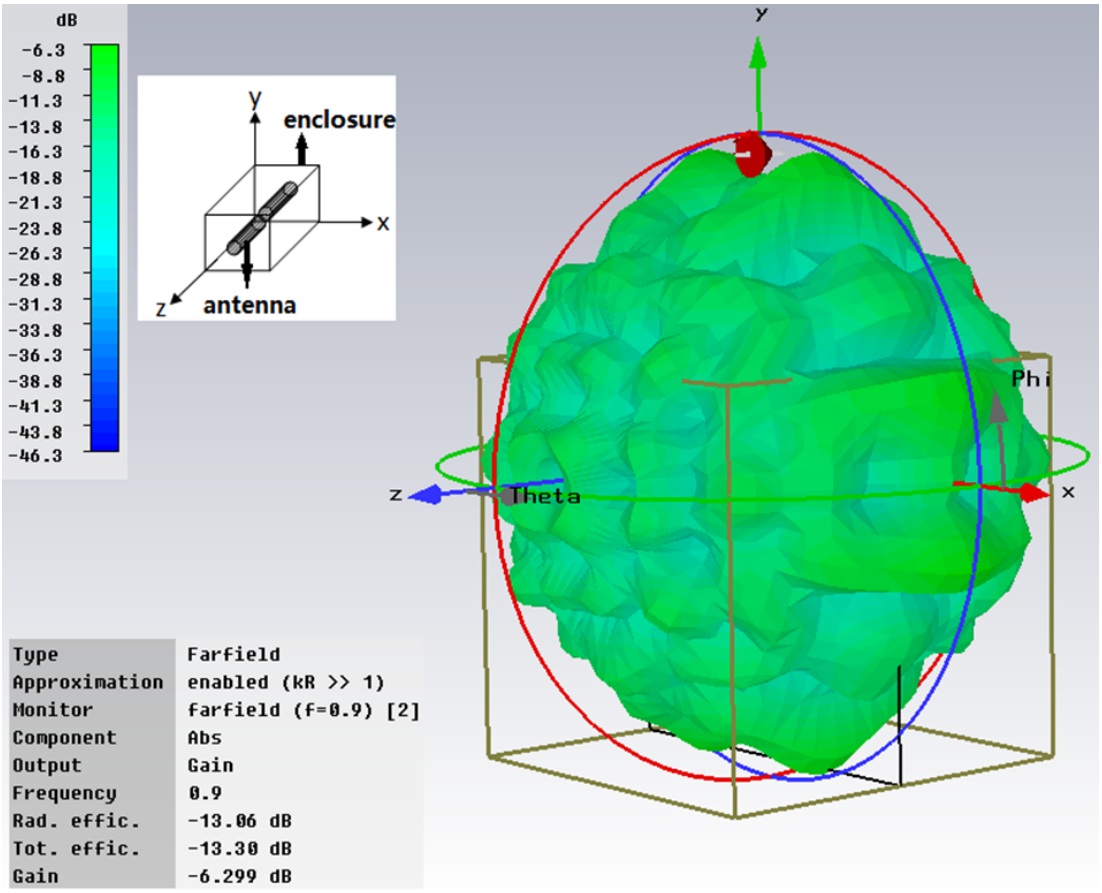

Figure 6.12: Simulated radiation pattern of the antenna at 900 MHz in the sandy soil with a sensor node enclosure.

6.5 Path Loss in Soil

As discussed in Section 6.4, the low radiation efficiency of the buried antenna is due to the dielectric power loss in the soil. With an RFID sub-soil system, the dielectric power loss will lead to a high path loss between the RFID reader and the sub-soil sensor node. This section presents simulations and the simulation results exploring the path loss in the sandy soil. Three factors, including the depth of the sensor node in the soil, the centre frequency of the EM waves and the soil moisture content have been considered in the simulations. As described in Section 5.3.2, the overall path gain or loss between the above-ground reader antenna and the underground node antenna refers to the S-parameter, S_{21} in the CST simulations.

Figure 6.13 shows the diagram of the EM model for characterising the path loss in the soil, where the gap between the antenna and the sensor node enclosure inner surface, g, was set to 20 mm in order to minimise the effect of the soil on the return loss performance of the sensor node antenna. The height of the reader antenna h was 500 mm, and this height positions the soil tank within the far-field region of the reader antenna at frequencies from 600 MHz to 1200 MHz. The thickness of the sensor node enclosure t and the side length of the soil tank s have the same settings as in the simulations as shown in Section 6.4, which were 5 mm and 2000 mm respectively. In the simulations, the path loss was characterised at depths d ranging from 100 mm to 1000 mm and the soil moisture content from 5% to 25%.

Both the free-space radiation and the dielectric absorption by soil degrade the power density of the signal arriving at the sensor node's antenna. Theoretically, there will be higher path loss when the sensor node is buried at a deeper position in the soil. Figure 6.14 presents the simulated path loss at 900 MHz in dry sandy soil (5% moisture content). As predicted, the path loss in the soil increases with increasing depth, and in soil is 15 dB/m more than in air at 900 MHz. The simulations have also investigated the path loss in the sandy soil at the frequencies from 600 MHz to 1200 MHz. The simulation results as presented in Figure 6.15 show that the path loss in the dry sandy soil increases at high frequency. The simulated path loss in the dry sandy soil at 600 MHz is 40 dB/m, and the path loss then increases to 60 dB/m with increasing frequency to 1200 MHz.

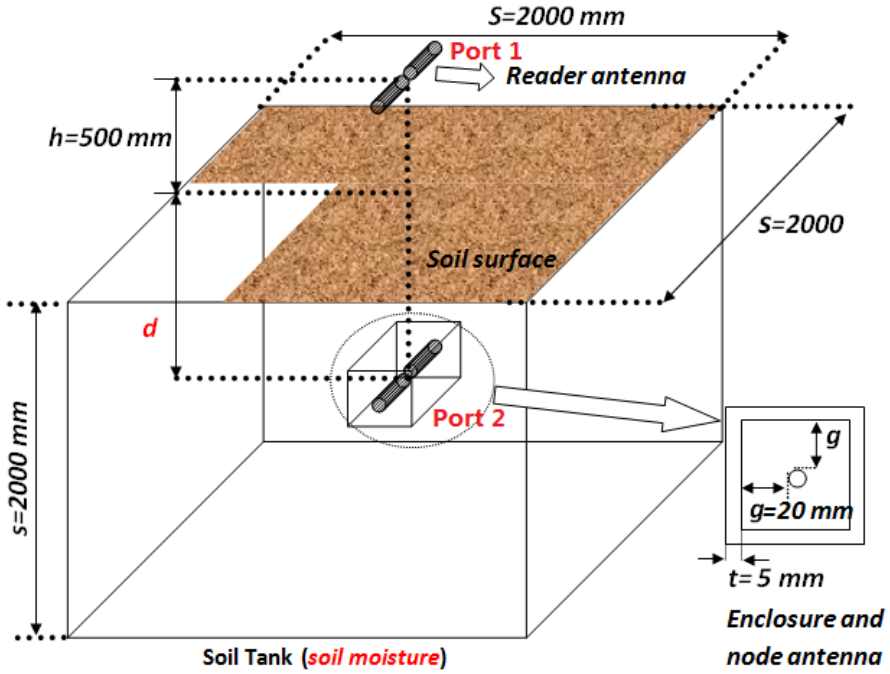

Figure 6.13: Diagram of the EM model for characterising the path loss in sandy soil.

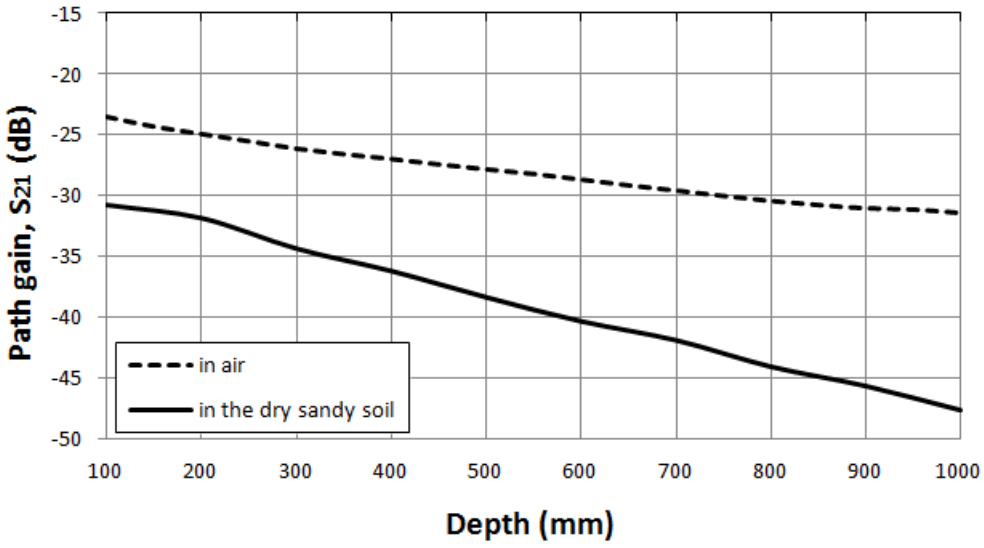

Figure 6.14: Simulated path loss (the depth of the sensor node d=1 m) in the dry sandy soil (5% moisture content) at 900 MHz.

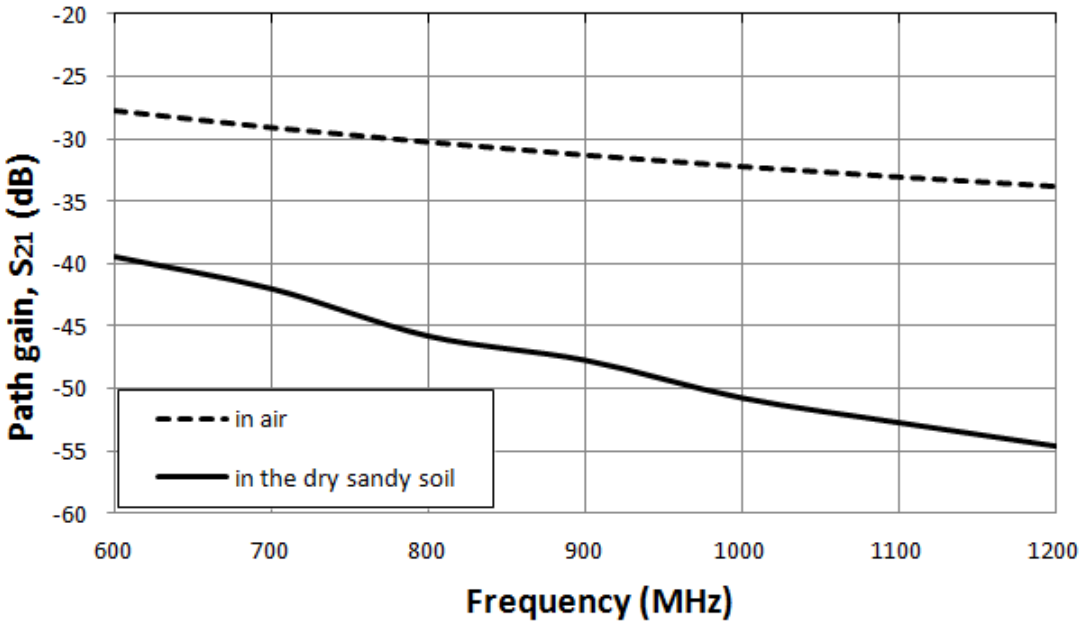

Figure 6.15: Simulated path loss (d=1 m) in the dry sandy soil (5% moisture content) at the frequency from 600-1200 MHz.

In addition to frequency, soil moisture is another key factor affecting the path loss in soil as the water in soil is the primary content leading to RF energy absorption. Figure 6.16 presents the simulation results showing the power loss per meter in the sandy soil compared to that in air. As shown from the results, the high soil moisture significantly affects the simulated path loss, especially at higher frequencies. At 1200 MHz, the simulated path loss in the wet soil (25% soil moisture content) is 40 dB/m greater than in the dry sandy soil (5% soil moisture content), and the power loss in the wet sandy soil (25% soil moisture content) can be 60 dB/m. It is also found that the path loss increases slowly when the soil moisture increases from 5% to 15%, especially at low frequency.

6.6 Summary

This chapter presents the simulations and results based on EM models for the RFID sub-soil system. The simulation results show that the soil around the buried antenna can impact the sub-soil antenna performance which includes the return loss (the resonant frequency), the radiation efficiency and the radiation pattern. In practice, the impact of the soil can degrade the performance of the proposed

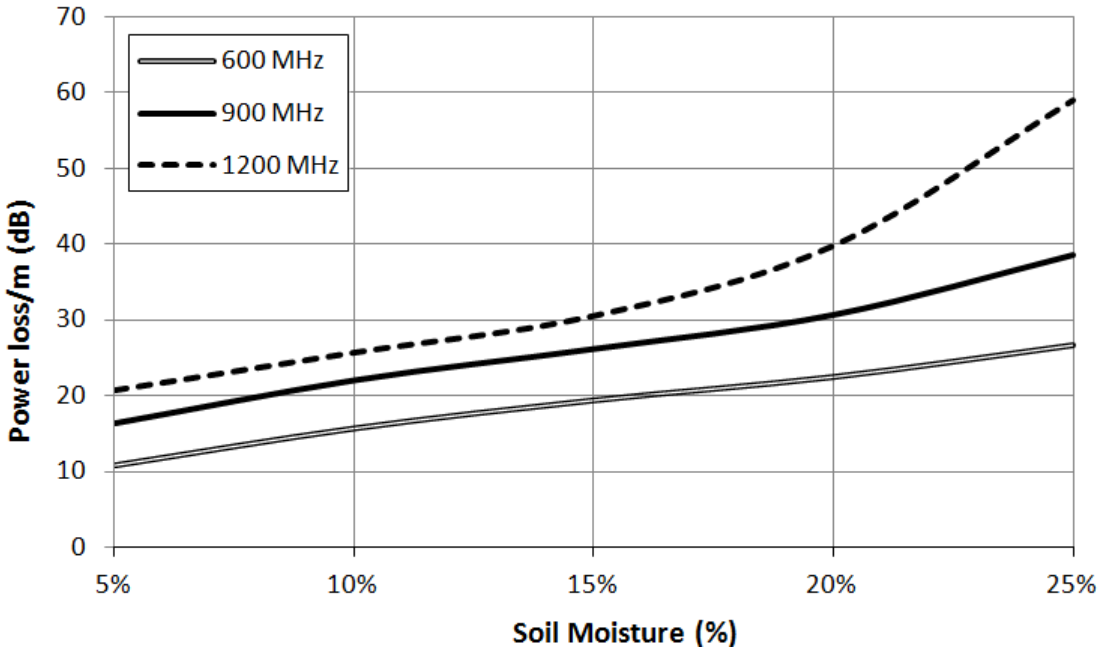

Figure 6.16: Simulated extra power loss per meter in the sandy soil at various moisture levels from 5%-25% at 600 MHz, 900 MHz and 1200 MHz.

RFID sub-soil system. For example, the soil around the sensor node antenna can vary the resonant frequency of the antenna from the value measured in air, which limits the energy harvested by the sensor node. The simulation results also indicate that the use of a sensor node enclosure for containing the sub-soil antenna can help reduce the impact on the antenna's return loss performance from the sandy soil. However, the performance improvement only becomes obvious when the gap between the sensor node antenna and the inner wall of the enclosure is greater than 20 mm. Increasing the gap will expand the overall size of the sensor node, and so it will affect the system deployment efficiency. The path loss in the sandy soil has been measured and investigated through the simulations. As summarised from the simulation results, the path loss increases when the sensor node is deployed at a deeper position in the soil. Operating frequency of the system and soil moisture both affect the path loss in soil, and there will be higher path loss at higher soil moisture content and high frequency. In practice, the high path loss in the soil can potentially affect the achievable depth of the sub-soil sensor node. High transmission power can be required to improve the system performance, especially in wet soil or at high frequency.

Chapter 7

PXI-based RFID Reader Platform

7.1 Introduction

With the proposed RFID sub-soil system described in Chapter 4, the RFID reader powers and interrogates the RFID sub-soil sensor nodes and logs sensor measurements from them. In this research, there is a need to design and implement a programmable RFID reader platform which is capable of not only communicating with an RFID sensor node prototype but also evaluating the performance of the sensor node prototype in soil. However, commercial RFID readers are designed based on industrial protocols. They provide limited ability to implement a custom communication protocol and to evaluate the performance of the sensor node prototype. During the design process of the RFID reader platform, the sensor node prototype described in Chapter 8 had not been fabricated. Hence commercial tags were used to substitute for the RFID sensor node. Commercial tags are designed based on RFID industrial protocols, and the protocol selected in this work was the EPC C1G2 protocol [6] as described in Chapter 2. The main functional requirements of the RFID reader platform are described below.

- The RFID reader platform must be able to communicate with an RFID EPC C1G2 RFID tag and to implement the functions of reading the tag ID and writing data to the tag.
- The RFID reader platform will be used to evaluate a custom RFID sensor node in this research. Thus the RFID reader platform must provide users

with the ability to modify the physical layer protocol and must operate in a wide frequency band.

- The RFID reader platform must be configurable and be able to perform signal processing functions for tag performance evaluation, and the signal processing functions must be readily modifiable.

In order to read the tag ID or write data to the tag, the RFID reader platform has to meet the timing requirements specified in the EPC C1G2 protocol [6]. Figure 7.1 presents the link timing parameters of the *Inventory* round in the EPC C1G2 protocol, where T_1 and T_2 are the two key timing parameters. T_1 specifies the maximum allowable time in which the RFID tag must respond to an RFID command signal and T_2 specifies the maximum allowable time in which the RFID reader must respond to a tag response by issuing a subsequent RFID command. For example, with an RFID system, once the RFID reader has started interrogating the tag by issuing a *Query* command, the tag has to respond to the *Query* command by transmitting a *RN16* tag response signal within T_1. When the *RN16* response signal is received by the RFID reader, the RFID reader then has to issue a *Ack* command signal within T_2. The RFID tag can only be successfully read from or written to when the RFID system meets both of these timing requirements. T_1 and T_2 are dependent on $Tari$ as:

$$T_1 = 10Tari, \tag{7.1}$$

$$T_2 = 20Tari, \tag{7.2}$$

where $Tari$ specifies the period of the encoded reader command [6]. As specified in the EPC C1G2 protocol, $Tari$ ranges from 1.56 μs to 25 μs. Therefore, T_1 has a range of 15.6 μs to 250 μs, and T_2 has a range of 31.25 μs to 500 μs.

Tag sensitivity is one of the typical parameters used to quantify tag performance. Tag sensitivity refers to the minimum incident power at the tag which is required for interrogating the tag. At a given transmit power of an RFID reader, a tag with lower tag sensitivity can be typically read at a longer distance from the RFID reader. In this work, the RFID reader platform aims to evaluate tag

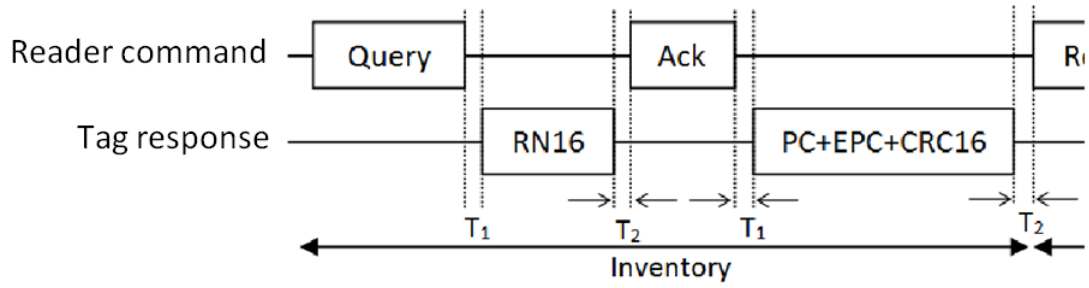

Figure 7.1: Link timing parameters in the *Inventory* round [6]

sensitivity over a frequency band. At a given operating frequency, the method of tag sensitivity evaluation in a free-space environment is based on measuring the minimum transmit power P_{min} of the reader platform at which the tag responds to the reader platform at that frequency. The tag sensitivity P_{tag} is then calculated as:

$$P_{tag}(dBm) = P_{min}(dBm) + G_t(dB) - P_L(dB) \tag{7.3}$$

where G_t is the gain of the reader platform transmitting antenna and P_L is the Free Space Path Loss (FSPL) [81] between the RFID reader platform and the tag. As shown in Equation 2.11, P_L is a function of the distance to the tag and the operating frequency of the RFID reader. In order to measure the minimum transmit power P_{min} needed to interrogate the tag, the RFID reader must have a variable power output with an power accuracy of less than 1 dB.

This chapter presents the design and implementation of the RFID reader platform which is capable of reading tag ID, writing data to the tag and evaluating tag sensitivity. The RFID reader platform is built using a National Instruments (NI) PXI system [109] and the motivation for using the PXI system is discussed in Section 7.2. Section 7.3 presents details of the RFID reader platform design, and the implementation of the RFID reader platform is described in Section 7.4. The operation of the implemented RFID reader platform has been validated, and is illustrated in Section 7.5.

7.2 Motivations

Using the PXI system to design and implement the RFID reader platform is primarily motivated by the fact that commercial RFID readers do not meet the design requirements of the RFID reader platform required for this work. With a commercial RFID system, the RFID reader generates Continuous Wave (CW) signals and RFID commands to power and interrogate the RFID tags respectively, and then receives tag response signals backscattered from the RFID tags. Those commercial RFID readers are strictly designed based on industrial protocols, and they have limited ability for exploring modifications to the physical layer protocol or operating over a wide frequency band. Therefore, a commercial RFID reader is unable to communicate with a custom RFID sensor node whose design is not based on an industrial protocol. In addition, when using a commercial RFID reader to read an RFID tag, the RFID reader will only give the reading result and can provide little information, for example about the power measurement of the backscattered signal for analysing the tag performance. It is therefore difficult to use a commercial RFID reader to evaluate the performance of an RFID sensor node or an RFID tag.

It is now becoming popular to develop RFID readers using Software Defined Radio (SDR) techniques [110]. Figure 7.2 presents the architecture of a SDR communication system, where signal processing functions traditionally implemented using hardware components are implemented using software executing on computation devices, such as a Personal Computer (PC). As shown in Figure 7.2, the PC performs signal processing algorithms such as signal modulation, demodulation, encoding and decoding. The digitally modulated baseband signal from the PC is converted to an analogue baseband signal using a Digital-to-Analogue Converter (DAC). Within the Transmitter (Tx) hardware, the baseband signal is up-converted to RF and transmitted through an antenna. On the receiver chain, the received RF signal by the receiving antenna is down-converted to an Intermediate Frequency (IF) signal. The Analogue-to-Digital Converter (ADC) then converts the IF signal to a digital signal which can be processed by the PC. This SDR-based system enables users to modify the physical layer protocol and to customise signal measurement algorithms.

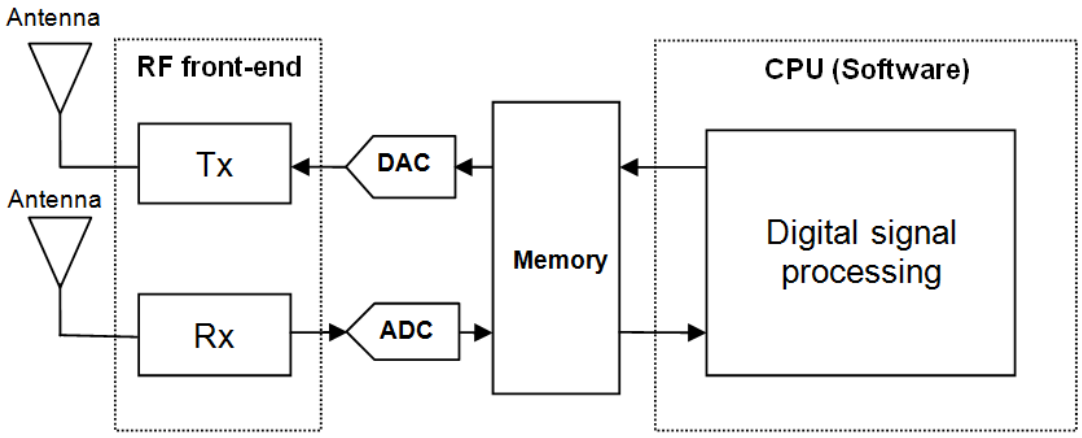

Figure 7.2: Simplified block diagram of a SDR communication system.

The LabVIEW-based Ultra High Frequency (UHF) RFID tag test and measurement system [111] is one example of implementing SDR-based RFID readers. This system operates in the frequency range of 800 to 1000 MHz and is capable of testing RFID tag performance using the EPC C1G2 protocol [6]. The RFID tag test system is built based on the architecture shown in Figure 7.2, which uses a PC-based controller to perform signal processing algorithms for encoding and modulating reader command bits, and demodulating and decoding the digital baseband of the tag response signals. However, the communication between the system and the tag is only based on a *Query* command signal and a *RN16* tag response signal, and the system is unable to access the tag's memory, such as reading the tag ID or writing data to the tag. This limitation is due to the fact that the RFID tag test system is unable to respond to a tag response signal within T_2 as specified in the EPC C1G2 protocol. In order to respond to a tag response signal, the system software needs to:

1. fetch the baseband data of the signal from the system RF front-end hardware;

2. implement digital demodulation and decoding;

3. generate bits of a subsequent command based on recovered bits from the demodulated signal;

4. pass the modulated baseband data to the system RF front-end hardware.

The response time for issuing a subsequent command is primarily affected by the

data buffering latency which is caused by data transfer between the system software and RF front-end hardware. This buffering latency typically ranges from milliseconds to seconds [112] which causes the system to fail in meeting the timing requirement T_2, whose maximum value is 500 μs.

There is one SDR-based RFID reader solution by VISN [113] which is primarily designed for RFID protocol conformance tests. This solution uses a Field-Programmable Gate Array (FPGA) module, which comprises of thousands of programmable logic gates. Those logic gates are configurable and can be used to implement signal processing functions at a clock rate of up to 500 MHz [114]. Figure 7.3 shows the architecture of the RFID reader solution by VISN [113], where the PC is only used to pre-compile the FPGA module and log testing results. As shown in Figure 7.3, the FPGA is used to implement the functions of signal modulation, demodulation, encoding and decoding. Both digital and analogue signal processing within the RFID reader solution are performed using the hardware, which enables the RFID reader solution to meet the timing requirement T_2 as specified in the EPC C1G2 protocol. However, the solution by VISN [113] is designed based on RFID industrial protocols and does not support a custom communication protocol.

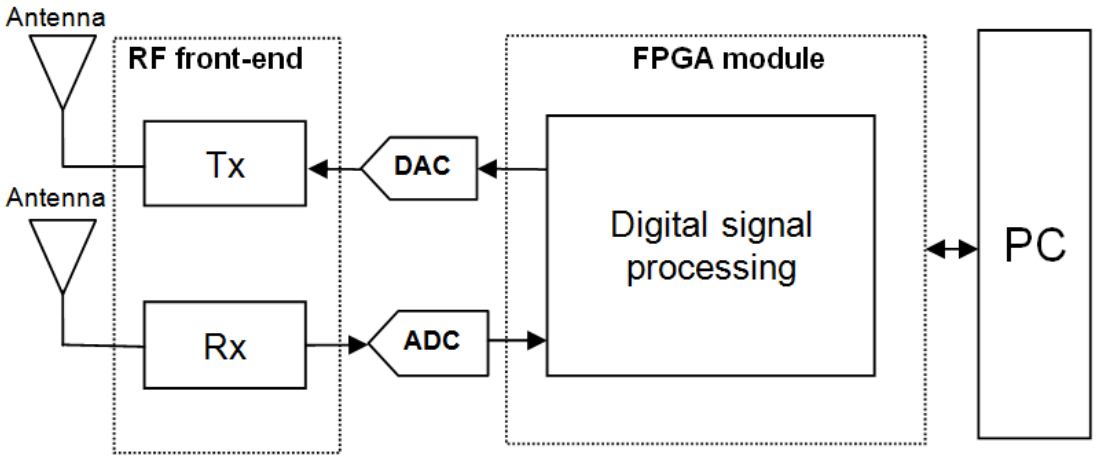

Figure 7.3: Simplified block diagram of an FPGA-based RFID reader.

7.3 RFID Reader Platform Design

The RFID reader platform in this work is built using a NI PXI system [109], and it is configurable and controlled using LabVIEW software [115]. The PXI system consists of a NI PXIe-1075 18 Slot Express Chassis and PXI modules including a NI PXIe-8133 1.73 GHz Quad-Core controller, a NI PXIe-5673 6.6 GHz Vector Signal Generator (VSG), a NI PXIe-5663 6.6 GHz Vector Signal Analyser (VSA) and a NI PXIe-7965R FlexRIO FPGA. Figure 7.4 presents the block diagram showing the architecture of the PXI system. The PXI controller is a PC-based controller which runs a Windows Operating System (OS) and LabVIEW. PC peripherals, such as mouse, keyboard and monitor are interfaced to the PXI controller through three USB connectors and a VGA connector. The key feature of the system is that the PXI modules are configured and controlled using LabVIEW executing on the PXI controller. The PXI modules are housed in the PXI chassis which provides PCI buses for the PXI modules. The PCI buses are typically used for Peer-to-Peer (P2P) data streaming between two modules. P2P streaming enables direct, point to point transfers between the PXI modules without sending data through the controller Central Processing Unit (CPU) or memory. The maximum P2P streaming rate provided by the PXI chassis is approximately 800 MegaBytes (MB)/s [109] which significantly improves the data transmission efficiency within the PXI system. The details of the PXI modules are shown below.

1. NI PXIe-8133 1.73 GHz Quad-Core PXI Controller
    - Windows 7 OS with LabVIEW 2011
2. NI PXIe-5673 6.6 GHz Vector Signal Generator
    - 85 MHz to 6.6 GHz carrier frequency range
    - Greater than 100 MHz of RF bandwidth
    - Controllable RF power with 0.1 dB power accuracy
    - Up to + 10 dBm RF power output
3. NI PXIe-5663 6.6 GHz Vector Signal Analyser
    - 10 MHz to 6.6 GHz carrier frequency range

- Less than -158 dBm/Hz typical noise floor at 1 GHz

4. NI PXIe-7965R FlexRIO FPGA
   - DSP-focused Virtex-5 SX95T FPGA
   - 512 MB on-board memory

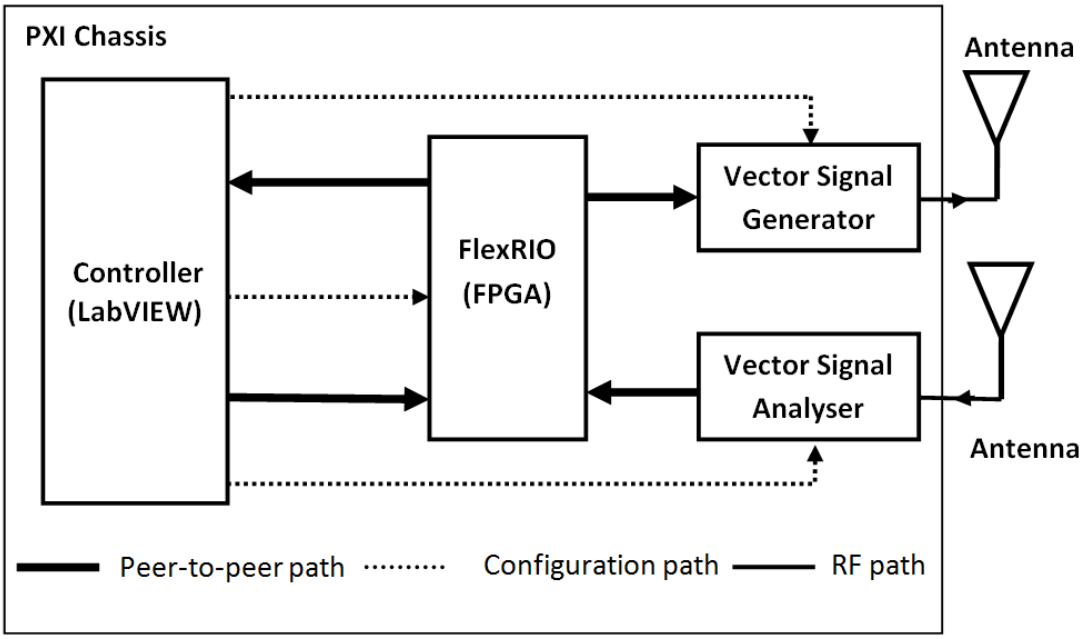

Figure 7.4: Block diagram of the platform hardware.

The VSG shown in Figure 7.4 can be used to generate an arbitrary signal. Figure 7.5 presents a block diagram showing the architecture of the VSG, where the VSG converts the modulated In-phase (I) and Quadrature-phase (Q) baseband data to a pair of I and Q baseband analogue signals using two 16-bit DACs. The two baseband signals are then independently mixed with two carrier signals produced by the Local Oscillator (LO), each of which is 90 degrees out of phase. The mixed signals are finally summed to produce an RF signal output. A variable RF amplifier is used to control the power level of the RF signal (the VSG transmit power). With the PXI chassis and controller, the transmit power and operating frequency of the VSG and the sampling rate of the VSG DAC are configurable using LabVIEW. The operating frequency of the VSG ranges from 85 MHz to 6.6 GHz, the maximum transmit power is +10 dBm with 0.1 dB power accuracy, and the DAC has a maximum sampling rate of 400 Mega Samples (MS)/s. The

sampling rate depends on the data rate of the digitally modulated I and Q signals, termed as the IQ rate.

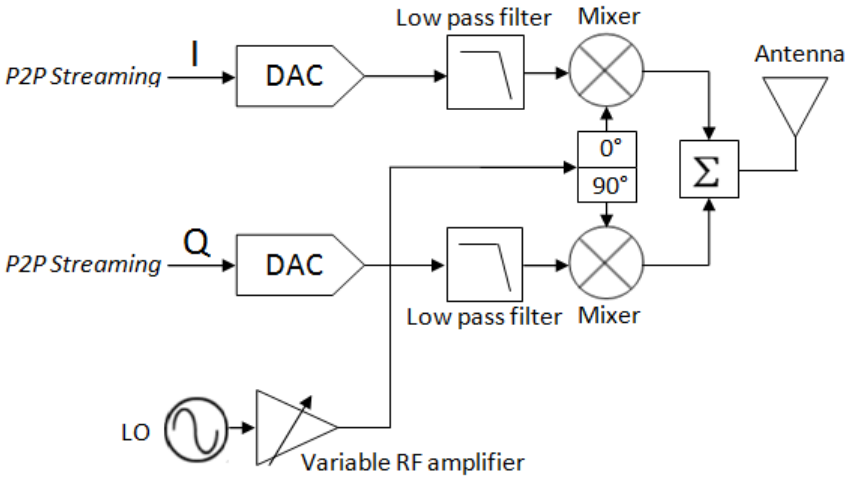

Figure 7.5: Simplified block diagram of the PXI VSG module.

Figure 7.6 illustrates the architecture of the VSA module, where the RF signal received by the VSA antenna is attenuated by the in-built attenuator. The VSA module implements a two-stage signal down-conversion. In the first stage, a mixer and a LO are used to down-convert the attenuated RF signal to an Intermediate Frequency (IF) signal. The IF signal is then sampled using a 16-bit ADC. In the second stage, the VSA digitally down-converts the IF signal to a pair of I and Q baseband signals using a Digital Down-Converter (DDC) [116]. The operating frequency of the VSA ranges from 10 MHz to 6.6 GHz and the on-board ADC achieves a maximum sampling rate of 150 MS/s. Both the operating frequency and the sampling frequency are configurable using LabVIEW. The VSA has a low noise floor which is less than -158 dBm/Hz in the 120 MHz to 3.3 GHz frequency range. This leads to a better receiver sensitivity performance than commercial RFID readers.

The FlexRIO FPGA module is used for achieving the functions of reading from or writing to the tag. The architectures of the FlexRIO FPGA and controller modules are shown in Figure 7.7, where the FlexRIO FPGA module primarily includes a Virtex-5 SX95T FPGA [114] and a 512 MB on-board memory. P2P data streaming provided by the PXI system enables direct data streaming between the FPGA and the PXI controller memory independently from the controller CPU.

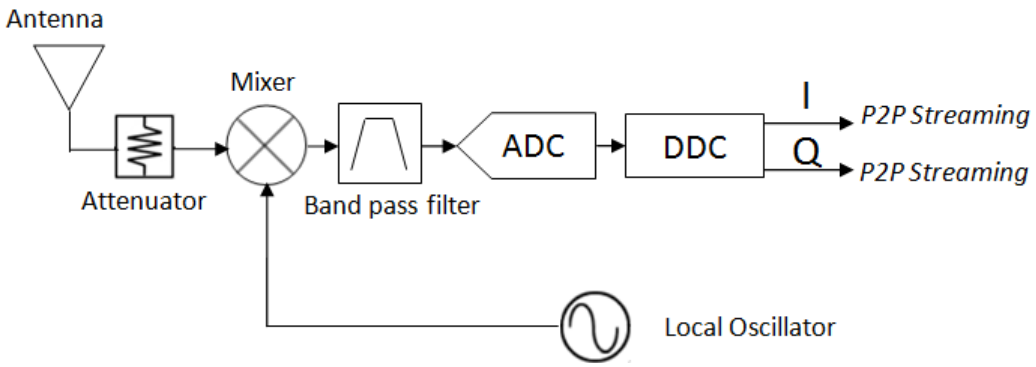

Figure 7.6: Simplified block diagram of the PXI VSA module.

Therefore, the controller CPU can perform signal processing while waiting for data transfer. The FPGA performs the signal processing for implementing the physical layer. Signal processing algorithms are developed using LabVIEW and then compiled into the FPGA. Figure 7.7 also presents the functional diagram of the FPGA algorithm design. As shown in Figure 7.7, the command builder algorithm generates the data bits of a reader command, and the generated command bits are then encoded and modulated by the PIE encoder algorithm and the ASK modulator algorithm. The PIE and ASK modulation formats are based on the specifications in the EPC C1G2 protocol [6]. The digitally modulated command data is finally passed to the VSG through P2P data steaming. The response detector algorithm continuously fetches and processes the digitally down-converted data from the VSA aiming to detect a tag response signal from the fetched data. Once a tag response signal has been detected, the baseband data of the signal is buffered to the ASK demodulator algorithm which maps the baseband signal samples to either a '0' bit or a '1' bit. The FM0 decoder then implements FM0 decoding format [6] to recover data bits from the demodulated baseband signal. The state machine plays the key role of controlling the sequence of generating the reader commands based on the function of reading the tag ID and writing data to the tag as shown in Figure 2.7. Through P2P data streaming, a LabVIEW Host program executing on the PXI controller CPU controls the FPGA. The control function primarily includes starting, stopping and resetting signal processing algorithms performed on the FPGA. When the FPGA algorithms have been reset, the FPGA is ready to perform a new round of the signal processing for reading from or writing to the tag. The LabVIEW Host program can also control or read

parameters that are set in the FPGA algorithms.

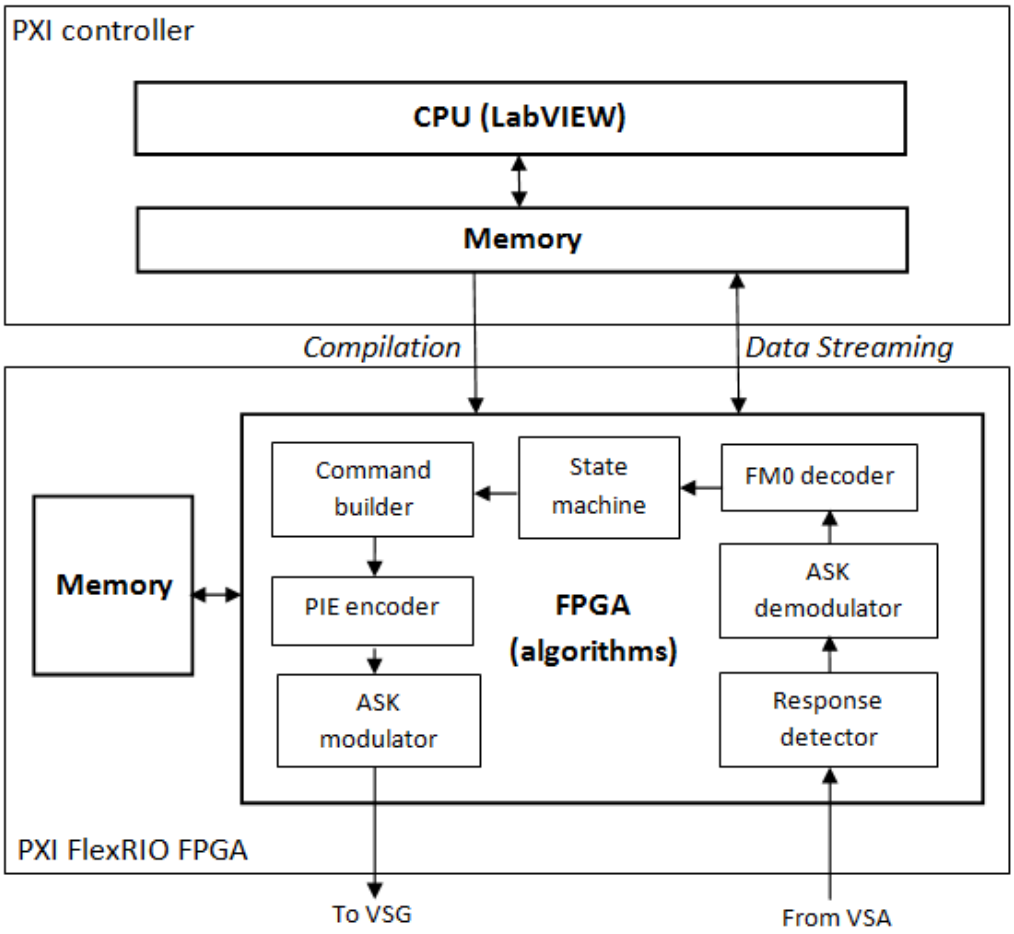

Figure 7.7: Architectures of the PXI controller and FPGA modules and the block diagram of the FPGA signal processing algorithms.

The signal processing functions for evaluating tag sensitivity are performed in a LabVIEW program executing on the PXI controller. The FlexRIO FPGA module is not used to perform the sensitivity evaluation algorithm due to the two reasons mentioned below.

1. The measurement of the minimum power at which the tag responds to the RFID reader is based on generating a *Query* command signal and receiving an $RN16$ tag response signal. Hence, there is a relaxed timing requirement compared to the timing requirement of T_2;

2. Implementing a function on an FPGA is more difficult than on a host program because of the limited resources available on an FPGA. Therefore,

it is preferable that a function is implemented on a host program on a PC if the timing requirements are met.

Without using the FlexRIO FPGA module, the signal processing functions of signal encoding, modulation, demodulation and decoding are performed on the PXI controller. Through P2P streaming paths shown in Figure 7.4, the PXI controller directly sends the modulated baseband signal to the VSG and fetches the digitally down-converted baseband signal from the VSA. Figure 7.8 presents the flowchart of the LabVIEW program which is designed to implement the tag sensitivity evaluation algorithm. As shown in Figure 7.8, the power and frequency loops are used to sweep the transmit power and operating frequency of the RFID reader platform. The power loop enables the program to record the minimum transmit power P_{min} at which the tag responds to the *Query* command signal generated by the RFID reader platform. The design of the frequency loop aims to measure the minimum power over an operating frequency band. Tag sensitivity is finally calculated from the measured minimum transmit power P_{min} based on Equation 7.3.

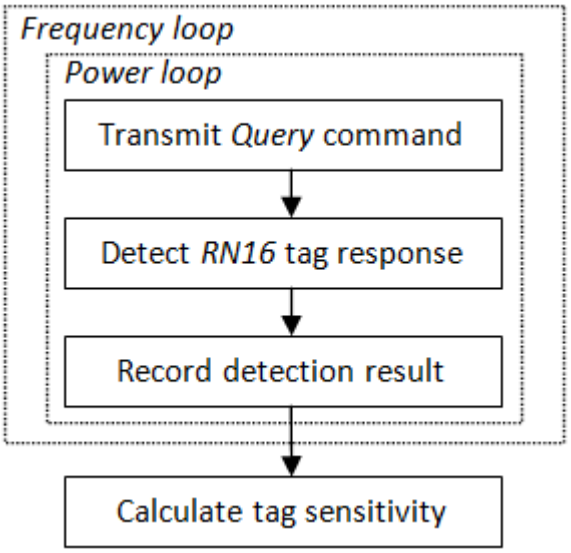

Figure 7.8: Flowchart of the algorithm design for evaluating tag sensitivity.

7.4 RFID Reader Platform Implementation

7.4.1 Experimental arrangement

Figure 7.9 shows the block diagram of the experimental arrangement for evaluating a commercial RFID tag using the implemented RFID reader platform. This experimental arrangement is only used for validating the operation of the implemented RFID reader platform, the result of which will be described in Section 7.5. The example tag being used for the operation validation is a UPM Rafsec Dogbone passive RFID tag [117]. The reader employs two 2 dBi omnidirectional antennas [118] which operate in the frequency range of 860 to 900 MHz. As shown in Figure 7.9, one antenna is connected to the VSG and the other one to the VSA. The two antennas are physically separated by 0.4 m, and the RFID tag is placed at the mid-point between the antennas. Figure 7.10 presents a photograph of the experimental arrangement.

7.4.2 FPGA algorithms

The FPGA signal processing algorithms as shown in Figure 7.7 have been developed using LabVIEW FPGA [115], and the LabVIEW files are included in Appendix C. LabVIEW provides a graphical programming environment. Instead of lines of code, users develop algorithms by creating and wiring a range of functional blocks termed as LabVIEW FPGA Virtual Instruments (VIs). Each LabVIEW FPGA VI includes a number of functional palettes such as numeric calculation functions and logic operation functions. The process of compiling the FPGA module consists of two stages. The LabVIEW FPGA firstly converts the LabVIEW VIs to a file which can be read and consumed by a Xilinx compiler. The Xilinx compiler then takes the requested logic from the file and analyses it, synthesises it down to a lower-level representation and maps it to the FPGA hardware resources [119].

Based on the design shown in Figure 7.7, the signal processing functions have been grouped into two function loops which are presented in Figure 7.11: the generation function loop and the recovery function. Using the two loops enables the generation and recovery functions to be executed in parallel on the FPGA,

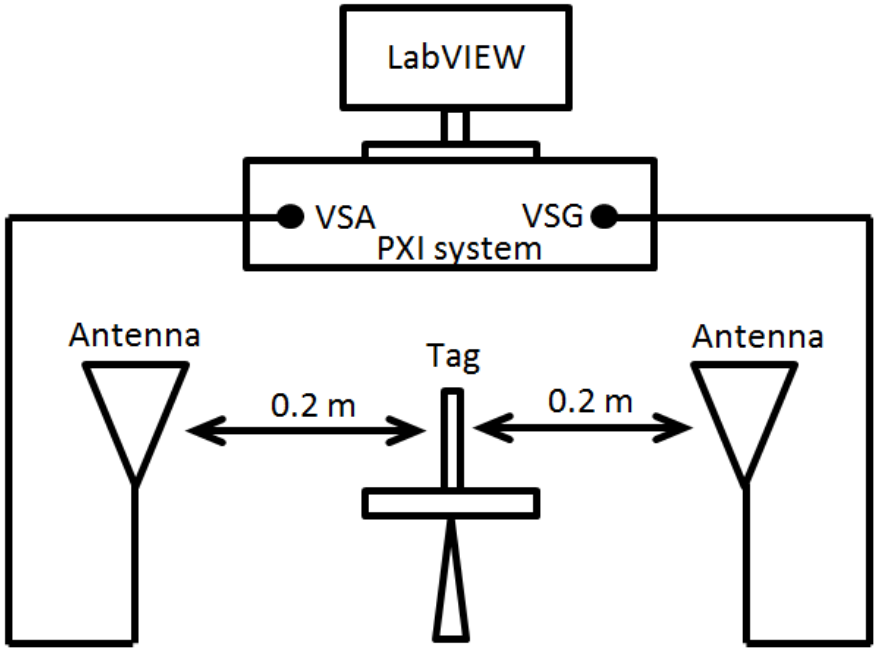

Figure 7.9: Experimental arrangement for evaluating a commercial RFID tag using the implemented RFID reader platform.

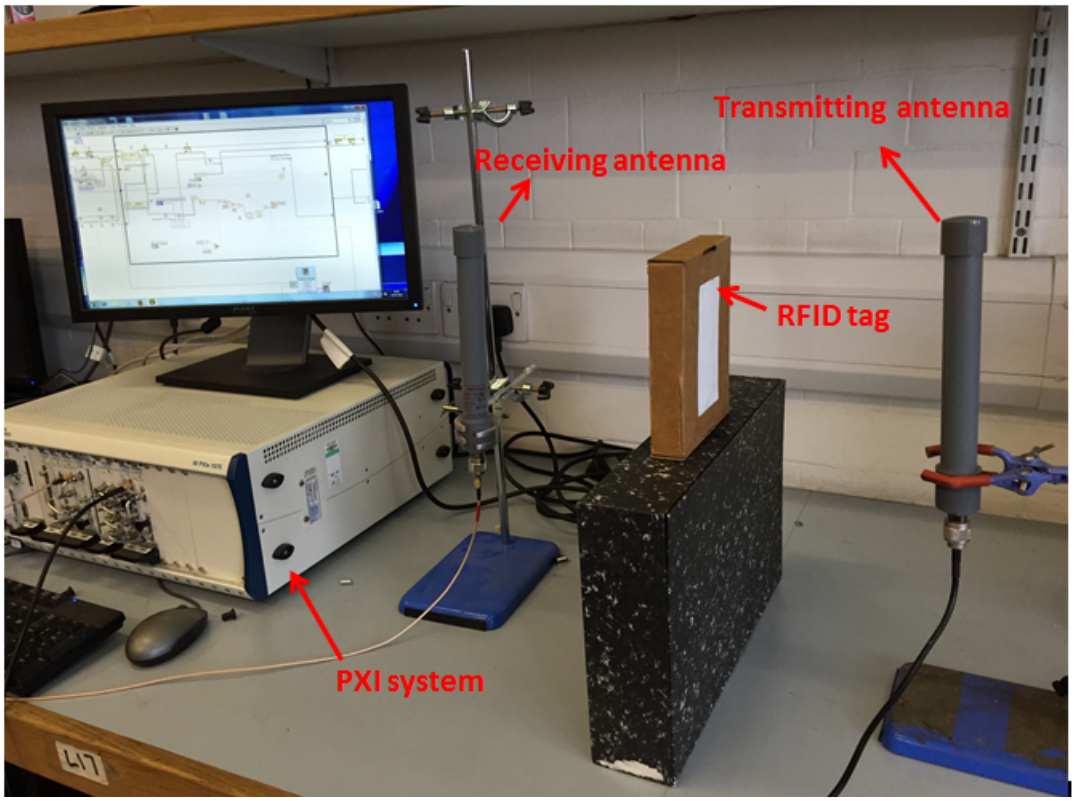

Figure 7.10: Photograph of the experimental arrangement.

which helps to maximise the computation efficiency and to reduce the amount of time taken to respond to a tag response signal. As shown in Figure 7.11, the FPGA First In First Out (FIFO) buffer is used to transfer the recovered data bits from the recovery function loop to the generation function loop. The digitally modulated command data from the ASK modulator algorithm is passed to the VSG through the VSG FIFO buffer. The response detector algorithm fetches the baseband signal from the VSA FIFO buffer. The Host FIFO buffer is used to transfer the baseband signal to a LabVIEW Host program in which the baseband signal is processed for either monitoring or debugging purposes.

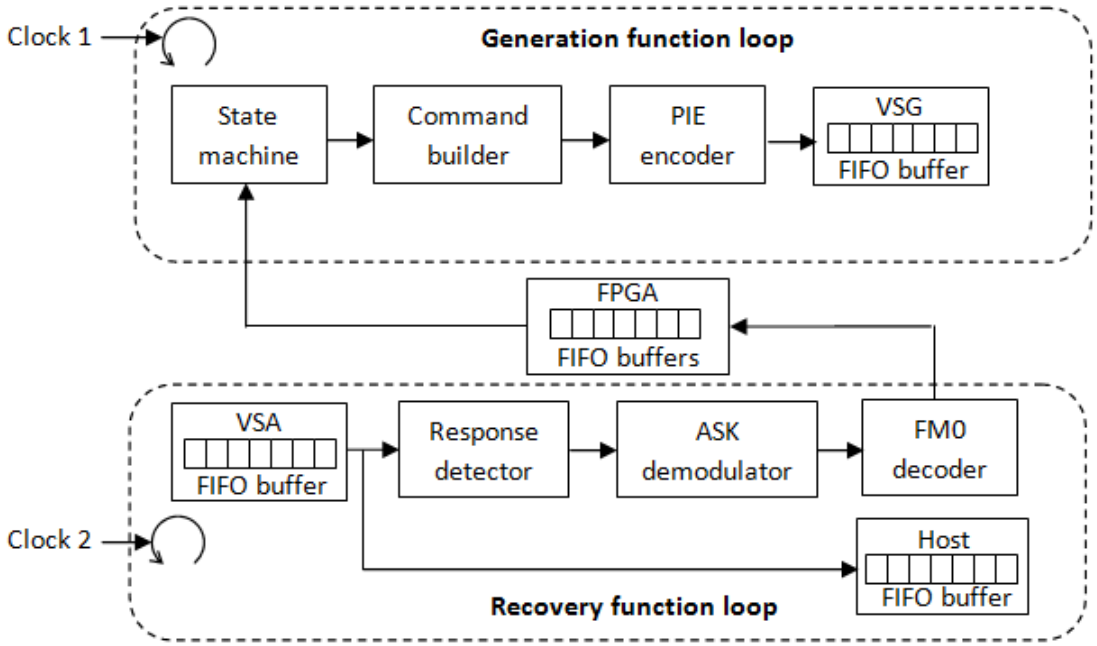

Figure 7.11: Block diagram of the LabVIEW FPGA algorithms.

7.4.2.1 The generation function loop

As described in Chapter 2, the RFID reader is required to issue a sequence of reader command signals for reading the tag ID or writing data to the tag. The state machine algorithm in the generation function plays the important role of controlling the sequence of issuing the reader commands. The command builder algorithm generates the data bits of a command based on the command structure. Table 7.1 presents the summary of three command structures, where all of the commands start with their elementary bits which are specified in the EPC C1G2

protocol [6]. The *Query* command belongs to the first structure, to which a 5-bit Cyclic-Redundancy Check (CRC-5) [6] needs to be appended to the elementary bits. For the second and third structures, the commands are required to re-echo the 16-bit data which is recovered from the most recent *RN16* or *Handle* tag response signal received by the RFID reader. The commands of the third structure need to include a CRC-16 [6] at the end of the commands.

Figure 7.12 presents the diagram showing the interconnections of the implemented state machine and command builder algorithms. As shown in Figure 7.12, the **Read/Write** terminal 'tells' the state machine algorithm to perform the function of reading from or writing to the tag, the **Name_out** terminal 'tells' the command builder algorithm the name of the command which needs to be generated, the **Indicate** terminal is used to report if the tag is successfully read from or written to. The **Read/Write** and **Indicate** terminals are linked to the LabVIEW Host program using two LabVIEW Read/Write controls which enable the LabVIEW Host program to control or monitor the parameters of the FPGA algorithms. The **Name_ out** terminal outputs one of the five potential enumerated values based on the names of the reader commands as shown in Figure 2.7 which are *Query*, *Ack*, *Req_RN*, *Read* and *Write*. The command builder algorithm shown in Figure 7.12 uses the **Name_in** terminal to accept the value from the **Name_out** terminal of the state machine algorithm, and the generated command bits are passed to the PIE encoder algorithm from the **Bits_out** terminal.

Table 7.1: Structures of the RFID reader commands.

	Command	Structure
1	*Query*	Elementary bits + CRC-5
2	*Ack*	Elementary bits + *RN16* or *Handle*
3	*Req_RN*, *Read* and *Write*	Elementary bits + *RN16* or *Handle* + CRC-16

During the implementation of the state machine algorithm, an important consideration was that the state machine algorithm should only 'tell' the command builder to generate a command (except for the first *Query* command) once a tag response signal has been detected. Figure 7.13 indicates the flowchart of the

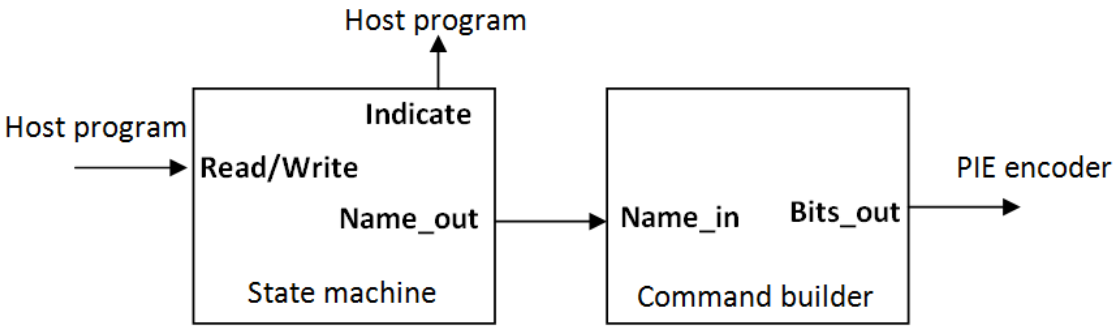

Figure 7.12: Connections of the state machine and command builder algorithms.

implemented state machine algorithm. As shown in Figure 7.13, the **Name_out** terminal does not update its value until the recovered data bits of a tag response signal have been passed to the FPGA FIFO buffer. A timer has been implemented to count the waiting time for the recovered bits. Once the elapsed time exceeds the timing requirement T_1 (described in Section 7.1), the **Indicate** terminal updates its value to '1' which indicates that the tag has failed to respond to the RFID reader platform. When performing the function of reading from the tag, the **Name_ out** terminal updates its value following the sequence of *Query*, *Ack*, *Req_RN* and *Read* commands. For the function of writing to the tag the sequence of commands needs to be changed to *Query*, *Ack*, *Req_RN*, *Req_RN* and *Write*. When responding to the *Read* command signal or the *Write* command signal, the tag can issue an error response signal which indicates that the tag fails to be read from or written to. The data bits of the error response signal starts with a '1' bit. Therefore the **Indicator** terminal only updates its value to '2' which represents that the tag is successfully read from or written to when the first bit of the recovered data is a '0' bit. Otherwise, the **Indicator** terminal updates its value to '1' which indicates that the tag has failed to respond to the RFID reader platform.

The primary consideration in the implementation of the command builder algorithm was the method of generating the elementary bits of a reader command. In this work, the elementary bits of the reader commands were pre-set using the LabVIEW Host program. The FPGA could directly fetch the elementary bits from the Host program when performing the signal processing algorithms. However, it was found that fetching data directly from the Host program caused a delay which resulted in the failure in meeting the timing requirement T_2 as

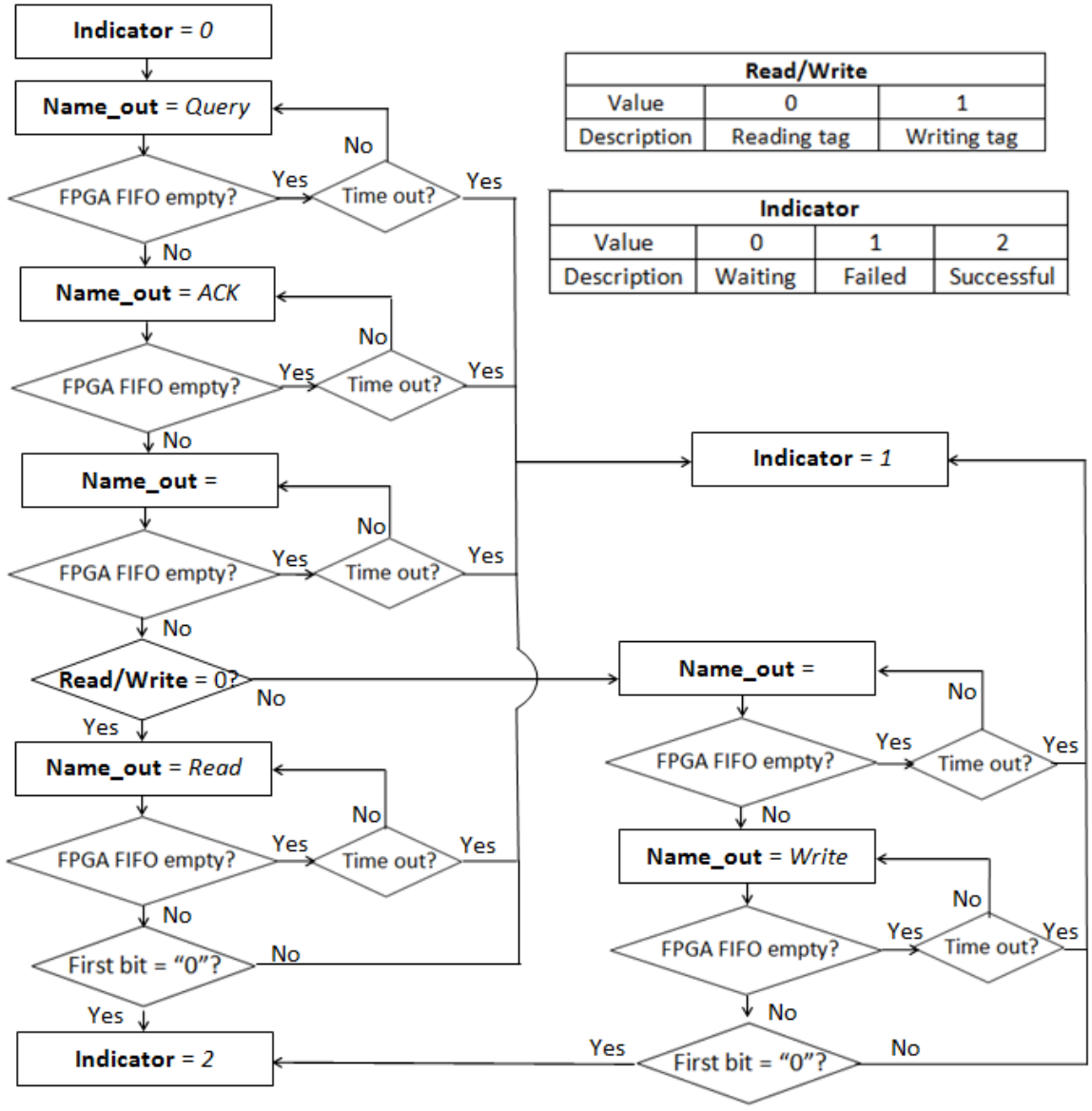

Figure 7.13: Flowchart of the implemented state machine algorithm.

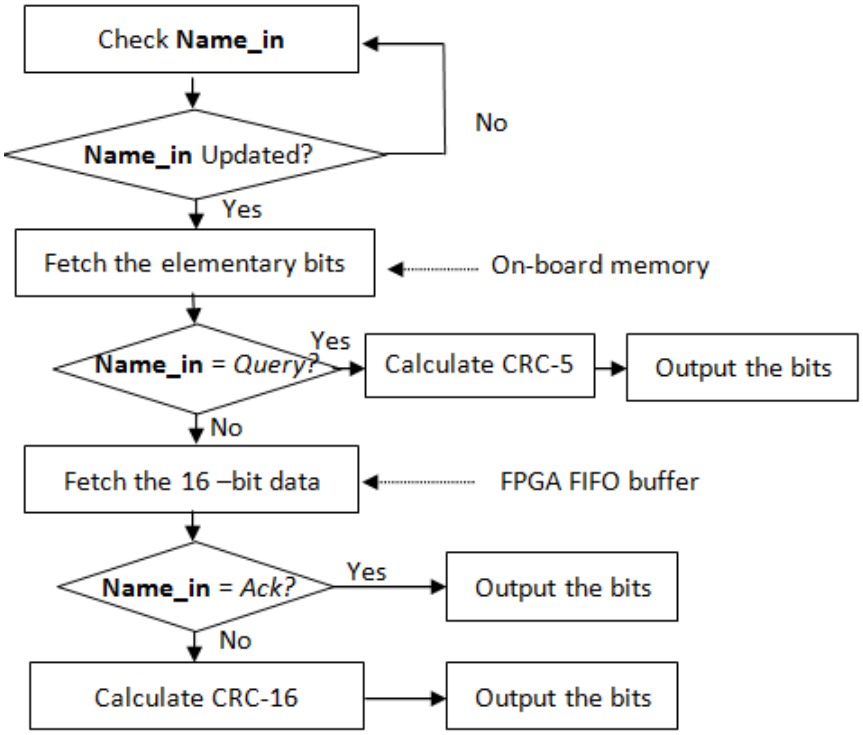

Figure 7.14: Flowchart of the implemented command builder algorithm.

described in Section 7.1. In order to address this problem, the elementary bits of the commands were pre-written into the on-board memory of the FlexRIO. The delay caused by fetching the data from the on-board memory did not have a significant effect on meeting the timing requirements. Figure 7.14 presents the flowchart of the implemented command builder algorithm, where the command builder algorithm only starts to fetch the command elementary bits from the on-board memory when the value of the **Name_In** is updated. A CRC-5 calculator has been implemented to calculate a CRC-5 for the *Query* command. The CRC-5 calculator is based on using the polynomial of $X_5 + X_3 + 1$ [6]. Except for the *Query* command, the state machine algorithm appends the most recent 16-bit data recovered from the *RN16* or *Handle* signals to the elementary bits. The CRC-16 of the *Req_RN*, *Read* and *Write* commands is calculated by a CRC-16 calculator which was implemented based on using the polynomial of $X_{16} + X_{12} + X_5 + 1$ [6].

The PIE encoder algorithm has been implemented to encode the generated

command bits from the command builder algorithm. Figure 7.15 shows an example of the encoded signals of a '0' bit and a '1' bit which have different pulse intervals. As shown in Figure 7.15, $Tari$ defines the data rate which refers to the time for transmitting a '0' bit. A '0' bit symbol starts from logic 1 and ends with logic 0, and PW defines the Pulse Width of logic 0 [6]. The overall interval for transmitting a '1' bit varies from 1.5 $Tari$ to 2 $Tari$, and PW typically has the interval of 0.5 $Tari$ [6]. The values of $Tari$, and PW are set in the LabVIEW Host program. The PIE encoder algorithm uses two Read/Write controls for reading the values of $Tari$ and PW. Using the Read/Write controls helped to avoid re-compiling the FPGA when there was a need to modify the values of $Tari$ and PW. The encoded signal is finally modulated by the ASK modulation algorithm. The ASK modulator algorithm was easy to implement as the EPC C1G2 protocol uses the simplest form of ASK modulation which is also called On-Off Keying. The implemented ASK modulator algorithm converts the encoded signal to a pair of I and Q baseband components, where the I component follows the value of the encoded signal and the Q component is always zero.

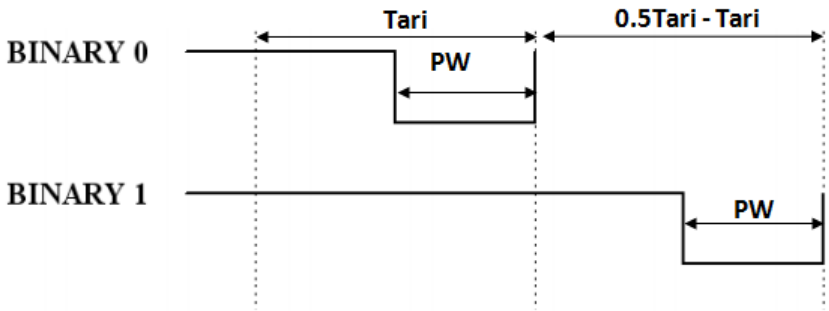

Figure 7.15: Encoded signals with PIE scheme.

7.4.2.2 The recovery function loop

Figure 7.16 presents the baseband amplitude of a captured tag response signal in time domain, where the tag response signal has the higher Peak-to-Peak (P-P) amplitude than the P-P amplitude of the Continuous Wave (CW) signal. The implementation of the response detector algorithm is based on measuring the amplitude of the baseband signal and evaluating the amplitude difference between the baseband signal and the CW signal. The amplitude difference between the baseband signal and the CW signal D is calculated as:

$$D = A[n] - A_{cw}, \tag{7.4}$$

where A refers to the measured baseband signal amplitude, n is the sample index and A_{cw} is the CW baseband signal amplitude. Figure 7.17 presents the block diagram showing the implementation of the response detector algorithm, where the signal amplitude is measured from the down-converted I and Q signals:

$$Amplitude = \sqrt{I^2 + Q^2}. \tag{7.5}$$

The unit of the I and Q components is the volt. As shown in Figure 7.17, when the absolute value of the calculated amplitude difference is greater than a threshold, the baseband signal is then buffered for demodulation. The selection of the threshold value depends on the environmental noise. The author used the PXI VSA to evaluate the strength of noise signals in the laboratory where the testing arrangement was located. The peak amplitude of these noise signals was measured, and the threshold value was then set to 20 times the peak amplitude of the noise signal.

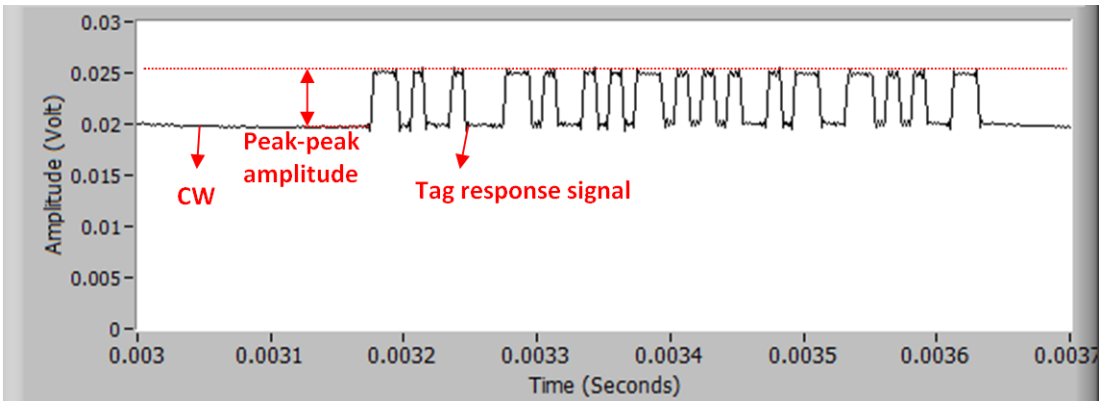

Figure 7.16: Baseband signal of a captured tag response signal in time domain.

With the test arrangement as shown in Figure 7.10, the tag response signal arriving at the receiving antenna contains DC parts which are primarily due to the leakage power from the transmitting antenna. The ASK demodulator algorithm demodulates the buffered baseband signal based on comparing the baseband signal amplitude to the threshold value used for detecting a tag response signal.

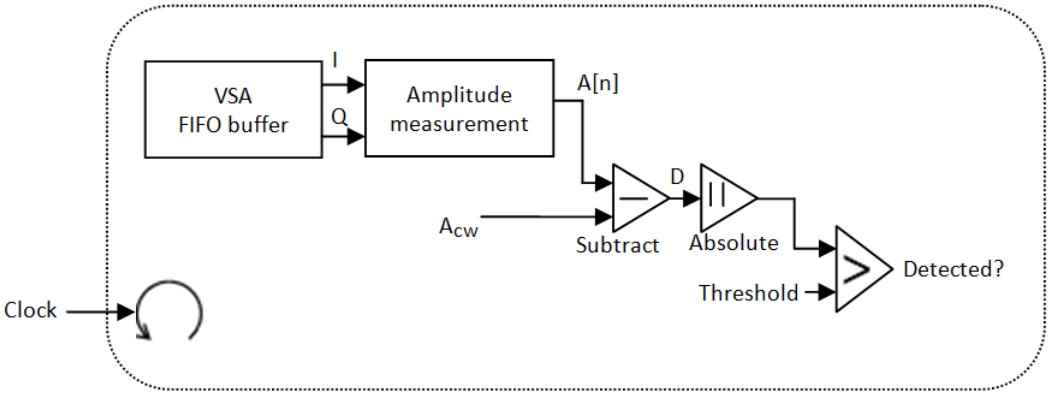

Figure 7.17: Diagram showing the principle of the response detector algorithm.

Implementation of the FM0 decoder algorithm is based on measuring the time intervals between neighbouring edges (rising or falling) of the demodulated tag response signal. Figure 7.18 gives an example of an encoded signal with the FM0 scheme. The measurement result was either a short time interval, T_S or a long time interval, T_L as shown in Figure 7.18. Two continuous short intervals were considered as a '0' bit and a long interval represented a '1' bit.

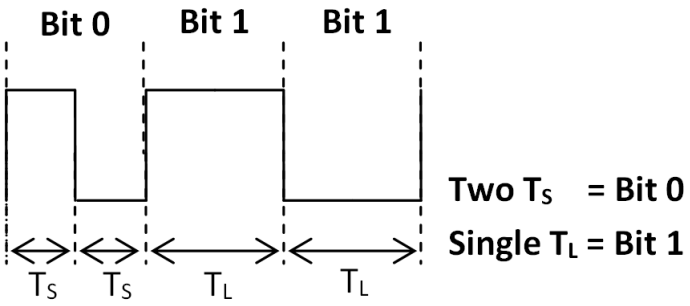

Figure 7.18: Encoded signal with FM0 coding scheme.

7.4.3 The FPGA clocks

As shown in Figure 7.11, the generation and recovery function loops are controlled using two FPGA clocks. A high clock rate is typically desirable as it leads to a high FPGA execution rate and therefore helps the RFID reader platform to meet the timing requirement T_2. However, a high clock rate increases the rate of writing data to the HOST FIFO buffer or the VSG FIFO buffer, which could result in buffer overflow. When the problem of buffer overflow happens, the VSG

or Host FIFO buffers was overwritten, and therefore part of the data stored in the buffer was lost. Increasing the buffer size could be helpful, but there is limited space for buffers on the FPGA. Finding the appropriate clock rates for the two loops is based on tuning the two clock rates from high to low frequency. Whenever a buffer overflow error was reported, there was a need to reduce the clock rate. Through the LabVIEW Host program, the response time to a tag response signal was measured from the baseband signal in order to check if the RFID reader platform met the timing requirements at two clock rates. Figure 7.19 presents a sceenshot of the LabVIEW Host program showing the received baseband signal amplitude (time-domain) at the clock rates of 40 MHz for the recovery function loop and 5 MHz for the generation loop. As shown in Figure 7.19, the measured responding time to the *RN16* tag response is approximately 150 μs (when *Tari* is 25 μs), which is shorter than the timing requirement T_2.

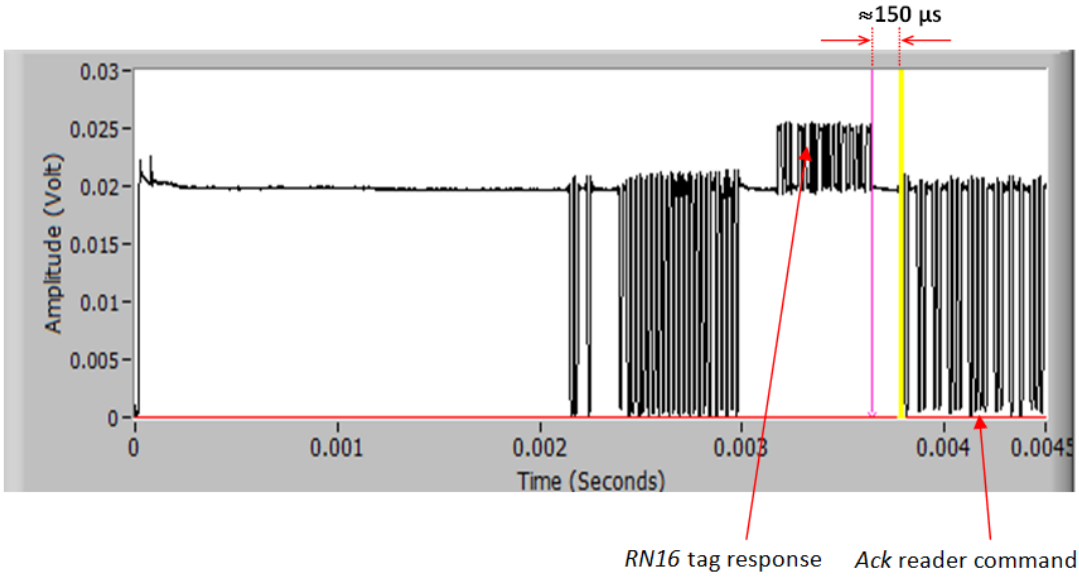

Figure 7.19: Screenshot of the LabVIEW Host program showing the RFID baseband amplitude signal at the clock rates of 40 MHz for the recovery loop and 5 MHz for the generation loop.

7.4.4 Tag sensitivity evaluation algorithm

As descried in Section 7.3, the signal processing functions for evaluating tag sensitivity are performed in a LabVIEW program running on the PXI controller.

Figure 7.20 shows the flowchart of the implemented LabVIEW program. The program initially configures the PXI system, and the parameters of the configuration include the starting transmit power of the VSG, the starting operating frequency of the VSG and VSA and the sampling rates of the VSA and VSG (IQ rate). Once the PXI system has been configured, the program encodes and modulates a *Query* command signal based on using the PIE coding format and the ASK modulation format. The VSG is then controlled by the LabVIEW program to up-convert the modulated baseband signal. The up-converted signal is finally transmitted through the transmitting antenna. The transmission of the *Query* command signal triggers the VSA to start down-converting signals arriving at the receiving antenna. The program fetches and processes data from the VSA for detecting a tag response signal, and the detection result is recorded locally. When the transmit power has reached the ending power which is set by the user, it is initialised to the starting power and the operating frequency increases to the next level. Based on the recorded results, the program searches for the minimum transmit power at which a tag response is detected. The data processing in the LabVIEW program also provides following measurements:

- the power level of the tag response baseband signal;
- the peak-peak amplitude of the tag response baseband signal;
- the link frequency of the tag response baseband signal, termed as the Backscatter Link Frequency (BLF).

Graphic User Interfaces (GUI) have been implemented for operating the RFID reader platform and reporting the evaluation and measurement results by using a number of controls and indicators on the LabVIEW front panel. Figure 7.21 presents a screenshot of a LabVIEW GUI where users are able to set the power and frequency sweeping parameters for evaluating tag sensitivity. The RFID reader platform only starts to operate when the 'Sweep' button control has been pressed by the user. Through the 'Status' window shown in Figure 7.21, users can monitor the evaluation progress by checking the transmit power and operating frequency at which the tag performance is being measured. Two meter indicators are used to report the measured BLF and P-P amplitude of the tag response baseband signal. A down-converted RFID baseband signal and a zoomed tag response baseband signal in time-domain are also presented in Figure 7.21.

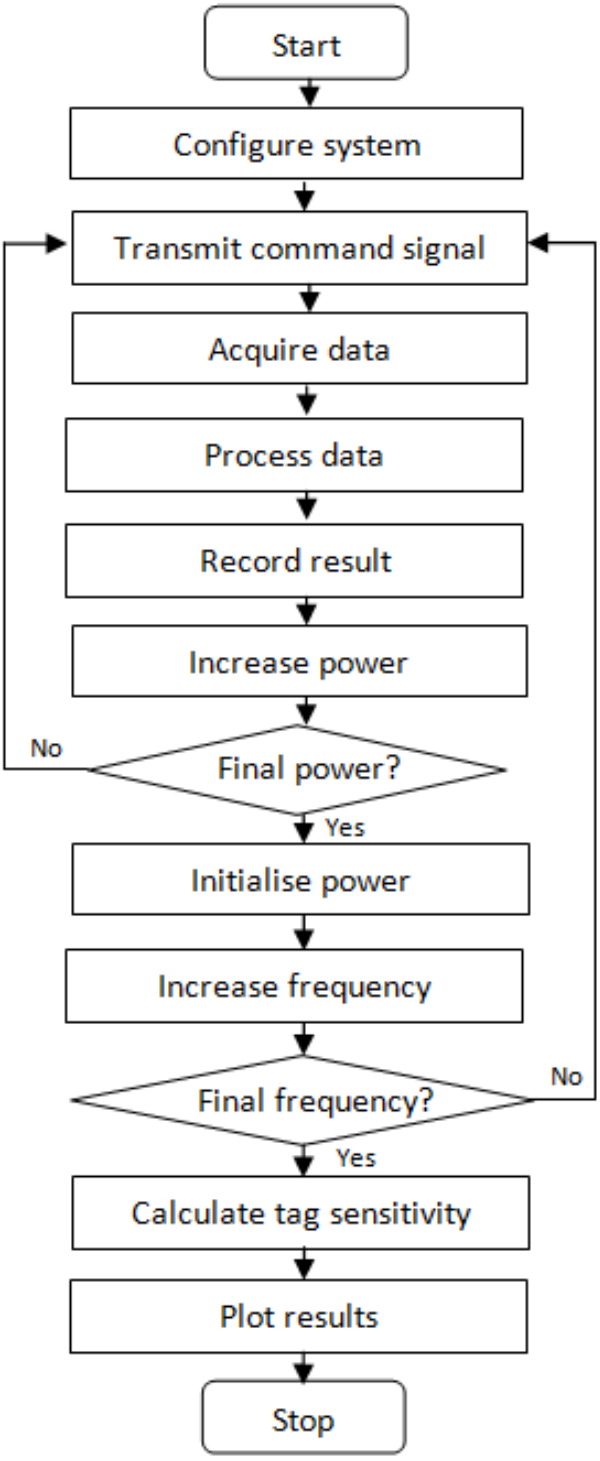

Figure 7.20: Flowchart of the implemented LabVIEW program for evaluating tag sensitivity.

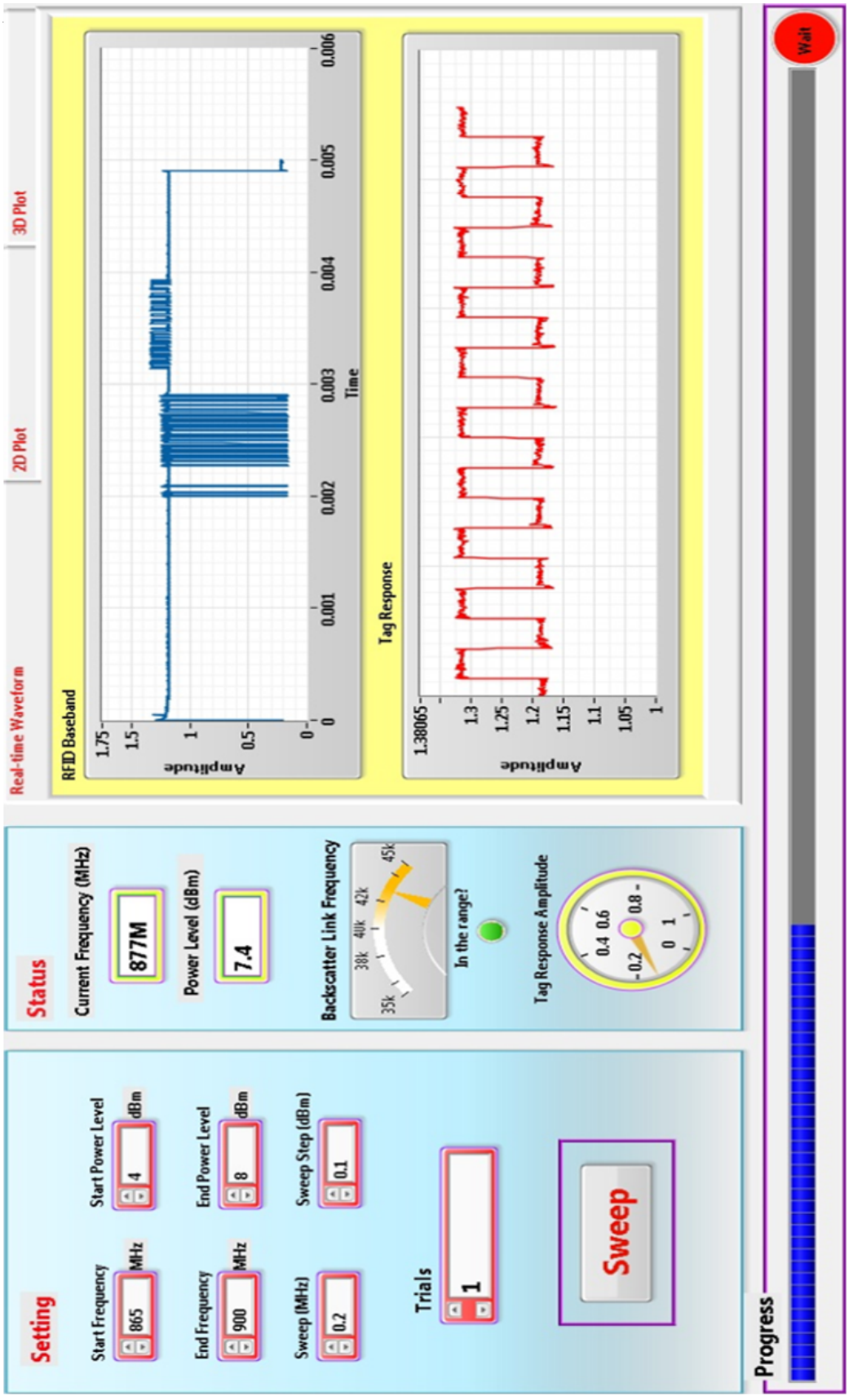

Figure 7.21: Screenshot of a LabVIEW GUI showing that the RFID reader platform is performing tag sensitivity evaluation.

7.5 RFID Reader Platform Validation

With the experimental arrangement as shown in Figure 7.10, the RFID reader platform was used to firstly write a 32-bit integer number '0X00000000' to the tag, and then read the number back from the tag by accessing the tag's memory. Figure 7.22 presents a LabVIEW GUI screenshot showing the baseband signal of the RFID transmissions when writing to the tag. On the LabVIEW GUI, the number being selected to write is represented by a LabVIEW colour constant whose length is 32 bits. The corresponding number for the colour black in LabVIEW is '0X00000000'. The reason for using colour constants is just for demonstration purpose. Two circular power meters on the GUI report the power measurements of the CW baseband signal and the backscattered signal. A screenshot of the GUI as shown in Figure 7.23 presents the result of reading the number from the tag. It is shown in Figure 7.23 that the tag is successfully read and that the colour read from the tag matches the colour which has been written to the tag.

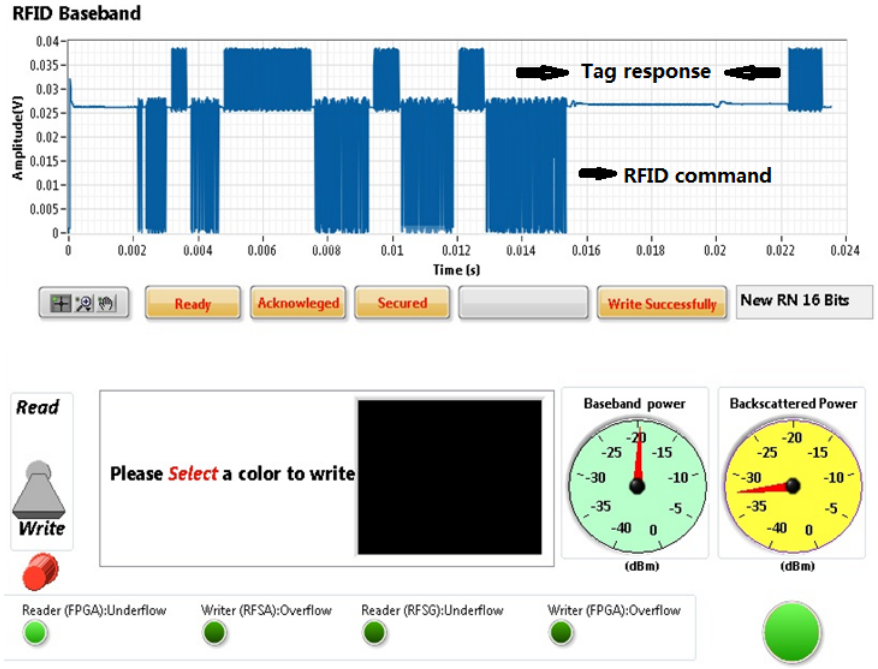

Figure 7.22: The LabVIEW GUI screenshot when implementing the function of writing the colour 'Black' to the tag at the operating frequency of 870 MHz and the transmit power (VSG) 9 dBm.

Evaluation of the tag sensitivity was validated in the 865 MHz to 900 MHz operating frequency range. The RFID reader platform was configured to sweep

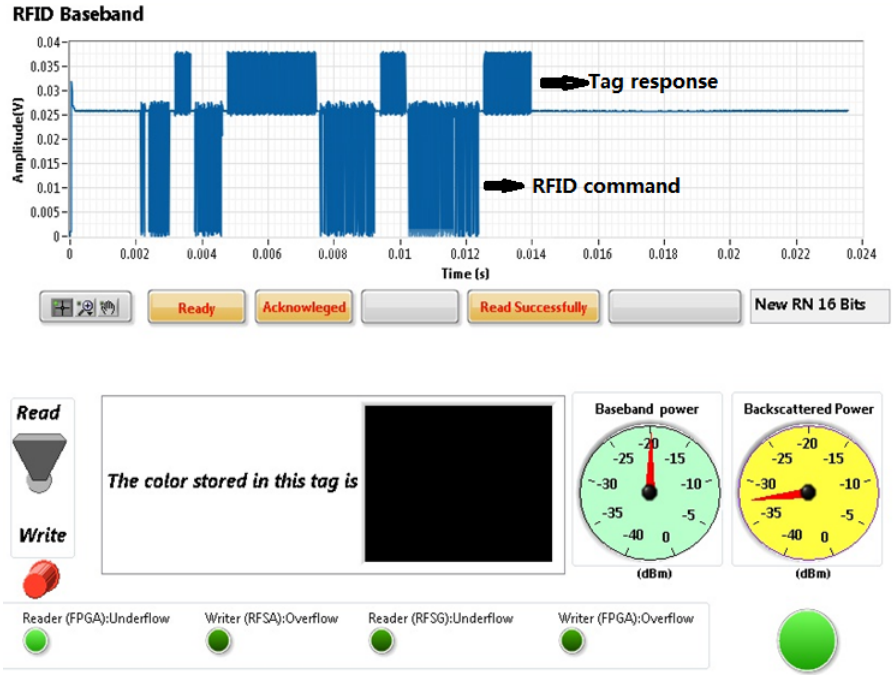

Figure 7.23: The LabVIEW GUI screenshot when implementing the function of reading tag at the operating frequency of 870 MHz and the transmit power (VSG) 9 dBm.

the operating frequency from 865 MHz to 900 MHz with an increment of 5 MHz and the transmit power (from the VSG) from 2 dBm to 6 dBm with an increment of 0.5 dBm. Figure 7.24 presents the screenshot of a GUI showing the 3D plot of the measured P-P amplitude of the tag response baseband signal versus the transmitted power (from the antenna) and operating frequency of the RFID reader platform. The unit of the amplitude in the plot is the volt, and the pink area in the plot indicates that the tag did not respond to the RFID reader platform. As shown in Figure 7.24, the measured peak-to-peak amplitude of the tag response signal increases with increasing transmit power and decreasing operating frequency. Figure 7.25 presents the evaluated tag sensitivity in 865 MHz to 900 MHz operating frequency range, showing that the lowest value of the tag sensitivity is approximately -12.5 dBm when the operating frequency is 900 MHz. The evaluated result is comparable to the tag sensitivity measured by a recent research activity [120], although more accurate evaluation results can be obtained by improving the experimental arrangement, for example by using an anechoic chamber.

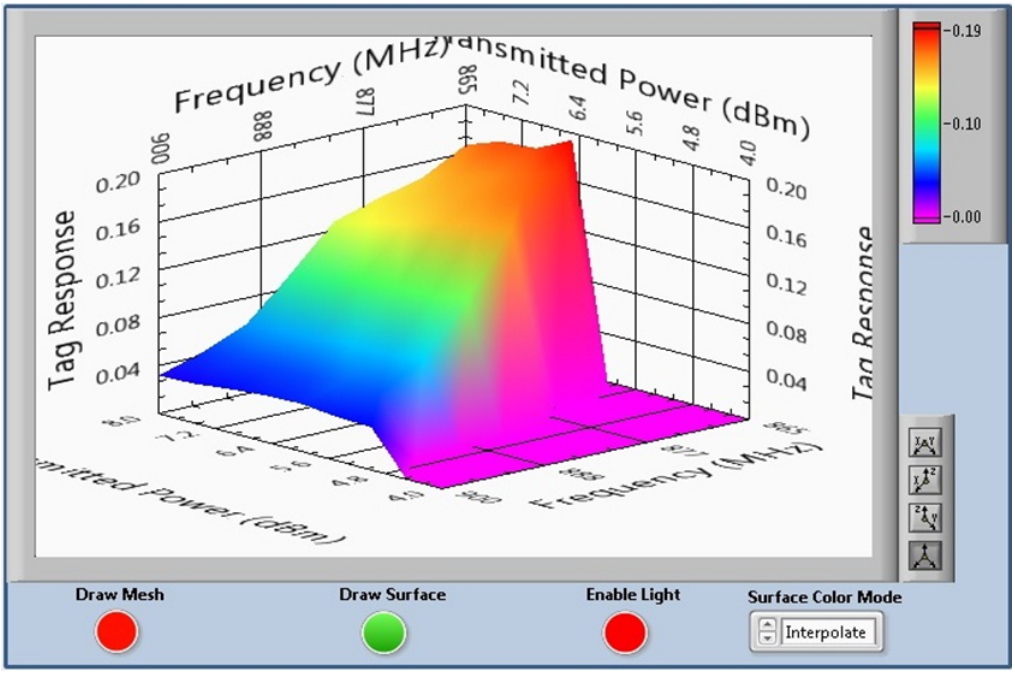

Figure 7.24: 3D plot of the measured amplitude of the tag response signal versus the transmit power and centre frequency of the RFID reader.

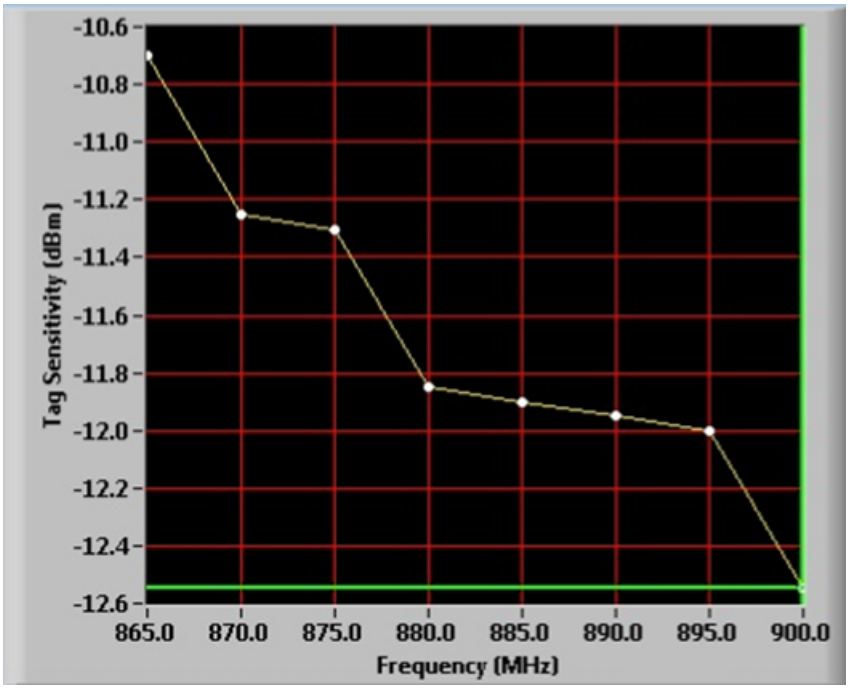

Figure 7.25: The plot of the evaluated tag sensitivity versus the centre frequency.

7.6 Summary

This chapter describes the design and implementation of a PXI-based RFID reader platform. The PXI-based RFID reader platform enables users to customise a communication protocol using software, and has a wide operating frequency range from less than 100 MHz to 6.6 GHz. One key feature of the PXI-based RFID reader platform is that the platform is configured and controlled using LabVIEW software. This feature provides the ability to implement system performance measurement and evaluation. In addition, the PXI-based RFID platform includes an FPGA module which can be complied to perform real-time signal processing functions. Algorithms for the FPGA are developed using LabVIEW. The design and implementation of the RFID reader platform is based on using RFID EPC C1G2 protocol. The RFID reader platform uses the FPGA to perform signal processing functions for implementing the physical layer, which enables the RFID reader platform to meet the timing requirements specified in the protocol. With an RFID EPC C1G2 commercial tag, the implemented RFID reader platform is capable of reading the tag ID or writing data to the tag, and evaluating the tag sensitivity. The algorithms for the FPGA are challenging to implement, and there are three factors leading to the challenge as described below.

- Algorithm design - There was no existing LabVIEW FPGA VI for implementing the physical layer specified in the RFID EPC C1G2 protocol. The algorithms needed to be developed independently by the author, who had no prior experience in programming for FPGAs before.

- Timing consideration - The RFID reader has to issue the required command for responding to a tag response signal within the maximum allowable time of 500 μs. There was a need to repeatedly modify and improve the code in order to meet the timing requirement.

- Program compiling - Whenever making a modification to the FPGA program, there was a need to re-compile the FPGA. With the developed LabVIEW FPGA VIs in this work, the compilation process took up to 1.5 hours, which lead to approximately 5 months of effort for developing the algorithms for the FPGA.

The operation of the implemented RFID reader platform has been validated.

At the time of implementing the RFID reader platform, there was no instrument found which could perform the same functions. The PXI-based reader platform will be used to evaluate the performance of a passive RFID sensor node prototype whose design and implementation are presented in Chapter 8. In addition, it will be involved in a series of practical experiments as will be described in Chapter 9.

Chapter 8

RFID Sensor Node Prototype

8.1 Introduction

This chapter presents the design and implementation of an embedded passive RFID sensor node which is capable of harvesting energy from RF fields and transmitting sensory data using backscatter modulation. The sensor node will be used as part of the RFID sub-soil system prototype. The system prototype performance will be evaluated in a sub-soil wireless channel, which is described in Chapter 9. The motivation for designing the sensor node is discussed and the basic design requirements are analysed in Section 8.2. The system design has been described in terms of energy harvesting, energy storage and management, and sensory data logging, decoding and modulation in Section 8.3. A sensor node prototype has been fabricated and the detailed information on its implementation is presented in Section 8.4. Section 8.5 illustrates the functional testing of the fabricated sensor node prototype, and the testing has investigated the charging time of the sensor node, the power consumption of the sensor node prototype and the backscatter wireless communication. Section 8.6 presents the evaluation of the charging time of the sensor node. The following elements are considered in the evaluation: the power harvested by the sensor node, the sensor node antenna and the capacitance of the on-board capacitor which is used for storing energy.

8.2 Motivation and Design Requirements

8.2.1 Motivation

The proposed RFID sub-soil system described in Chapter 4 consists of an RFID reader and a number of RFID sub-soil sensor nodes. Chapter 7 has presented a PXI-based RFID reader platform. This work is primarily motivated by the demand for a passive RFID sensor node prototype in developing the proposed RFID sub-soil system. The sensor node prototype will be used as a research platform for the system performance evaluation. The system performance includes the energy harvesting capability and the performance of the communication link. Since this research is not focussing on developing sub-soil sensors, the sensor node prototype will be designed based on integrating passive RFID technology and commercial sensors.

Commercial passive RFID tags have been widely used in applications such as transportation and supply-chain management [70]. Those tags are able to achieve the functions of RF energy harvesting and backscatter communication, and there can be a potential method of designing the sensor node prototype based on using an RFID tag. However, commercial RFID tags and readers provide the limited information for analysing the system performance. With a commercial RFID tag, the tag circuit is highly integrated to an Integrated Circuit (IC) and it does not allow interfacing with commercial sensors or an external circuit for monitoring its system voltages. In addition, the tag is strictly designed based on an industrial protocol, and so it cannot be used to explore the appropriate physical layer protocols for wireless communications through soil. Some embedded RFID sensor nodes have been developed which include a programmable RFID circuit [121, 122]. The programmable circuit of the sensor nodes uses a microcontroller and electronic components to sample and encode sensory data from commercial sensors. The encoded sensory data is then modulated through a backscatter modulator which is controlled by the microcontroller. However, these embedded sensor nodes require on-board batteries to power the node circuit and are not capable of harvesting RF energy.

8.2.2 Design requirements

Chapter 3 has described the design requirements of the proposed RFID sub-soil system from an application perspective. This section discusses the design requirements of the RFID sensor node prototype which is used for research purposes.

The sensor node prototype must be able to harvest energy from RF fields. - The sensor node prototype must contain an antenna and a rectifier which are used to harvest energy from the EM fields. The harvested energy is stored using an energy storage device. The storage device will be triggered to release the stored energy for supplying the sensor node circuit.

The operation of the sensor node prototype must be modifiable. - The sensor node prototype is able to log sensor measurements from commercial sensors. The logged data is then encoded, and the encoding format is modifiable. An embedded system can be typically used to achieve data logging and encoding, which is controlled through a programmable microcontroller.

The sensor node prototype must have a compact size. - The sensor node must have a size of which the maximum dimension has to be less then 10 cm, and so it can be easily deployed in soil for the system performance evaluation. The size of the sensor node prototype primarily depends on the node antenna and circuit. This work does not consider the design of the sensor node antenna, but will consider the trade-off between the antenna size and the sensor node performance. The size of the sensor node circuit can be minimised by using Printed Circuit Board (PCB) technology and Surface Mounted Devices (SMD).

The sensor node prototype must allow for monitoring its system voltages. - The sensor node prototype will be interfaced with external devices for monitoring its system voltages. The external devices must not create a significant power dissipation which distorts the voltage measurements. A supporting circuit will be designed for electrically isolating the sensor node circuit and the external devices.

8.3 Sensor Node Design

8.3.1 Energy harvesting

Without an on-board battery, the sensor node harvests energy from the EM field generated by the RFID reader in order to power the node circuit. Figure 8.1 presents the block diagram of the passive RFID sensor node design, where the energy is harvested through an antenna, a matching circuit and a rectifier. The antenna couples energy from RF fields, and the matching circuit matches the impedance of the antenna to the rectifier. The impedance matching minimises the RF signal reflections from the rectifier to the antenna, which maximises the power of the signal input at the rectifier. The rectifier then converts the coupled RF energy to a DC voltage supply.

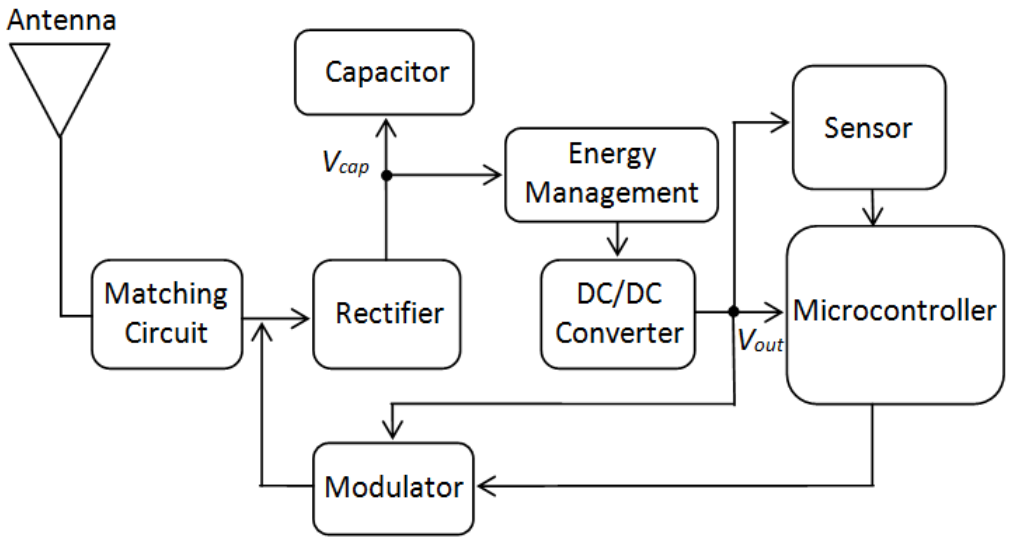

Figure 8.1: Block diagram of the sensor node design

With an RF energy harvesting system, the operating frequency and the RF to DC conversion efficiency are two crucial factors which affect the energy harvesting. When operating at a high frequency, RF signals propagate with a high path loss in air and in soil [7], which limits the energy that can be harvested by the sensor node. Decreasing frequency helps reduce the path loss, but lower frequencies require a larger antenna to achieve the efficient performance in energy harvesting, which will lead to a larger sensor node size. The conversion efficiency measures the ability to convert the harvested RF signal to a DC signal. It is

always desirable to achieve a high conversion efficiency as it leads to a shorter time for harvesting sufficient energy.

A Powercast P2110 RF power harvester [123] was chosen for the sensor node prototype. The P2110 harvester operates in 902 to 928 MHz frequency range, and this range is within one of most popular frequency bands, 860 to 960 MHz which is adopted by one of the most popular RFID protocols: the EPC C1G2 protocol [6]. This frequency band provides an appropriate balance between the path loss and the antenna size. The maximum achievable conversion efficiency of the P2110 harvester is 70 % [123].

The node antenna is another factor which affects the amount of the energy harvested by the sensor node. Since this work does not involve antenna design and fabrication, it is necessary to choose an appropriate commercial antenna for the sensor node. In terms of radiation pattern, antennas can be grouped into omni-directional antennas, such as a dipole antenna, and direction antennas, such as a patch antenna. Directional antennas typically have higher gain than omni-directional antennas, which can enhance the sensor node's efficiency in energy harvesting . However, using a directional antenna can bring problems in practice as the orientation of the sensor node is hard to control as described in Chapter 3. For research purposes, an 1 dBi PCB dipole antenna [124] is selected, which has a compact size with the maximum dimension of 16 cm. The antenna interfaces to the sensor node through a SMA (SubMiniature version A) connector.

8.3.2 Energy storage and management

Since the development of sensing technology is not a focus in this research, the sensor node uses off-the-shelf sensors. Soil moisture and soil temperature are two key parameters for crops growth, and a temperature sensor and a soil moisture sensor are two sensors of interest for the sensor node design. As presented in Table 2.1, the anticipated peak power consumption of these sensors will be more than 100 milli-watts. The converted DC energy from the P2110 harvester is typically not adequate to supply the sensor node directly. This can be solved by using a capacitor to accumulate the converted energy. When the voltage across the capacitor increases to a threshold value, the stored energy is released from

the capacitor for supplying the sensor node circuit. As shown in Figure 8.1, the P2110 harvester includes an energy management module which compares the voltage of the capacitor V_{cap}, and two in-built threshold voltages V_{max}, 1.25 V [123] and V_{min}, 1.02 V [123]. The comparison result triggers the operation of the DC/DC converter. Figure 8.2 illustrates the triggering process, where the DC/DC converter is only triggered to provide a system voltage V_{out}, 3.3 V [123] when the capacitor has been charged to V_{max}. When V_{cap} drops below V_{min}, the system voltage is stopped and the capacitor restarts accumulating the energy converted from the rectifier. As shown in figure 8.2, T_d refers to the time when V_{max} drops to V_{min} and the sensor node circuit is supplied by V_{out}, termed as the discharging time. T_c is the time during which the capacitor is charged from V_{min} to V_{max}, termed as the charging time. Both T_d and T_c are affected by the capacitance of the capacitor. The theoretical energy that can be used to supply the sensor node is given by:

$$Energy = \frac{1}{2}C(V_{max}^2 - V_{min}^2), \tag{8.1}$$

where C is the capacitance and V_{max} and V_{min} are the threshold voltages. A high capacitance C leads to large amount of energy stored in the capacitor which allows the sensor node to have a long discharging time T_d or a high energy budget. However, increasing capacitance also leads to a long charging time T_c which is not desirable as it will lead to an unacceptable speed of the farm machinery as described in Chapter 4. Thus, there is a need to select an appropriate capacitance, and the selection will depends on the trade-off between the energy budget of the sensor node and the charging time or the speed of the farm machinery as will be discussed in Chapter 11.

Regarding the capacitor, it can be an ordinary capacitor or a super-capacitor. In this work, the sensor node uses a super-capacitor. A super-capacitor is also known as a Electric Double-Layer Capacitor (EDLC) or electrochemical capacitor, which does not contain heavy metals, such as zinc (Zn), nickel (Ni), copper (Cu) and even lead (Pb). The key feature of a super-capacitor is that it has higher energy density than an ordinary capacitor [125, 126]. This feature enables a super-capacitor to have a smaller physical size than an ordinary capacitor with the small capacitance, which will allow the size of the sensor node to be

reduced. In addition, super-capacitors, especially those that are being used in the applications of memory back-up [125], have the characteristic of low leakage current, which make them ideal components for energy harvesting systems. In the sensor node design, the voltage rating of the super-capacitor has to be higher than the maximum threshold voltage V_{max}. Most of commercial super-capacitors [127, 128, 129, 130] have the Equivalent Series Resistance (ESR) ranging from mΩ to hundreds of mΩ. A lower ESR is desirable as it maximises the energy output from the capacitor.

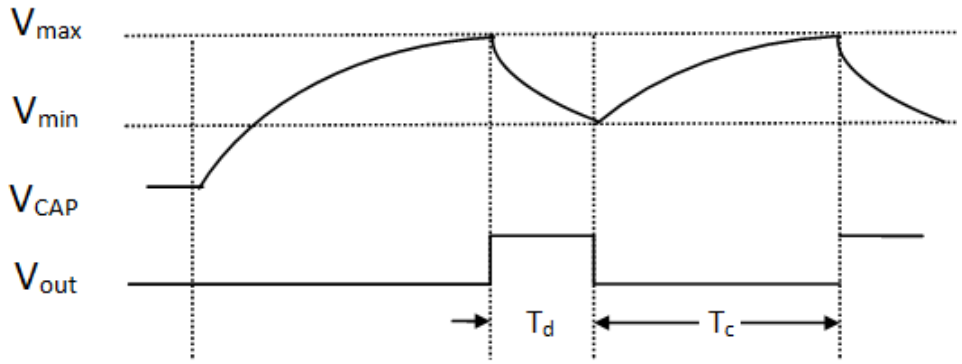

Figure 8.2: The DC/DC converter is triggered based on comparing the super-capacitor voltage V_cap and the in-built threshold voltages, V_{max} and V_{min}.

8.3.3 Sensory data logging, decoding and modulation

In the node prototype design, sensory data is provided by a TMP 37 temperature sensor [45]. The TMP 37 sensor can be directly interfaced to a microcontroller without the need of using signal conditioning circuitry. The TMP 37 temperature sensor outputs an analogue voltage linearly proportional to temperature in Celsius. For power consumption considerations, the sensor node requires a low-power microcontroller and the one selected for this work is Microchip PIC18LF14K22 microcontroller [131]. The PIC18LF14K22 microcontroller is designed with eXtremely Low Power (XLP) technology, and it only consumes 900 uA at 3.3 V when running at 1 MHz [131]. It is capable of sampling sensory data from commercial sensors through either 10-bit Analogue-to-Digital Converters (ADCs) or the integrated communication buses, such as Serial Peripheral Interface (SPI) bus and Inter-Integrated Circuit (I2C) bus. Through a C program running on the

microcontroller, an on-board ADC of the microcontroller is configured to sample measurements from the TMP 37 temperature sensor and also to encode the measurement samples based on using the FM0 encoder scheme [6].

With a passive RFID system, an RFID tag generates a modulated backscatter signal by varying its antenna-load reflection coefficient. Following this principle, an RF switch, SKYWORKS AS193-73 [132] is used to modulate the encoded sensory data by varying the sensor node antenna-load impedance. Figure 8.3 shows the schematic of the backscatter modulator using an RF switch, where the antenna can be switched to either a 50 Ω load or ground. The 50 Ω load results in a low antenna-load reflection, and negligible power is reflected back from the antenna. When the antenna is grounded, the reflection coefficient greatly increases, which generates a high power reflection. The RF switch is driven by two digital control voltages, however a single voltage can be used in conjunction with a digital inverter device to generate the opposite voltage.

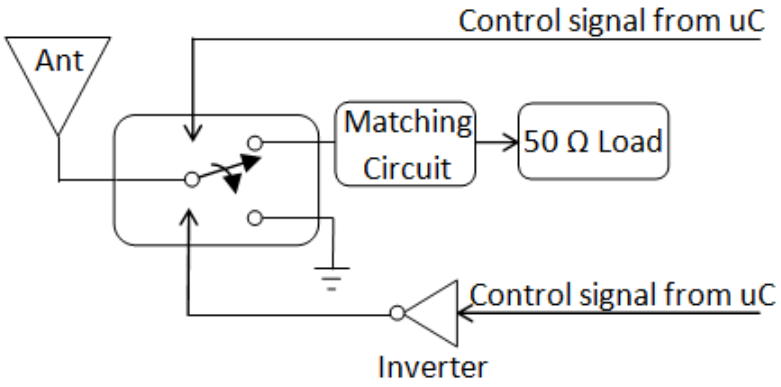

Figure 8.3: Schematic of backscatter modulator using an RF switch

8.4 Sensor Node Prototype Implementation

8.4.1 Prototype hardware

Based on the sensor node design described in Section 8.3, the implementation of the sensor node used two antennas in the first instance: one for energy harvesting and the other one for backscatter modulation. However, using the two antennas

led to a large sensor node size and the two antennas can potentially affect each other. Therefore, the implementation was finally based on using a single antenna for both energy harvesting and backscatter modulation. Figure 8.4 presents the schematic diagram of the implemented node prototype circuit, where the node antenna is interfaced with the RF input of the RF switch, J_1. One of the outputs of the RF switch, J_2, is connected to the RF input of the P2110 RF harvester, and other output of the RF switch, J_3, is grounded. Since the input impedance of the P2110 RF energy harvester is matched to 50 Ω, the harvester can be seen as the 50 Ω load which is part of the backscatter modulator as shown in Figure 8.3.

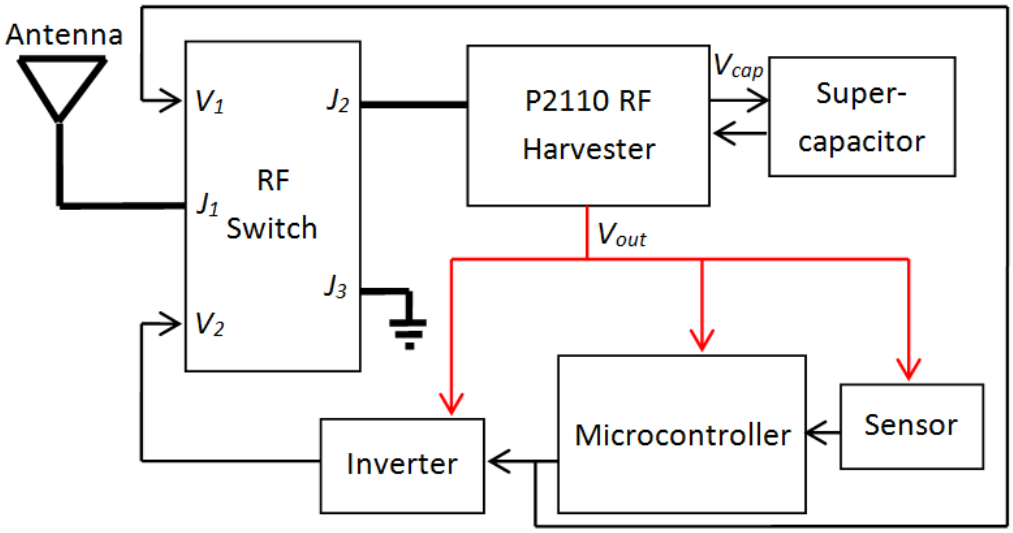

Figure 8.4: Schematic of the sensor node prototype circuit

One concern with this design is that the RF switch is not electrically controlled until the super-capacitor has been charged to the threshold voltage V_{max}, and so there can be an uncertain path loss within the RF switch. The path loss from the switch input J_1 to the switch output J_2 has been measured at the frequency of 915 MHz using a National Instruments (NI) PXI system [109]. Figure 8.5 presents the block diagram showing the experimental arrangement for the path loss measurement, where the NI PXIe-5673 VSG and PXIe-5663 VSA are interfaced with the port, J_1, and the port, J_2 and the two pins for the control voltages are left open. The path loss is measured from the VSG transmit power

P_t and the received power P_r at the VSA:

$$P_L(dB) = P_r(dB) - P_t(dB). \tag{8.2}$$

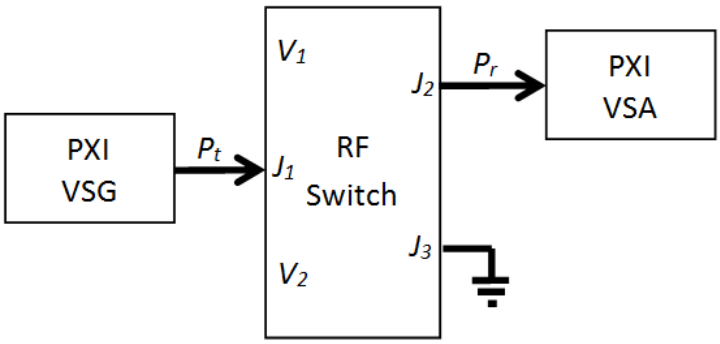

Figure 8.5: RF switch testing diagram

The measurement results are shown in Table 8.1, and it is observed that the RF switch has a path loss between J_1 and J_2 when it is not electrically powered. The path loss in the switch will affect the charging time T_c shown in Figure 8.2. However, since the path loss is steady this will not affect the basic functions of the sensor node prototype.

Table 8.1: Measured path loss (at 915 MHz) of the RF switch when it is electrically isolated from the control voltages.

$P_t(dBm)$	$P_r(dBm)$	Measured P_L (dB)
-20	-22.6	-2.6
-10	-12.6	-2.6
-5	-7.6	-2.6
0	-2.6	-2.6
2	-0.6	-2.6
4	1.3	-2.7
5	2.3	-2.7

The DC energy converted from the P2110 harvester is stored using a Cellergy CLC04P010L12 10 mF super-capacitor [130]. The nominal voltage of the

super-capacitor is 4.2 V which is higher than the threshold voltage V_{max}. With the capacitance of 10 mF, the stored energy (when the super-capacitor is charged from V_{min} to V_{max}) is approximately 2.6 mJ which is calculated based on Equation 8.1. The stored energy can easily maintain the peak power consumption of hundreds milli-watts for milli-seconds. When the super-capacitor has been charged to the threshold voltage V_{max}, the in-built DC/DC converter is triggered to provide the supply voltage V_{out} of 3.3 V. The microcontroller then reads the temperature sensor through an on-board 10-bit ADC. The ADC uses the supply voltage, 3.3 V as its reference voltage, and so the resolution of the 10-bit ADC is 3.2 mV. The TMP 37 sensor provides a 500 mV output at 25 $^{\circ}C$ and an output scale of 20 mV/$^{\circ}C$ [45]. Therefore the resolution of sensor measurements sampled by the ADC is 0.16 $^{\circ}C$. The sensor measurements are encoded by the microcontroller with the FM0 encoder scheme, and a stream of digital encoded output is then generated by the microcontroller. The digital output is used as the control signal to control the backscatter RF switch.

When prototyping the sensor node hardware, Surface Mounted Devices (SMDs) are selected in order to minimise the sensor node size. Figure 8.6 presents the photograph of the fabricated sensor node PCB whose size is 35 mm $\times$ 80 mm. A printed 1 dB 915 MHz dipole antenna as presented in Figure 8.7 is connected to the sensor node through a 50 Ω SMA connector, and this connection method provides the flexibility to evaluate the prototype performance by using various antennas. The PCB is designed using Altium Designer software [133], and the schematics and the Altium files of the PCB design are included in Appendix D. The traces for RF signals on the PCB are designed as 50 Ω CoPlanar WaveGuide (CPWG) transmission lines [134]. Two lines of pin headers are soldered on the board, one is for programming the microcontroller and another one will allow monitoring the voltage across the super-capacitor V_{cap} and the supply voltage V_{out}.

8.4.2 Microcontroller program

The microcontroller is programmed in C using MPLAB Integrated Development Environment (IDE) toolkit [135]. All the C code and the files for compiling the microcontroller in this implementation are included in Appendix E. The microcontroller program primarily consists of four steps and the flow of the program

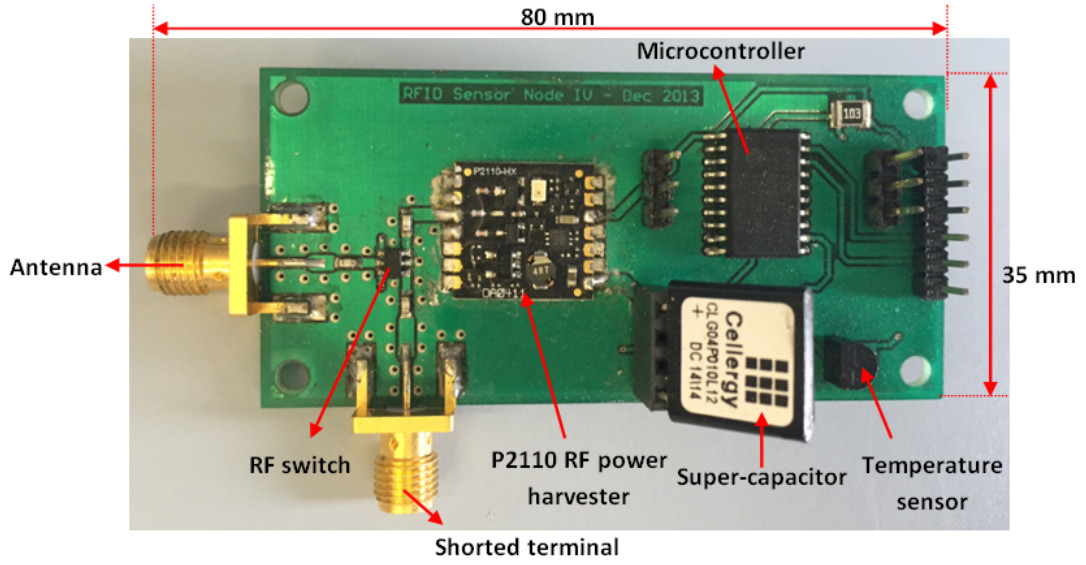

Figure 8.6: Photograph of the sensor node prototype PCB .

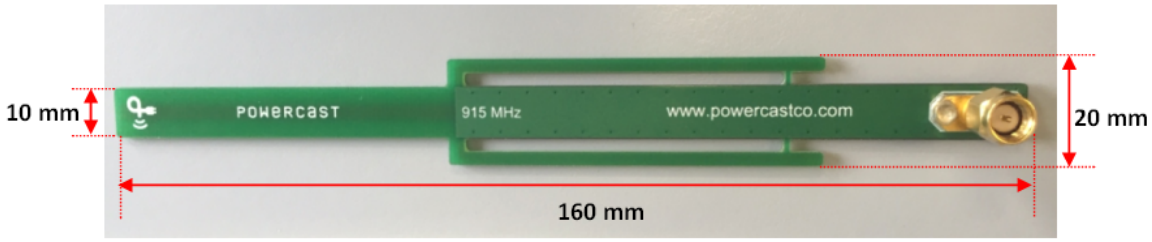

Figure 8.7: Photograph of the sensor node antenna .

is shown in Figure 8.8. When the supply voltage becomes available, the microcontroller initialises one analogue pin for sampling sensor measurements and one digital pin for controlling the RF switch. The corresponding ADC interfaced to the analogue pin is then configured to sample voltage outputs from the TMP 37 temperature sensor. Once the microcontroller has obtained a 10-bit sensor measurement, it adds a five-zero preamble before and a two-zero ending after the sensor measurement. As presented in Figure 8.9, the sensory data bits generated by the microcontroller are '00000000010001100' given to the 10-bit sensor measurement of '0000100011'. The final step is to encode the sensory data bits by implementing the FM0 encoder scheme as specficied in RFID EPC C1G2 protocol [6]. The microcontroller then outputs the encoded signal via the digital pin to drive the RF switch for implementing backscatter modulation. Once two sensor measurements have been sampled, encoded and modulated, the microcontroller

enters the sleep mode at which the power consumption of the microcontroller drops to nano-watts [131]

The implementation of the microcontroller program includes two crucial parameters: the data rate of the encoded sensor measurements and the frequency at which the microcontroller is clocked. Running at a higher frequency enables a higher data rate, but it also requires a higher energy budget. The power consumption of the microcontroller (core) can increase to 4 mW at 16 MHz, and the power consumption is 0.9 mW at 1 MHz. A trade-off has been made between the data rate and the power consumption. As specified in the EPC C1G2 protocol, the minimum data rate f_{tag} of the tag-to-reader link is 40 kHz [6]. Since the sensor node only transmits a single sensory data each time, the data rate in this work is set to quarter of the f_{tag}, which is 10 kHz. This data rate allows the microcontroller to run at 1 MHz.

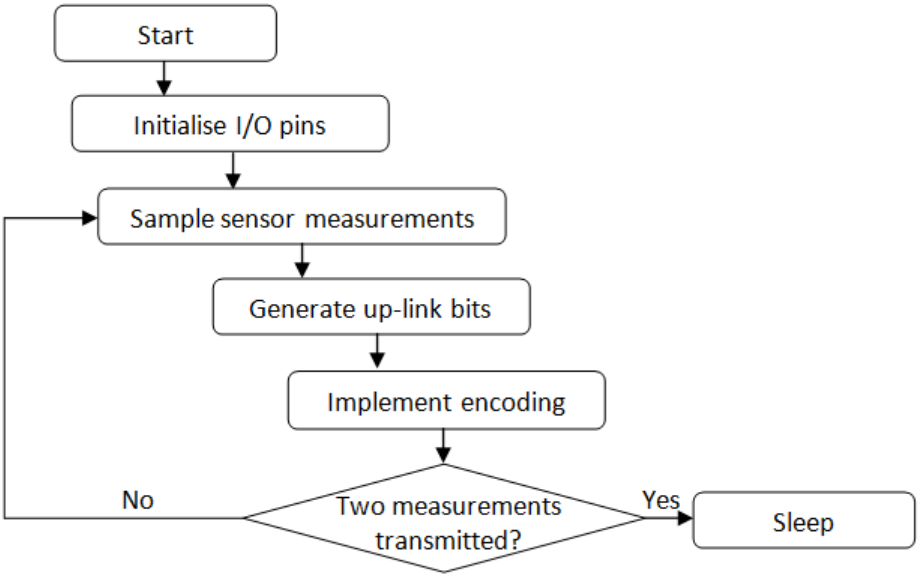

Figure 8.8: Flow of the microcontroller program designed for logging and encoding the sensor measurements.

8.4.3 Energy budget estimation

The power budget (at 3.3 V) of the sensor node prototype is shown in Table 8.2, where the power consumption of the microcontroller has been measured and

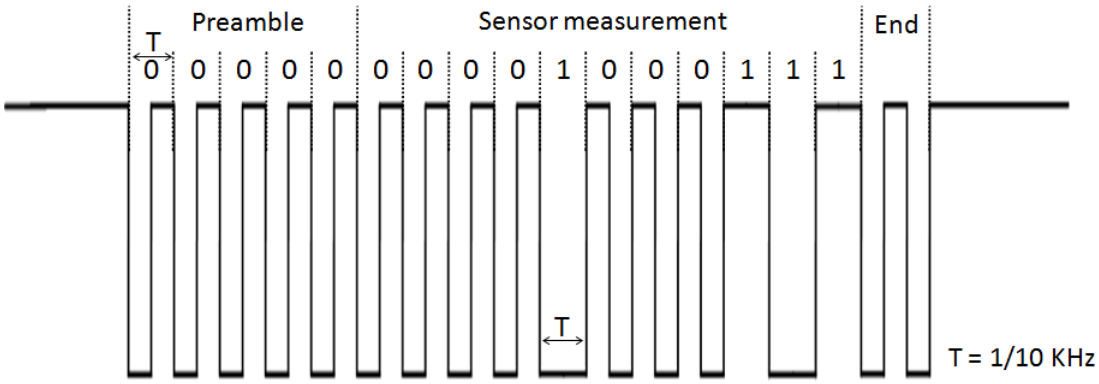

Figure 8.9: Encoded waveform of the up-link bits, generated from the example sensor measurement of '0000100011'.

other power consumptions are provided by the manufacturers [45], [132] and [136]. The power budget information is only used to estimate and understand the peak power consumption of the sensor node prototype. As shown in Table 8.2, the power consumption of the microcontroller accounts for most of the budget and the peak power consumption of the sensor node can reach 1.68 mW. For expected sub-soil sensor nodes in practice, on-board sensors will account for most of the energy budget. As presented in Table 2.1, the power consumption of the soil moisture sensor is 90 mW. The minimum required power-on time, T_{on} during which the sensor node circuit has to be supplied is estimated as:

$$T_{on} = (N + 1) \times L \times \frac{1}{D}, \tag{8.3}$$

where N represents the number of sensor measurements that need to be transmitted by the sensor node , L is the number of the sensory data bits (with the preamble and ending), and D is the data rate. Given that the sensor node transmits two 17-bit sensory data at the data rate of 10 kHz, the minimum power-on time is calculated as 5.1 ms.

Table 8.2: Power budget of the sensor node prototype

Device	Peak power consumption (μW)
Microcontroller	900 (at 1 MHz)
Sensor [45]	165
RF switch [132]	495
Inverter [136]	120
Total	1680

8.5 Prototype Functional Testing

The fabricated sensor node prototype has been tested using the PXI/LabVIEW RFID reader implementation as described in Chapter 7 and a NI myDAQ instrument [137]. The prototype testing has investigated the charging time of the sensor node, the sensor node power consumption and the backscatter wireless communication. The charging time refers to the time during which the on-board super-capacitor is charged from the low threshold voltage, V_{min} to the high threshold voltage,V_max. Figure 8.10 presents the diagram of the testing arrangement. As shown in Figure 8.10, the PXIe-5673 VSG is used to generate Continuous Wave (CW) signals for powering the sensor node, and the PXIe-5663 VSA receives and down-converts the backscattered signal from the sensor node. This RFID reader implementation uses the monostatic antenna configuration which uses a single 8 dBi Cellular path antenna [138] for both transmission and reception. The reception path is isolated from the transmission path using a Mini-Circuit ZEDC-15-2B directional RF coupler [139]. The sensor node prototype is located 0.4 m away from the patch antenna, at which the sensor node is within the far-field of the reader antenna. The NI myDAQ instrument is interfaced to the sensor node for sampling and recording the super-capacitor's voltage V_{cap} and the supply voltage V_{out}. The PXIe-8133 controller executes a LabVIEW program in which the data acquired by the VSA and the myDAQ are processed for the performance testing. LabVIEW GUIs are designed for logging data and reporting measurements, and the LabVIEW files are included in Appendix F.

When sampling the system voltages of the sensor node prototype, the key

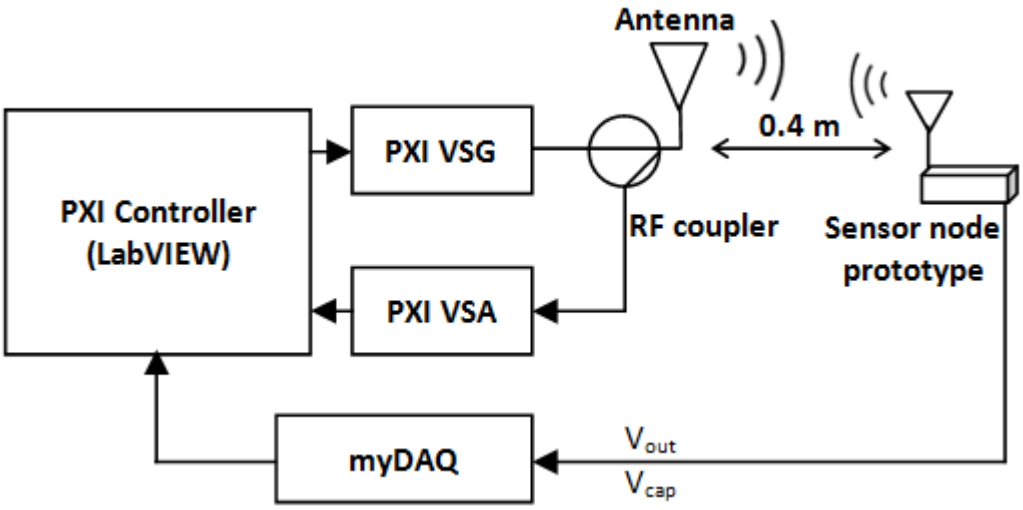

Figure 8.10: Block diagram of the experimental arrangement for testing the sensor node prototype.

concern is that there will be a current leakage flowing from the sensor node system to the myDAQ instrument. This current leakage leads to a power dissipation and affects the fidelity of measurements. Therefore, two voltage buffers with high input resistance are used to electrically isolate the sensor node power system from the myDAQ instrument. Figure 8.11 presents the implemented voltage buffers using two Texas Instruments LMC 6462 operation amplifiers [140] which have high input resistance, typically greater than 10 TΩ [140].

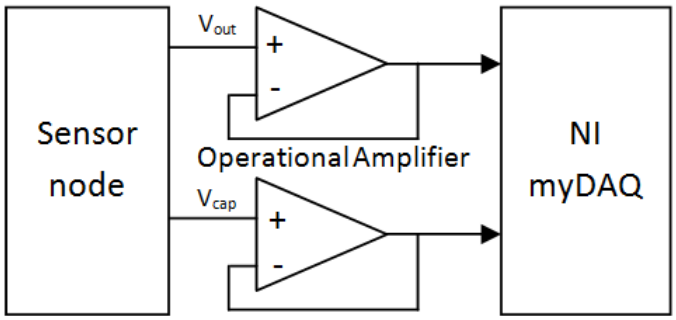

Figure 8.11: Implementation of two voltage buffers for sampling the system voltages of the sensor node.

The prototype was tested at 915 MHz which is at the centre of the operating frequency range of the P2110 RF power harvester [123]. The PXI reader implementation is configured with the settings as shown in Table 8.3. The operation

frequency of the PXI VSG and VSA is 915 MHz. The transmit power of the PXI VSG is 8 dBm, and the transmitted power from the reader antenna (8 dBi gain) is 16 dBm. The PXI VSA receives signals with the sampling rate of 500 kHz which is 25 times higher than the data rate of the demodulated signal in the sensor node. The PXI controller processes the received data at the VSA every 6 ms for detecting and demodulating the backscattered signal from the sensor node.

Table 8.3: Settings of the PXI reader implementation.

Settings	**Value**
Operating frequency (VSG and VSA)	915 MHz
Transmit power (VSG)	8 dBm
Acquisition time (VSA)	6 ms
Sampling rate (VSA)	500 kHz

The average power consumption P_o (watts) of the sensor node prototype is calculated according to Equation 8.4.

$$P_o = \frac{E_s}{T_d}, \tag{8.4}$$

where E_s (joules) represents the energy that is released from the super-capacitor when the super-capacitor voltage V_{cap} drops from V_{max} to V_{min}, and T_d (s) refers to the time when the sensor node circuit is being supplied by V_{out}. The energy E_s is calculated from the capacitance of the super-capacitor and the two threshold voltages according to Equation 8.1. The time T_d is measured from the voltage signal recorded by the myDAQ instrument. The communication link testing includes the demodulation and recovery of the sensor measurements from the backscattered signals that are received at the VSA. In addition, the power of the backscattered signal, P_b, is calculated from the I and Q components of the baseband signal:

$$P_b = \frac{I^2 + Q^2}{50}, \tag{8.5}$$

where the unit of I and Q is the volt and 50 represents the characteristic impedance of the VSA in ohms.

Figure 8.12 presents a screenshot of a LabVIEW GUI showing testing results. The graph of the system voltage signals indicate that the sensor node has been powered off and on for 10 periods within 1000 s. A zoomed screenshot of the LabVIEW GUI is shown in Figure 8.13, where the measured (average) charging time T_c is 110.6 s and the measured (average) discharging time T_d is 9.9 s. The calculated average power consumption of the sensor node prototype is 264.1 μW. Figure 8.12 also presents a backscattered baseband signal from the sensor node, where the unit of the baseband signal amplitude is the volt. The temperature value recovered from the baseband signal is 19.7 $^{\circ}C$, which is comparable to the value measured by an off-the-shelf digital thermometer. The measured power of the backscattered signal is -42.7 dBm.

The testing results show that the sensor node prototype successfully achieves the functions of harvesting RF energy and transmitting sensor measurements through backscatter modulation. Although the charging time performance, T_c is unsatisfactory from a practical view, it can be improved by increasing the transmit power. In the prototype performance testing, the transmit power of the PXI VSG is 8 dBm. In practice, the maximum Effective Isotropic Radiated Power (EIRP) that is permitted in the UHF band is 36 dBm (4 W) [1]. A high transmission power is typically achieved by using an RF amplifier. As presented in Figure 3.1 increasing transmit output power, P_t, of the RFID reader increases the power harvested by the sensor node, P_r, and therefore shortens the time for harvesting a certain amount of energy. Section 8.6.1 describes the charging time performance evaluation of the sensor node prototype by considering the harvested power. In addition to the transmit power, the power harvested by the sensor node is also affected by the node antenna which is used to couple energy from the EM field generated by the RFID reader implementation. The charging time performance of the sensor node prototype has also been evaluated by using four various commercial antennas, and the evaluation result is presented in Section 8.6.2.

As described in Section 8.3, the capacitance of the super-capacitor affects the charging time T_c. Using a low capacitance helps shorten the charging time of

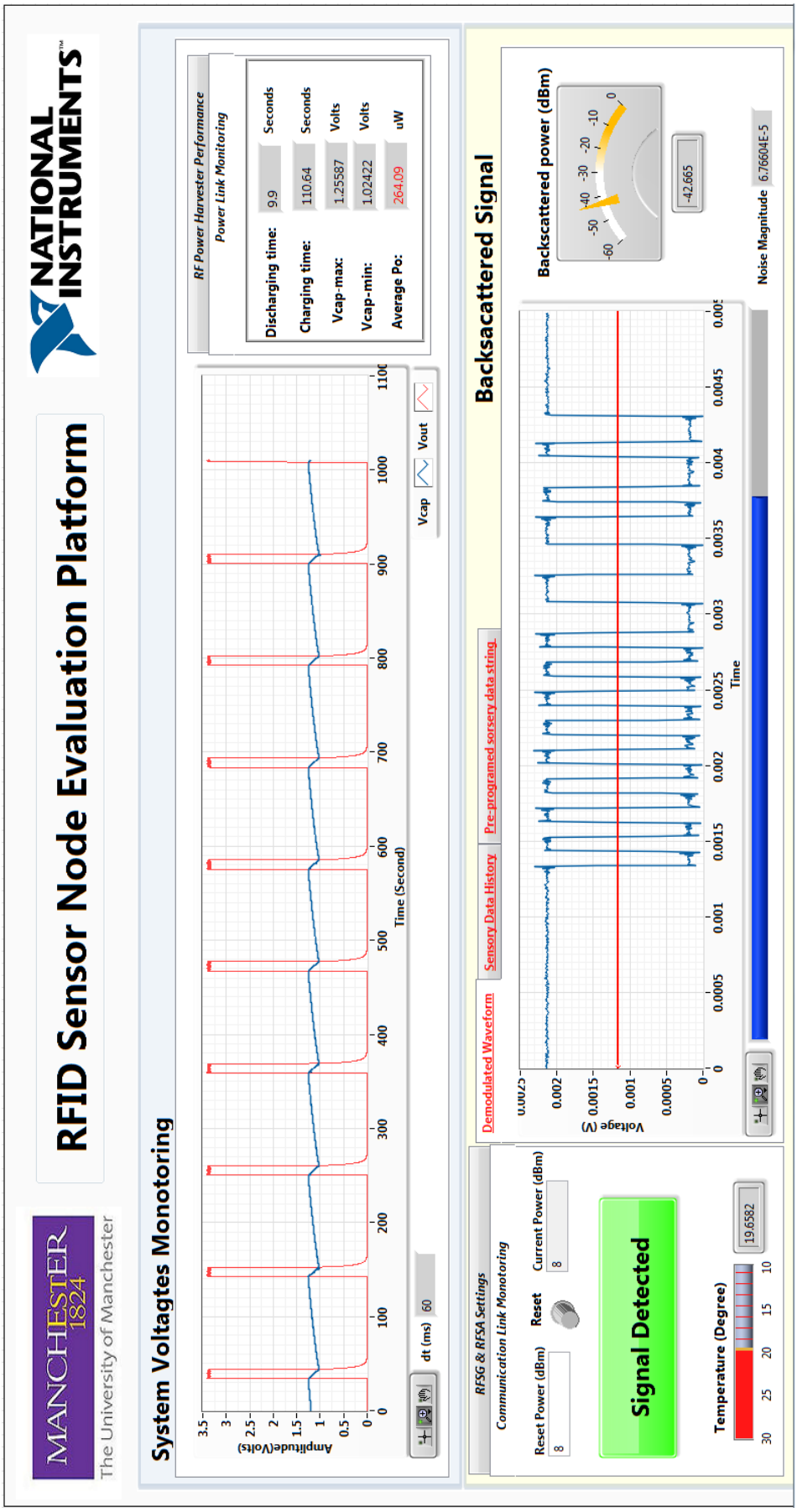

Figure 8.12: Screenshot of the LabVIEW GUI showing the evaluation results.

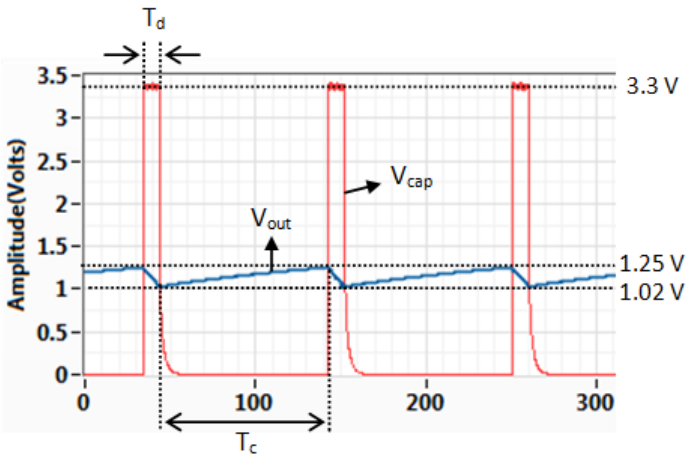

Figure 8.13: The zoomed screenshot of the labVIEW GUI showing system voltage signals.

the sensor prototype. However, a low capacitance limits the amount of energy stored in the capacitor at a given capacitor voltage. If the energy stored in the super-capacitor does not meet the energy budget of the sensor node prototype, the operation of the sensor node prototype will be affected. The sensor node prototype uses a 10 mF super-capacitor to store the harvested energy. It is observed from the testing result that the measured discharging time T_d (9.9 s) is approximately 2000 times the minimum required power-on time T_{on} estimated in Section 8.4.3. This observation implies that the charging time of the sensor node can be shortened by using a capacitor with a capacitance lower than 10 mF. This has been investigated as described in Section 8.6.3.

8.6 Prototype Performance Evaluation

8.6.1 Harvested power

In order to measure the charging time of the sensor node at a specific power harvested by the sensor node, the testing arrangement shown in Figure 8.10 has been modified and the modified arrangement is presented in Figure 8.14. As shown in Figure 8.14, the signal output of the PXI VSG is directly linked to the RF input of the sensor node through a coaxial cable. The power P_r harvested by the sensor node antenna is calculated by subtracting the cable loss from the transmit power of the VSG P_t. The myDAQ instrument is interfaced to the sensor node for

recording the super-capacitor voltage V_{cap}. A LabVIEW program running on the PXI controller configures the VSG to increase the transmit power from -9 dBm to 0 dBm with a step of 0.2 dBm. The charging time T_c is measured from the recorded voltage signal. At each power, the charging time measurement has been repeated by 50 times in order to determine the error bars of the measurement.

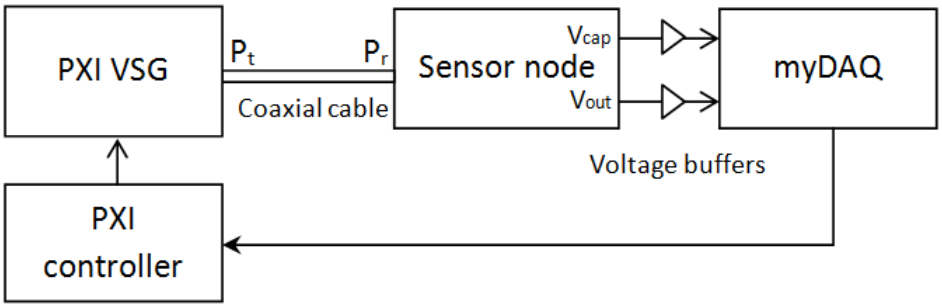

Figure 8.14: Modified testing arrangement for measuring the charging time T_c at a specific power harvested by the sensor node.

Figure 8.15 presents the plot of the measured charging time T_c versus the harvested power. It is shown from Figure 8.15 that the measured charging time continues to decrease with increasing power. The rate of change of the charging time with respect to the power reduces as the power increases. This means that the same change in the power leads to a greater change in the charging time at a higher power level. There is also an observation from Figure 8.15 that the error bound of the measured charging time decreases with increasing power. As shown in Figure 8.15, the measurements have an error bound ranging from ± 1 s to ± 10 s when the harvested power is less than -5.6 dBm. When the harvested power increases above -5.6 dBm, the error bound of the measurements is less than 0.5 s. The primary factor that gives rise to the error can be the stability of the power harvesting efficiency provided by the P2110 chip-set. The power harvesting efficiency provided by the P2110 chip-set is primarily dependent on the conversion efficiencies of the on-chip rectifier and DC/DC converter. The P2110 manufacturer provides limited information of the rectifier and the DC/DC converter.

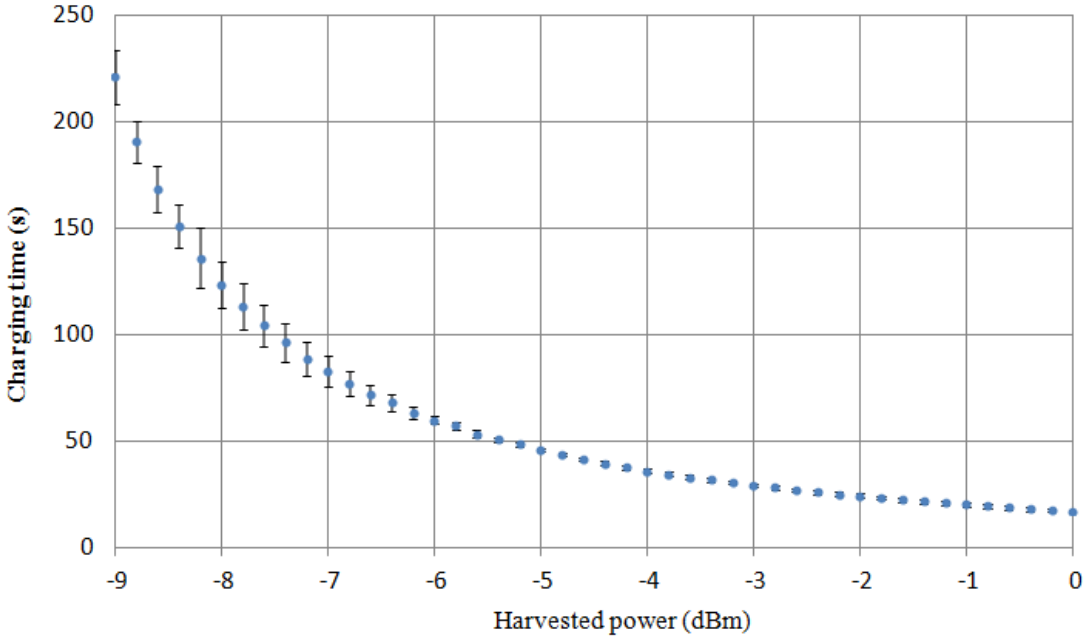

Figure 8.15: Plot of the measured charging time versus the received power by the sensor node prototype.

8.6.2 Sensor node antenna

With the testing arrangement presented in Figure 8.10 and the configuration of the PXI system shown in Table 8.3, the charging time performance T_c of the sensor node prototype has been evaluated at 915 MHz by using various antennas. In addition to the dipole antenna described in Section 8.3, three commercial antennas have been selected for the performance evaluation, which include a patch antenna [124], a blade antenna [141] and a monopole antenna [142]. The operating frequency bands of those antennas all cover the frequency of 915 MHz. The reason for using commercial antennas is that this research is not focusing developing antennas. When using one of the selected antennas, the PXI system was configured to power the sensor node until the sensor node was powered on and off for 10 periods, and the average charging time was then measured. In the performance evaluation, the orientation of the antennas was adjusted to ensure that the peak gain of the antenna is at the direction of the reader antenna. Table 8.4 shows details of the antennas and the charging time measurements.

As shown in Table 8.4, the measured charging time when using the patch antenna is approximately 88 s shorter than when using the dipole antenna. This is

Table 8.4: Evaluation of the charging time performance using various antennas.

Antenna	*Dimensions (mm)	Peak Gain (dBi)	Charging time (s)
Dipole	160 × 20 × 2	1 [124]	110.6
Patch	200 × 60 × 40	8 [124]	22.8
Blade	84 × 21.5 × 5	2 [141]	90.2
Monopole	59 (length) × 10 (diameter)	2 [142]	–

(* Dimensions excluding SMA connector.)

due to the patch antenna has a higher gain than the dipole antenna. However, the patch antenna has the largest physical size which will lead to an unrealistic sensor node size. In addition, its directional pattern is not desirable since the orientation of the sensor node is not controllable in practice as described in Chapter 3. The quarter-wavelength monopole antenna has the smallest size, but it is not efficient in harvesting energy. When using the monopole antenna, the voltage of the super-capacitor, V_{cap} did not reach the threshold voltage V_{max} within 1000 s. The measured charging time when using the blade antenna is shorter than the measurement when using the dipole antenna, and the blade antenna has a smaller size than the dipole antenna. The blade antenna seems to be a better choice for the sensor node antenna than the dipole antenna. However, the blade antenna requires to use a ground plane in order to achieve the efficient performance in energy harvesting, which will bring the same practical problem as when using a directional antenna.

8.6.3 Super-capacitor

There was a plan to use a 1 mF super-capacitor in order to shorten the charging time T_c of the sensor node prototype. With a capacitance of 1 mF, the energy that can be used to supply the sensor node prototype is 0.26 mJ which is calculated based on Equation 8.1. This amount of energy completely meets the estimated energy budget as shown in Section 8.4.3. At the time when undertaking this work, the minimum capacitance of off-the-shelf super-capacitors was 10 mF. There are two methods of providing a capacitance of 1 mF. The first method is

based on using ten 10 mF super-capacitors which are connected in series, and the other method is based on using a 1000 uF ordinary capacitor. With the experimental arrangement presented in Figure 8.10, the sensor node performance was firstly evaluated using ten Cellergy CLC04P010F12 10 mF super-capacitors [130] and then using a 1000 uF aluminium electrolytic capacitor [143]. Regarding the evaluation results, the DC/DC converter failed to provide a 3.3 V output when the the 10-capacitor pack has been charged to V_{max}. With the 1000 uF electrolytic capacitor, the sensor node prototype operated successfully, and the measured charging time T_c was 20 s, which was shortened by 90 s compared to the measurement when using a single 10 mF super-capacitor. The evaluation result implies that the 10 mF super-capacitor can experience a serious self-discharge phenomenon. With the self-discharge phenomenon, there will be a voltage drop across the super-capacitor when it is under an open-circuit condition [144], [145]. The self-discharge causes energy loss, and so affects the time for charging the super-capacitor up to a certain voltage, and will also affect the actual energy that can be used to supply the sensor node.

The self-discharge characteristic of capacitors has been investigated using a measurement arrangement as presented in Figure 8.16. As shown in Figure 8.16, the under test capacitor C is firstly charged to V_{max} 1.25 V, and the NI myDAQ instrument is used to sample and log the open-circuit voltage of the capacitor. A voltage buffer was implemented using a LMC6462 operational amplifier [140] in order to provide high input resistance. The voltage samples are reported in the GUI of a LabVIEW program running on the PC. In addition to the 10 mF Cellergy super-capacitor and the 1000 uF electrolytic capacitor, the following commercial super-capacitors have been tested: Panasonic EECF5R5H105 1 F super-capacitor [127], PowerStor HV0810-2R7105-R 1F super-capacitor [128] and AVX BZ015B303ZSB 30 mF super-capacitor [129]. These three super-capacitors are advertised as low leakage super-capacitors which can be used in memory back-up applications. Figure 8.17 presents a screenshot of the LabVIEW GUI comparing the measured open-circuit voltage of the five capacitors over 6 hours. As shown in Figure 8.17, the super-capacitors have a difference in self-discharge characteristic. The open-circuit voltage of the 1000 uF electrolytic capacitor declines slowly than the voltage of the Cellergy 10 mF super-capacitor and the AVX 30 mF super-capacitor. Only the Panasonic super-capacitor and the PowerStor

super-capacitor have a lower self-discharge rate than the rate of the 1000 uF electrolytic capacitor. However, these two 1 F capacitors will lead to a long charging time.

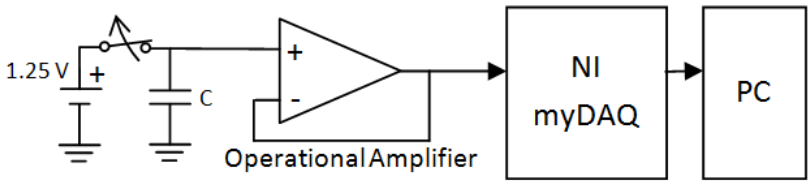

Figure 8.16: Capacitor and super-capacitor self-discharge measurement arrangement diagram.

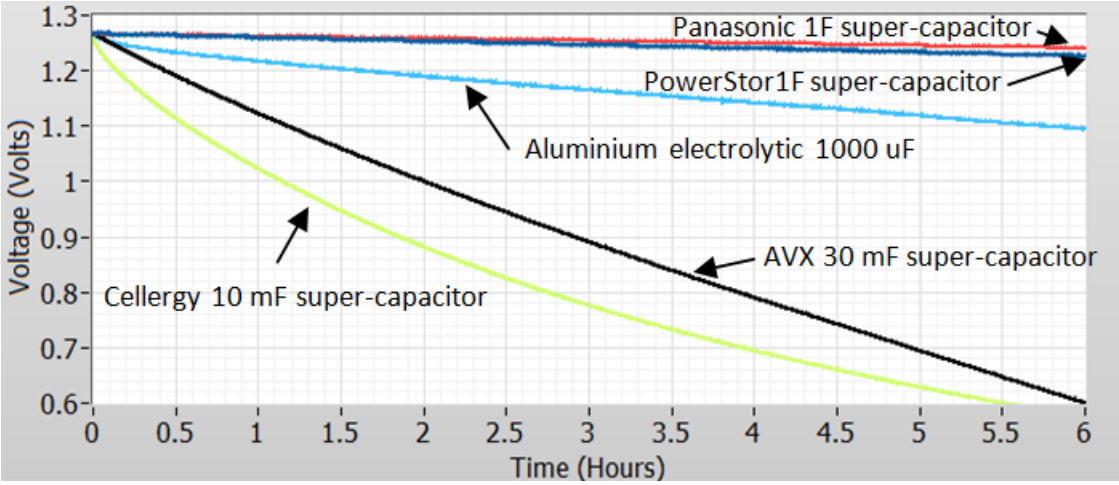

Figure 8.17: Screenshot of a LabVIEW GUI comparing the measured open-circuit of the five capacitors using the experimental setup shown in Figure 8.16.

Recent research has explored the self-discharge characteristic of super-capacitors [144, 145, 146]. Ricketts and Ton-That [144] describes the self-discharge of super-capacitors in terms of two mechanisms: 1) the self-discharge due to Faradix impurity reactions; and 2) the current leakage through the double-layer at the electrolyte-carbon interface. It is analysed in their research that the first mechanism appears to dominate the self-discharge in the first 8 hours of the self-discharge. Merrett [146] argues that the traditional leakage current is not significant and the self-discharge phenomenon is in fact predominantly due to internal charge redistribution [146] which is also known as the dielectric relaxing

phenomenon. The effect of the redistribution can only be eased when the super-capacitor has been typically charged more than 2 hours. In Diab et al's research [145], the self-discharge of super-capacitors has been characterised through experiments, and the experimental results show that the self-discharge rate is affected by the factors including temperature and initial voltage across the super-capacitor.

8.7 Summary

This chapter describes the design and implementation of a passive RFID sensor node prototype. The design of the sensor node prototype uses a P2110 module to convert the RF energy harvested by the node antenna to DC energy. The converted DC energy then is accumulated using a super-capacitor. Once the super-capacitor has been charged to a threshold voltage V_{max}, a DC/DC converter provides a system voltage for supplying the sensor node circuit until the capacitor voltage drops to a low threshold voltage V_{min}. A low power microcontroller is used to sample and encode sensor measurements from a temperature sensor, and the microcontroller is programmed using C. The encoded signal is finally modulated by a backscatter modulator which is designed based on using an RF switch. The fabricated sensor node prototype has been tested at 915 MHz using a testing arrangement which primarily includes a NI myDAQ instrument and the PXI reader implementation presented in Chapter 7. The testing result shows that the sensor node prototype successfully achieves the functions of RF energy harvesting and transmitting sensor measurements through backscatter communication. Chapter 9 presents the implementation of a sub-soil sensor node based on using the fabricated sensor node prototype and also describes practical experiments for evaluating the the sub-soil sensor node performance in soil.

One of the key performance of the sensor node prototype is the charging time during which the super-capacitor voltage increases from the low threshold voltage V_{min} to the high threshold voltage V_{max}. The charging time performance has been evaluated by considering the power harvested by the sensor node, the sensor node antenna and the super-capacitor. The evaluation result shows that the measured charging time decreases with increasing power that is harvested by the sensor node antenna. The charging time measurement has an error bound

higher than 1 s when the harvested power is lower than -5.6 dBm. A large or a directional antenna helps shorten the charging time of the sensor node prototype. However, a large antenna will make the sensor node hard to deploy in practice, and a directional antenna can bring problems as the orientation of the sensor node within the soil is not controllable. Thus, there is a need to make a trade-off between the sensor node performance and size, as will be further discussed in Chapter 11. When choosing a super-capacitor for the sensor node design, there is a need to consider the capacitance and self-discharge of the super-capacitor. With the sensor node prototype, a low capacitance helps shorten the time for charging the capacitor to the threshold voltage V_{max}. However, a low capacitance limits the amount of the energy that can be used to supply the sensor node. Selecting an appropriate value of the capacitance is essential in the system design, which will be discussed in Chapter 11. A high self-discharge rate is not desirable as it leads to a high energy loss which affects the operation of the sensor node.

Chapter 9

Sub-soil Experiments

9.1 Introduction

The CST simulation results presented in Chapter 6 show that the loss in soil can be more than 50 dB/m and that the soil surrounding a sub-soil antenna affects the antenna return loss, efficiency and radiation pattern. However, there is always a concern that the soil models in the simulations do not match reality. In this research, a series of practical experiments have been performed to evaluate the sub-soil performance of the sensor node prototype. The design and implementation of the sensor node prototype have been presented in Chapter 8. The experiments are based on using the PXI-based RFID reader platform which has been described in Chapter 7. In the experiments, the charging time of the sensor node prototype and the power of the backscattered signal at the RFID reader antenna have been used as two parameters for the performance evaluation of the sensor node prototype. As described in Chapter 8, the charging time of the sensor node prototype refers to the time taken to charge the super-capacitor from the low threshold voltage V_{min} to the high threshold voltage V_{max}. Another objective of the experiments is to characterise the path loss in the soil. The variables being considered in the experiments are the height of the RFID reader antenna, the depth of the sensor node prototype and the soil moisture content.

In this chapter, Section 9.2 describes the experimental method for the performance evaluation and the path loss characterisation. A data logging system has been designed and implemented for recording the system voltages of the RFID sensor node prototype. The design and implementation of the data logging system

are presented in Section 9.3. Section 9.4 describes the experimental arrangement. Section 9.5 discusses considerations on the accuracy and repeatability of the experimental results presented in Chapter 10.

9.2 Experimental Method

9.2.1 Soil environment

Originally, there was a plan to carry out the experiments in an outdoor environment such as a farm. Within a farm, the sensor node would be buried underground and the reader platform would be located above the ground. However, the outdoor environments will be challenging to carry out. It is typically hard to get access to a mains power supply outdoors. High capacity batteries, such as an vehicle battery can be used to power the experimental equipment including the PXI system. However, the experiments can easily take a few weeks and the typical vehicle battery is only able to supply the PXI system for less than a day. Under adverse weather conditions, such as rain and wind, the experimental arrangement is vulnerable to mechanical and electrical damage. In addition, there can be a problem outdoors if the experimental equipment or the RFID sensor node prototype failed to work.

In this work, the experiments were performed in the Dyehouse, a laboratory which is located in the basement of the Sackville Street Building, at the University of Manchester. The Gardening Team of the University provided a soil planter whose size is 1 m $\times$ 1 m $\times$ 0.5 m (length $\times$ width $\times$ height). An important concern with the experiments in the Dyehouse is the size of the soil planter. According to the CST simulation results shown in Chapter 6, signal leakages can propagate along the side walls of the soil tank and arrive at the sensor node antenna rather than travelling through the soil directly. Therefore, a small size soil tank does not match reality and so can affect the fidelity of result. The CST simulation results also show that using RF absorbers around the soil tank surface leads to a negligible effect of power leakages when the side length of the soil tank size is greater than 1 m. Hence, four pieces of RF absorbers were attached to the side surfaces of the soil planter when performing the experiments.

9.2.2 Sensor node performance evaluation

The performance evaluation of the sensor node is based on the scenario shown in Figure 9.1. As shown in Figure 9.1, the sensor node prototype is deployed within the soil planter at a depth D and the antenna of the RFID reader platform, termed as the reader antenna, is located at a distance, H, above the soil surface. The sensor node prototype was enclosed within an enclosure. The enclosure creates an air gap for the sensor node antenna, which helps improve the antenna performance. In the experiments, the sensor node performance has been measured in the power link and the communication link. In the power link, the sensor node prototype harvested energy from Continuous Wave (CW) signals that were generated by the RFID reader platform, and the charging time of the sensor node was measured. In the communication link, the sensor node transmitted sensor measurements using backscatter modulation. The reader platform received and down-converted the backscattered signals arriving at the reader antenna, and measured the signal power. The following parameters have been considered in the experiments:

- the transmission power of the RFID reader platform,
- the depth of the sensor node within the soil,
- the orientation of the reader antenna,
- the height of the reader antenna above the soil surface,
- the soil compactness,
- the soil moisture content,

where the transmission power, the depth of the sensor node and the soil moisture content are the variables for the experiments. In the experiments, the reader antenna was positioned parallel to the soil surface and the height of the reader antenna was maintained at 0.5 m above the soil surface. According to Equation 2.1, this height ensures the soil planter to be within the far-field of the reader antenna at 915 MHz. It was desired to maintain the soil compactness throughout the experiments. However, controlling the soil compactness is difficult, as discussed in

Section 9.5. In order to compare the sensor node performance in the soil with its performance in air, the performance evaluation of the sensor node was also performed when the soil planter was not filled with soil. The performance evaluation in air has considered two variables: the transmission power of the RFID reader platform and the distance between the reader antenna and the sensor node.

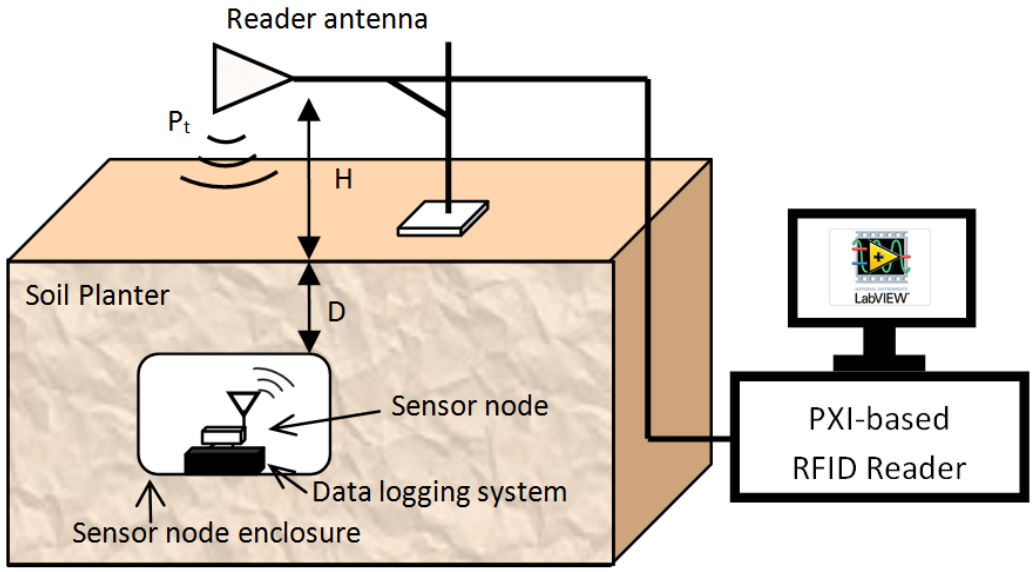

Figure 9.1: Diagram of the experimental arrangement.

As described in Chapter 8, the charging time of the sensor node prototype is measured from the system voltages of the sensor node, and the voltage signals are recorded by the NI myDAQ instrument. In the experiments, it is not desirable to wire the sensor node prototype to a device outside the soil planter for recording the prototype system voltages. The wires connecting the prototype and the device would provide a leakage path between the reader antenna and the sensor node antenna, and this affects the fidelity of measurements. Instead, the method of measuring the charging time is based on using an independent data logging system, shown in Figure 9.1, which is interfaced and attached to the sensor node prototype. During the experiments, the sensor node prototype was deployed within the soil planter along with the data logging system. The data logging system continuously sampled the sensor node's system voltages, and stored the voltage samples onto a standard Secure Digital (SD) card. The data logging system was powered using an on-board battery. The data logging system

and the sensor node prototype were electrically isolated using a voltage buffer with a high input resistance. When the experiments were completed, the system was retrieved from the soil and the experimental data was exported from the SD card to a PC for data processing and analysis. Details of the design and implementation of the data logging system are described in Section 9.3.

9.2.3 Path loss characterisation

The path loss in this work refers to the overall power losses of the RF signal propagating from the the reader antenna to the sub-soil sensor node antenna. The generic method of calculating the path loss between the antennas is based on using the Friis equation [81]:

$$P_{loss}(dB) = P_t(dB) + G_t(dB) + G_r(dB) - P_r(dB), \tag{9.1}$$

where P_t is the transmit power of the RFID reader platform, G_t refers to gain of the reader antenna gain (measured in air), G_r refers to the gain of the sensor node antenna (measured in air) and P_r is the power harvested by the sensor node. The transmit power P_t is configurable on the reader platform, and the gains of the reader antenna and the node antenna are specified by the antenna manufacturers. But there is a problem in measuring the harvested power, P_r which would typically be measured with an RF cable connection between the node antenna and a VNA. As discussed in the previous subsection, there is a possibility that a leakage path could be caused by a cable connecting the sensor node prototype and a device outside the soil planter. Instead, the power harvested by the sensor node was deduced from the measured charging time of the sensor node. As described in Chapter 8, the charging time of the sensor node prototype has been used as a parameter to evaluate the performance of the sensor node prototype. The plot of the measured charging time versus the power harvested by the sensor node prototype is presented in Figure 8.14. The experiments have compared the characterised path loss in soil and in air. The path loss in soil has been evaluated by considering the height of the reader antenna, the depth of the sensor node and the soil moisture content.

9.3 Data Logging System

As described in Section 9.2, the data logging system is buried along with the sensor node prototype, and is capable of sampling the system voltages of the sensor node prototype and writing these samples to a standard SD card. This section describes the details of the system design as well as its implementation.

9.3.1 System requirements descriptions

- **The system must have an operating time of more than a week** - Once the data logging system has been buried within the soil planter, it is not easy to retrieve it from the soil for replacing or charging the battery. So the system must have an operating time of more than one week, as this period will allow a series of experiments to be conducted without the need to frequently replace the batteries.

- **The system must be electrically isolated from the sensor node** - When sampling the system voltages of the sensor node prototype, there could be a current leakage flowing into the data logging system from the sensor node. This current leakage is not desirable as it would distort the charging time measurements. The data logging system must have a high input resistance in order to minimise the current leakage to less than 1 nA.

- **The system must be able to keep track of time in order to provide timestamp information along with the voltage samples** - The data logging system can continuously perform data recording in the soil over a period of a week. The timestamp information provides a convenient way to locate the corresponding item of data within a series of experiments. During the experiments, the data logging system must not miss an item of data. This can be indicated from the timestamp information.

- **The system must be able to store all of the data sampled over the experimental period** - The SD card must have a sufficient size to store all of the data over the experimental period. The required size, S_m (Byte) of the SD card is estimated as:

$$S_m = f_s \times Length \times Days \times 86400, \tag{9.2}$$

where f_s is the sampling frequency in Hz, *Length* is the number of bytes in measurement data point, *Days* represents the number of days for which the experiments will last, and 86400 refers to the number of seconds per day.

9.3.2 System design

Figure 9.2 presents the block diagram of the data logging system design where a battery is used to power the data logger with a system voltage V_b. The system voltages of the sensor node, V_{cap} and V_{out} are sampled using a microcontroller. Two voltage buffers are used in the design to provide high input resistance and to electrically isolate the sensor node prototype and the system. A Real-Time Clock (RTC) is used to achieve time keeping, and the time information is read from the RTC by the microcontroller. The sampled data from the sensor node and the corresponding time information are combined to a data packet on the microcontroller. All data over the course of the experiments are written to a standard removable SD card.

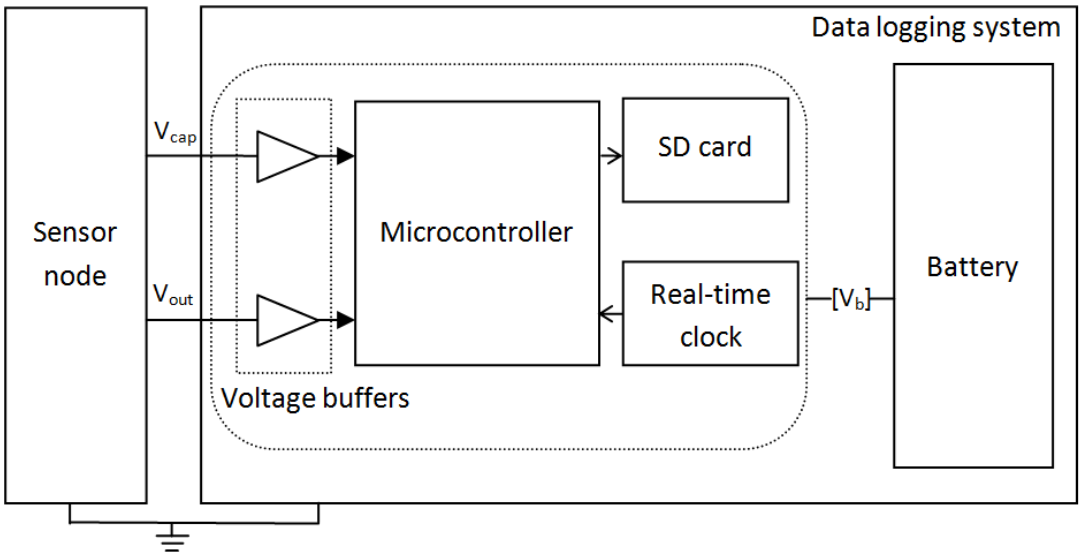

Figure 9.2: Digram of the data logging system design.

9.3.3 System hardware implementation

Figure 9.3 presents a photograph of the implemented system hardware, where the system PCB stacks on an EVE ER34615 Lithium battery cell [147], and the sensor node prototype PCB is fixed to the data logging system PCB. The system PCB size is determined by the physical size of the battery, and the stacking structure aims to minimise the horizontal area of the system hardware. The battery's nominal voltage is 3.6 V. The key feature of the battery is that it has an energy capacity of 19 Ah [147] which is higher than most off-the-shelf batteries with the same physical size. Two photographs of the data logging system PCB are shown in Figure 9.4 and the schematics of the PCB design can be found in Appendix G.

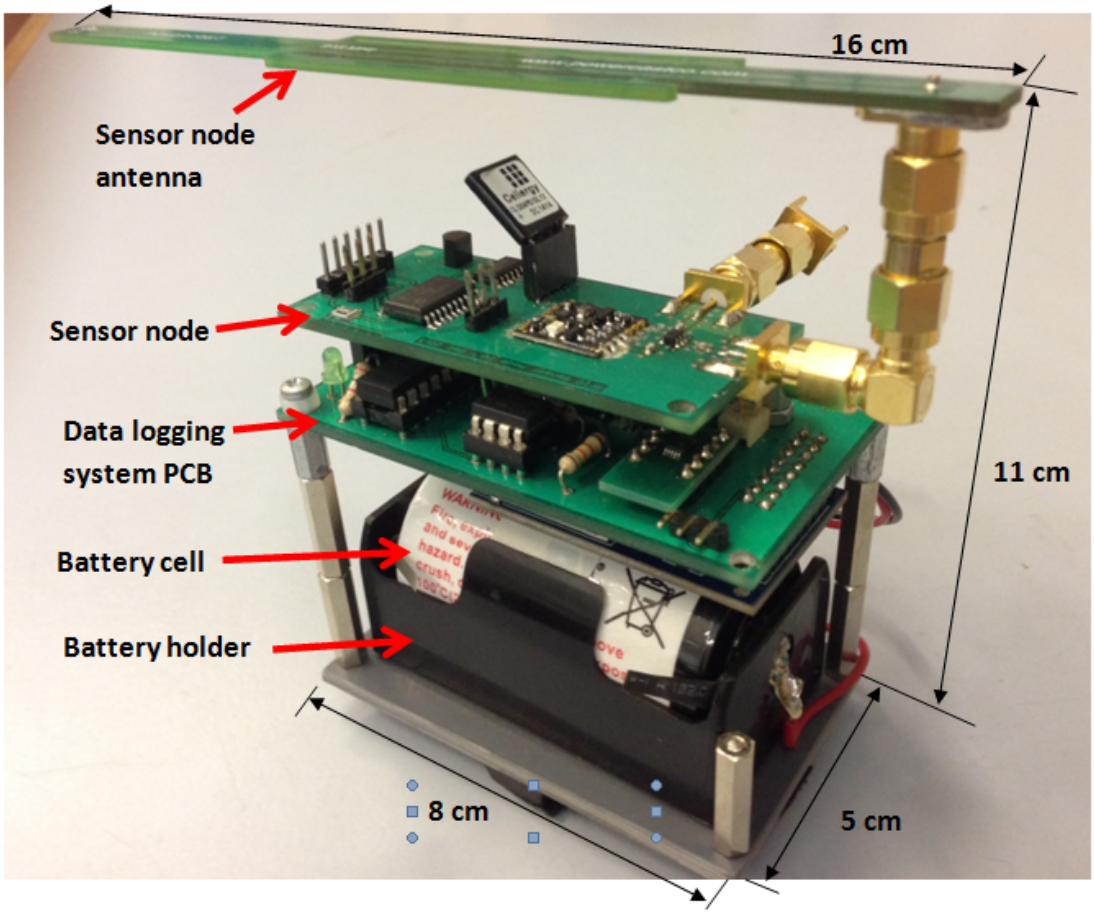

Figure 9.3: Photograph of the data logging system with the sensor node.

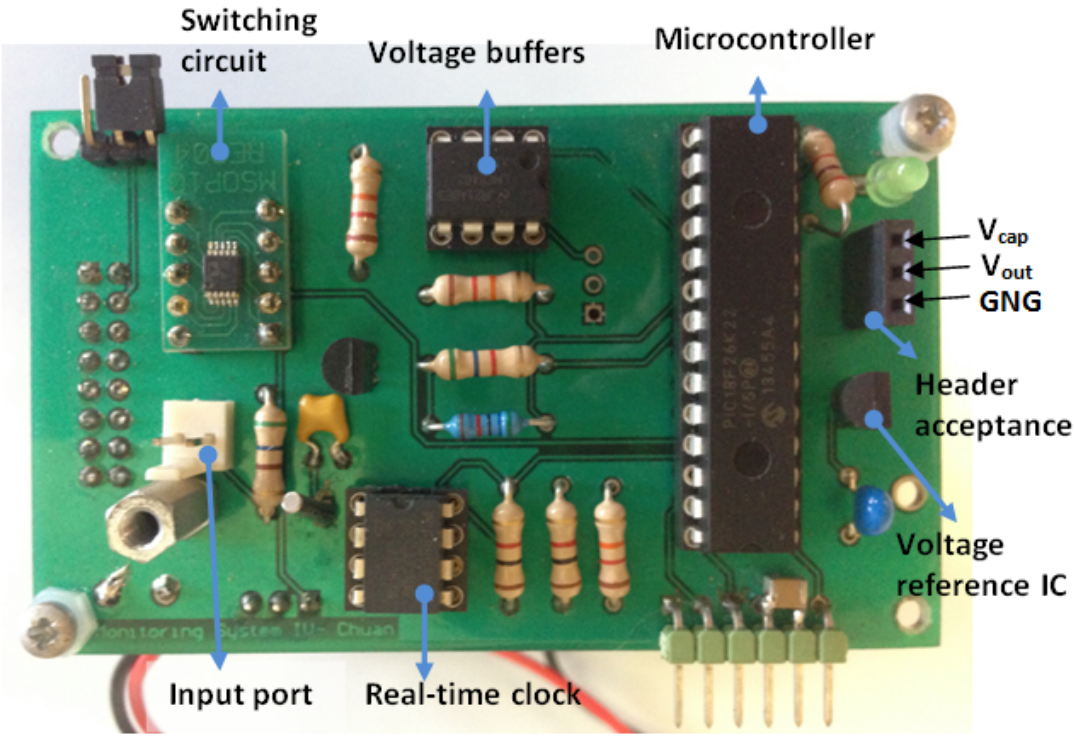

(a) Data logging ystem PCB (front).

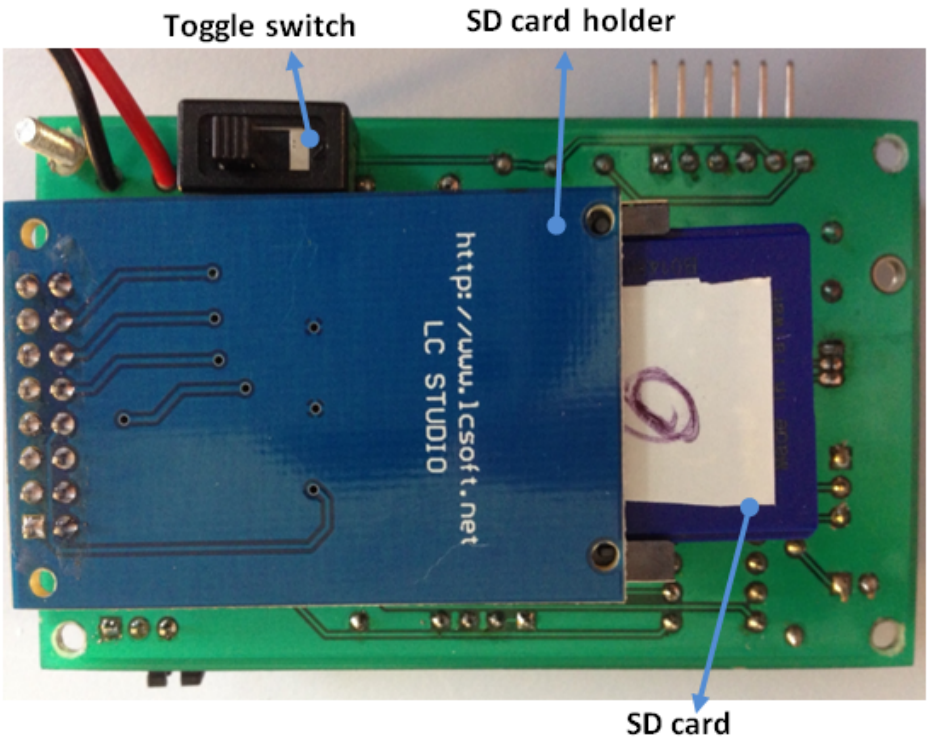

(b) Data logging system PCB (back).

Figure 9.4: Photograph of the data logging system PCB.

As shown in Figure 9.4a, the voltage outputs of the sensor node are linked to the inputs of the voltage buffers through a three-pin header acceptance. As the core component in the system, a Microchip PIC18LF26K22 microcontroller [148] implements data sampling using two in-built ADC channels to convert the sampled voltages to digital signals. Since the system voltage V_b that is provided by the battery can slightly drop with the discharge of the battery, a MCP1525 [149] precision voltage reference IC is used to provide the ADC channels with a constant positive reference, 2.5 V, and the negative reference is grounded, 0 V. There are two reasons for selecting the 2.5 V reference IC, which are that:

- its reference voltage covers the range of the super-capacitor voltage, V_{cap}, of the sensor node prototype;
- it can be supplied by the battery voltage, V_b without the need to use DC/DC converters.

With the selected precision voltage reference IC, there was a concern that the system voltage, V_{out} of the sensor node ranges up to 3.3 V which exceeds the provided reference voltage. Hence, a voltage divider has been designed using two 10 MΩ resistors to halve the buffered system voltage, V_{out}. The halved voltage is sampled by the in-built ADC of the microcontroller. When processing the experimental data, the system voltage has been recovered in software by doubling the logged value. The implementation of the voltage buffer is based on using a unity gain amplifier. The operational amplifier being selected in this work is the Texas Instruments LMC 6462 [140]. This amplifier has a typical input resistance greater than 10 TΩ [140], and is single-supplied by the battery voltage V_b without the need of employing DC/DC converters.

The microcontroller logs time information from an NXP PCF 8563 Real-Time Clock (RTC) [150]. Data is transferred between the microcontroller and the RTC serially via a two-line bidirectional Inter-Integrated Circuit (I2C) bus. A Transcend 2 GB SD card [151] is connected to the microcontroller through the Serial Peripheral Interface (SPI) buses. A switching circuit is designed using an ADG 804 multiplexer [152]. It is controlled by the microcontroller to power off the SD card when the system is implementing data sampling, and it only switches on the power when writing data to the SD card. This design helps to reduce the

average power consumption of the system and to maximise the system's operating lifetime. The data logging system is manually powered on and off through a toggle switch mounted on the back of the PCB. When the PCB has been powered on, the system only starts data sampling once its input port has received a rising edge triggering signal from an external device such as a NI myDAQ instrument.

9.3.4 System software implementation

A C program running on the microcontroller controls the data logging system, and the program is compiled using MPLAB Integrated Development Environment (IDE) toolkit [135]. All files that have been created for programming the microcontroller are included in Appendix H. The flowchart of the C program is shown in Figure 9.5. When the data logging system has been powered on, the program configures and initialises Input/Output (I/O) ports of the microcontroller. These ports are primarily used for sampling the system voltages of the sensor node, communicating with the RTC and the SD card, and accepting the triggering signal. Once a triggering signal has been received, the RTC is initialised and then starts keeping time. Inside the loop of data sampling, the program firstly fetches the voltage samples from the two ADC channels and then reads the time information from the RTC based on using the I2C communication protocol.

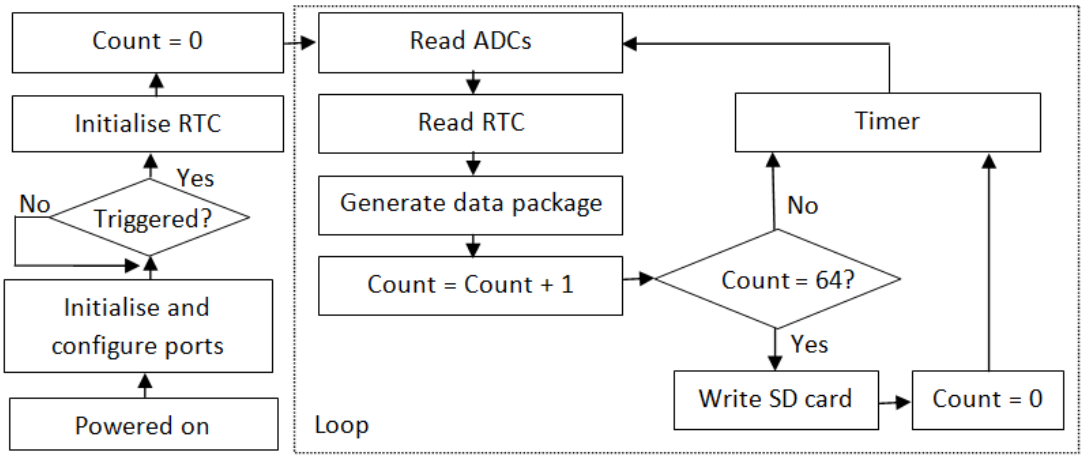

Figure 9.5: Flow diagram of the data logging system program.

The basic time information includes four elements: days, hours, minutes and seconds, and each element accounts for 1 byte. Before taking the next sample, a data packet is generated in the program by combing the two samples from the ADCs and the time information from the RTC. Figure 9.6 presents the format of a data packet whose overall length is 8 bytes, where the first 4 bytes are time information and the next three bytes are two 10-bit samples from the ADCs. The final byte is a pre-set symbol in the program, and it is designed for differentiating two neighbouring data packets.

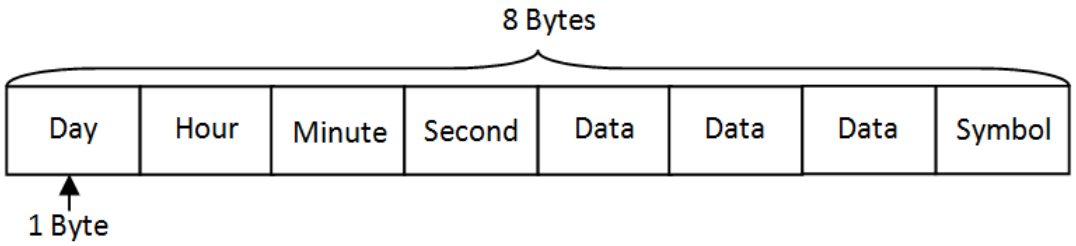

Figure 9.6: Format of a data packet.

An internal timer in the microcontroller is used to control the frequency of sampling data. The selection of the sampling frequency is based on a trade-off between the system power consumption and the system capability. A higher sampling frequency enables the system to perform more precise data sampling, but it always leads to the microcontroller consuming more power. The sampling frequency being used in this work is 10 Hz, which leads to an acceptable power consumption that enables the data logging system to constantly operate for more than a week. The sampling frequency of 10 Hz will be sufficient for sampling the system voltages of the sensor node prototype as both the charging time T_c and discharging time T_d of the sensor node described in Chapter 8 are longer than a second.

According to the SD specification [153], the SD card should be written to with blocks of data, which are 512 bytes long. Thus, the generated data packet (8 bytes) is temporarily stored in the internal memory of the microcontroller, and they will be written to the SD card when 64 data packets have been generated. The program for writing to the SD card based on SD Specification version 1.00 [153]. The microcontroller is required to run at its maximum frequency of 16 MHz in order to minimise the time for writing data to the SD card.

However, running at a high frequency leads to the microcontroller consuming a large amount of power, which shortens the operating lifetime of the system. In this implementation, the microcontroller runs at 16 MHz only for writing to the SD card, and the frequency is then switched to 1 MHz for sampling data and processing data. The scheme of switching between the two frequencies aims to maximise the operating lifetime of the data logging system.

Before writing data to an SD card, there is the typical need to format the SD card based on using a formatting protocol, such as FAT32 which is recognised by Windows Operating System (OS). This allows the stored data on the formatted SD card can be read from files that are visible in Windows OS. However, the implementation of the program for formatting SD cards by the microcontroller can require a few months of effort. In this work, the SD card being used is not formatted and data is written to the card in RAW format. Writing data in RAW format means that Windows OS cannot directly recognise the data that is stored on the SD card. So a software program, HxD - Freeware Hex Editor and Disk Editor [154] is used to get access to the card's memory. Figure 9.7 presents a screenshot of the software user interface showing the stored data packets and the corresponding addresses of the card's memory. Using the software, the stored data can be selected over a range of addresses, and the selected data can be exported to a '.txt' file for data processing. The SD card has a size of 2 GB. Given that the sampling frequency is 10 Hz and the number of bytes in a data packet is 8, the 2 GB SD card enables the data logging system to store the sampled data over 2485 days. This period is calculated according to Equation 9.2.

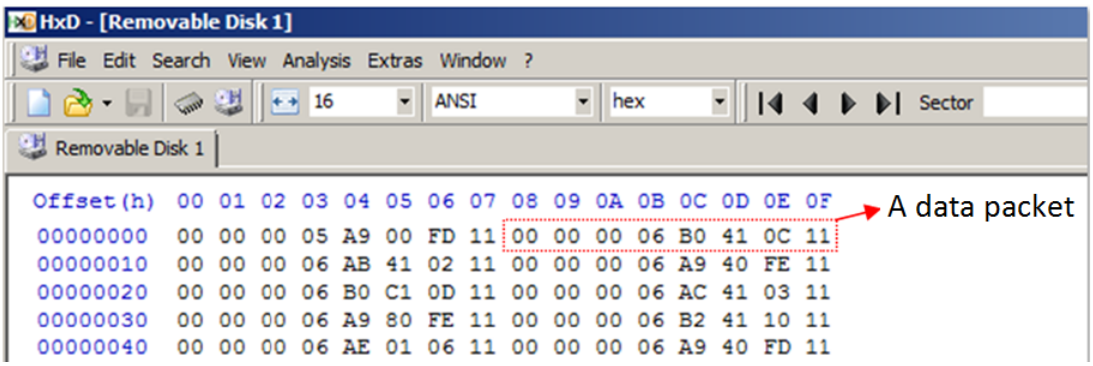

Figure 9.7: Screenshot of the HxD disk editor.

9.4 Experimental Arrangement

The design of the PXI-based RFID reader platform has been described in Chapter 7, and the performance testing of the sensor node prototype using the RFID reader platform is presented in Chapter 8. In the experiments, the path loss in the soil limited the energy that can be harvested by the sensor node. Therefore, a Mini-Circuit ZHL-1000-3W+ RF amplifier [155] has been used to increase the transmit power. Figure 9.8 presents the block diagram of the reader platform implemented for the experiments.

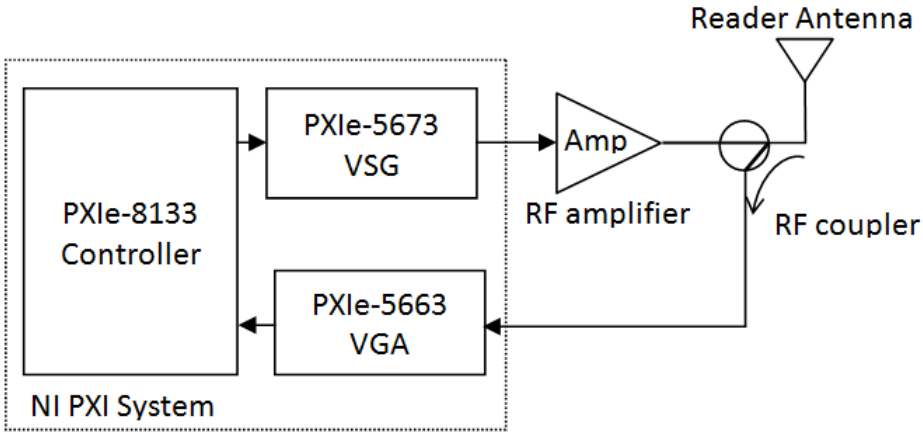

Figure 9.8: Block diagram of the RFID reader platform in the experiments.

As shown in Figure 9.8, the ZHL-1000-3W+ amplifier amplifies the signal output of the PXIe-5673 Vector Signal Generator (VSG), and the amplified signal is transmitted through the reader antenna [138]. The amplifier is powered using an independent power supply unit with a supply voltage of 24 V. Signals received by the reader antenna are coupled to the PXIe-5663 Vector Signal Analyser (VSA) using a Mini-Circuit ZEDC-15-2B Directional RF coupler [139]. The reader platform is controlled by LabVIEW software running on the PXIe-8133 controller. The details of the RF coupler, the RF amplifier and the reader antenna are shown below.

1. Mini-Circuit ZEDC-15-2B Directional Coupler
    - 1 MHz to 1000 MHz frequency range
    - 15 dB coupling factor

2. Mini-Circuit ZHL-1000-3W+ High Power Amplifier
    - 500 MHz to 1000 MHz frequency range
    - 40.5 dB gain (measured at 915 MHz)
    - +37 dBm output power at 1 dB compression
3. Cellular Patch Antenna (PATCH-A0007-01)
    - 8 dBi gain
    - 70 degree beamwith
    - Linear polarisation

With the RFID reader platform, the transmission power P_{out} that is transmitted out from the reader antenna is expressed as:

$$P_{out}(dB) = P_t(dB) + G_{amp}(dB) + G_{ant}(dB) - P_{lt}, \tag{9.3}$$

where P_t is the transmit power of the VSG, G_{amp} and G_{ant} are the gains of the amplifier and the reader antenna, and P_{lt} is the cable loss and the insertion loss of the RF coupler. The power of the backscattered signal P_{in} arriving at the reader antenna can be expressed as:

$$P_{in}(dB) = P_r(dB) + C(dB) - G_{ant}(dB) + P_{lr}, \tag{9.4}$$

where P_r is the signal power measured at the VSA, C is the coupling factor of the RF coupler, G_{ant} is the gain of the reader antenna and P_{lr} refers to the cable loss in the receiving path.

During the process of preparing the experimental arrangement, the size of the sensor node enclosure was a key consideration. The CST simulation results presented in Chapter 6 show that the soil affects the return loss of the sub-soil antenna and that increasing the sensor node enclosure size helps reduce the effect of the soil. As shown in Figure 6.9, the simulated return loss of the sub-soil antenna, at 900 MHz, is comparable to the measurements in air when the air gap between the sub-soil node antenna and each inner surface of the sensor node enclosure is greater than 2 cm. In this work, the implemented sensor node enclosure is made of a PVC material (lossless to the RF signals at 900 MHz), and its shape has

been designed as a cube with a side length of 17 cm (excluding the thickness of the enclosure walls). Figure 9.10 presents a photograph showing that the sub-soil node is placed diagonally across the implemented sensor node enclosure. The minimum air gap between the node antenna and each inner side-surface of the enclosure g_{min}, shown in Figure 9.11, is 2.5 cm. As shown in Figure 9.3, the overall height of the sub-soil node, including antenna, is 11 cm , and therefore the air gap between the node antenna to the inner top-surface of the enclosure is 6 cm. The thickness of the enclosure walls is 5 mm, which makes the enclosure strong enough to withstand the pressure from the soil. The enclosure is covered by a lid with a waterproof design, and it was also sealed using water-proof tape before deploying it into the soil.

Before deploying the sub-soil node in the soil planter for the performance evaluation, the RTC of the data logging system was initialised and synchronised in time with the RFID reader platform. This process was aiming to match the time stamps of the recorded data packets to the corresponding experiments. Figure 9.9 shows the arrangement for initialising the RTC of the data logging system. The myDAQ instrument shown in Figure 9.9 was interfaced to the input port of the data logging system. The PXIe-8133 controller was used to control the myDAQ instrument to send a triggering signal to initialise the RTC of the data logging system. At the same time, the controller recorded the actual time at its internal clock when the signal was sent. Once the data logging system received the triggering signal, the RTC started keeping time from 00/00/00/00 (days/hours/minutes/seconds).

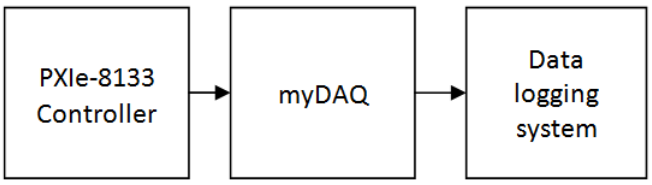

Figure 9.9: Simplified diagram of the arrangement for initialising the RTC of the data logging system .

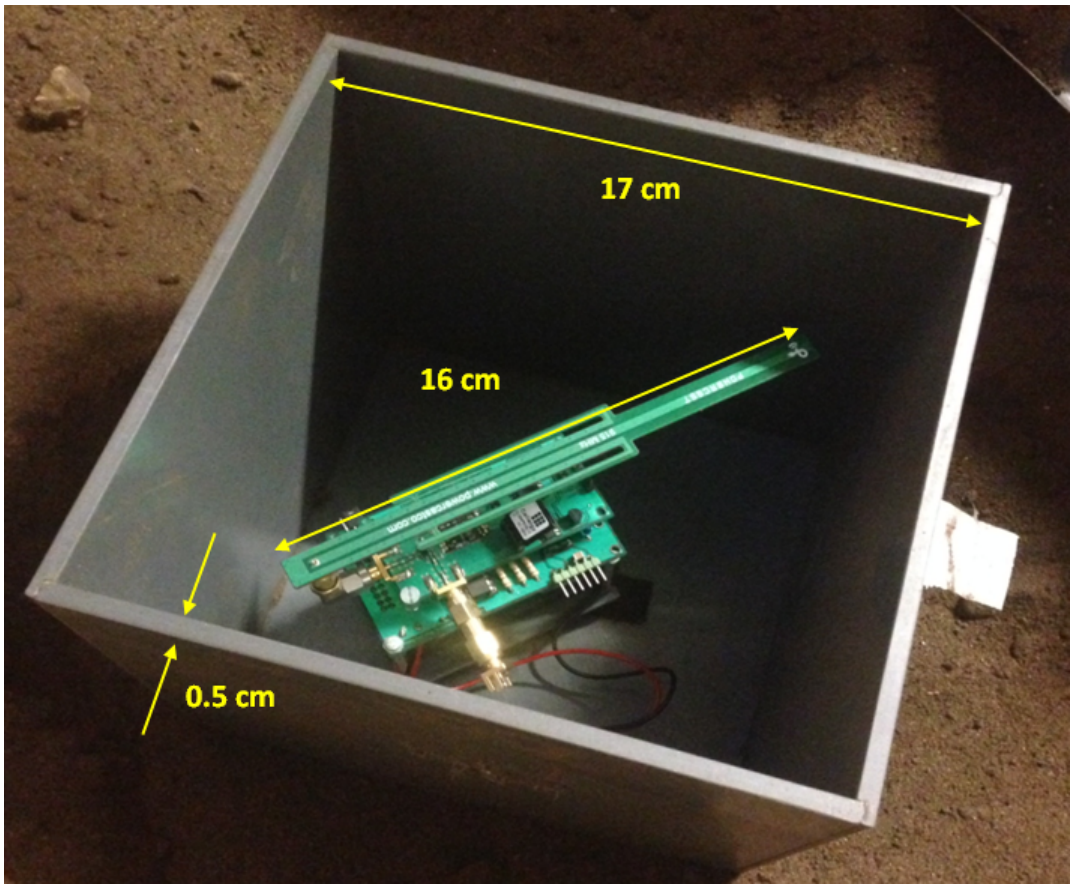

Figure 9.10: Photograph of the sub-soil sensor node - before burying.

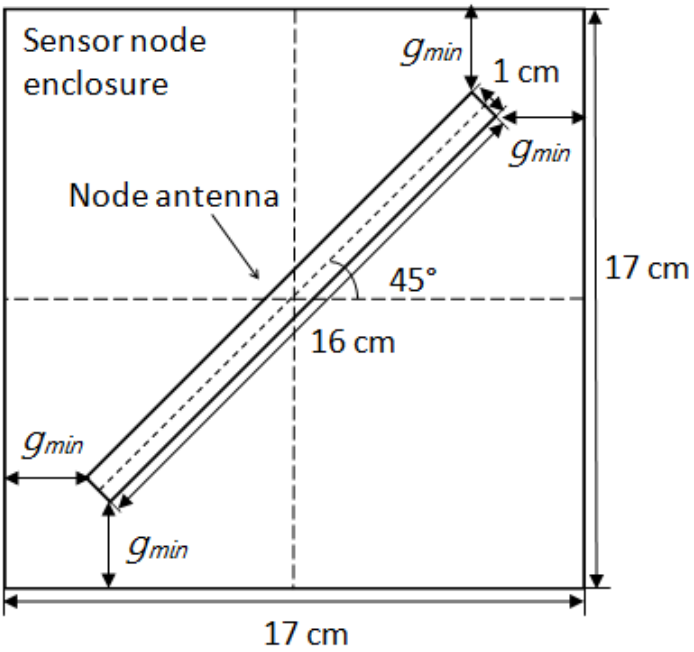

Figure 9.11: Schematic diagram showing the top view of the sub-soil node within the sensor node enclosure.

In the experiments, the sensor node performance was firstly evaluated in air and then in soil. Figure 9.12 presents the simplified diagram of the experimental arrangement for the performance evaluation in air. The node enclosure was fixed at the bottom of the empty soil planter. The propagation distance shown in Figure 9.12 refers to the vertical distance between the reader antenna and the top surface of the node enclosure, which has been varied from 0.5 m to 0.9 m in increments of 0.05 m.

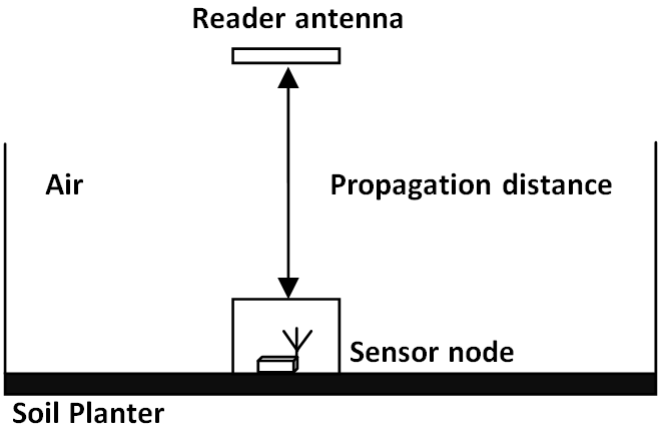

Figure 9.12: Simplified diagram of the experimental arrangement for evaluating the sub-soil system performance in air.

When completing the experiments for the performance evaluation of the sensor node in air, the dry soil was shovelled into the soil planter without displacing the node enclosure. Figure 9.13 presents the simplified diagram of the experimental arrangement for the performance in the soil. The reader antenna was placed parallel to the soil surface and the RF signal was transmitted downwards. The height of the reader antenna was always maintained at 0.5 m above the soil surface. The depth of the sub-soil node refers to the vertical distance between the soil surface and the top surface of the node enclosure. The depth of the sub-soil node has been varied from 0 m to 0.4 m in increments of 0.05 m. At a given depth, the corresponding propagation distance is: depth + 0.5 m, which ranges from 0.5 m to 0.9 m with increasing depth from 0 m to 0.4 m. The 0 m depth represents a scenario where the node is just inserted into the soil and there is no soil above its top surface. Figure 9.14 shows the simplified diagram of the experimental arrangement when the depth of the sensor node is 0 m, where the propagation distance equals to the height of the reader antenna.

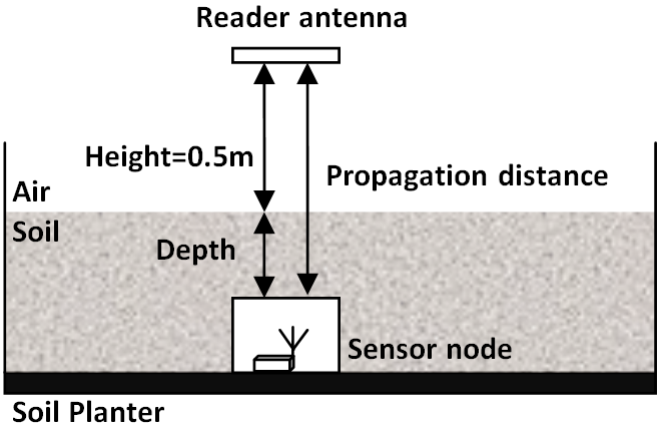

Figure 9.13: Simplified diagram of the experimental arrangement for evaluating the sub-soil system performance in the soil.

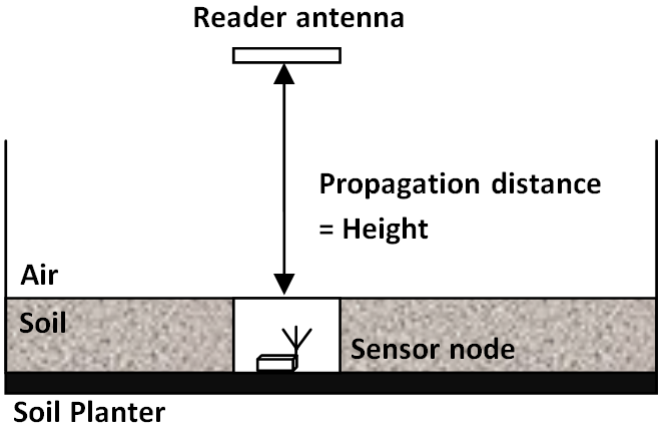

Figure 9.14: Simplified diagram of the experimental arrangement when the depth of the sensor node is 0 m.

The experiments have considered two soil moisture levels: dry and wet. The sensor node performance was firstly evaluated in the dry soil. The dry soil was then watered with approximately 15 L of water for evaluating the sensor node performance in the wet soil. With the size of the soil planter, this volume of water is far more than the typical amount for gardening purposes, for example watering flowers. Figure 9.15 presents a photograph of the experimental arrangement in the Dyehouse laboratory where the reader antenna is installed on a clamp stand above the soil planter and the antenna height is varied through adjusting the clamp.

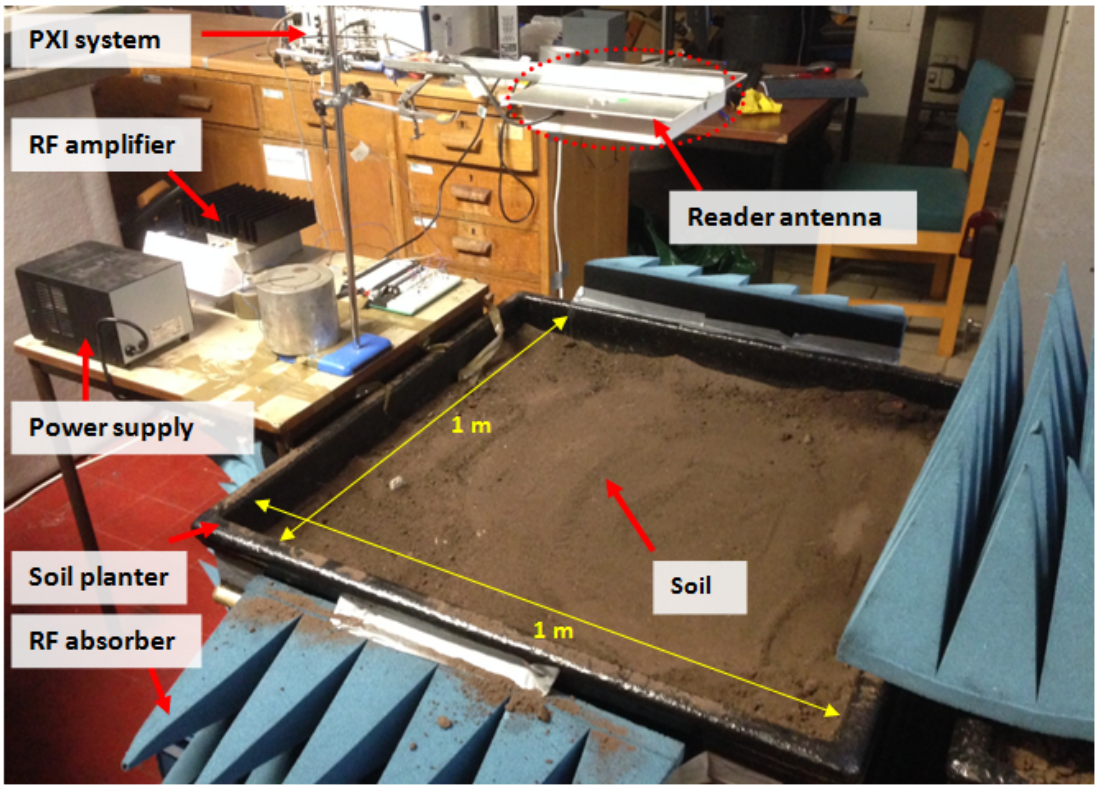

Figure 9.15: Overview of the experimental setup in a laboratory.

The performance evaluation of the sensor node is based on using variable transmission power up a maximum Effective Radiated Power (ERP) of 2 watts, according to the Office of the communications (Ofcom) regulations [156]. A LabVIEW program has been implemented for the performance evaluation, and Figure 9.16 presents the flowchart of the LabVIEW program. The RFID reader platform was controlled by the LabVIEW program to sweep the transmit power with an increment of 1 dBm. At each transmit power, the RFID reader platform was controlled to detect the backscattered signal from the sub-soil node. Once a backscattered signal was detected, the signal power was measured and recorded locally. The transmit power increased to the next level when this power had been maintained for 500 s or the backscattered signal from the sub-soil node had been detected times. Once this power sweep was completed the experimental arrangement was then changed by varying the distance between the reader antenna and the sensor node antenna, the the depth of sensor node, or the soil moisture content.

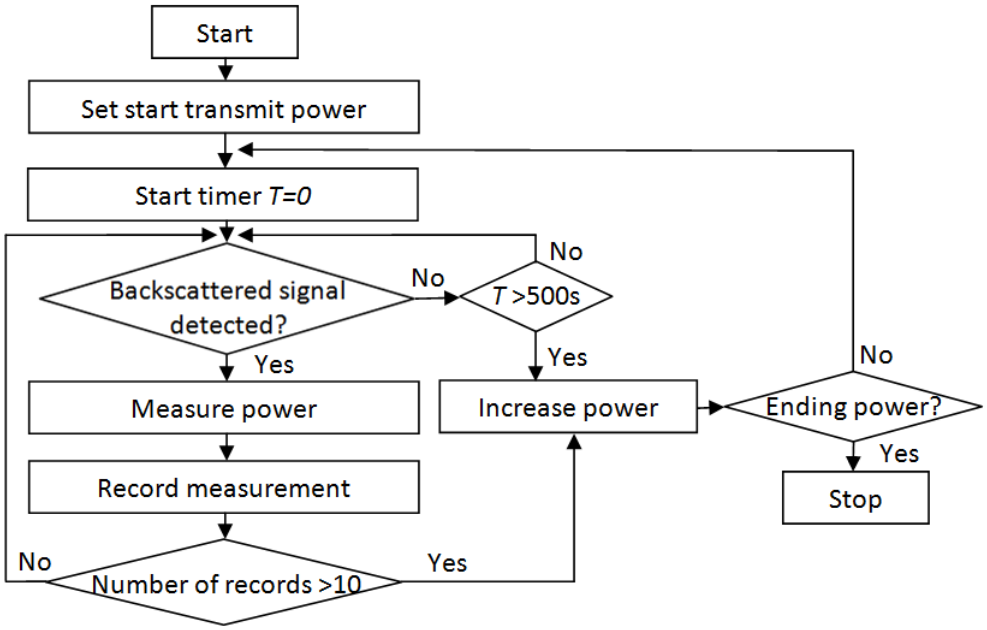

Figure 9.16: Flowchart of the LabVIEW program for the experiments.

9.5 Accuracy and Repeatability of Measurements

With the experimental arrangement shown in Figure 9.13, the method of increasing or decreasing the depth of the sensor node is based on shovelling a certain amount of soil into or out of the soil planter. The soil surface should be of equal depth across the soil planter, which means that the soil surface is parallel to the bottom of the planter. In the experiments, the depth of the sensor node and the height of the reader antenna were manually measured using a tape measure. The author found that the accuracy of either these measurements was within $\pm$ 1 cm. This was primarily due to the difficulty in validating that the top surface of the node enclosure, the soil surface and the bottom surface of the reader antenna were parallel to each other.

The reader antenna is a directional antenna. In the experiments, a slight change of the antenna's orientation or position affected the power of RF signal arriving at the sub-soil sensor node, and therefore affecting the experimental results. A fixed antenna orientation was desirable over the duration of experiments in order to minimise the affect of the changing antenna orientation. However,

the reader antenna was frequently repositioned on the clamp stand in the experiments for adjusting the antenna height with increasing or decreasing soil surface. When reinstalling the antenna to the clamp stand, it was difficult to validate the repeatability of the antenna's orientation. The effect of the reader antenna orientation has been evaluated in the experiments. With the experimental arrangement shown in 9.12, the author has removed the reader antenna from the clamp stand, and then installed the antenna on the clamp stand at the same position. This process has been repeated 5 times. A spirit level was used to ensure that the reader antenna is parallel to the soil surface. The experimental results indicate that the characterised path loss has an error bound within ± 0.5 dB.

The soil compactness and moisture content are also two concerns. The soil compactness within the soil planter can potentially affect the experimental results. In the experiments. there were limited equipment and methods available for measuring how compact the soil was. Moreover, the soil within the soil planter was watered in the experiments for evaluating the system performance in the wet soil. However it was difficult to validate that the soil moisture content was uniformly distributed at the depth from 0 m to 0.4 m.

The repeatability of the experimental results have been studied by repeating the sensor node performance evaluation and evaluating the error bars for the experimental results. In the experiments, the RFID reader platform has been controlled to sweep the transmission power from the reader antenna at a given depth of the sub-soil node. This process has been repeated 10 times by re-running the LabVIEW program described in Section 9.4. The sensor node performance was firstly evaluated with increasing depth from 0 m to 0.4 m. The performance evaluation was then repeated by decreasing depth from 0.4 m to 0 m. Before measuring the depth of the sub-soil node and the height of the reader antenna, the soil surface was repeatedly patted using a shovel. This method was seeking to maintain the soil compactness throughout the experiments and also to flatten the soil surface. After watering the soil within the soil planter, the watered soil has been left for 3 days before undertaking the performance evaluation of the sensor node. This process allowed the soil moisture becoming more uniformly distributed across the soil planter. Figure 9.17 presents two photos comparing the measurements of the dry soil conductivity and the wet soil conductivity using

a HI 98331 direct soil conductivity meter [157], where the measured conductivity in the wet soil is 0.08 mS/cm and the measurement in the dry soil is 0 mS/cm.

(a) Measured conductivity in the dry soil. (b) Measured conductivity in the wet soil.

Figure 9.17: Measured conductivity in the dry soil and the wet soil.

9.6 Summary

This chapter describes the experiments for the sensor node performance evaluation as well as the path loss characterisation. The charging time of the sensor node and the power of the backscattered signal from the sensor node were used as performance indicators for these experiments. The path loss characterisation was based on deducing the power harvested by the sensor node. The following variables have been considered in the experiments: the transmission power of the reader platform, the distance between the reader antenna and the sensor node antenna, the depth of the sensor node and the soil moisture content. The design and implementation of a data logging system have been presented. The implemented data logging system was deployed along with the sensor node in a

soil planter. The data logging system recorded the system voltages of the sensor node without the need of a wire connecting the sensor node to an external device outside the soil planter. The details of the experimental arrangement have been described. During the process of performing the experiments, the experimental results were affected by a range of factors and these factors have been analysed. A study of the accuracy and repeatability of the experimental results has been conducted based on repeating the sensor node performance measurements and evaluating the error bars. The experimental results are presented and analysed in Chapter 10.

Chapter 10

Experimental Results and Analysis

10.1 Introduction

This chapter presents the experimental results from the experiments described in Chapter 9. Section 10.2 presents the results of the sensor node performance evaluation in air and in soil. Section 10.3 presents the analysis of the results of the path loss characterisation, where the characterised path loss in the soil is compared to the results in air. The effect of the soil moisture content on the path loss is also presented and analysed. The results imply that there is a near-field coupling effect between the reader antenna and the sub-soil sensor node antenna. Section 10.4 describes the investigation of the existence of the near-field coupling effect through an experiment, and presents an analysis of the results obtained.

10.2 Sensor Node Performance Evaluation

As described in Chapter 9, the charging time of the sensor node and the power of the backscattered signal from the sensor node were used for the performance evaluation of the sensor node. With the sensor node prototype presented in Chapter 8, the charging time of the sensor node refers to the time when the super-capacitor is charged from the low threshold voltage V_{min} to the high threshold voltage V_{max}. In the experiments, the data logging system, presented in Section 9.3, was used to measure the charging time of the sensor node. The PXI-based RFID reader platform, presented in Chapter 7, was used to measure the power of the backscattered signal.

10.2.1 Performance evaluation in air

Firstly, the sensor node performance has been evaluated in air. In Chapter 9, Figure 9.12 shows the simplified diagram of the experimental arrangement for the performance evaluation in air, where the node enclosure was fixed at the bottom of the soil planter and the soil planter was not filled with soil. The two variables being considered in the experiments were the transmission power radiated from the reader antenna and the propagation distance between the reader antenna and the sensor node.

Figure 10.1 and Figure 10.2 present the measured charging time and the power of the backscattered signal with increasing transmission power at a propagation distance of 0.7 m. With increasing power from 21.5 dBm to 26.5 dBm, the charging time of the sensor node drops from approximately 65 seconds to 20 seconds, and the backscattered power is increased by 10 dB. The experimental results shown in Figure 10.1 and Figure 10.2 are expected. With a fixed path between the reader antenna and the sensor node, a higher transmit power increases the signal power arriving at the sensor node and so results in a shorter charging time as well as a higher signal power backscattered from the sensor node.

The propagation distance is another factor which affects the sensor node performance. Figure 10.3 and Figure 10.4 present the plots of the measured charging time and the measured power of the backscattered signal as a function of the propagation distance at the transmission power of 23.5 dBm. It is observed that

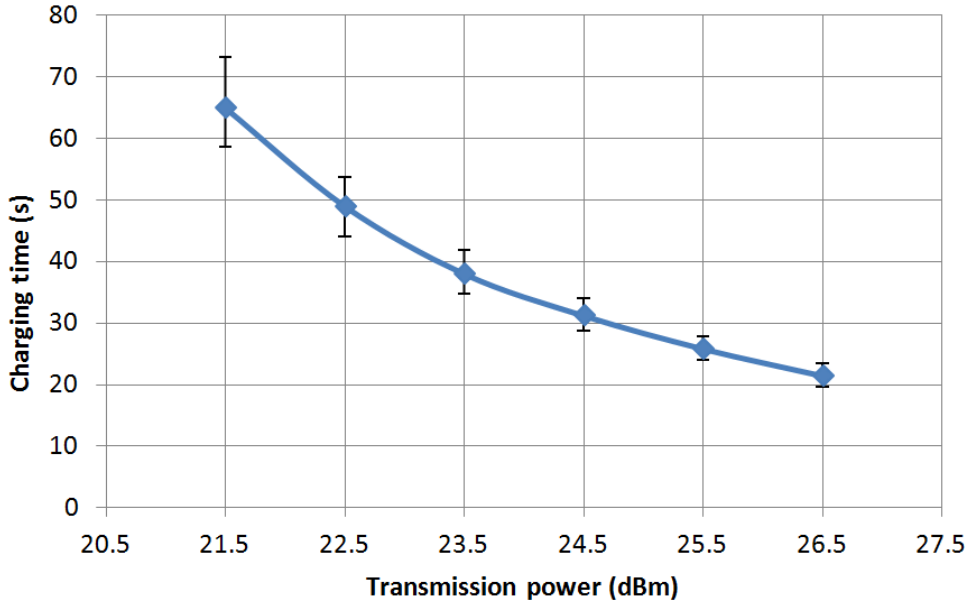

Figure 10.1: Measured charging time of the sensor node with increasing transmission power in air at a propagation distance of 0.7 m.

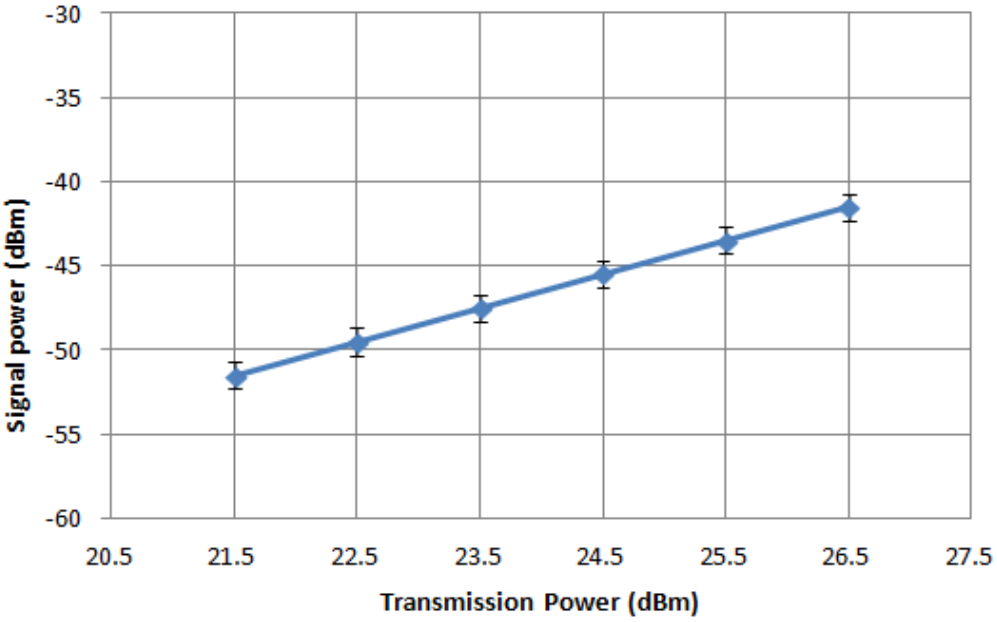

Figure 10.2: Measured power of the backscattered signal with increasing transmission power in air at a propagation distance of 0.7 m.

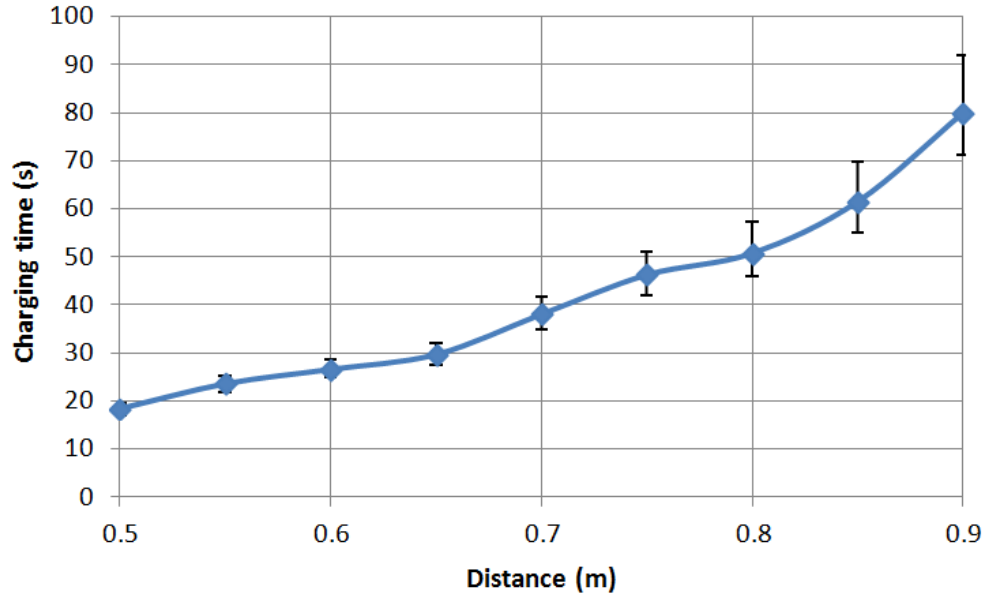

Figure 10.3: Measured charging time with increasing propagation distance in air at a transmission power of 23.5 dBm.

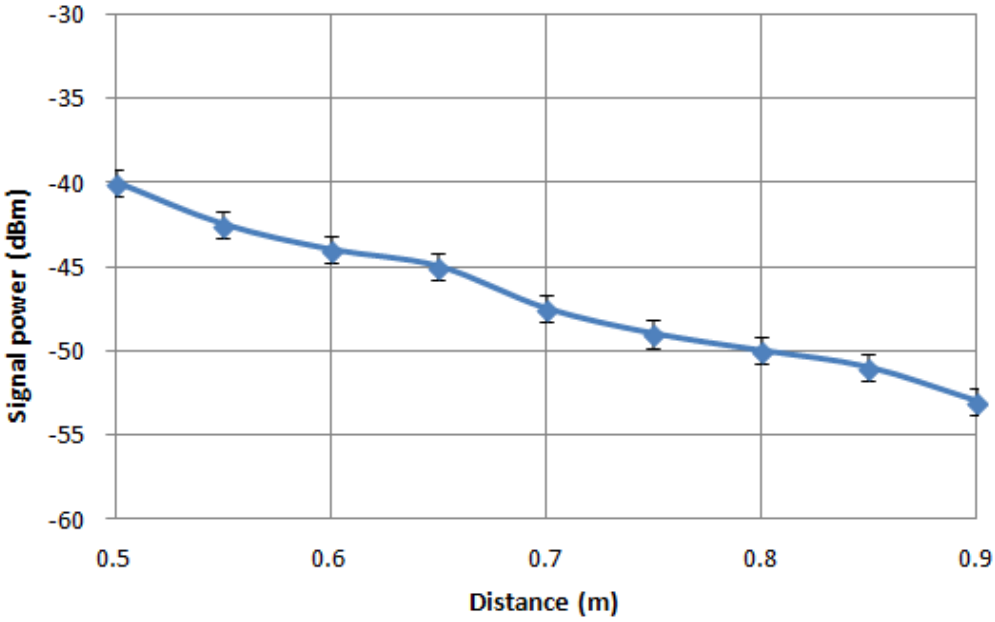

Figure 10.4: Measured power of the backscattered signal with increasing propagation distance in air at a transmission power of 23.5 dBm.

the sensor node achieves shorter charging time when the propagation distance decreases and that the power of the backscattered signal is increased by 13 dB with decreasing propagation distance from 0.9 m to 0.5 m. This is primarily due to the Free-Space Path Loss (FSPL) which increases with increasing propagation distance at a given frequency. A high FSPL limits the power harvested by the sensor node and also attenuates the backscattered signal arriving at the reader antenna.

As shown in Figure 10.1 and Figure 10.3, it is also observed that the error bound of the measured charging time increases when either the transmission power decreases or the propagation distance increases. This is due to the characteristic of the sensor node that the charging time is more sensitive to the change in the power harvested by the sensor node at a lower power level, as described in Chapter 8. The power measurements, shown in Figure 10.2 and Figure 10.4, have an error bound of $\pm$ 0.6 dBm. The primary factors that affect the repeatability of the measurements in air were the accuracy of recovering the reader antenna orientation and measuring the distance between the reader antenna and the sensor node. These factors have been analysed in Chapter 9. In conclusion, the results of the performance evaluation in air show that a higher transmission power or a shorter propagation distance leads to a shorter charging time and a higher power of the backscattered signal arriving at the reader antenna.

10.2.2 Performance evaluation in soil

After completing the experiments for the performance evaluation of the sensor node in air, dry soil was shovelled into the soil planter without displacing the node enclosure. The aim of this process was to minimise the effect of the change in the sensor node orientation on the experimental results. Figure 9.13 has presented the simplified diagram of the experimental arrangement for the performance evaluation in soil. The height of the reader antenna was maintained at 0.5 m above the soil surface. The two variables being considered in the performance evaluation in soil were the transmission power at the reader antenna and the depth of the sensor node.

Figure 10.5 and Figure 10.6 present the plots of the measured charging time and the measured power of the backscatter signal against the depth of the sensor node within the dry soil at transmission powers of 28.5 dBm, 29.5 dBm and 30.5 dBm. As shown in Figure 10.5 and Figure 10.6, both the transmission power and the depth affect the measurements. As would be expected, a higher transmission power leads to a shorter charging time and a higher power of the backscattered signal arriving at the reader antenna at a given depth.

As described in Chapter 2, the power loss due to RF absorption has always been considered as one of the primary factors which leads to the high path loss in soil. Therefore, it was thought that a larger depth would lead to a higher absorption loss, and result in a longer charging time and a lower power backscattered signal. As shown in Figure 10.5, the measured charging time continues to increase with increasing depth of the sensor node from 0 m to 0.25 m. In the depth range of 0.25 m to 0.4 m, there is an observation from Figure 10.5 that the measured charging time does not necessarily increase with increasing depth. At a transmission power of 28.5 dBm, the charging time drops by over 20 s when the depth increases from 0.25 m to 0.35 m, and it subsequently increases to a maximum value of 100 s at the depth of 0.4 m. When the transmission power increases, the error bound of the measured charging time decreases. This is primarily due to that the rate of change of the charging time with respect to the power harvested by the sensor node reduces as the power increases. At transmission powers of 29.5 dBm and 30.5 dBm, the measured charging time stops increasing with increasing depth from 0.25 m to 0.35 m, which was not expected. The measured signal power shown in Figure 10.6 indicates an overall decline of 5 dB with increasing depth from 0 m to 0.4 m at a given transmission power. However,the measured signal power can increases with increasing depth in some regions such as from 0.05 m to 0.1 m, 0.2 m to 0.25 m and 0.35 m to 0.4 m. This does not meet the expectation that the measured signal power should decrease with increasing depth. The experimental results shown in Figure 10.5 and Figure 10.6 implies that the sensor node performance is affected by other factors in addition to the power loss due to RF absorption. This will be further discussed in Section 10.3.

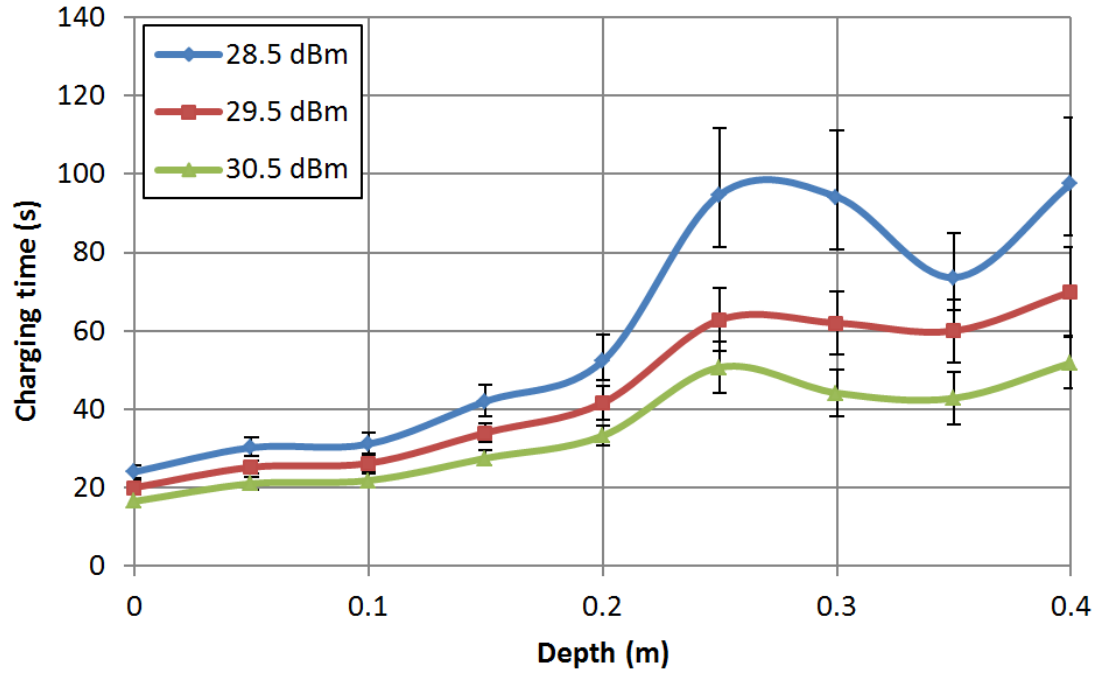

Figure 10.5: Measured charging time with increasing depth in the dry soil at the transmission powers of 28.5 dBm, 29.5 dBm and 30.5 dBm.

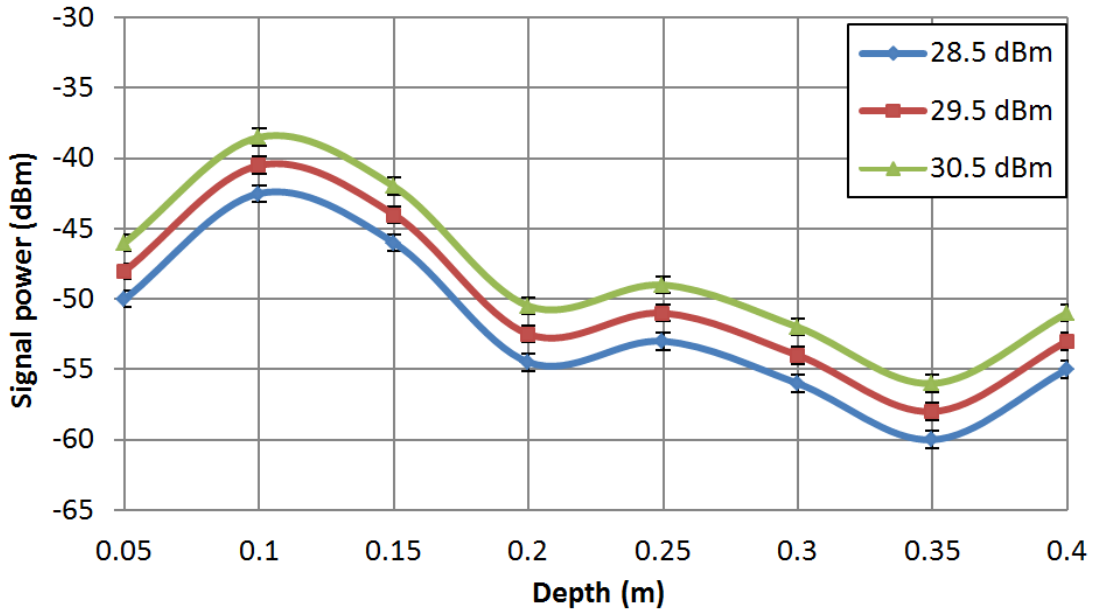

Figure 10.6: Measured power of the backscattered signal with increasing depth in the dry soil at the transmission powers of 28.5 dBm, 29.5 dBm and 30.5 dBm.

As discussed in Chapter 2, water content is the primary material leading to RF absorption in the soil. Therefore, there was an expectation that the increase of the soil moisture content would result in a sharp increase in the measured charging time at a given transmission power and depth of the sensor node. Figure 10.7 compares the plots of the measured charging time versus the depth in the dry soil and in the wet soil at a transmission power of 29.5 dBm. Compared to the measurements in the dry soil, the measured charging time in the wet soil is slightly longer at a depth in the 0.05 m to 0.2 m range, and then becomes shorter in the 0.25 m to 0.4 m range. However, the error bounds of the two plots shown in Figure 10.7 are overlapping when the depth of the sensor node is above 0.2 m. This indicates that the increase of the soil moisture content does not significantly affect the charging time, which was not expected before the experiments were undertaken.

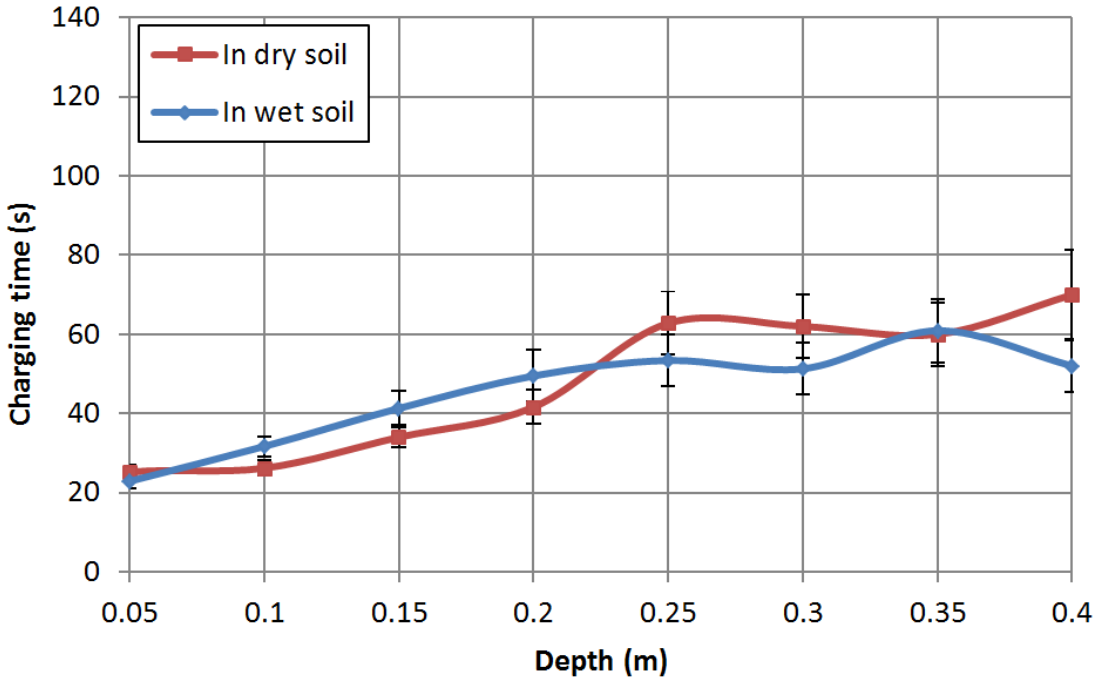

Figure 10.7: Comparison of the measured charging time in the dry soil and in the wet soil at a transmission powers of 29.5 dBm.

In conclusion, the experimental results presented in this section indicate that:

- the measured charging time does not necessarily increase with increasing depth from 0 m to 0.4 m;

- the measured power of the backscattered signal does not necessarily decrease with increasing depth from 0 m to 0.4 m;
- the soil moisture does not significantly affect the measured charging time at a given depth.

The experimental results imply that the sensor node performance in the soil is affected by other factors in addition to the absorption loss of the soil.

10.3 Path Loss Characterisation

The method of characterising the path loss has been described in Chapter 9, and is based on deducing the power harvested by the sensor node at a transmission powers of 24.5 dBm in air and 29.5 dBm in the soil. The error bounds of the characterised path loss was deduced from the error bounds of the measured charging time. Figure 10.8 compares the characterised path loss in air and the calculated Free-Space Path Loss (FSPL). The FSPL was calculated according to the Friis equation [81] at 915 MHz. The propagation distance in the calculation includes the gap between the sensor node antenna and the top surface of the node enclosure. It is observed from Figure 10.8 that the two plots are in good agreement, and the difference between the characterised path loss and the calculated FSPL is within $\pm$ 1 dB. This proves the validity of the experimental approach of the path loss characterisation.

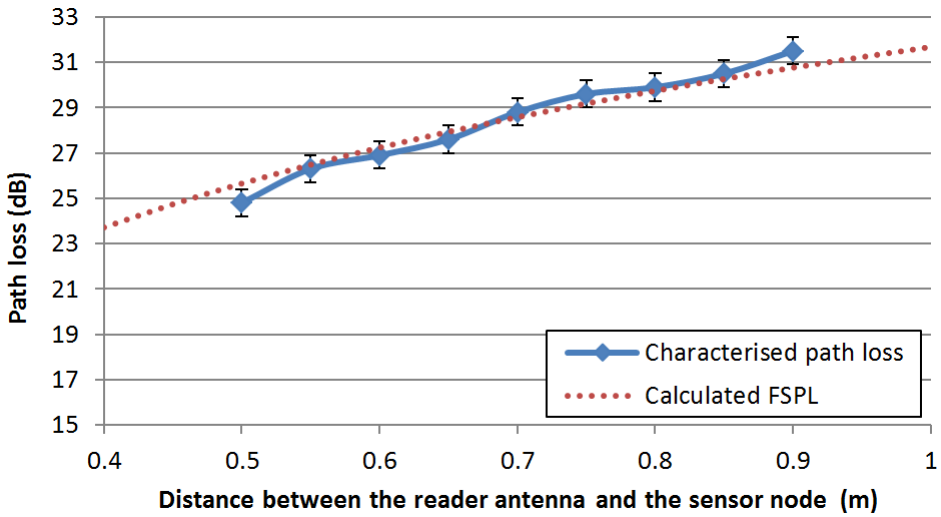

Figure 10.8: Comparison of the measured path loss in air and calculated FSPL.

Figure 9.14 has presented the simplified diagram of the experimental arrangement when the depth of the sensor node is 0 m. At the depth of 0 m, the sensor node enclosure was just inserted below the dry soil surface, and the propagation distance between the reader antenna and the top surface of the sensor node enclosure equals to the height of the reader antenna above the soil surface. Figure 10.9 compares the characterised path loss in the dry soil, at a depth of 0 m, and the characterised path loss in air with increasing propagation distance (in this case reader antenna height) from 0.5 m to 0.9 m. When considering the error bounds of the results shown in Figure 10.9, it is observed that the values of the characterised path loss in the soil are approximately 5 dB higher than the measurements in air. At the depth of 0 m, there was no soil above the sub-soil node, and therefore no power loss due to RF absorption by the soil. The only factor leading to the increase of the path loss by 5 dB is the effect of the soil surrounding the sensor node enclosure on the performance of the sensor node antenna. During the calculation of the path loss according to Equation 9.1, the gain of the sensor node antenna G_r used the value measured in air. However, due to the effect of the soil, the actual gain of the sensor node antenna in the soil was less than the measured gain in air. The results presented in Figure 10.9 indicate that the actual gain of the sensor node, towards the direction of the reader antenna, is 5 dB lower than the antenna gain measured in air.

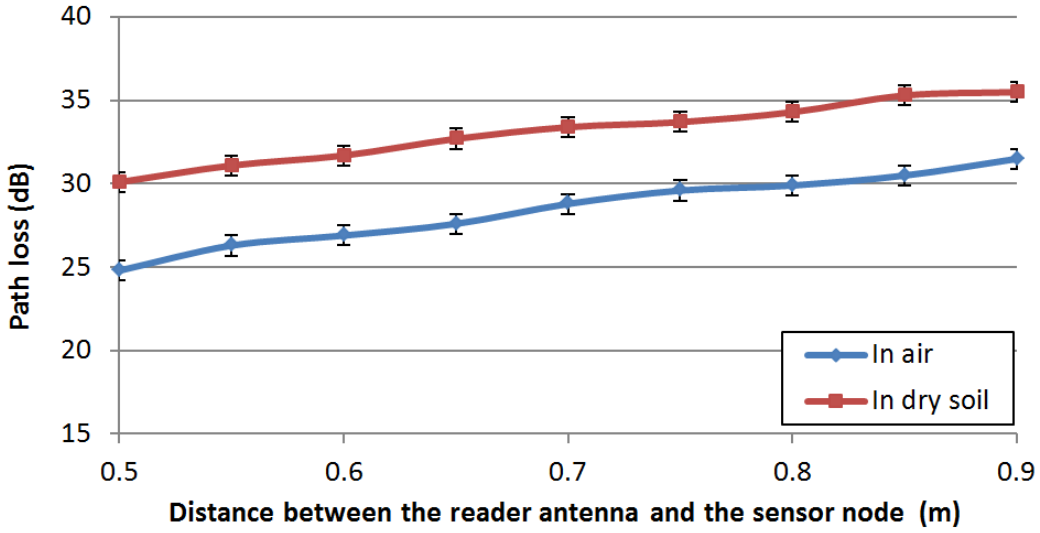

Figure 10.9: Measured path loss across the propagation distance when the sub-soil node is at a depth of 0 m .

Figure 10.10 shows the plot of the characterised path loss in the dry soil with increasing depth of the sensor node from 0 m to 0.4 m. With the experimental arrangement shown in 9.13, the height of reader antenna was maintained at 0.5 m above the soil surface, and so the depth range of 0 m to 0.4 m gives to a propagation distance range of 0.5 m to 0.9 m.

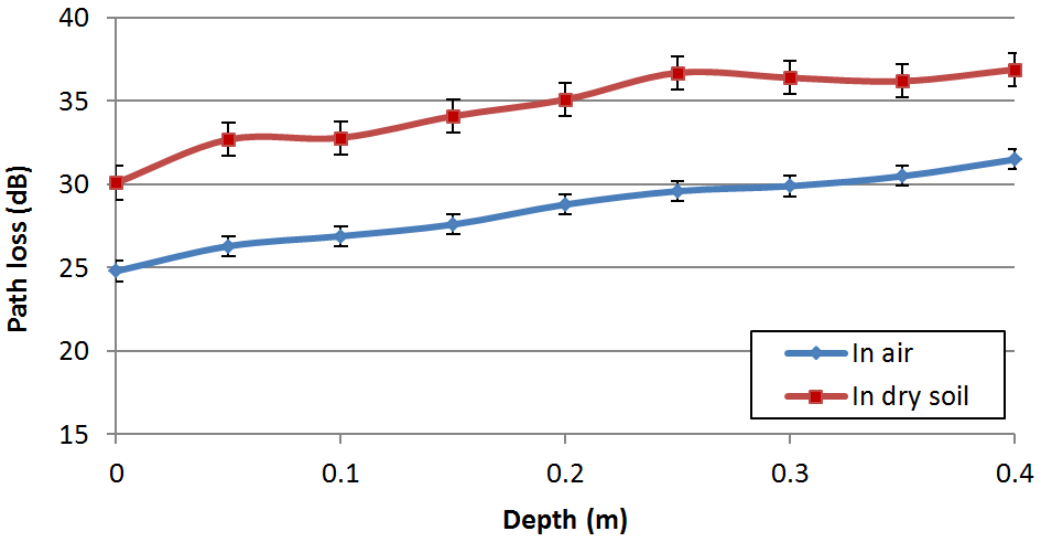

Figure 10.10: Measured path loss in the dry soil with increasing of the depth.

As shown in Figure 10.10, the characterised path loss is compared to the path loss characterised in air at a propagation distance of 0.5 m to 0.9 m. It is observed that the characterised path loss in the soil has higher error bounds than that in air, which is primarily due to the effect of the factors analysed in Chapter 9, including the accuracy of measuring the depth and the soil compactness. As shown in Figure 10.10, the characterised path loss in the soil increases with increasing depth up to 0.25 m. The path loss then does not increase and approximately remains constant when the depth increases from 0.25 m to 0.4 m. The difference between the values of the characterised path loss in the soil and in air decreases as the depth increases from 0.25 m to 0.4 m. Figure 10.11 compares the characterised path loss in the dry soil and in the wet soil with increasing depth of the sensor node from 0.05 m to 0.4 m. It is observed that the error bars of the characterised path loss in the dry soil and in the wet soil overlap, especially in the 0.2 m to 0.4 m depth range. This means that the characterised path loss may not be primarily affected by the soil moisture content at a given depth.

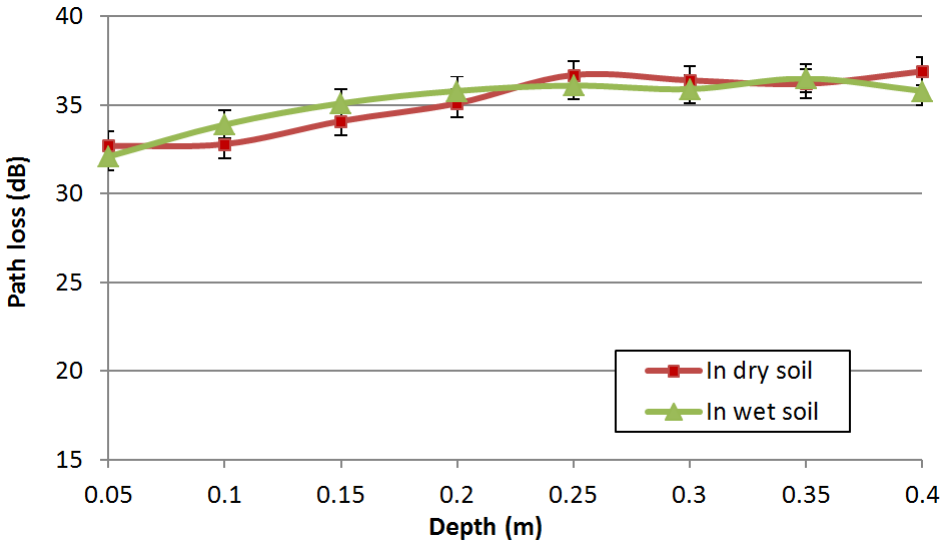

Figure 10.11: Comparison of the measured path loss in the dry soil and in the wet soil.

The experimental results presented in Figure 10.10 and Figure 10.11 do not agree the CST simulation results presented in Chapter 6. The simulation results show that the path loss between the reader antenna and the sub-soil antenna always increases with increasing depth or soil moisture content. The observations in the experimental results imply that the energy transfer between the reader antenna and the sensor node antenna is potentially affected by another mechanism in addition to EM wave propagation.

With the size of the sensor node enclosure as shown in Figure 9.10, the soil was within the near-field of the sensor node antenna. The reader antenna was placed at a height of 0.5 m above the soil surface. This height exceeds the minimum distance of the far-field region at 915 MHz which is calculated according to Equation 2.1. However, it is hard to validate that the soil is within the far-field region of the reader antenna in the experimental environment. Therefore, there can be a near-field energy coupling between the reader antenna and the sensor node antenna. With the effect of the near-field coupling, the energy is directly coupled to the sensor node antenna from the reader antenna through the soil. Due to the coupled energy, the power harvested by the sensor node does not decrease with increasing depth or soil moisture content. Further investigation on the near-field coupling effect is presented in Section 10.4.

10.4 Near-field Coupling Effect Investigation

In this research, an experiment has been performed to investigate the effect of the near-field coupling effect described in Section 10.3. This experiment is only designed for validating the existence of near-field coupling. Figure 10.12 presents the experimental arrangement, where the sensor node antenna is enclosed within the sensor node enclosure and is wired to the PXIe-5663 VSA using an RF cable. The sensor node enclosure was buried in the wet soil at a depth of 0.2 m. The PXIe-5673 VSG and PXIe-5663 VSA were used to measure the path loss between the reader antenna and the sensor node antenna (including the antenna gains) at a frequency of 915 MHz. In the experiment, the depth of the sensor node antenna was fixed, and the path loss was measured by varying the height of the reader antenna in the range of 0.25 m to 0.75 m. This measurement process was repeated twice. Since the depth is fixed, the variation of the reader antenna height should only affect the FSPL between the reader antenna and the sensor node antenna. If the near-field coupling effect did not exist, the plot of measured path loss with increasing height would have the same rate of increase as the FSPL calculated with the Friis equation [81].

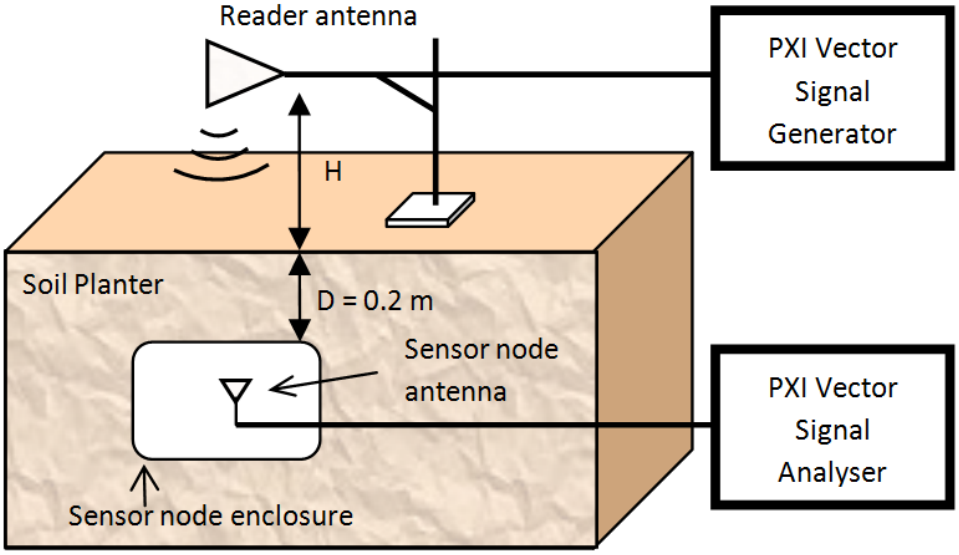

Figure 10.12: Experimental arrangement for investigating the near-field coupling effect.

Figure 10.13 compares the plots of the measured path loss and calculated FSPL versus the height of the reader antenna. Given a height, H, of the reader antenna, and a sensor node depth of 0.2 m, the corresponding distance for calculating the FSPL is: H + 0.2 m. As shown in Figure 10.13, the measured plot is not in agreement with the calculated plot of the FPSL. Generally, both the measured path loss and the calculated FSPL increase by 6 dB with increasing antenna height from 0.27 m to 0.78 m. However, the measured path loss slightly decreases when the height increases from 0.32 m to 0.43 m and from 0.55 m to 0.61 m. As shown in Figure 10.13, the distance between the two local minimums is approximately half of the wavelength, 0.5λ ($\lambda \approx 0.33$ m at 915 MHz). This observation indicates that the measured path loss with increasing height is associated with the wavelength of RF signals, which can be due to the near-field coupling effect. Due to the complex nature of near-field, this work did not further investigate details of the near-field effect. However, it is important to consider the near-field coupling effect for the RFID sub-soil system design and implementation. In practice, the system performance can be optimised by taking advantage of the near-field coupling effect. The system performance optimisation will be discussed in Chapter 11.

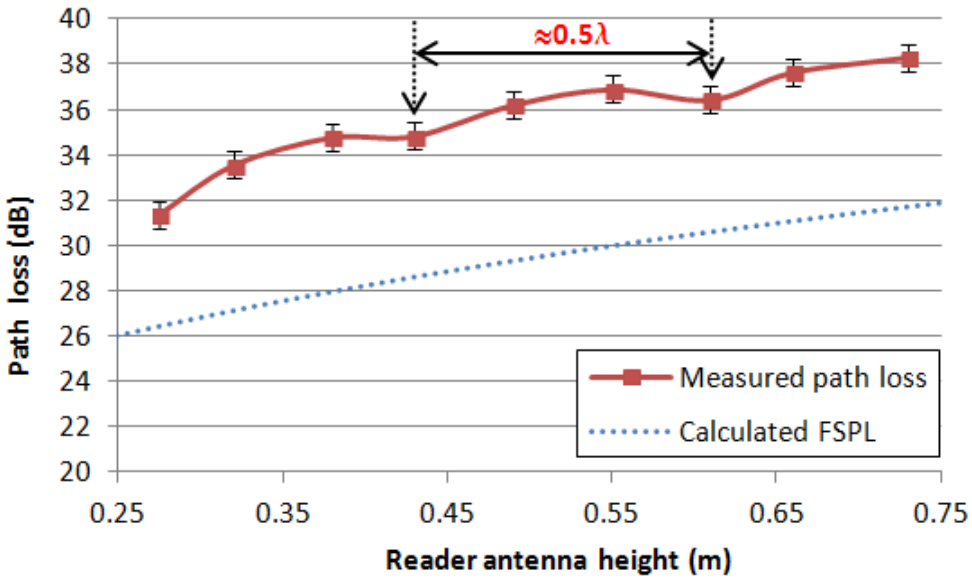

Figure 10.13: Path loss measurements for investigating the near-field effect.

10.5 Summary

This chapter presents the results of the sensor node performance evaluation and the path loss characterisation from a series of practical experiments. The results of the sensor node performance evaluation in air show that a higher transmission power or a shorter propagation distance results in a better sensor node performance - a shorter charging time and a higher power of the backscattered signal arriving at the reader antenna. When the sensor node is deployed within the dry soil, the results show that the sensor node performance does not necessarily degrade with increasing depth from 0 m to 0.4 m. A comparison of the measured charging time in the dry soil and in the wet soil has been presented. It is shown that the soil moisture content has limited effect on the charging time measurement at a given depth. This implies that the power loss due to RF absorption by the soil is not the primary factor that affects the sensor node performance.

The characterised path loss in the dry soil has been compared to the characterised path loss in air. At a depth of 0 m, the characterised path loss is 5 dB higher than the characterised path loss in air. This is due to the effect of the soil on the sensor node antenna performance. There is also an observation that the characterised path loss remains constant with increasing depth of the sensor node from 0.25 m to 0.4 m, even though the increase of the depth increases the FSPL and the power loss due to RF absorption by the soil. The characterised path loss in the dry soil has also been compared to the characterised path loss in the wet soil. It is observed that the increase of the soil moisture content does not significantly affect the characterised path loss.

As analysed from the experimental results, the sensor node performance in the soil can be affected by the near-field coupling effect between the reader antenna and the sensor node antenna. With the near-field coupling effect, energy is directly coupled to the sensor node antenna from the reader antenna. The existence of the near-field coupling effect has been investigated through an experiment. In practice, the near-field coupling effect can be potentially used to optimise the sensor node performance, and the method of the performance optimisation is discussed in Chapter 11.

Chapter 11

System Design Considerations

11.1 Introduction

With the proposed RFID sub-soil system described in Chapter 4, the charging time of the RFID sensor node and the power of the backscattered signal are the key parameters which can be used to indicate the system performance. As described in Chapter 8, the charging time of the sensor node prototype refers to the time taken to charge the on-board super-capacitor from the low threshold voltage V_{min} to the high threshold voltage V_{max}. Figure 11.1 presents a system concept diagram, where the following parameters will have an impact on the system performance.

- The frequency of the RF signal generated by the RFID reader (the system operating frequency)
- The type of the RFID reader antenna
- The height of the RFID reader antenna above the ground
- The transmission power of the RFID reader
- The ambient RF noise around the tractor
- The soil type and moisture content
- The depth of the sensor node within the soil
- The type and the volume of the sensor node antenna

- The air gap around the sensor node antenna
- The energy budget of the on-board sensors
- The volume of the on-board sensors
- The capacitance of the capacitor for storing the harvested energy
- The tractor speed

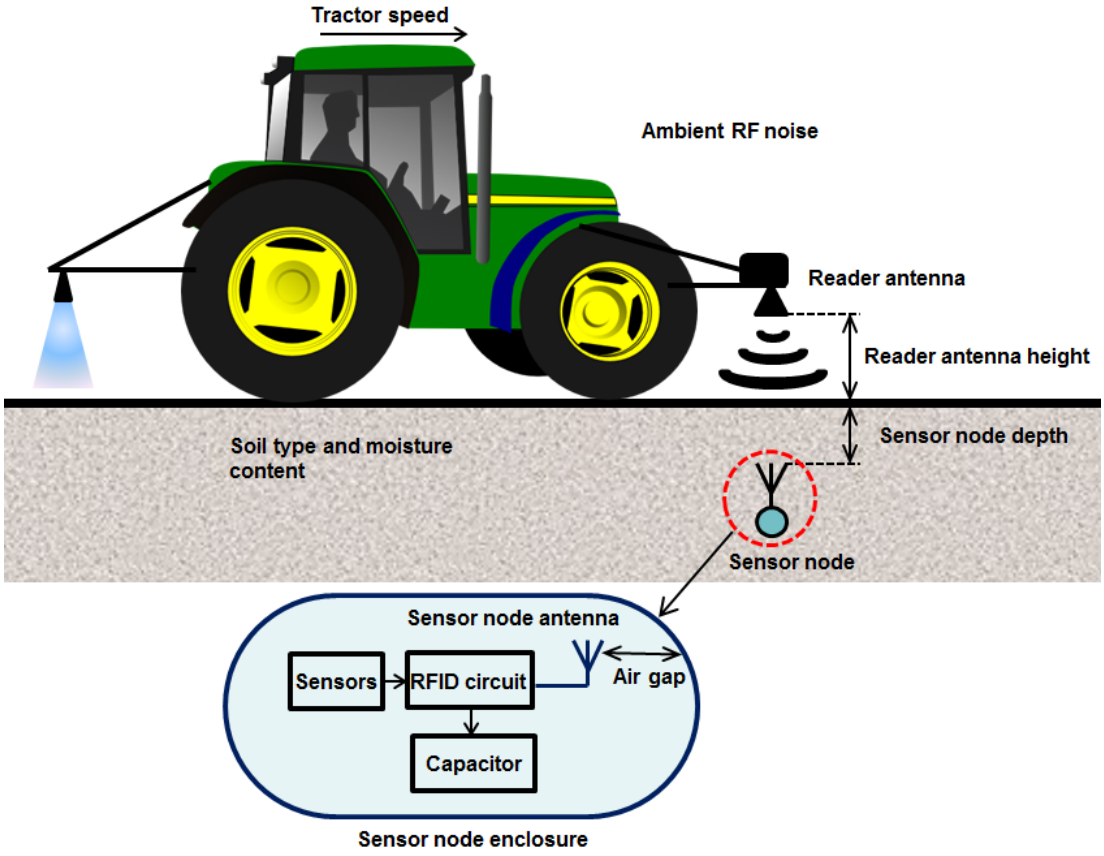

Figure 11.1: Block diagram showing the key elements in the system design.

In practice, the frequency of the RF signal, the type of the RFID reader antenna, the height of the RFID reader antenna, the transmission power of the RFID reader, and the tractor speed are the variables which can be controlled by farmers. The soil type, the depth of the sensor node, the type and the volume of the sensor node antenna, the air gap around the sensor node antenna, the energy budget of the on-board sensors and the sensor node capacitor are the

fixed parameters. The soil moisture content and the ambient RF noise around the tractor are the two variables which cannot be controlled. In this chapter, Section 11.2 to Section 11.12 describe the considerations of these parameters on the system design. A series of trade-offs between the parameters can be considered, and the information of the trade-offs is summarised in Section 11.13.

11.2 Reader Antenna Type

As described in Chapter 4, directional antennas are a solution for the RFID reader system design as they typically have a high gain and can be used to maximise power radiation towards the direction of the sensor node. The patch antenna is one of the well-known directional antennas. Figure 11.2 presents the radiation pattern, in a horizontal plane, of a linearly-polarized 900-MHz patch antenna [8]. As shown in Figure 11.2, the peak gain of the antenna is 9 dBi and the horizontal beamwidth of the antenna is 65 degrees. The beamwidth of an antenna typically refers to the angle encompassed between the points where the gain has decreased 3 dB below the peak gain.

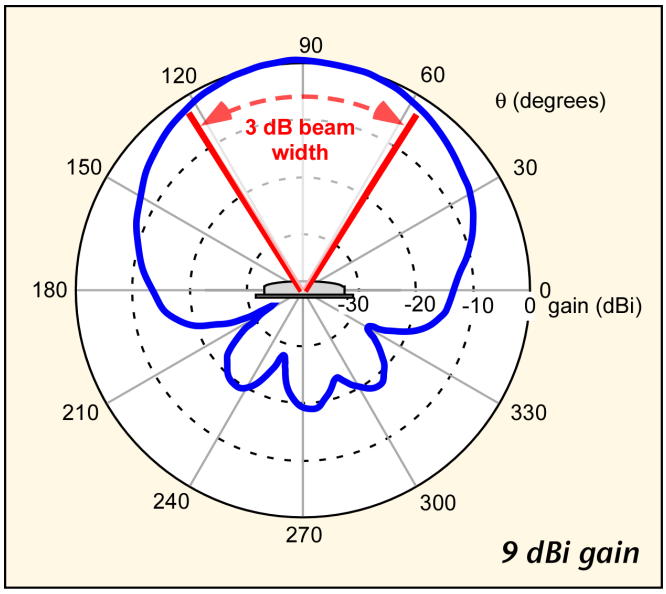

Figure 11.2: Radiation pattern of an example 900 MHz patch antenna [8].

With the proposed RFID sub-soil system shown in Chapter 4, the RFID reader moves with the tractor to interrogate a number of sensor nodes. When using a

patch antenna as the reader antenna, the beamwidth provided by the patch antenna is one of the key parameters. At a given tractor speed, a wide beamwidth leads to a long time when the sensor node can harvest energy, as described in Section 11.12. However, the beamwidth of an antenna typically increases at the expense of the antenna gain. Table 11.1 compares the gain and the beamwidth of the five commercial RFID reader antennas (linear polarised). It is observed that the antenna with a higher gain has a smaller horizontal beamwidth or vertical beamwidth. Therefore, the trade-off between the reader antenna gain and beamwidth needs to be considered in the system design, which is described in Section 11.13.

Table 11.1: Comparison of the commercial RFID reader antennas.

Antennas	Gains	Horizontal beamwidth	Vertical beamwidth
MTI MT-263006 [158]	12.5 dBi	42 degrees	42 degrees
LAIRD PA9-12 [159]	12 dBi	55 degrees	40 degrees
MTI MT-263003 [160]	10 dBi	50 degrees	50 degrees
TIMES-7 A4030L [161]	7.5 dBi	62 degrees	62 degrees
IMPINJ THRESHOLD [162]	5 dBi	100 degrees	50 degrees

11.3 Reader Antenna Height

The height of the RFID reader antenna is a key consideration in the system design. At a given depth of the sensor node, the Free-Space Path Loss (FSPL) between the reader antenna and the sensor node decreases as the reader antenna height decreases. Therefore, the system performance can be improved based on lowering the reader antenna height. However, it is necessary to consider that an unacceptably low height of the reader antenna can bring problems in some circumstances. For example, the farming arrangements in a field can put the reader antenna at risk, or the reader antenna can damage the crops which have a body height above the ground exceeding the reader antenna height. Hence,

the minimum allowable height of the RFID reader antenna will be depend on a specific field.

In addition, in the system design it is important to consider the potential near-field coupling effect when adjusting the reader antenna height. The experimental results presented in Chapter 10 indicate that the system performance can be affected by the near-field coupling effect between the RFID reader antenna and the sensor node antenna. With the existence of the near-field coupling effect, a lower height does not necessarily result in a better system performance. This has been validated through the experiments described in Section 10.4. In practice, it is worth considering the optimisation of the system performance by taking advantage of the near-field coupling effect. The method of system performance optimisation is based on tuning the height of the RFID reader antenna above the soil surface. With this method, the RFID reader antenna can be held using an on-tractor mechatronic system - a mechanical arrangement which is controlled by an electronic system. During the optimisation of the system performance, the reader antenna is positioned above the sensor node. The height of the reader antenna is controlled through the mechatronic system to move it up and down. The time taken to receive the signal from the sensor node is measured and compared against the reader antenna height.

In addition to the RFID reader antenna height, the depth of the sensor node is another dependent parameter of the near-field coupling effect. This means that the tuned reader antenna height at which the system performance is optimised can be affected as the depth of the sensor node varies. Within a large field, a number of sensor nodes can be deployed at various depths within the soil to achieve sub-soil sensing for various crops. In this scenario, there is a need to repeat the optimisation process in order to tune the reader antenna height for each of the sensor nodes. When deploying a sensor node, the location information of the sensor node can be provided by a Global Position System (GPS). The GPS system can be also used to locate the sensor node. In practice, when the RFID reader travels with the tractor to interrogate the sensor nodes, the on-board mechatronic system adjusts the reader antenna height automatically according location data provided by the GPS module.

11.4 Transmission Power

In Chapter 10, the experimental results show that a higher transmission power radiated from the RFID reader antenna leads to a shorter charging time of the sensor node and a higher backscattered power arriving at the RFID reader antenna. Therefore, in practice the system performance can be improved by increasing the transmission power of the RFID reader. In the system design, the signal generated by the RFID reader is amplified using an RF amplifier. As described in Section 11.2, the RFID reader can use a directional antenna which helps to maximise power radiation towards the ground.

Various countries limit the maximum radiated power in a selected frequency band, for example: the UK Office of Communication (Ofcom) limits the transmission power in the 856.6 MHz to 867.6 MHz frequency band to 2 W Effective Radiated Power (ERP) [156]. The proposed system can potentially use a power level exceeding the power limits as long as the system complies with guidelines for human exposure to EM fields. Table 11.2 summarises the minimum general population/uncontrolled power density exposure limits, specified in Federal Communications Commission (FCC) guidelines [1], in the frequency range of 0.3 MHz to 100,000 MHz.

Table 11.2: Power density exposure limits [1].

Frequency Range (MHz)	0.3-1.34	1.34-30	30-300	300-1500	1500-100,000
Power Density (S)(mW/cm^2)	100	100/f^2	0.2	f/1500	1.0

f = frequency in MHz

The system design needs to consider a minimum safe distance between the reader antenna and any people surrounding the reader antenna, such as the tractor driver. The minimum safe distance R can be estimated using Equation 11.1:

$$R = \sqrt{\frac{PG}{4\pi S}} \tag{11.1}$$

where S (mW/cm^2) refers to the power density limit, P (mW) refers to the power delivered to antenna, G (dBi) refers to the antenna gain in direction of the tractor driver, and R (cm) is the distance to the radiation centre of the antenna. As

proposed in the system design, the RFID reader uses a directional antenna which primarily radiates energy towards the ground, and so minimises radiation at other directions. For example, when using a patch antenna with the radiation pattern shown in Figure 11.2, the antenna gain in the potential direction of the tractor driver. Figure 11.3 shows the calculated safe distance with increasing power, at 900 MHz, delivered to the reader antenna. The reader antenna is assumed to have an antenna gain of 0 dBi at the direction of the tractor driver or people surrounding the antenna. It is observed that the calculated safe distance, based on the FCC guidelines, is 0.63 m when the power delivered to the antenna is 30 W.

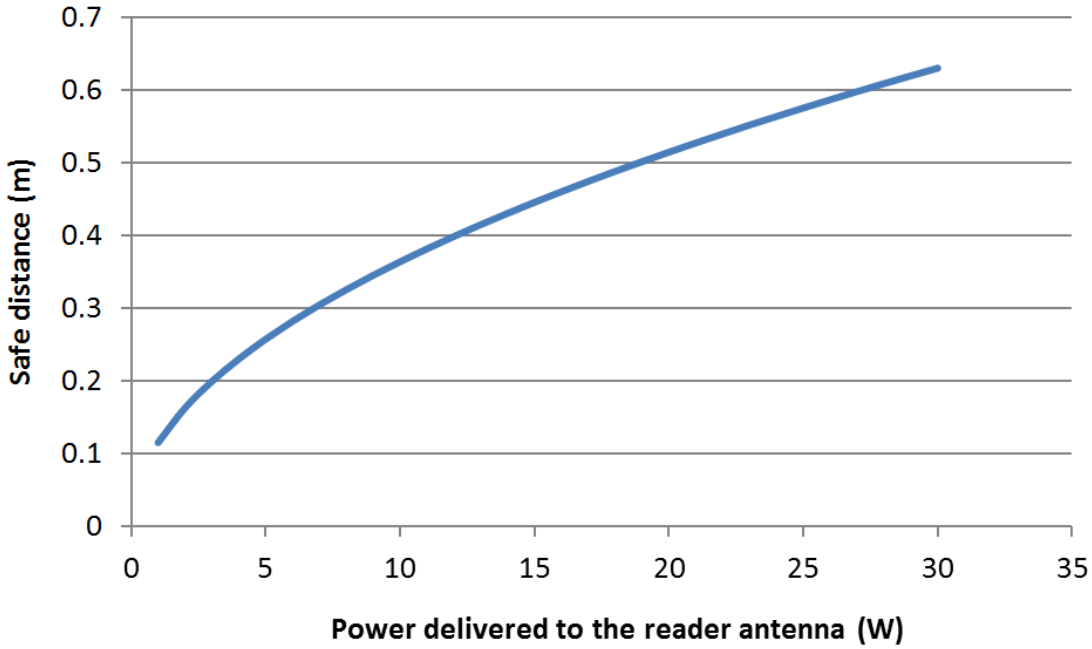

Figure 11.3: Plot of the calculated safe distance with increasing power, at 900 MHz, delivered to the reader antenna which is assumed to have an antenna gain of 0 dBi at the direction of the tractor driver or people surrounding the antenna.

As described in Chapter 10, the characterised path loss at a sensor node depth of 0.4 m in the dry soil is 37 dB. Therefore, at a transmission power of 30 W (44.8 dBm) the received power by the sensor node prototype is 7.8 dBm. According the plot of the measured charging time of the sensor node prototype with increasing power received by the sensor node shown in Figure 8.15, a received power of 7.8 dBm can lead to a charging time of a few seconds.

Although a high transmission power helps improve the system performance, the transmission power of the RFID reader still needs to be controlled within an acceptable range. One of the primary concerns is that high EM radiation can have an influence on crop growth. In practice, crops positioned close to a sensor node can absorb RF energy, which can give rise to an increase in the temperature within the crop body. This would not be conducive to crop growth. Therefore, the effect of EM radiation on crop growth will need to be considered and explored in future work. There is also the need to consider the risk of using a high transmission power if accidents occur. For example, if the reader antenna falls down from the tractor or the driver forgets to turn off the RFID reader. With the possibility of those accidents, an on-vehicle protection system has to be designed and interfaced to the RFID reader. The protection system would be capable of sensing the status of the tractor and the RFID reader. When either the tractor or the RFID reader behaves abnormally, the protection system will cut off the supply power of the RFID reader immediately.

11.5 Ambient RF Noise

Ambient RF noise around the proposed RFID reader system is one of the primary concerns in the system communication link. As described in Chapter 4, the RFID reader is mounted on a tractor. There is a concern that electromagnetic disturbances come from the the vehicle itself as well as its Electrical Sub-Assembly (ESA). ESA refers to an electrical and/or electronic device or set(s) of devices intended to be part of a vehicle, such as on-board electronic or communication systems. The typical strength of the electromagnetic noise generated by the agriculture or forestry tractor is 55 dB (μV/m) [163] in the frequency band of 400 MHz to 900 MHz. This noise strength was measured at 3 meters from the tractor. The power of the noise signal received by an isotropic antenna can be estimated from a noise strength according to Equation 11.2 [164]:

$$P_r(dBm) = E(dB(\mu/m)) + 20log_{10}f(MHz) - 77.2, \tag{11.2}$$

where P_r is the received noise power, E is the noise strength and f is the signal frequency. At a noise strength of 55 dB (μV/m) and a frequency of 900 MHz ,

the estimated noise power is -81.3 dBm. With the proposed system, the ambient noise generated by the tractor can lead to a low Signal-to-Noise Ratio (SNR) at the RFID reader antenna. This has a significant impact on the Bit Error Rate (BER) performance of the system communication link.

In the system design, it is necessary to increase the backscattered signal power in order to improve the system performance in the communication link. As described in Section 11.4, one of the potential methods of improving the backscattered signal power is based on increasing the transmission power. In addition, the power of the backscattered signal arriving at the RFID reader antenna can be improved by reducing the reader antenna height. This method seeks to shorten the Free-Space Path Loss (FSPL) between the reader antenna and the sensor node antenna. In the system design it is also worth characterising the noise generated by farm machinery. Based on the characterisation results, there is a possibility to filter the noise through a hardware filter or signal processing functions. The noise characterisation and filter design are not part of research in this work.

11.6 Soil Type and Soil Moisture Content

In the proposed system shown in Figure 11.1 the soil leads to: 1) the high path loss between the RFID reader antenna and the sensor node antenna, and 2) the effect on the performance of the sensor node antenna. The two problems are primarily due to dielectric properties of the soil. As described in Chapter 2, soil is a lossy dielectric medium to RF signals and its dielectric behaviour is significantly affected by the water content and the texture. Li et al. [7] characterised the path loss in sub-soil wireless channel. The characterisation results show that the path loss in the soil increases with increasing soil moisture content and percentage of clay and sand particles in the soil. Therefore, in the system design it is necessary to consider the variation of the soil relative dielectric constant in various soil types and at various soil moisture content levels.

Peplinski et al. [2] provided expressions of the relative dielectric constant of a soil medium in terms of the soil's textural composition (sand, silt and clay fractions) and the volumetric moisture content. These expressions are presented in Chapter 2. As described in Chapter 5, the calculated real and imaginary parts

of the sandy soil dielectric constant increase with increasing soil moisture content. Table 11.3 compares the texture and the calculated dielectric constant at 900 MHz of the four typical soil types specified in [2]. It is observed that the variations of the real and imaginary parts of the dielectric constant in the four typical soil types are less than 4.4 and 0.31 respectively in the soil moisture content range of 5% to 25%.

Table 11.3: Comparison of the real and imaginary parts of the relative dielectric constant at 900 MHz of the four soil types [2].

Soil types	Sand (%)	Silt (%)	Clay (%)	Moisture=5%		Moisture=25%	
				$\epsilon^{'}$	$\epsilon^{''}$	$\epsilon^{'}$	$\epsilon^{''}$
Field 1	50	35	15	6.78	0.48	20.5	1.54
Field 2	40	55	5	6.24	0.31	18.65	1.23
Field 3	30	60	10	6.0	0.31	17.53	1.32
Field 4	15	65	20	5.60	0.30	16.1	1.46

11.7 Sensor Node Depth

The depth of the sensor node within the soil is a key parameter which farmers are interested in. In practice, the sensor node is deployed at a fixed depth below the ground, and the depth depends on the effective rooting depths of the crops in a field. For example, radish typically has a rooting depth of 0.1 m while the typical rooting depth of potatoes is 0.4 m [97]. When designing the proposed system, it is crucial to consider the potential effect of the sensor node depth on the system performance. The experimental results presented in Chapter 10 show that the measured charging time of the sensor node increases by 70 s when increasing the depth of the sensor node from 0.1 m to 0.4 m at a transmission power of 28.5 dBm. This increase of depth also results in a decrease of the backscattered signal power by 12 dB.

In addition, the system design needs to consider the potential near-field coupling effect between the sensor node antenna and the RFID reader antenna as

described in Chapter 10. With the near-field coupling effect, the system performance does not necessarily degrade as the depth of the sensor node increases. This scenario only exists at certain ranges of the sensor node depth. As discussed in Section 11.3, the system performance can be optimised by taking advantage of the near-field coupling effect. The system performance optimisation is based on tuning the height of the reader antenna. When a sensor node has been buried within the soil, the depth of the sensor node can gradually change due to vibration in the soil environment. A change of the sensor node depth has a significant effect on the tuned reader antenna height at which the system performance is optimised. With this concern, there will be the need to implement the process of the system performance optimisation monthly.

11.8 Sensor Node Antenna

In the system design, the sensor node antenna is one of the key parameters which affects the performance and the physical volume of the sensor node. As described in Chapter 8, the charging time of the sensor node prototype has been evaluated using the four different antennas: the patch antenna [138], the dipole antenna [100], the blade antenna [141] and the monopole antenna [142]. The evaluation results show that the measured charging time has the minimum value when the sensor node used the patch antenna. However, the patch antenna has the largest physical size, 200 mm $\times$ 60 mm $\times$ 40 mm which leads to an unrealistically large sensor node enclosure. The sensor node enclosure can be reduced by using the monopole antenna which has the smallest physical size, 59 mm (length) $\times$ 10 mm (diameter). However, the monopole antenna results in an unacceptable sensor node performance, as described in Chapter 8. With the monopole antenna, the on-board super-capacitor of the sensor node failed to be charged to the high threshold voltage, V_{max} within 1000 s. When using the monopole antenna in the system design, it is necessary to consider the method of improving the system performance by increasing the transmission power of the RFID reader. The sensor node operated successfully with the dipole antenna whose maximum physical length is 160 mm. Compared to the dipole antenna, the blade antenna has a smaller physical volume, 84 mm $\times$ 21.5 mm $\times$ 5 mm,

and achieves a better performance in energy harvesting. However, the blade antenna requires a ground plane, and so has a directional radiation pattern. When using the blade antenna in the system design, it is necessary to consider the control of the sensor node's orientation during the system deployment. The sensor node must have an orientation so that the main beam of the antenna is directed towards the ground. Figure 11.4 presents a concept diagram showing the deployment of a cone-shape sensor node, where the yellow area refers to the directional radiation pattern of the blade antenna. This shape can help control the sensor node's orientation within the soil in order to direct the main beam of the antenna towards the ground.

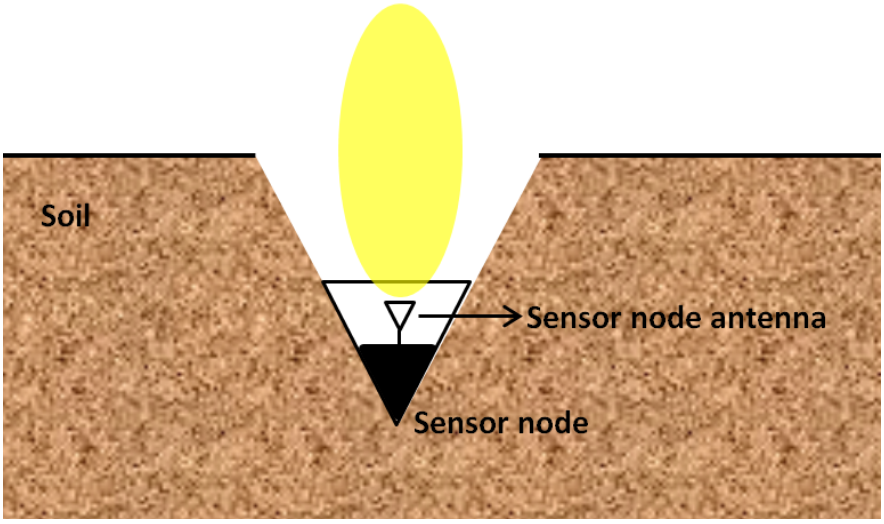

Figure 11.4: The concept diagram showing the deployment of a cone-shape sensor node.

In the system design, it is desirable to reduce the physical size of the sensor node. One potential method of reducing the sensor node antenna size is based on increasing the operating frequency of the RFID sub-soil system. The physical size of a half-wavelength dipole antenna versus the antenna resonant frequency has been investigated through the CST simulations described in Chapter 5. The simulation results show that the antenna length is shortened by approximately 40 mm when the frequency is increased from 900 MHz to 1.2 GHz. However, the CST simulation results presented in Figure 6.16 show that the simulated path loss increases by approximately 5 dB/m with increasing frequency from 900 MHz to 1.2 GHz when the sensor node is deployed in dry sandy soil. An increase of

the path loss leads to a longer charging time of the sensor node, and so can result in a slower tractor speed.

11.9 Air Gap Around the Sensor Node Antenna

The air gap provided by the sensor node enclosure has an influence on the system performance. The CST simulation results presented in Chapter 6 indicate that a larger air gap helps reduce the effect of the soil on the resonant frequency and return loss performance of the antenna. As shown in Figure 6.10, the characterised return loss of the antenna at 900 MHz increases from 5 dB to 10 dB with increasing air gap from 10 mm to 20 mm. However, a larger air gap increases the size of the sensor node enclosure.

The CST simulation results presented in Figure 6.9 show that the effect of the soil leads to a shift in the antenna resonant frequency by 250 MHz from 900 MHz at an air gap of 10 mm. Instead of increasing the air gap provided by the enclosure, the return loss performance of the antenna can be improved through tuning the physical length of the antenna. At a tuned length, the antenna is expected to achieve resonance at 900 MHz in the soil. This method has been explored through CST simulations. The simulations are based on the EM model for investigating the effect of the sensor node enclosure, as described in Section 6.4. In the simulations, the air gap, g, provided by the sensor node enclosure was set to 10 mm, the half length l, of the dipole antenna and the soil moisture content were the two variables. Figure 11.5 compares the simulated return loss of the dipole antenna in the dry sandy soil, 5% moisture content, at the three values of the antenna half length l. It is observed that the resonant frequency of the antenna increases with decreasing length, and the antenna achieves resonance at 900 MHz in the soil when the antenna half length is 54 mm. This proves the validity of the method based on tuning the antenna physical length.

Figure 11.6 shows the simulated return loss of the dipole antenna which has the tuned physical length, l = 54 mm, at an air gap, g, of 10 mm and the soil moisture contents of 5%, 15% and 25 %. The simulation results indicate that the soil moisture content does not significantly affect the antenna return loss at 900 MHz. However, it is observed that the antenna bandwidth (-10 dB)

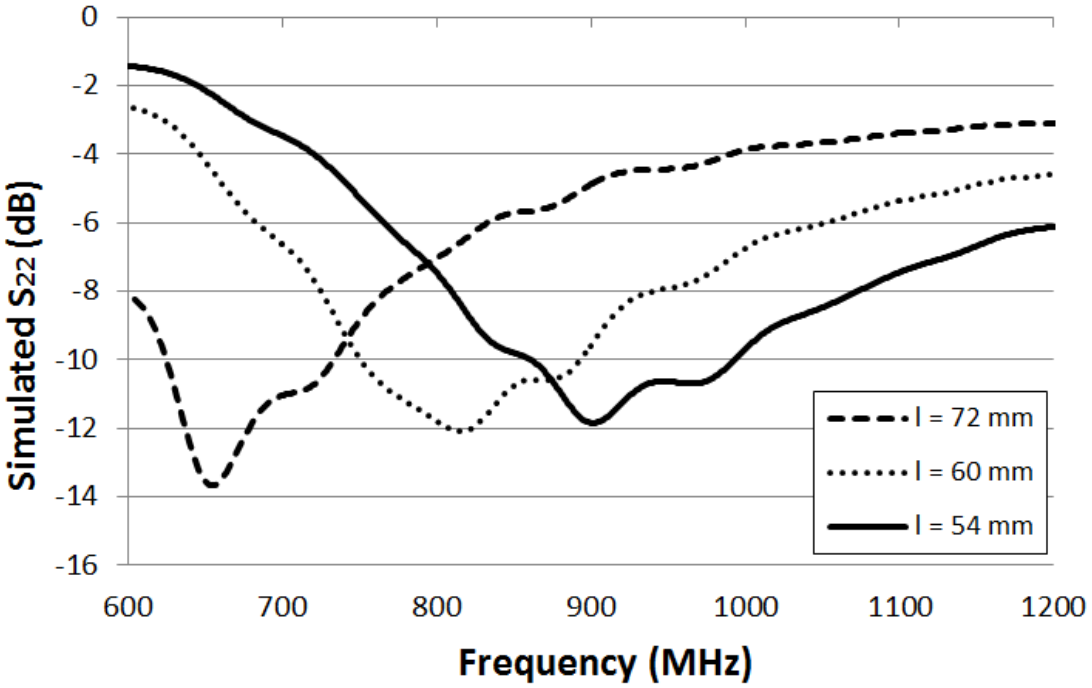

Figure 11.5: Simulated return loss of the dipole antenna when the dipole antenna half length, l = 72 mm, 60 mm and 54 mm at an air gap, g, of 10 mm.

increases with increasing soil moisture content. This implies that the electrical characteristics are affected by the increase of the soil moisture content. In the system design, the method based on tuning the physical length of the antenna can be used to improve the antenna return loss performance in soil without the need of increasing sensor node size. However, one concern with this method is that the tuned length could be affected by soil conditions, such as the soil moisture content. This effect will bring problems in practice as it is not sensible to replace the sensor node antenna with variations of the soil moisture content. In addition to the soil moisture content, the tuned length of the antenna can be affected by the factors shown below.

- The soil composition.
- The soil density.
- The depth of the sensor node.

The effects of these factors can be explored in future work.

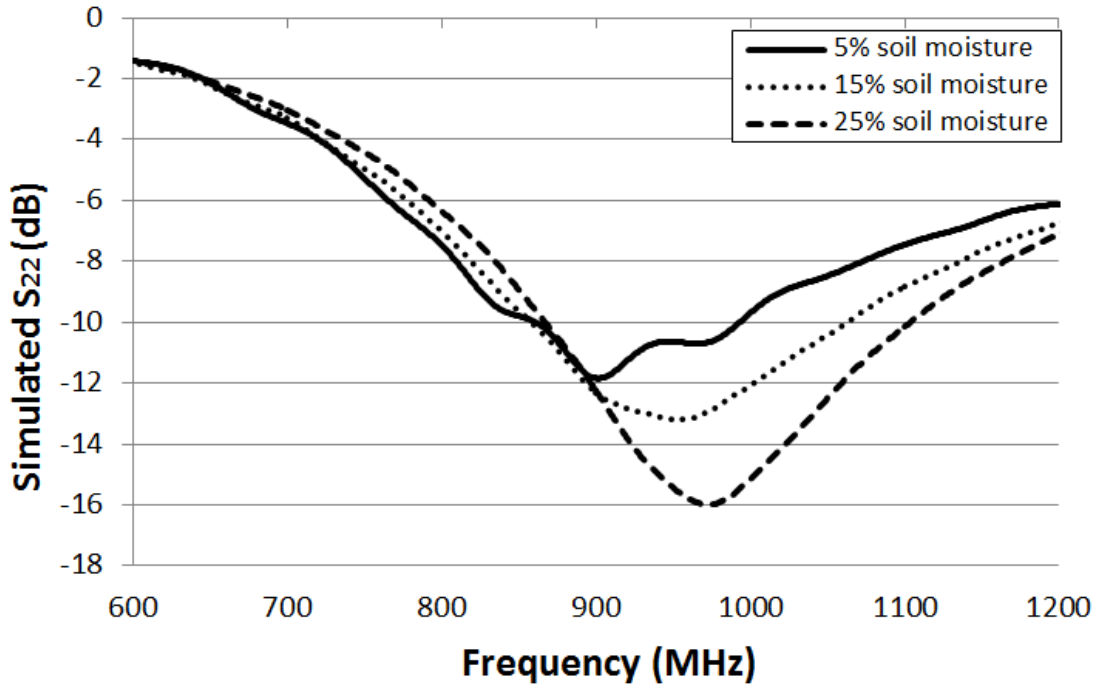

Figure 11.6: Simulated return loss of the buried dipole antenna whose half length, l is 54 mm at an air gap, g, of 10 mm and the soil moisture levels of 5%, 15% and 25%.

Instead of tuning the antenna physical length, the system performance can be optimised based on adjusting the operating frequency of the RFID reader. This method seeks to match the operating frequency to the resonant frequency of the sensor node antenna in the soil. With this method, it is necessary to explore the range of change in the resonant frequency of the sensor node antenna in the soil. The RFID reader antenna and the RF circuit of the sensor node must be able to operate in a wide frequency range which covers the resonant frequency of the sensor node antenna in the soil. During the process of the system performance optimisation, the RFID reader antenna is positioned above the sensor node. The reader system is then configured to sweep the operation frequency. The time taken to receive the signal from the sensor node is measured, and compared against the operating frequency.

11.10 On-board Sensors

The sensor node prototype presented in Chapter 8 includes a TMP 37 temperature sensor [45] and the node's peak power consumption is 1.68 mW. This power consumption is not realistic for the case that the sensor node is required to measure the soil moisture content. As described in Chapter 4, the proposed sensor node will include a soil temperature sensor and a soil moisture sensor, and can also include other sensors such as a pressure sensor, a soil pH sensor or a soil oxygen sensor. Table 2.1, presented in Chapter 2, compares the typical power consumption of the commercial sensors. In practice, the sensors that farmers would like to use have a higher energy budget, for example, the SM 150 soil moisture sensor [41]. However, the use of these sensors lead to a higher energy budget of the sensor node, and so results in a longer charging time of the sensor node.

The SM 150 soil moisture sensor operates with a peak power consumption of 90 mW [41] which is 546 times higher than the power consumption of the TMP 37 temperature sensor. In addition, it requires a minimum warming-up time of 1 second. When integrating the SM 150 moisture sensor into the sensor node prototype described in Chapter 8, the energy budget of the sensor node reaches 91.68 mW with a required power-on time of more than 1 s. With this energy budget, the super-capacitor of the sensor node needs to have a capacitance of at least 1.4 F. This capacitance is calculated based on Equation 11.4. It has been analysed in Chapter 8 that the charging time of the sensor node increases as the capacitance of the super-capacitor increases. For example, as presented in Figure 10.5, the measured time for charging up the 10 mF super-capacitor of the sensor node is 50 s at a depth of 0.4 m and a transmission power of 30.5 dBm. When increasing the capacitance to 1.4 F, the sensor node will have a charging time of more than an hour. This will lead to an unacceptably slow tractor speed. In order to improve the system performance, the design trade-offs described in Section 11.13 need to be considered.

The volume of the sensors is also one of the key parameters in the system design. The maximum dimension of the five commercial sensors are compared in Table 2.1 which is shown in Chapter 2. The TMP 37 temperature sensor has a maximum length of 0.48 cm [45]. The ICT02 soil oxygen sensor [43] has the largest volume with a maximum dimension of 6.5 cm. Increasing volume of the

sensor leads to a larger sensor node enclosure, which would affect the system deployment efficiency.

11.11 Sensor Node Capacitor

As described in Chapter 4, the sensor node uses a capacitor to store the energy harvested by the sensor node antenna. The value of capacitance of the capacitor is one of the key parameters that needs to be considered in the system design. As shown in Equation 8.1, the capacitance determines the amount of energy that can be stored in the capacitor. The capacitance also affects the charging time of the sensor node. A higher capacitance allows the capacitor to supply the on-board sensors with a higher energy budget. However, the charging time of the sensor node increases with increasing capacitance. This leads to a slow tractor speed.

In the system design, it is important to consider a minimum value of the capacitance at which the energy stored in the capacitor meets the energy budget of the sensor node. As shown in Chapter 8, the sensor node prototype with the 10 mF super-capacitor has a charging time of 110 s at a transmission power of 16 dBm. The measured discharging time is 9.9 s, which is approximately 2000 times of the minimum required power-on time estimated using Equation 8.3. This indicates that the charging time of the sensor node can be shortened by using a capacitor with a capacitance of less than 10 mF. The minimum value of the capacitance can be estimated using Equation 11.3.

$$4 \times (P_{peak} \times T) = \frac{1}{2} \times C \times (V_{max}^2 - V_{min}^2), \tag{11.3}$$

where P_{peak} (W) is the peak power consumption of the sensor node, T (s) is the required power-on time, C (F) is the value of the capacitance, V_{max} (V) and V_{min} (V) are the two threshold voltages of the P2110 RF harvester, which are 1.25 V and 1.02 V [123]. The left side of Equation 11.3 refers to the energy required by the sensor node, where 4 is a factor for compensating the energy loss within the P2110 RF harvester [123] and the energy loss due to the leakage current of the capacitor. The right side of the equation represents the stored energy that can be used to supply the sensor node. Through arranging Equation 11.3, the

minimum value of the capacitance is expressed as:

$$C = 15 \times P_{peak} \times T. \tag{11.4}$$

When using the commercial sensors, shown in Table 2.1, as the on-board sensor, the peak power consumption of the sensor node prototype can range from 1.68 mW to 250 mW. Figure 11.7 shows the plot of the estimated minimum capacitance, according to Equation 11.4, with increasing peak power consumption of the sensor node up to 250 mW at a required power-on time of 1 s. It is observed that the estimated capacitance increases as the peak power consumption increases. When the peak power consumption of the sensor node is 250 mW, the sensor node needs a capacitor with a capacitance of at least 3.75 F. As described in Section 11.10, a capacitance of 1.4 F can lead to an unacceptably slow tractor speed. When using a 3.75 F capacitor for the system design, it is important to consider the design trade-offs described in Section 11.13.

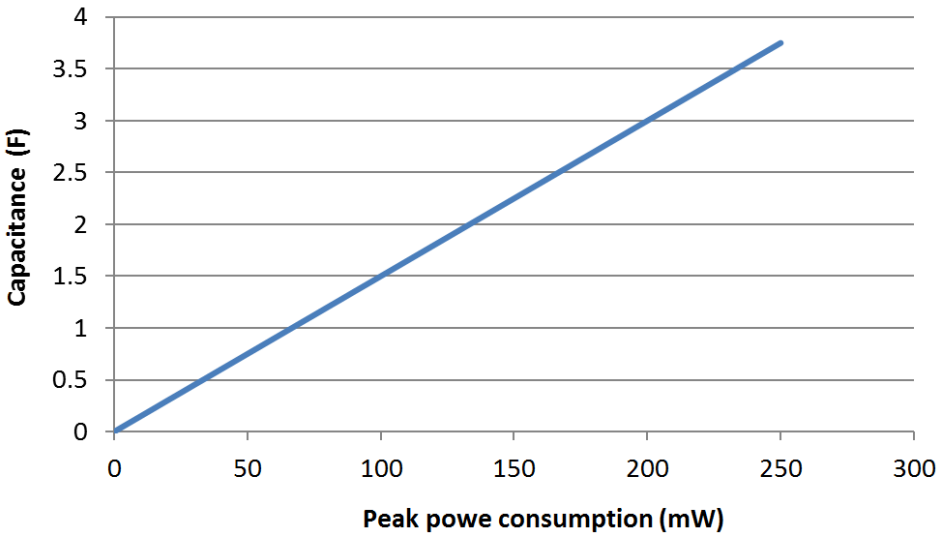

Figure 11.7: Plot of the estimated value of the capacitance with increasing peak power consumption of the sensor node at a required power-on time of 0.5 s.

In addition to the capacitance, there is a need to consider the self-discharge of the capacitor in the system design. As described in Chapter 8, this project has explored the self-discharge characteristic of super-capacitors and has also compared the self-discharge of the 5 commercial capacitors. In the system design, it is desirable to select a capacitor which has a low self-discharge rate. The Panasonic 1 F super-capacitor [127] is one of the optimal capacitors. As presented

in Chapter 8, the measured open-circuit voltage of the Panasonic 1 F supercapacitor drops by less than 0.1 V over 6 hours.

11.12 Tractor Speed

As described in Chapter 4, the RFID reader is mounted on a tractor, and travels with the tractor to interrogate the sub-soil sensor nodes. The tractor speed is one of the key parameters in the system design as it affects the *powering time* during which the each sensor node can harvest energy from the EM field generated by the RFID reader. Figure 11.8 presents a diagram showing that a sub-soil sensor node is within the coverage of the RFID reader antenna, where the yellow area refers to the radiation pattern of the reader antenna.

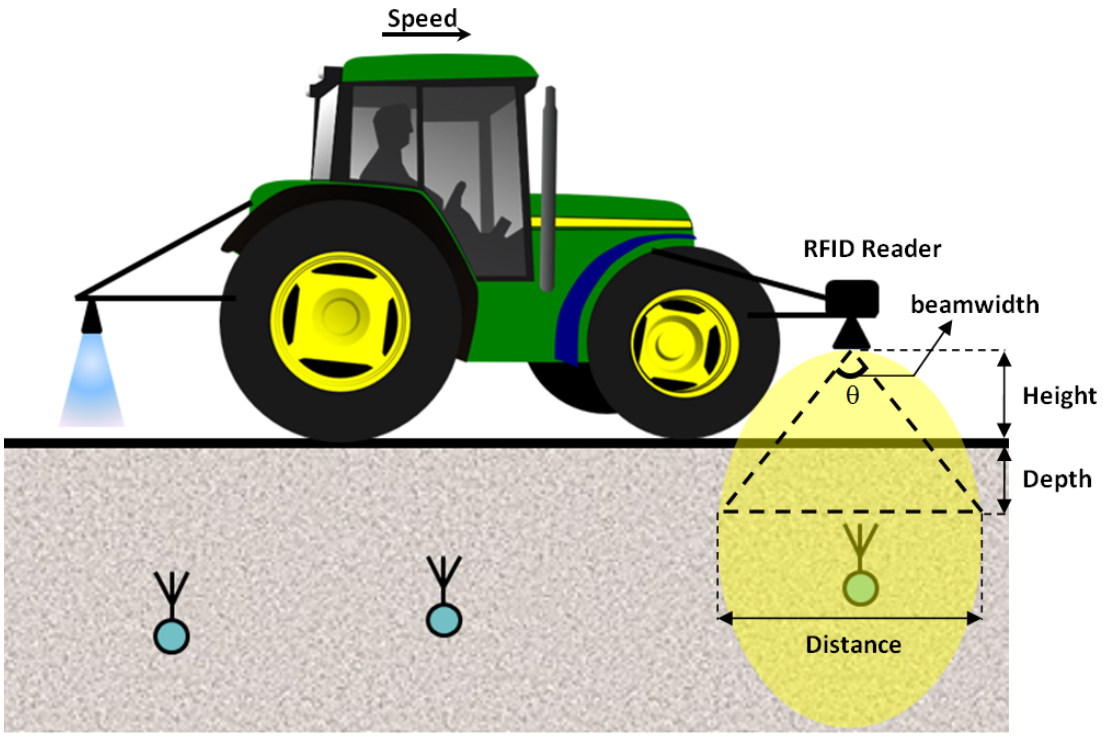

Figure 11.8: System concept diagram showing a sensor node is within the radiation coverage of the RFID reader antenna.

Based on the scene shown in Figure 11.8, the *powering time*, T_p (s) can be estimated using Equation 11.5.

$$T_p = \frac{Distance}{\nu} \tag{11.5}$$

where *Distance* (m) refers to the distance between the two locations at which the sensor node just enters and leaves the radiation coverage of the reader antenna, and the V (m/s) refers to the tractor speed. The *Distance* (m) can be calculated as:

$$Distance = 2 \times \left[(H + D) \times \tan(\frac{\theta}{2}) \right] \tag{11.6}$$

where H (m) refers to the height of the RFID reader antenna above the ground, D (m) refers to the depth of the sensor node within the soil and θ refers to the effective beamwidth of the RFID reader antenna in degrees. The final expression of the *powering time*, T_p (s) is:

$$T_p = \frac{2 \times \left[(H + D) \times \tan(\frac{\theta}{2}) \right]}{\nu}. \tag{11.7}$$

In practice, a tractor typically runs at a speed of 5.5 Kilometres Per Hour (kph) for ploughing operations [101]. According to Equation 11.7, the calculated *powering time* that is provided at the typical tractor speed is 0.8 s. The calculation is based on one of the realistic scenarios where the reader antenna height is 0.5 m, the depth of the sensor node is 0.4 m, and the beamwidth of the reader antenna, θ, is 70 degrees [138].

At the typical tractor speed, the sensor node can fail to harvest a sufficient energy for triggering the on-board DC/DC converter within the *powering time*. Therefore, it is necessary to slow down the tractor speed in order to maximise the *powering time*. Figure 11.9 presents the calculated *powering time* based on the realistic scenario with decreasing tractor speed from 5.5 kph to 0.1 kph. It is indicated that the *powering time* is extended by 48 s with decreasing tractor from 5.5 kph to 0.5 kph. However, a decrease of the tractor speed can affect farming efficiency, which may not be accepted.

Using a wide beamwidth antenna helps to maximise the *powering time*. Figure 11.10 shows the calculated *powering time* versus the beamwidth of the reader antenna at a tractor speed of 5.5 kph. It is observed that the *powering time* increases by 1 s when the antenna beamwidth increases from 40 degrees to 100 degrees.

However, as described in Section 11.2, an antenna with a wider beamwidth typically has a lower gain which limits the energy harvested by the sensor node. In addition, the *powering time* can be maximised by using the two RFID reader design described in Chapter 4. At a given tractor speed, this design doubles the *powering time* compared to the design of using a single RFID reader.

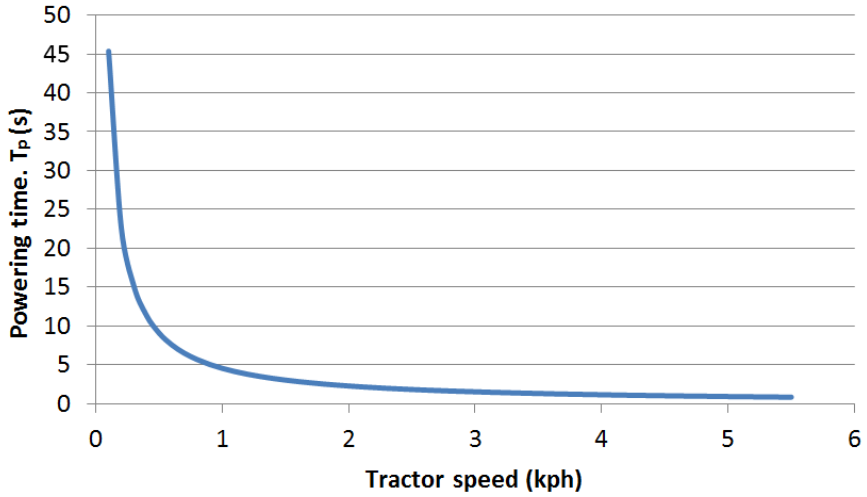

Figure 11.9: Plot of the calculated *powering time* against the tractor speed.

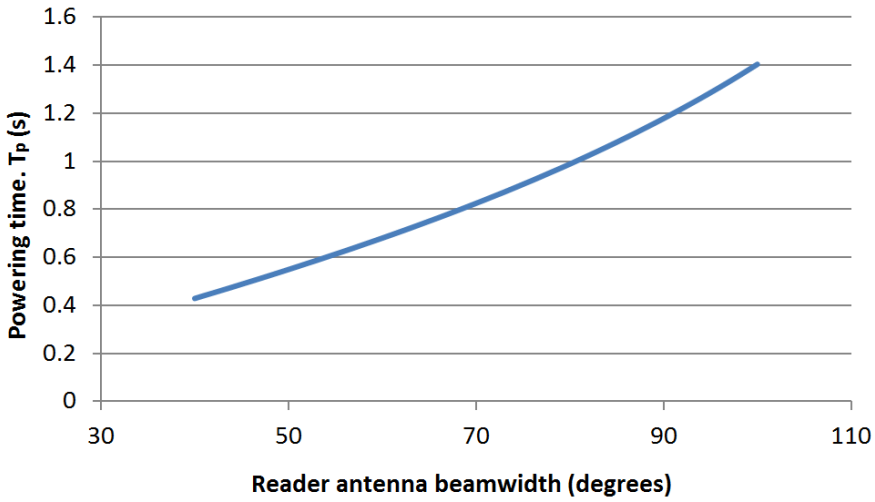

Figure 11.10: Plot of the calculated *powering time* against the reader antenna beamwidth.

Rather than mounting the RFID reader on farm machinery, farmers may prefer to carry a hand-held RFID reader for interrogating the sensor nodes. The system design with a hand-held RFID reader is described in Section 11.13.

11.13 Design Trade-offs

In the system design, it can be difficult to meet all design requirements described in Chapter 3 as design requirements can conflict. For example, although a smaller sensor node size helps improve the system deployment efficiency, it leads to a longer charging time and so can result in an unacceptably slow tractor speed. Hence, there is the need to consider design trade-offs. Table 11.4 summaries the potential design trade-offs between the parameters including the operating frequency band of the system (A), the beamwidth of the RFID reader antenna (B), the gain of the RFID reader antenna (C), the height of the RFID reader antenna (D), the transmission power of the RFID reader (E), the depth of the sensor node (F), the volume of the sensor node antenna (G), the air gap around the sensor node antenna (H), the volume of the on-board sensors (I), the energy budget of the on-board sensors (J), the capacitance of the on-board capacitor (K), the volume of the sensor node (L) and the tractor speed (M).

Table 11.4: Summary of the design trade-offs.

Parameters	B	C	D	E	F	G	H	I	J	K	L	M
A ↑	–	–	↓	↑	↓	↓	–	–	↓	↓	↓	↓
B ↑	–	↓	↓	↑	↓	↑	↑	–	↓	↓	↑	↑
C ↑	↓	–	↑	↓	↑	↓	↓	–	↑	↑	↓	↓
D ↓	–	–	–	↓	↑	↓	↓	–	↑	↑	↓	↑
E ↑	–	–	↑	–	↑	↓	↓	–	↑	↑	↓	↑
F ↑	–	–	↓	↑	–	↑	↑	–	↓	↓	↑	↓
G ↑	–	–	↑	↓	↑	–	–	–	↑	↑	↑	↑
H ↑	–	–	↑	↓	↑	–	–	–	↑	↑	↑	↑
J ↑	–	–	↓	↑	↓	↑	↑	–	–	↑	↑	↓
L ↑	–	–	↑	↓	↑	↑	↑	↑	↑	↑	–	↑
M ↓	–	–	↑	↓	↑	↓	↓	–	↑	↑	↓	–

As shown in Table 11.4, ↑ and ↓ represent an increase and a decrease respectively in the value of the parameters. These design trade-offs are described below.

1. **System operating frequency** - The RFID system can operate at a higher frequency, and this leads to a smaller physical size of the sensor node antenna and a smaller physical volume of the sensor node. However, the path loss between the RFID reader antenna and the sensor node increases with increasing operating frequency. Therefore when using a higher operating frequency, it is necessary to consider the following designs:
   - to lower the height of the RFID reader antenna,
   - to increase the transmission power of the RFID reader,
   - to deploy the sensor node at a smaller depth,
   - to use the sensors with a lower energy budget,
   - to reduce the tractor speed.

2. **Reader antenna beamwidth** - The RFID reader can use a wider beamwidth antenna. This helps extend the time when the sensor node can harvest energy, and so can allow accelerating the tractor speed. However, an antenna with a wider beamwidth typically has a lower gain which limits the energy harvested by the sensor node. The following methods can be required to improve the system performance:
   - lowering the height of the RFID reader antenna,
   - increasing the transmission power,
   - deploying the sensor node at a smaller depth,
   - using a larger sensor node antenna,
   - increasing the air gap around the sensor node antenna,
   - using the sensors with a lower energy budget.

3. **Reader antenna gain** - A higher gain of the reader antenna maximises EM radiation towards the direction of the sensor node. This can potentially allow:

- increasing the height of the RFID reader antenna,
- decreasing the transmission power,
- deploying the sensor node at a larger depth,
- using a smaller sensor node antenna,
- decreasing the air gap around the sensor node antenna,
- using the sensors with a higher energy budget.

However, the gain of an antenna typically increases at the expense of the antenna beamwidth. A narrow antenna beamwidth limits the time when the sensor node can harvest energy, and this can lead to a slow tractor speed.

4. **Reader antenna height** - At a given depth of the sensor node, the FSPL between the reader antenna and the sensor node antenna decreases with decreasing height of the reader antenna. Therefore the reader antenna height can be lowered for:

   - avoiding using a high transmission power,
   - deploying the sensor node at a larger depth,
   - minimising the volume of the sensor node antenna,
   - minimising the air gap around the sensor node antenna,
   - using the sensors with a higher energy budget,
   - maximising the tractor speed.

   As describe in Section 11.3, the system performance can be optimised based on adjusting the reader antenna height.

5. **Transmission power** - A higher transmission power improves the system performance, and it also provides the possibility to:

   - increase the height of the reader antenna,
   - deploy the sensor node at a larger depth,
   - minimise the volume of the sensor node antenna,
   - minimise the air gap around the sensor node antenna,

- use the sensors with a higher energy budget,
- accelerate the tractor speed.

As described in Section 11.4, the effect of EM radiation on crop growth needs to be assessed and considered.

6. **Sensor node depth** - When the sensor node is deployed at a larger depth within the the soil, there is a higher path loss between the reader antenna and the sensor node antenna. This will potentially lead to:
   - a lower height of the reader antenna,
   - a higher transmission power of the reader,
   - a larger volume of the sensor node antenna,
   - a larger air gap around the sensor node antenna,
   - a smaller energy budget of the sensor,
   - a slower tractor speed.

7. **Volume of the sensor node antenna** - The sensor node can use a physically larger antenna which is typically more efficient in energy harvesting. With increasing antenna size:
   - the reader antenna height can be increased,
   - the transmission power can be reduced,
   - the sensor node can be deployed at a larger depth,
   - the sensor node can use the sensors with a higher energy budget,
   - the volume of the sensor node increases,
   - the tractor can run at a faster speed.

8. **Air gap around the sensor node antenna** - A larger air gap reduces the effect of the soil on the performance of the sensor node antenna. This improves the system performance, and can allow:
   - increasing the reader antenna height,

- decreasing the transmission power,
- deploying the sensor node at a larger depth,
- using a physically smaller sensor node antenna,
- decreasing the sensor node volume,
- using the sensors with a higher energy budget,
- accelerating the tractor speed.

In the system design, it is necessary to consider the method of optimising the system performance based on adjusting the operating frequency, as described in Section 11.9.

9. **Sensors energy budget** - The total energy budget of the sensor node significantly depends on the energy budget of the on-board sensors. With increasing energy budget of the sensors, there can be the need to:
   - lower the height of the reader antenna,
   - increase the transmission power of the RFID reader,
   - deploy the sensor node at a smaller depth,
   - use a larger sensor node antenna,
   - increase the air gap around the sensor node antenna,
   - use a capacitor with a larger capacitance,
   - increase the volume of the sensor node,
   - slow down the tractor.

10. **Sensor node volume** - Farmers may deploy a limited number of sensor nodes manually, and a large sensor node volume can be acceptable. This scenario can allow:
    - increasing the volume of the sensor node antenna,
    - increasing the air gap around the sensor node antenna,
    - using the sensors with a larger volume.

A larger volume of the sensor node antenna or air gap provides the possibility to:

- increase the height of the RFID reader antenna,
- decrease the transmission power,
- deploy the sensor node at a larger depth,
- use the sensors with a higher energy budget,
- accelerate the tractor speed.

11. **Tractor speed** - Farmers may accept slower tractor speeds, and this increases the time when the sensor node can harvest energy, which can potentially allow:

    - increasing the height of the RFID reader antenna,
    - decreasing the transmission power of the RFID reader,
    - deploying the sensor node at a deeper position,
    - minimising the volume of the sensor node antenna,
    - minimising the air gap around the sensor node antenna,
    - using the sensors with a higher energy budget.

In the system design, it is also worth considering a scenario where farmers would prefer to carry the RFID reader by hand and move it manually over a field to interrogate sub-soil sensor nodes. For example, the proposed RFID sub-soil system can be primarily used to measure soil temperature and soil moisture content. Since the difference of these measurements at various locations within an one-hectare field should not change significantly, the density of the sensor nodes deployed in the field can be less than 5 nodes per hectare. In practice, farmers can directly locate a sensor node using a GPS module. A hand-held RFID reader then is used to dwell over the sensor node for interrogating the node. Figure 11.11 shows a concept diagram of the system with the hand-held RFID reader, where the hand-held RFID reader is configured to generate the EM field to power the sensor node. As shown in Figure 11.11, the reader user is able to optimise the system performance by adjusting the operating frequency, as

described Section 11.9, and increasing the transmission power of the hand-held reader through the control panel. In addition, the system performance can be optimised by manually adjusting the height of the reader antenna, as described in Section 11.3. Once the hand-held reader has received the backscattered signal from the sensor node, the reader indicators notify the user to switch off the reader. The user can then walk or drive to the location of another sensor node.

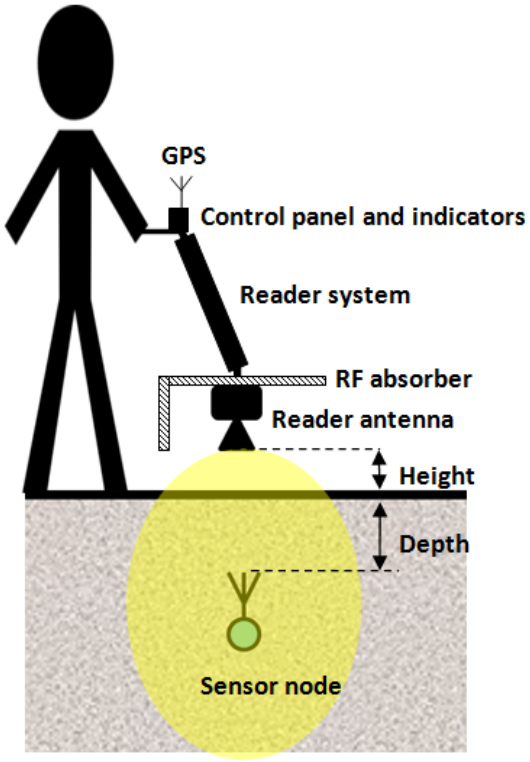

Figure 11.11: The system concept diagram showing that the sensor node is interrogated using the hand-held RFID reader.

With the proposed hand-held RFID reader, it can dwell over a sensor node for a period of up to a few minutes. Therefore, in practice the hand-held RFID reader provides a longer time when the sensor node can harvest energy than the on-vehicle reader. In addition, compared to the on-vehicle reader, the hand-held RFID reader is more flexible to control for implementing the system performance optimisation, and leads to a lower cost. However, the key concern of using the hand-held reader is the effect of the EM emission on the reader user. In the system design, the hand-held RFID reader system must comply with the FCC exposure guidelines [1]. The distance between the reader antenna and the user

body must exceed a minimum safe distance calculated based on Equation 11.1. A directional and high gain antenna, for example the 12.5 dBi MTI MT-263006 [158] antenna, is an optimal solution for the hand-held reader design. In practice, the directional antenna is used to maximise the EM emission in the direction of the sensor node. As described in Section 11.2, a higher antenna gain typically leads to a narrower antenna beamwidth. This helps to minimise the EM emission in the direction of the hand-held reader user. Additionally, as shown in Figure 11.11, the RF absorbers can be positioned between the user and the reader antenna. This method seeks to minimise the power density at the user body.

11.14 Summary

With the proposed RFID sub-soil system, the system performance is affected by the parameters including the operating frequency of the system, the type of the RFID reader antenna, the height of the RFID reader antenna above the ground, the transmission power of the RFID reader, the ambient RF noise around the tractor, the soil type and soil moisture content, the depth of the sensor node within the soil, the type and the volume of the sensor node antenna, the air gap around the sensor node antenna, the energy budget of the on-board sensors, the volume of the on-board sensors, the capacitance of the capacitor for storing the harvested energy, the tractor speed. The considerations of these parameters on the system design are discussed. In the system design, two design requirements can be conflicting. This brings the challenge to meet all design requirements. In the system, it is necessary to consider a series of design trade-offs. These design trade-offs are summarised and described.

In practice, the system performance can be potentially improved by 1) using a reader antenna with a higher gain, 2) lowering the reader antenna height above the ground, 3) increasing the transmission power of the RFID reader, and 4) reducing the tractor speed. In addition, the system performance can be optimised by 1) tuning the height of the reader antenna, and 2) adjusting the operating frequency of the system. Rather than mounting the RFID reader on farm machinery, farmers would prefer to interrogate the sensor nodes using a hand-held RFID reader. This scenario is analysed and described.

Chapter 12

Conclusions and Future Work

12.1 Conclusions

This thesis presents the research carried out into the development of an RFID sub-soil sensing system for supporting precision agriculture. The recent implementations of Wireless Sensor Network (WSN) systems in agriculture have been reported. The majority of these implementations have two common designs: 1) the systems use wired sensor nodes to avoid the problems of RF communication through soil; and 2) the sensor nodes are equipped with an on-board battery to supply the sensor node. However, these two designs can lead to problems in practice. The wired systems are always slow to deploy and are at risk of being damaged by farm machinery, and batteries are environmentally unacceptable. Passive RFID technology provides a solution for the implementation of a non-battery and non-wired sensor node. The sensor node is capable of harvesting energy from ElectroMagnetic (EM) fields and transmitting sensor measurements wirelessly. In this research, the proposed RFID sub-soil system integrates passive RFID technology and sub-soil sensing technology. The key feature of the system is that the sensor node does not contain a battery. Thus, once a node has been deployed, there is potentially no need to retrieve it for charging or maintenance. However, the high path loss of the sub-soil wireless channel leads to the challenge for the system to achieve an acceptable Quality of Service (QoS). The high path loss can potentially limit the energy that can be harvested by the sensor node and affect the Bit Error Rate (BER) performance of the communication link. A larger node antenna can be used to improve the system performance, but this will increase the sensor node enclosure size and so can affect the system deployment.

The high level design of the RFID sub-soil system has been presented in Chapter 4. The proposed RFID sub-soil system comprises a number of sub-soil sensor nodes and an RFID reader. The RFID sensor node is buried at a fixed depth within the soil and the RFID reader is mounted on a farm machinery, such as a tractor. The sensor node contains sensors and an RFID circuit that is used to harvest energy from EM fields and to transmit the sensor measurements provided by the sensors. The RFID reader basically comprises a transmitter and a receiver. In practice, the transmitter of the RFID reader generates a Continuous Wave (CW) signal to power the sensor nodes and the receiver of the RFID reader receives and demodulates the backscattered signals. The demodulated sensor measurements can be shared with other precision agriculture systems via a wireless local area network or a cellular mobile system.

The emphasis of this research is on achieving effective wireless communication through soil. The objectives of this research have been described in Chapter 1, and the corresponding achievements for these objectives are summarised below.

- CST EM simulations have been undertaken to characterise the effect of the soil on the sub-soil antenna performance and to investigate the path loss in the soil.
- A Software Defined Radio (SDR) RFID reader platform has been implemented using a National Instruments (NI) PXI system and NI LabVIEW software.
- An embedded passive RFID sensor node prototype has been designed, implemented and evaluated.
- Sub-soil experiments have been carried out to evaluate the performance of the sensor node prototype and also to characterise the path loss in the soil.
- Considerations for the future system design have been analysed and design trade-offs have been provided.

The CST simulation results presented in Chapter 6 show that the soil surrounding the antenna affects the antenna return loss, radiation efficiency and radiation pattern. This effect is not desirable as it limits the energy that can be harvested by the sub-soil sensor node. The use of a larger sensor node enclosure

helps reduce the impact on the antenna performance. However, a larger enclosure increases the overall size of the sensor node, which would make the sensor node difficult to deploy in practice. In the system design, a compromise between the system performance and the sensor node size needs to be considered. The simulations have characterised the path loss in the frequency band of 600 MHz to 1200 MHz and at a soil moisture contents from 5 % to 25 %. The simulation results show that the path loss increases with increasing frequency and increasing soil moisture content. In practice, the high path loss in soil can result in an unacceptable system performance. High transmission power can be used to improve the system performance.

The PXI-based RFID reader platform is configured and controlled using LabVIEW software. The platform includes an FPGA module which can be used to perform real-time signal processing functions. This allows the reader platform to meet timing requirements specified in the RFID EPC C1G2 protocol. The RFID reader platform has been used in the trials of reading from and writing to an example UPM Rafsec Dogbon RFID tag. In addition, the reader platform has allowed the evaluation of the tag sensitivity. At the time of implementing the RFID reader platform, there was no instrument found which could perform the same functions. In this research, the RFID reader has been implemented to evaluate the performance of the passive RFID sensor node prototype described in Chapter 8 and has also been used for a series of sub-soil experiments described in Chapter 9.

The design of the RFID sensor node prototype in this work was motivated by the fact that commercial RFID tags or sensor nodes do not meet the requirements of the desired RFID sensor node in this research. The implementation of the passive RFID sensor node prototype employs a printed dipole antenna and a P2110 module to harvest energy from EM fields at a centre frequency of 915 MHz. The operation of the sensor node prototype has been successfully tested using the PXI-based RFID reader platform. In addition, the sensor node performance has been evaluated. One of the key parameters of the sensor node is the charging time during which the capacitor voltage, V_{cap}, increases from the low threshold voltage, V_{min}, to the high threshold voltage, V_{max}. In the performance evaluation of the sensor node, the charging time of the sensor node has been measured,

and the following elements have been considered: 1) the power harvested by the sensor node; 2) the sensor node antenna; and 3) the capacitance of the on-board capacitor. The evaluation results show that the charging time decreases with increasing power harvested by the sensor node. A larger antenna helps shorten the charging time. However, increasing the antenna size can lead to an unacceptable sensor node size. The evaluation results also indicate that the self-discharge rate of the on-board capacitor affects the sensor node performance. In the system design, it is desirable to select a capacitor with a lower self-discharge rate.

In the sub-soil experiments, the charging time of the sensor node prototype and the power of the backscattered signal at the RFID reader antenna have been used as two parameters for the performance evaluation of the sensor node prototype. The following variables have been considered in the experiments: the transmission power of the RFID reader platform, the height of the RFID reader antenna, the depth of the sensor node and the soil moisture content. The method of measuring the charging time is based on using an independent data logging system which was deployed within the soil planter along with the sensor node prototype. The use of the data logging system was motivated by the need to avoid the potential leakage power along the wires linking the sensor node prototype to any devices outside the soil planter. During the experiments, the data logging system continuously sampled the system voltages of the sensor node and stored voltage samples on a standard Secure Digital (SD) card. The design and implementation of the data logging system have been described in Chapter 9.

The experimental results of the sensor node performance evaluation in air show that the sensor node performance is improved with increasing transmission power or decreasing propagation distance between the reader antenna and the sensor node. When the sensor node is buried within the soil, the experimental results indicate that the sensor node performance does not necessarily degrade with increasing depth from 0 m to 0.4 m. It is also shown that the soil moisture content has a limited effect on the charging time of the sensor node at a given depth. This implies that the power loss due to RF absorption by the soil is not the primary factor that affects the sensor node performance. The experimental results of the path loss characterisation show that the soil surrounding the sensor node affects the node antenna performance. With this effect, the characterised

path loss at a depth of 0 m is 5 dB higher than the characterised path loss in air. The experimental results also indicate that the characterised path loss remains constant with increasing depth of the sensor node from 0.25 m to 0.4 m, and that the increase of the soil moisture content does not significantly affect the characterised path loss. As determined from the experimental results, there can be a near-field coupling effect between the reader antenna and the sensor node antenna. With the near-field coupling effect, energy can be directly coupled to the sensor node antenna from the reader antenna. This has a significant impact on the sensor node performance. The existence of the near-field coupling effect has been investigated through an experiment which has been described in Chapter 10.

With the proposed RFID sub-soil system, the system performance is affected by the following parameters: the operating frequency of the system, the type of the RFID reader antenna, the height of the RFID reader antenna above the ground, the transmission power of the RFID reader, the ambient RF noise around the tractor, the soil type and soil moisture content, the depth of the sensor node within the soil, the type and the volume of the sensor node antenna, the air gap around the sensor node antenna, the energy budget of the on-board sensors, the volume of the on-board sensors, the capacitance of the capacitor for storing the harvested energy, the tractor speed. In the system design, it is necessary to consider these parameters. The considerations of these parameters on the system design have been described in Chapter 11. In practice, farmers can improve the system performance by using the methods summarised below.

- using a reader antenna with a higher gain,
- lowering the reader antenna height above the ground,
- increasing the transmission power of the RFID reader,
- reducing the tractor speed.

Farmers can also take advantage of the near-field coupling effect to optimise the system performance. The process of the system performance optimisation is based on adjusting the height of the reader antenna. In addition, there is the possibility to optimise the system performance through adjusting the operating frequency of the RFID reader. This method seeks to match the operating frequency to the resonant frequency of the sensor node antenna in the soil. Due to the challenge

to meet all design requirements, the trade-offs between the parameters will need to be considered in the system design. These design trade-offs have been summarised and described in Chapter 11.

Over the period of this PhD project, the paper entitled "LabVIEW-Based Emulation Platform for RFID Sub-soil System" was presented in the 1st Applied Radio System Research (ARSR) conference in April 2012. The author presented a project poster in the Electrical and Electronic Engineering (EEE) School Postgraduate Poster Conference, the University of Manchester, in November 2012. The poster was awarded the runner-up prize of the best posters. In January 2014, the paper entitled "Development of Plough-able RFID Sensor Network System for Precision Agriculture" was published in IEEE Radio Wireless Week (RWW) conference. The author attended the conference and also demonstrated the operation of the passive RFID sensor node prototype (as one of five demonstratives in the conference). Following the conference presentation and the technical demonstration, the research has received interests from academic institutions and industrial companies. This research was also referenced by an article, entitled "Ploughable sensors help farmers get more crop per drop" in New Scientist Magazine on 30 January 2014. All of the experience has supported the author to achieve the objectives of this PhD project.

12.2 Future Work

In this work, the sensor node performance evaluation has been based on practical trials with a soil planter indoors. However, the laboratory environment can never completely replicate a real application environment. The next phase of this research could focus on evaluating the sensor node performance in a farm field. The indoor experiments presented in Chapter 9 involved a sensor node depth range of 0 m to 0.4 m which is limited by the soil planter being used in the experiments. This range could be extended to a maximum depth of 1 m in the outdoor experiments, which would be able to cover the depth of most of crop roots [96]. It was implied from the indoor experimental results that the near-field coupling effect has an impact on the sensor node performance at a depth range of 0 m to 0.4 m. In the outdoor experiments, it will be necessary to further investigate and

characterise the near-field coupling effect.

The dielectric behaviour of the soil is one of the dependent parameters of the path loss in the soil. Due to the limitation on the time for this PhD research, the practical experiments in this work have not considered the soil type. In practice, there are many types of soil used for agricultural applications, such as peaty soil, chalky soil, silty soil, clay soil, and sandy soil. All these soil types can affect the system performance. Thus, future research could investigate the effect of soil types on the path loss in soil. Practical experiments can be carried out to evaluate and compare the system performance with various types of soils.

The sensor node prototype implemented in this work employs the printed dipole antenna shown in Chapter 8. The choice of this antenna was primarily for research purposes. The experimental results presented in Chapter 10 show that the antenna performance is still affected by the soil even though the sensor node enclosure provides an air gap of larger than 20 mm. Future work can include the design of antennas for underground applications. There are three objectives in the underground antenna design: 1) characterise the effect of the soil on the antenna, 2) minimise the effect of the soil on the antenna performance; and 3) minimise the physical size of the antenna. In the characterisation of the effect of the soil, it is necessary to consider the following parameters: the soil type, the soil moisture content, the soil compactness, the depth of the antenna within the soil. The following parameters can be used to evaluate the antenna performance in the soil: return loss, resonant frequency, gain, radiation pattern. Generally a small antenna can lead to an unacceptable antenna performance. For example, the sensor node can use a printed 900 MHz inverted F antenna [165] which has a small size of 4.3 cm $\times$ 2.0 cm. The maximum gain of the inverted F antenna is -0.12 dBi, which would lead to an unacceptably long charging time of the sensor node in practice. Hence, it will be important to consider the trade-off between the antenna physical size and the system performance in the system design.

One of the key elements of the proposed RFID sensor node is the on-board sensors. The development of sub-soil sensing technology can be explored in future work. The potential sensors which farmers would be interested in include: temperature sensors, soil moisture sensors, pH sensors, oxygen sensors, chemical

sensors for measuring soil nutritional ingredients. Since the sensor node does not contain a battery, the energy budget of the on-board sensors has a significant impact on the sensor node performance. As described in Chapter 11, the soil moisture sensor requires a high energy budget which would lead to an unacceptably long charging time of the sensor node. In the development of sub-soil sensors, the key objective is to minimise the energy budget of the sensors. The energy budget of a sensor will be evaluated using two parameters: 1) the peak power consumption of the sensor node; and 2) the response time or warm-up time of the sensor. In addition, the energy budget for reading the sensor needs to be considered. In the sensor design, a lower energy budget of the sensor node can limit the sensor performance, such as the accuracy of sensor measurements. Therefore, there can be a design trade-off between the sensor energy budget and the sensor performance.

With the proposed system, there will be a sensor network system which consists of a number of RFID sensor nodes in a field. One of key works in the future is to design and evaluate an RFID sensor node network system prototype. The design of the RFID sensor network system will need to investigate the following issues.

- What should be the node topology in a field?
- What is the appropriate distance between two nodes?
- If the nodes need to be closely spaced, how to avoid the problem of communication collision when two nodes are transmitting sensor measurements at the same time?

In addition to sub-soil sensing, the proposed RFID sensing system can be used to achieve above-ground environmental monitoring. Greenhouse monitoring is one of the potential applications. Within a greenhouse, passive RFID sensor nodes can be deployed to measure temperature, humidity and pressure within the greenhouse. These sensor nodes are wirelessly powered and interrogated by using a hand-held RFID reader. In practice, farmers can carry the RFID reader and move it manually within the greenhouse. The RFID reader can dwell over the sensor node for collecting sensor measurements. This approach helps ensure that the sensor node is able to harvest a sufficient energy that meets the energy

budget of the sensor node.

Although the proposed RFID sub-soil system in this work is designed for precision agriculture, this technology can be also applied in many other applications in environments where the use of batteries are undesirable or prohibited. Brownfield monitoring is one of the potential applications. Brownfields are usually associated with hazardous waste or pollution. Governments have increased investment on detecting environmental data of the brownfields for example by means of sensor systems and Geographic Information System (GIS) tools in order to evaluate redevelopment of these lands. An RFID-based wireless communication and sensor systems can provide a low-cost solution for monitoring brownfields. With an RFID sensing system, a number of passive RFID sensor nodes are deployed in brownfield land. The environmental monitoring of the brownfield can be efficiently achieved by using RFID readers to wirlessly power and interrogate these sensor nodes.

References

[1] Federall Communications Commission. *Guidelines for human exposure to radio frequency fields.* OET Bulletin 65, Edition 97-01, 1997.

[2] N. R. Peplinski, F. T. Ulaby, and M. C. Dobson. Dielectric properties of soils in the 0.3 - 1.3 ghz rnage. *IEEE Trabsactions on Geoscience and Remote Sensing*, Vol.33, pages:803 – 807, May 1995.

[3] Campbell Scientific CR5000 Datalogger. [Online]. Available at: `https://www.campbellsci.co.uk/cr5000-overview.`

[4] WSN System Overview . [Online]. Available at:`http://elf.cs.pub.ro/pm/wikihs2010/doku.php?id=hidden:overview`.

[5] P. V. Nikitin, K. V. S. Rao, and S. Lazar. An overview of near field uhf rfid. In *IEEE International Conference on RFID*, pages 167 – 174, 2007.

[6] *EPC Radio-Frequency Identity Protocols Class-1 Generation-2 UHF RFID Protocol for Communications at 860 MHz-960 MHz Version 1.2.0.* EPCglobal Inc, October 2008.

[7] L. Li, M. C. Vuran, and I. F. Akyildiz. Characteristics of underground channel for wireless underground sensor networks. In *Proceedings of the IFIP Mediterranean Ad Hoc Networking Workshop (Med-HocNet 07), Corfu*, June 2007.

[8] Patch antenna. [Online]. Available at: `https://en.wikipedia.org/wiki/Patch_antenna`.

[9] Farming for profit in the Egyptian desert. [Online]. Available at: `http://www.ruralpovertyportal.org/country/voice/tags/egypt/egypt_farming`.

[10] P. Patil, H. Vidya, S. Patil, and U. Kulkarni. Wireless sensor network for precision agriculture. *Proceedings of International Conference on Computational Intelligence and Communication Networks (CICN)*, Pages:763–766, October 2011.

[11] V. J. Adamchuk, J. W. Hummel, M. T. Morgan, and S. K. Upadhyaya. On-the-go soil sensors for presicison agriculture. *Computer and electronics in agriculture*, Vol. 44, pages:71–91, 2004.

[12] L. Ruiz-garcia, L. Lunadei, P. Barreiro, and J. I. Robla. Review a review of wireless sensor technologies and applications in agriculture and food industry: State of the art and current trends. *Sensors*, Vol. 9, pages:4728–4750, June 2009.

[13] Y. Kim, R. G. Evans, and W. M. Iversen. Remote sensing and control of an irrigation system using a distributed wireless sensor network. *IEEE Transactions on Instrumentation and Measurement*, Vol. 57, pages:1379–1387, July 2008.

[14] S. Yoo, J. Kim, S. Ahn, J.Sung, and D. Kim. Automated agriculture system based on wsn. In *IEEE International Symposium on Consumer Electronic (ISCE)*, pages 1–5, 2007.

[15] A. Garcia-Sanchez. *Wireless Sensor Networks for Precison Agriculture: Methods and Experiences.* Novel Sensor Technologies for Plant Phenotyping. [Online]. Available at:`http://www.plant-phenotyping-network.eu/lw_resource/datapool/_items/item_155/garcia-sanchez.pdf.`, 2012.

[16] R. Morais, M. A. Fernandes, S. G. Matos, C. Serodio, P. Ferreira, and M. Reis. A zigbee multipowered wireless acquision device for remote sensing applications in precision agriculture. *Elsevier Computers and Electronics in Agriculture*, Vol.62, pages:94–106, 2008.

[17] A. Baggio. Wirelss sensor networks in precision agriculture. In *Workshop on Real-World Wireless Sensor Networks (REALWSN 2005)*, 2005.

[18] A. Chehri, P. Fortier, and P. M. Tardif. Security monitoring using wireless sensor networks. In *Communication Networks Services Research*, pages 13–17, May 2007.

[19] G. Werner-Allen et al. Deploying a wireless sensor netwoek on an active volcano. *IEEE Internet Computing*, Vol.10, no. 2, pages:18–25, 2006.

[20] A. Sheth et al. Senslide: a sensor network based landslide prediction system. In *SenSys'05*, pages 280 – 281, 2005.

[21] K. Fisher, E. Wallen, P. P. Laenen, and M. Collins. Battery waste management life cycle assessment. *Final Report for Environmental Resources Management*, 2006.

[22] K. Finkenzeller. *RFID Handbook: Radio-Frequency Identification Fundamentals and Applications*. J. Wiley and Sons, 2003.

[23] A. K. Skrivervik. Implantable antennas: The challenge of efficiency. In *7th European Conference on Antenna and Propagation (EUCAP 2013)*, pages 3516–3520, 2013.

[24] M.M.Khan, A.Alomainy, and Y.Hao. Dual band and diverse radiation pattern antenna for power efficient and reliable on-body and off-body communications for healthcare applications. *IEEE Ant, Propag, Society Int. Symp.*, 2011.

[25] K.L.Wong and C.I.Lin. Characteristics of a 2.4-ghz compact shorted path antenna in close proximity to a lossy medium. *Micro. Opt. Technol. Lett*, 45(6):480 – 483, 2005.

[26] C. E. Johnson, R. L. Schafer, and S. C. Young. Controlling agriculture machinery. *Agriculture electronics-1983 and beyond: procedings of the national conference on agricultural electronics applications*, pages:114–119, 1983.

[27] J. V. Stafford. Implementing precision agriculture in the 21st century. *Elsevier: jornal of agriculture engineering research*, vol.76, pages:267–275, 2000.

[28] D. S. Fairchild. Soil information system for farming by kind of soil. *Proceedings of international interactive workshop on soil resource:their inventory, analysis and interpretations for use in the 1990's*, Pages:159–164, 1990.

[29] R. B. Ferguson and G. W. Hergert. Soil sampling for precision agriculture. *University of Nebraska-Lincoln EXTENSION*, EC154, 2009.

[30] M. Nemenyi, P.A. MesterhÃ¡zi, Zs. Pecze, and Zs. Stepan. The role of gis and gps in precision farming. *Elsevier Computers and Electronics in Agriculture*, Vol. 40:45 – 55, 2003.

[31] S. K. Seelan, S. Laguette, G. M. Casady, and G. A. Seielstad. Remote sensing applications for precision agriculture: A learning community approach. *Elsevier, Remote Sensing of Environment*, Vol. 88:157 – 169, 2003.

[32] S. Liaghat and S.K. Balasundram. A review: The role of remote sensing in precision agriculture. *Elsevier Remote Sensing of Environment*, Vol. 61:319 – 346, 1997.

[33] M.S. Moran, Y. Inoue, and E. M. Barnes. Opportunities and limitations for image-based remote sensing in precision crop management. *American Journal of Agricultural and Biological Sciences*, Vol. 5:50 – 55, 2010.

[34] A. D. Aggelopoulou, D. Bochtis, S. Fountas, K. C. Swain, T. A. Gemtos, and G. D. Nanos. Yield prediction in apple orchards based on image processing. *Precision Agriculture*, Vol. 12:448 – 456, 2010.

[35] J. D. Rhoades. Electrical conductivity methods for measuring and mapping soil sailinity. *Adv, Agronomy*, Vol. 49, pages:201–251, 1993.

[36] J. W. Hummel, L. D. Gaultney, and K. A. Sudduth. Soil property sensing for site-specific crop management. *Elsevier, Computers and electronics in agriculture*, Vol.14, pagess:121–136, 1996.

[37] R. Grisso, M. Alley, D. Holshouser, and W. Thomason. Precision farming tools:soil electrical conductivity. *Virgina Cooperation Extension(Virginia State University)*, Pages:442–508, 2009.

[38] Veris 3100. [Online]. Available at: `http://www.ext.colostate.edu/pubs/crops/00568.html`.

[39] EM38. [Online]. Available at: `http://www.fsaconsulting.net/mbia/land/land.html`.

[40] K. A. Sudduth, N. R. Kitchen, G. A. Bollero, D. G. Bullock, and W. J. Wiebold. Comparison of electromagnetic induction and direct sensing of soil electrical conductivity. *Agronomy Journal*, Vol.95, pages:472–482, 2003.

[41] SM150 Moisture Sensor. *From:*. a telephone meeting with Martin on 17th Feburary 2014.

[42] *Texas Instruments LMP91200 Configurable AFE for Low-Power Chemical Sensing Applications.* [Online]. Available at: `http://www.ti.com/lit/ds/snas571c/snas571c.pdf`.

[43] *ICTO2 Soil Oxygen Sensor.* [Online]. Available at:`http://www.ictinternational.com/products/icto2/icto2-soil-oxygen-sensor/`.

[44] *Honeywell Pressure Sensors.* [Online]. Available at: `http://uk.mouser.com/pdfdocs/HoneywellSSC.pdf`.

[45] Analog Devices TMP37. [Online]. Available at: `http://www.analog.com/static/imported-files/data_sheets/TMP35_36_37.pdf`.

[46] W. S. Lee abd V. Alchanatis, C. Yang, M. Hirafuji, D. Moshou, and C. Li. Sensing technologies for precision specialty crop production. *Elsevier, Computers and electronics in agriculture*, vol.74, pages:121–136, 2010.

[47] W. Dargie and C. Poellabauer. *Fundamentals of wireless sensor networks:theory and practice.* Wiley and Sons, 2010.

[48] J. Hautcoeur, L. Talbi, and M. Nedil. A comparative review of wireless sensor network mote technologies. In *2009 IEEE Sensors*, pages 1439–1442, 2009.

[49] *Tmote SKY.* [Online]. Available at: `http://www.eecs.harvard.edu/~konrad/projects/shimmer/references/tmote-sky-datasheet.pdf`.

[50] *MICA2 Wirelss Meausrement System.* [Online]. Available at: `http://www.eol.ucar.edu/isf/facilities/isa/internal/CrossBow/DataSheets/mica2.pdf`.

[51] *SHIMMER.* [Online]. Available at: `http://www.shimmersensing.com`.

[52] *IRIS Wireless Measurement System.* [Online]. Available at: `http://www.memsic.com/userfiles/files/datasheets/wsn/iris_datasheet.pdf`.

[53] A. Caicedo. *The sun small programmable object technology (Sun Spot): jave(tm) technology-based wireless sensor networks.* [Online]. Available at: `http://www.austinjug.org/presentations/SunSpots.pdf`.

[54] *EZ430-RF2500 Development Tool.* [Online]. Available at: `http://www.ti.com/lit/ug/slau227e/slau227e.pdf`.

[55] IEEE Standard 802.15.4. *IEEE Standard for Telecommunications and Information Exchange Between Systems - LAN/MAN - Specific Requirements - Part 15: Wireless Medium Access Control (MAC) and Physical Layer (PHY) Specifications for Wireless Personal Area Networks (WPANs).* 2002.

[56] IEEE Standard 802.15.1. *IEEE Standard for Telecommunications and Information Exchange Between Systems - LAN/MAN - Specific Requirements - Part 15: Wireless Medium Access Control (MAC) and Physical Layer (PHY) Specifications for Wireless Personal Area Networks (WPANs).* 2002.

[57] I. F. Akyildiz, W. Su, Y. Sankarasubramaniam, and E. Cayirci. Wireless sensor networks: a survey. *Elsevier Computer Networks*, Vol. 38, pages:393 – 422, March 2002.

[58] R. Raman. *Underground mine safety-are we doing enough?* Australasian Tunnelling Society. [Online]. Available at: `http://www.ictinternational.com/products/icto2/icto2-soil-oxygen-sensor/`.

[59] M. Lienard and P. Degauque. Natural wave propagation in mine environments. *IEEE Transaction on Antenna Propagation*, Vol. 48, no. 9, pages:1326–1339, 2000.

[60] P. Mariage, M. Lienard, and P. Degauque. Theoretical and experimental approach of the propagation of high frequency waves in road tunnels. *IEEE Transaction on Antenna Propagation*, Vol. 42, no. 1, pages:75–81, 1994.

[61] Z. Sun and I. F. Akyildiz. Channel modeling and analysis for wireless networks underground mines and road tunnels. *IEEE Transaction on Communications*, Vol.58, no. 6, pages:1758–1768, 2010.

[62] G. A. Kennedy and P. J. Foster. Low power wireless networks in underground mining. *Julius Kruttschnitt Mineral Research Centre*, Pages:60–67, 2004.

[63] A. G. Emslie, R. L. Lagace, and P. F. Strong. Theory of the propagation of uhf radio waves in coal mine tunnels. *IEEE Transaction on Antenna Propagation*, Vol. AP-23, no. 2, pages:192–205, 1975.

[64] M. Boutin, A. Benzakour, C. Despins, and S. Affes. Characterisation and modelling of a wireless channel at 2.4 and 5.8 ghz in underground channels. In *IEEE Wireless Communication System Symposium*, pages 517–521, 2006.

[65] I. F. Akyildiz and E. P. Stuntebeck. Wireless underground sensor networks: research challenges. *Elsevier Ad Hoc Networks*, Vol. 4, pages:669 – 686, July 2006.

[66] Z. Sun and I. F. Akyildiz. Underground wireless communciation using magnetic induction. In *IEEE International Conference on Communications (ICC) 2009*, pages 1–5, 2009.

[67] A. R. Silva. *Channel Characterization for Wireless Underground Sensor Networks*. Master's thesis, University of Nebraska-Lincoln, 2010.

[68] X. Yu, P. Wu, W, Han, and Z. Zhang. A survey on wireless sensor network infrastructure for agriculture. *Elsevier Computer standards and interfaces*, Vol.35, pages:59–64, May 2012.

[69] S. Finkenzeller. *RFID Sourcebook*. IBM, 2005.

[70] S. Lahiri. *RFID Sourcebook.* IBM, 2005.

[71] R. Weinstein. Rfid: a technical overview and its application to the enterprise. *IT Professional*, Vol. 7, pages:27 – 33, 2005.

[72] V. Chawla and D. S. Ha. An overview of passive rfid. *IEEE Communications Magazine*, Vol.45, pages:11–17, 2007.

[73] C. A. Balanis. *Antenna Theory: Analysis and Design.* John Wiley and Sons, 1997.

[74] C. A. Balanis. *Antenna Theory - Analysis and Design(second edition).* JOHN WILEY and SONS, INC, 1997.

[75] R. Schmitt. Understanding electromagnetic fields and antenna radiation takes no math. *Designfeature: electromagnetic fields*, Pages:77–87, 2000.

[76] A. D. Dehennis et al. A near-field-communication(nfc) enabled wireless fluorimeter for fully implantable biosensing applications. In *Solid-State Circuits Conference Digest of Technical Papers (ISSCC), 2013 IEEE*, pages 298 – 299, 2013.

[77] S. Ortiz. Is near-field communciation close to success? *Computer*, Vol. 39, no. 39, pages:18–20, 2006.

[78] E. Strommer, J. Kaartinen, J. Parkka, A. Ylisaukko-oja, and I. Korhonen. Application of near field communication for health monitoring in daily life. In *IEEE International Conference on Engineering in Medicine and Biology*, pages 3246 – 3249, 2006.

[79] K. Fotopoulou and B. W. Flynn. Optimum antenna coil structure for inductive powering of passive rfid tags. In *IEEE International Conference on RFID*, pages 71 – 77, 2007.

[80] *BBC News: Wireless energy promise powers up.* [Online]. Available at: `http://news.bbc.co.uk/1/hi/technology/6725955.stm`.

[81] G. Stuber. *Principles of mobile communication, second edition.* Kluwer Academic, 2001.

[82] *UPM Raflatac DogBone Tag.* [Online]. Available at: `http://www.rfidtags.com/documents/UPM-DogBone-Datasheet.pdf`.

[83] *Monza RFID tag chip.* [Online]. Available at: `http://www.impinj.com/`.

[84] R. Glidden, C. Bockorick, S. Cooper, C. Diorio, D. Dressler, V. Gutnik, C. Hagen, D. Hara, T. Hass, T. Humes, J. Hyde, R. Oliver, O. Onen, A. Pesavento, K. Sundstrom, and M. Thomas. Design of ultra-low-cost uhf rfid tags for supply chain applications. *IEEE Communications Magazine*, Vol. 44, pages:140–151, 2004.

[85] J. D. Gibson. *Principles of Digital and Analog Communications,*.

[86] Timothy Miller A, Brian Borchers B, Jan M. H. Hendrickx A, Sung ho Hong A, Henk A. Lensen C, and Piet B. W. Effect of soil moisture on landmine detection using ground penetration radar. In *Fifth International Symposium on Technology and the Mine Problem*, January 2002.

[87] T. W. Ammar, T. P. Weldon, and A. Y. Rathore. Wave propagation model and simulations for landmine detection. Technical report, University of North Carolina - Charlotte, Department of Electrical and Computer Engineering, 1999.

[88] D. J. Daniels. Gpr for landmine detection, an invited review paper. In *Proceedings of the Tenth International Conference on Ground Penetrating Radar, 2004*, pages 7–10, 21-24 June 2004.

[89] M. T. Hallikainen, F. T. Ulaby, M. C. Dobson, M. A. Erayes, and L. Wu. Microwave dielectric behavior of wet soil part i: Empirical models and experimental observations. *IEEE Transactions on Geoscience and Remote Sensing*, Vol. GE-23, pages:25 – 34, January 1985.

[90] P. W. Birkeland. *Pedology, Weathering and Geomorphological Research*. New York: Oxford University Press, 1974.

[91] M. C. Dobson, F. T. Ulaby, M. T. Hallikainen, and M. A. El rayes. Microwave dielectric behavior of wet soil part ii: Dielectric mixing models. *IEEE Trabsactions on Geoscience and Remote Sensing*, Vol. GE-23, pages:35 – 46, January 1985.

[92] J. A. Lane and J. A. Saxton. Dielectric dispersion in pure polar liquids at very high radar frequencies, iii, the effect of electrolytes in solution. *Proceedings of the royal society a mathematical physical and engineering sciences*, Vol.214, pages:531 – 545, 1952.

[93] A. Stogryn. Equations for calculating the dielectric constant of saline water. *IEEE Trabsactions on Microwave Theory and Techniques*, Vol.MTT - 19, pages:733 – 736, 1971.

[94] MATLAB. [Online]. Available at: `http://uk.mathworks.com/products/matlab/`.

[95] X. Yu, P. Wu, W. Han, and Z. Zhang. A survey on wireless sensor network infrastructure for agriculture. *Elsevier Computer standard and Interfaces*, Vol. 35, pages:59 – 64, May 2012.

[96] R. O. Ashley, W. H. Neibling, and B. A. King. Irrigation scheduling-using water-use tables. *Challenge of Agriculture, University of Idaho*, CIS 1039, 1996.

[97] *Vegetable Root Depth-to Gauge Watering Depth*. University of California Cooperative Extension. [Online]. Available at: `http://celosangeles.ucanr.edu/files/121762.pdf`, September 2011.

[98] *Usual Planting and Harvesting Dates for U.S. Field Crops.* United States Deparment of Agriculture, Demceber 1997.

[99] Planting and havesting times for garden vegetables. *IOWA STATE UNIVERSITY-Extension and Outreach*, PM 534, 2013.

[100] Constantine A. Balanis. *Modern Antenna Handbook.* John Wiley and Sons, 2011.

[101] A. O. Adewoyin and E. A. Ajav. Fuel consumption of some tractor models for ploughing operations in the sandy-loam soil of nigeria at various speeds and ploughing depths. *Agric Eng Int: CIGR Journal*, Vol. 15, No.3, pages:67–74, 2013.

[102] *Circulator and Isolater, unique passive devices.* Philips Semiconductors, Application Note 98035, 23 May 1998.

[103] CST STUDIO SUITE. [Online]. Available at: `https://www.cst.com/.`

[104] J. M. Tiusanen. Wideband antenna for underground soil scout transmission. *IEEE Antennas and Wireless Propagation Letters*, Vol.5, issue. 1, pages:517–519, 2006.

[105] S. Rahman. *PVC Pipe and Fittings: Underground Solutions for Water and Sewer Systems in North America.* 2nd Brazilian PVC Congress, 2007.

[106] Brain C. Wadell. *Transmission Line Design Handbook.* Artech House Antennas and Propagation Library, 1991.

[107] W. Stutzman and Gary Thiele. *Antenna Theory and Design.* 2nd Edition JOHN WILEY and SONS, 1998.

[108] B. K. Bellingham. Method for irrigation scheduling based on soil moisture data acquisiton. *the 2009 Irrigation Distrcit Conference, by the United States Committee on Irrigation and Drainage*, 2009.

[109] National Instrument PXI System. [Online]. Available at:`http://www.ni.com/pxi/.`

[110] R. G. Machado and A. M. Wyglinski. Software defined radio: Bridging the analogdigital divide. *Proceedings of the IEEE*, Vol.103, issue. 3, pages:409–423, 2015.

[111] P. V. Nikitin and K. V. S. Rao. Labview-based uhf rfid tag test and measurement system. *IEEE Transactions on Industrial Electronics*, Vol. 56, NO.7, pages:2374–2380, 2009.

[112] M. Buettner and D. Wetherall. *A Flexible Software Radio Transceiver for UHF RFID Experimentation: UW TR: UW-CSE-09-10-02 ABSTRACT.* [Online]. Available at: ftp://ftp.cs.washington.edu/tr/2009/10/UW-CSE-09-10-02.PDF.

[113] *NI-VISN-100 RFID Tester.* [Online]. Available at: `www.vi-china.com.cn`.

[114] XILINX Virtex-5 FPGA. [Online]. Available at:`http://www.xilinx.com/support/documentation/data_sheets/ds100.pdf`.

[115] National Instrument LabVIEW Software. [Online]. Available at: `http://www.ni.com/labview/`.

[116] *A Digital Downconverter for the NI 5734.* [Online]. Available at: `http://www.ni.com/example/31525/en/`, 2013.

[117] UPM Raflatac Dogbone RFID tag . [Online]. Available at:`http://www.upmraflatac.com/europ/eng/images/51_68732.pdf`.

[118] RFTECHNICS Omnidirectional Antenna . [Online]. Available at: `http://rftechnics.com/data/RFT_OMV_02_8690_Antenna.pdf`.

[119] *LabVIEW FPGA Compile Worker Compile Time Benchmarks.* [Online]. Available at:`http://www.ni.com/white-paper/14040/en/`, 2013.

[120] L. Catarinucci, D. De Donno, M. Guadalupi, F. Ricciato, and L. Tarricone. Performance analysis of passive uhf rfid tags with gnu-radio. In *2011 IEEE International Symposium on Antennas and Propagation (APSURSI).*, pages 541 – 544, 2011.

[121] J. Kimionis, A. Bletsas, and J. N. Sahalos. Design and implementaion of rfid systems with software defined radio. In *Proceedings of 6th European Conference on Antennas and Propagation (EUCAP)*, pages 3464–3468, 2012.

[122] P. V. Nikitin, S. Ramamurthy, R. Martinez, and K. V. S. Rao. Passive tag-to-tag communciation. In *Proceedings of 2012 IEEE International Conference on RFID*, pages 177–184, 2012.

[123] Powercast P2110 RF harvester. [Online]. Available at:http://www.powercastco.com/PDF/P2110-datasheet.pdf.

[124] Powercast P2110 Evaluation Board. [Online]. Available at:http://www.powercastco.com/PDF/P2110-EVB.pdf.

[125] M. Winter and R. J.Brodd. What are batteries, fuel cells, and supercapacitors? *Chemical Reviews*, Vol. 104, pages:4245–4269, 2004.

[126] R. Kotz and M. Carlen. Principles and applications of electrochemical capacitors. *Electrochimica Acta*, Vol. 45(15), pages:2483–2498, 2000.

[127] Panasonic 1F 5.5V Super-capacitor. [Online]. Available at:http://www.farnell.com/datasheets/1725487.pdf.

[128] PowerStor 1 F 2.7 V super capacitor. [Online]. Available at:http://www.farnell.com/datasheets/1640983.pdf.

[129] AVX 30mF 5.5V super capacitor. [Online]. Available at:http://www.avx.com/docs/catalogs/bestcap.pdf.

[130] Cellergy Supercapacitors. . http://www.mouser.com/pdfDocs/Cellergy_LineCard.pdf.

[131] Microchip PIC18LF14K22. [Online]. Available at:http://www.microchip.com/wwwproducts/Devices.aspx?dDocName=en538160.

[132] SKYWORKS AS193-73. [Online]. Available at:http://www.skyworksinc.com/uploads/documents/200186C.pdf.

[133] Altium Designer. *From:*. http://www.altium.com/.

[134] Rainee N. Simons. *Coplanar Waveguide Circuits, Components, and Systems*. John Wiley and Sons, 2004.

[135] MAPLAB IDE. [Online]. Available at:http://www.microchip.com/pagehandler/en-us/devtools/mplab/home.html.

[136] TEXS INSTRUMENTS hex inverter. [Online]. Available at:http://www.ti.com/lit/ds/symlink/sn74hc04.pdf.

[137] National Instrument MyDAQ. [Online]. Available at:`http://www.ni.com/mydaq/`.

[138] Cellular Patch Antenna A0007-01. [Online]. Available at:`http://www.wimo.com/`.

[139] Mini-Circuit ZEDC-15-2B Directional Coupler. [Online]. Available at:`www.minicircuits.com/`.

[140] Texas Instruments LMC6462 Operational Amplifier. [Online]. Available at:`http://www.ti.com/product/lmc6462`.

[141] EAD Blade Antenna . [Online]. Available at: `http://www.ead-ltd.com/antennas/gsm-cellular-3g-antennas/pentablade-penta-band-gsm-3g-blade-antenna`.

[142] GSM ANT-GHEL2-1 Antenna. *From:*. `http://docs-europe.electrocomponents.com/webdocs/129e/0900766b8129e5c9.pdf`.

[143] Panasonic 1000uF 16V Electrolytic Capacitor. [Online]. Available at: `http://www.farnell.com/datasheets/1897635.pdf`.

[144] B. W. Ricketts and C. Ton-That. Self-discharge of carbon-based supercapacitors with organic electrolytes. *Journal of Power Sources, ELSEVIER*, Vol. 89, pages:64–69, 2000.

[145] Y. Diab, P. Venet, H. Gualous, and G. Rojat. Self-discharge characterization and modeling of electrochemical capacitor used for power electronics applications. *IEEE Transactions on Power Electronics*, Vol. 24, pages:510–517, 2008.

[146] G. V. Merrett. Supercapacitor leakage in energy harvesting sensor nodes:fact or fiction? In *2012 9th International Conference on Networked Sensing Systems (INSS)*, pages 1–5, 2012.

[147] EVE ER34615 Lithium Battery. [Online]. Available at: `http://www.evebattery.com/asp_bin/upimg/pdf/20111210114340.pdf`.

[148] Microchip PIC18LF26K22 Microcontroller. [Online]. Available at:`http://www.microchip.com/wwwproducts/Devices.aspx?dDocName=en547748`.

[149] Microchip MCP1525 Voltage Reference IC. [Online]. Available at:http://ww1.microchip.com/downloads/en/DeviceDoc/21653a.pdf.

[150] NXP PCF 8563 Real-Time Clock. [Online]. Available at:http://www.nxp.com/documents/data_sheet/PCF8563.pdf.

[151] Transcend 2 GB SD Card. [Online]. Available at:http://uk.transcend-info.com/Products/No-6.

[152] Analog Devices ADG 804 multiplexer. [Online]. Available at:http://www.analog.com/static/imported-files/data_sheets/ADG804.pdf.

[153] Secure Digital Input/Output (SDIO) Card Specification Version 1.00. [Online]. Available at:http://www.sandisk.com/media/File/OEM/Manuals/SD_SDIO_specsv1.pdf.

[154] HxD Freeware Hex Editor and Disk Editor. [Online]. Available at:http://mh-nexus.de/en/hxd/.

[155] Mini-Circuit ZHL-1000-3W+ High Power Amplifier. [Online]. Available at:www.minicircuits.com/pdfs/ZHL-1000-3W.pdf.

[156] UK Office of Communcations. [Online]. Available at: www.ofcom.org.uk.

[157] HI 98331 Direct Soil Conductivity and Temperature Meter. [Online]. Available at: http://shop.hannainst.com/downloads/dl/file/id/1769/manhi_98331.pdf.

[158] MT-263006/N 902-928 MHz 12.5dBi V/H POLARITY DIRECTIONAL ANTENNA. [Online]. Available at: http://www.mtiwe.com/?CategoryID=219&ArticleID=72.

[159] Directional Flat Panel Antenna PA9-12. [Online]. Available at: http://www.lairdtech.com/products/pa9-12.

[160] MT-263003/N 902-928 MHz 10dBi V/H POLARITY DIRECTIONAL ANTENNA. [Online]. Available at: http://www.mtiwe.com/?CategoryID=219&ArticleID=71.

[161] SlimLine A4030L Linear Polarised UHF RFID Antenna. [Online]. Available at: http://www.times-7.com/a4030l-linear-polarised-uhf-antenna.html.

[162] Impinj Threshold Antenna. [Online]. Available at: `https://support.impinj.com/hc/en-us/articles/202755668-Threshold-Antenna-Datasheet`.

[163] The council of the european communities. *Council Directive on the suppression of radio interface produced by agricultural or forestry tractor(electromagnetic compability)*. 75/322/eec, 1975.

[164] *Telecommunications Analysis Services User's Reference Guide*. Dept. of Commerce, National Telecommunications and Information Administration, Institute for Telecommunication Sciences, Spectrum Utilization Division, 1979.

[165] 915MHz 868MHz and 955 MHz Inverted F Antenna. [Online]. Available at: `http://www.ti.com/lit/an/swra228c/swra228c.pdf`.

Appendixes - On CD ROM

- **Appendix A:** The specification of the EPC Class 1 Generation 2 RFID Protocol.
- **Appendix B:** The CST files for designing the RFID sub-soil system model described in Chapter 5.
- **Appendix C:** The LabVIEW code for implementing the RFID reader implementation presented in Chapter 7.
- **Appendix D:** The Altium Designer files for designing the sensor node prototype PCB presented in Chapter 8.
- **Appendix E:** The C code and the MPLAB files for programming the embedded system of the sensor node prototype presented in Chapter 8.
- **Appendix F:** The LabVIEW code for evaluating the sensor node prototype described in Chapter 8.
- **Appendix G:** The Altium Designer files for designing the SD data logging system PCB presented in Chapter 9.
- **Appendix H:** The C code and the MPLAB files for programming the embedded system of the SD data logging system presented in Chapter 9.